Technische Universität München

Department of Chemistry and Catalysis Research Center
Chair of Technical Electrochemistry

Studies on the Differentiation and Quantification of Degradation Phenomena in Silicon-Graphite Anodes for Lithium-Ion Batteries

Morten Wetjen

Vollständiger Abdruck der von der Fakultät für Chemie der
Technischen Universität München zur Erlangung des akademischen Grades eines

Doktors der Naturwissenschaften (Dr. rer. nat.)

genehmigten Dissertation.

Vorsitzende:	Prof. Dr. Corinna R. Hess
Prüfer der Dissertation:	1. Prof. Dr. Hubert A. Gasteiger
	2. Prof. Dr. Bastian Märkisch
	3. Prof. Dr. Andreas Hintennach

Diese Dissertation wurde am 20.07.2018 bei der Technischen Universität München eingereicht und durch die Fakultät für Chemie am 31.07.2018 angenommen.

Abstract

Silicon is the most promising anode active material for future lithium-ion batteries and an integral part of most development roadmaps to improve the energy density. However, the realization of its high theoretical specific capacity on a cell level is largely impaired by dramatic volumetric changes of the silicon particles upon repeated (de-)lithiation and ongoing side reactions at the silicon/electrolyte interface. For that reason, it is the overarching goal of this PhD thesis to develop a more comprehensive and quantitative understanding of the underlying degradation phenomena of blended silicon-graphite anodes and to evaluate their impact on practical lithium-ion batteries. Hence, we introduce a new $LiFePO_4$-based pseudo full-cell configuration to differentiate the degradation phenomena and investigate them *post mortem* by means of electron microscopy, impedance spectroscopy, and ^{19}F-NMR spectroscopy. Further, we introduce neutron depth profiling (NDP) as a powerful technique to monitor lithium concentration gradients in silicon and graphite-based anodes, which we use to investigate depth- and quantity-resolved the solid-electrolyte-interphase (SEI) growth across the entire thickness of an electrode. Finally, we evaluate new strategies to realize silicon-based anodes in lithium-ion batteries regarding their efficacy and applicability, including prelithiation of SiG//NMC811 full-cells, sacrificial salts in SiG//LNMO full-cells, and new electrolyte additives.

Kurzfassung

Silicium ist das vielversprechendste Anoden-Aktivmaterial für zukünftige Lithium-Ionen-Batterien und ein fester Bestandteil der meisten Entwicklungs-Roadmaps zur Verbesserung der Energiedichte. Die Realisierung der hohen theoretischen spezifischen Kapazität auf Zellebene wird jedoch durch dramatische volumetrische Änderungen der Siliciumpartikel bei wiederholter (De-)Lithiierung sowie fortlaufender Nebenreaktionen an der Silicium/Elektrolyt-Grenzfläche stark beeinträchtigt. Aus diesem Grund ist es das übergeordnete Ziel dieser Doktorarbeit ein umfassenderes und quantitatives Verständnis der zugrunde liegenden Abbauphänomene von gemischten Silicium-Graphit-Anoden zu entwickeln und ihre Auswirkungen auf praktische Lithium-Ionen-Batterien zu bewerten. Dazu führen wir eine neue $LiFePO_4$-basierte Pseudo-Vollzellen-Konfiguration ein, um die Abbauphänomene zu differenzieren und sie mittels Elektronenmikroskopie, Impedanzspektroskopie und ^{19}F-NMR-Spektroskopie *post mortem* zu untersuchen. Ferner stellen wir die Neutronentiefenprofilierung (NDP) als leistungsfähige Technik zur Bestimmung von Lithiumkonzentrationsgradienten in Silicium- und Graphitanoden vor, mit der wir das Wachstum der Festkörper-Elektrolyt-Grenzphase (SEI) Tiefen- und Mengen-aufgelöst über die gesamte Dicke einer Elektrode untersuchen. Abschließend evaluieren wir neue Strategien zur Realisierung von Silicium-basierten Anoden in Lithium-Ionen-Batterien hinsichtlich ihrer Wirksamkeit und Anwendbarkeit, einschließlich der Prälithiierung von SiG//NMC811-Vollzellen, des Einsatzes von Opfersalzen in SiG//LNMO-Vollzellen und neuer Elektrolytadditive.

Contents

List of Acronyms

Abbreviation	**Description**
BET	Brunauer-Emmett-Teller
BMS	Battery management system
CE	Coulombic efficiency
CCCV	Constant current constant voltage
CV	Cyclic voltammetry / constant voltage
EC	Ethylene carbonate
EDS	Energy dispersive X-ray spectroscopy
EIS	Electrochemical impedance spectroscopy
EMC	Ethyl methyl carbonate
DiFEC	Di-fluoroethylene carbonate
DMC	Dimethyl carbonate
DMSO-d6	Deuterated dimethyl sulfoxide
DOD	Depth-of-discharge
dQdV	Differential capacity
FEC	Fluoroethylene carbonate
LCO	Lithium cobalt oxide ($LiCoO_2$)
LEDC	Lithium ethylene dicarbonate
LiPAA	Lithium poly(acrylate)
LFP	Lithium iron phosphate ($LiFePO_4$)
LNMO	Lithium nickel manganese oxide ($LiNi_{0.5}Mn_{1.5}O_4$)
NDP	Neutron depth profiling
NMC	Lithium nickel manganese cobalt oxide ($LiNi_xMn_yCo_zO_2$)
NMR	Nuclear magnetic resonance
OEMS	On-line electrochemical mass spectrometry
SEI	Solid-electrolyte-interphase
SEM	Scanning electron microscopy
SiG	Silicon-graphite
STEM	Scanning transmission electron microscopy
SOC	State-of-charge
XRD	X-ray diffraction

1 Introduction

1.1 Dusk or Dawn of Lithium-Ion Batteries?

In the 1980's, many kinds of mobile gadgets, including video cameras, notebooks, and cellular phones, were gaining increasing popularity.[1] Secondary nickel-cadmium (Ni-Cd) batteries were the state-of-the-art technology at that time, however, their low practical energy density and serious environmental concerns inhibited them from meeting the increasing demand for mobile high-energy storage devices.[2] To overcome this drawback, several companies, including Exxon, Moli Energy, and Toschiba, were researching on lithium metal batteries.[3] Using metallic lithium as anode promised high energy densities because of its low atomic weight and low electrochemical potential.[4] However, these batteries were suffering from poor cycling performance and severe safety issues caused by the growth of lithium dendrites during the deposition of metallic lithium on the anode, which led occasionally to short circuits and even explosions.[5,6] Following a product recall of cellular phones using lithium/MoS_2 batteries from Moli Energy, which was triggered by a vent of combustible gases and flame formation causing injury to a consumer, companies and researchers were desperately looking for safer and more reliable alternatives.[7]

The lithium-ion battery was originally developed in Japan by Asahi Kasei Corporation and first commercialized by Sony Corporation in 1991.[8] To mitigate the problems associated with lithium metal anodes, the new cell chemistry was entirely based on a host-guest concept, also known as rocking-chair chemistry,[9] featuring two insertion electrodes in between which lithium ions are moved reversibly.[10] Lithium-ion batteries circumvent the need for metallic lithium by comprising a carbonaceous anode, e.g., graphite,[11] and a lithium-containing transition metal oxide cathode, e.g., $LiCoO_2$, which acts as the source for cyclable lithium ions.[12] The market launch of this new cell chemistry was preceded by more than 15 years of intensive research. In 1976, Stanley Whittingham proposed the first secondary battery consisting of a titanium disulfide (TiS_2) intercalation cathode and a lithium metal anode.[13–15] Just a few years later, Koichi Mizushima, John B. Goodenough, and Michael Thackeray extended the concept to lithium-containing transition metal oxide cathodes, including $LiCoO_2$ and $LiMn_2O_4$.[16,17] The way for the technological breakthrough was finally paved by the seminal work of Jeff R. Dahn and co-workers,[18,19] who were working at Moli Energy at that time. They described the intercalation of lithium ions into graphite and petroleum coke-based anodes as well as the irreversible reaction between the Li_xC compounds with a nonaqueous aprotic electrolyte. The concomitant passivation of the carbon/electrolyte interface, also known as solid-electrolyte-interphase (SEI),[20,21] allowed an excellent reversibility upon continued charge-discharge cycling, and thus offered a safer and more reliable alternative to the lithium metal anode.

After its introduction in the early 1990's, the lithium-ion technology was adopted immediately because of its high practical cell-level specific energy of ~80 Wh kg^{-1} which outperformed incumbent systems, including nickel-cadmium (20-40 Wh kg^{-1}) and nickel-metal-hydride (50-70 Wh kg^{-1}).[2] In addition, it convinced with a good cycling performance and the absence of memory effects.[3] Driven by the rapid development of the consumer electronics market, including laptops and smartphones, lithium-ion batteries went through a remarkable improvement process, yielding cell-level specific energies of up to 150 Wh kg^{-1}, high energy efficiency, and improved safety characteristics.[22] However, the next challenge is yet to come. As highlighted in recent publications by Thackeray *et al.*[2] and Gallagher *et al.*,[23] today's lithium-ion batteries are suitable for small-scale portable electronic devices but they are still too heavy, large, and expensive for larger applications. For example, the next generation of fully electrified battery electric vehicles (BEV's) requires target cell-level specific energies of 250-300 Wh kg^{-1} (viz., energy per mass), which correspond to a twofold increase of today's specific energy of the battery cells in the BMW i3.[24] For the energy density (viz., energy per volume) this discrepancy is even larger, requiring up to 800 Wh L^{-1} in 2025 on a cell-level which is ~3.5 times higher than the state-of-the-art value.[24] Looking at the battery costs reveals a similarly challenging situation. From 2010 to 2016, battery pack prices fell by roughly 80% from about 1000 US\$ kWh^{-1} to a current prize of ~225 US\$ kWh^{-1}.[25] With a further expansion of manufacturing capacity by global battery producers, including Panasonic, LG Chem, and BYD,[26] the prices are expected to decrease even further to below 190 US$ kWh^{-1} by 2020.[25] However, considering that a 300 km drive requires a battery pack with a name-plate energy of at least 56 kWh, it is clear that even at these reduced prices the battery pack cost would still amount to ~10,600 US$.[27] As corollary, despite the remarkable drop in battery prices, in the mid-term fully electrified vehicles will remain more expensive compared to variants with an internal combustion engine. For example, the nonsubsidized prices for a Chevy Bolt and Tesla Model 3 are still well above 35,000 US$ and 40,000 US$, respectively, while the average price for a new vehicle purchase in Europe amounts to just ~29,500 US$.[25] Finally, using lithium-ion batteries for automotive applications also raises the importance of a high rate capability. This property is crucial for the fast-charging of the batteries, e.g., in less than 15 min, to avoid high overpotentials and plating of metallic lithium which decreases the cycle life and increases the risk of short-circuits.[28] Although state-of-the-art batteries, e.g., in the BMW i3, reveal an excellent rate capability up to 5.0 h^{-1} (viz. charge or discharge in 12 min), an increasing acceptance in the mass market is only possible if future lithium-ion batteries with higher specific energies also reveal a similar rate capability.[24,29]

Since 1880, the average global temperature has increased by 0.08°C per decade.[30] During the previous 30 years, the rate has even more than doubled, risking a severe long-term impact on marine and terrestrial life.[31] CO_2 emissions account for ~80% of the contribution to global warming of current greenhouse emissions.[32] To slow down this development and comply with the CO_2 emission targets of the environmental agencies, e.g., 95 g_{CO2} km^{-1} for passenger cars by 2020 from the EEA,[33] it is mandatory for lithium-ion batteries to overcome the challenges posed by their implementation as energy source for fully electrified BEV's. Therefore, it is time for the lithium-ion battery to initiate the next dawn of high-energy storage devices and unleash its full potential with respect to specific energy, rate capability, and cost. The present PhD thesis is aimed to contribute to this development by critically evaluating silicon as the most promising anode material for future high-energy lithium-ion batteries.

1.2 Electrochemistry and Materials of Lithium-Ion Batteries

Figure 1.1 shows a schematic illustration of a lithium-ion battery. It consists of two insertion electrodes whose open-circuit cell voltage (OCV) is defined by the difference between the electrochemical potentials (V vs. Li^+/Li) of the respective redox active electrodes. During charge-discharge cycling, lithium ions are shuttled between the two electrodes through an electrolyte-soaked separator, while the electrons are conducted separately through an external circuit. To ensure sufficient ionic and electrical conductivity, the electrodes consist of porous mixtures of active material particles, conductive additives, and a polymeric binder, which are coated onto metal foil current collectors.

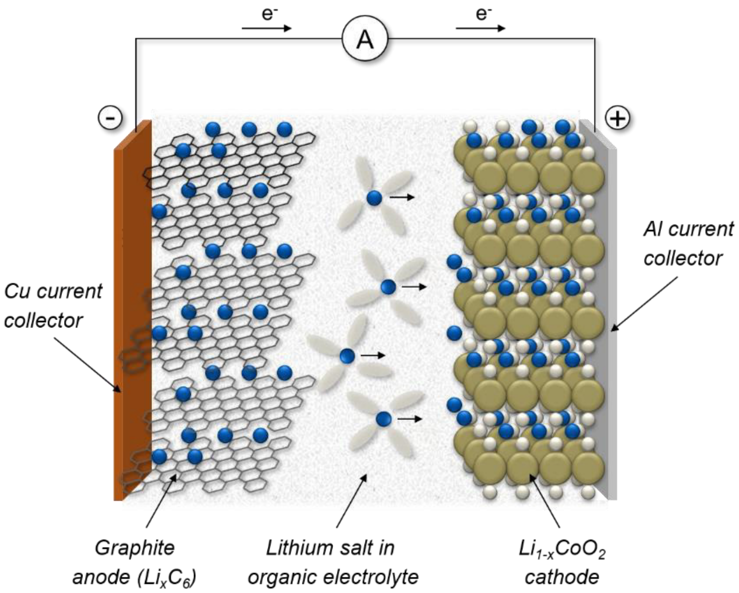

Figure 1.1 Schematic illustration of a lithium-ion battery consisting of a carbonaceous anode and a layered transition metal oxide cathode. During charge-discharge cycling, lithium ions are moved between the two electrodes through a carbonate-based electrolyte solution, while the electrons are moved separately through an external circuit. Image interpreted from Dunn *et al.*[34]

Active materials for lithium-ion batteries are commonly described by their specific capacity (mAh g^{-1}) and their mean potential during charge or discharge (V_{mean} vs. Li^+/Li). The former describes the number of lithium ions that can be inserted into/extracted from the materials. In accordance with Faraday's law ($Q^s = \frac{m}{M} \cdot z \cdot F$), the specific capacity Q^s of an active material is defined by the molar mass of its constituents M, the number of electrons transferred z, and the Faradaic constant F. The product of an active material's mean potential E_+ (or E_-) and its specific capacity Q_+^s (or Q_-^s) describes its specific energy W_+^s (or W_-^s) in Wh kg^{-1}. To calculate the specific energy for a negative/positive electrode pair, their mass balance needs to be considered as well, which is described by Equation [1]. As the specific capacities of the active materials from the negative and the positive electrode are usually not the same, electrode coatings are commonly prepared with different active material mass loadings (mg$_{AM}$ cm^{-2}). Therefore, the areal capacity (mAh cm^{-2}) is often the more meaningful measure to describe the balancing of a lithium-ion battery.

$$W_\pm^s = Q_\pm^s \times \Delta E_\pm = \frac{Q_+^s \times Q_-^s}{Q_+^s + Q_-^s} \times (E_+ - E_-) \qquad [1]$$

It is important to note that the above described specific energy only refers to the theoretical values of the active materials. On an electrode-level, the addition of inactive compounds, including conductive additives, the polymeric binder, as well as the current collector foil, results in a 15-20% lower specific energy.[35] During the assembly of lithium-ion cells, additional inactive but indispensable components need to be considered. This includes the electrolyte solution, the separator, and the packaging. As a result, the specific energy drops even further to about 50-60%, depending on the cell-design. By taking into account the battery management system, safety features, and the temperature control, the residual specific energy for the entire battery system finally shrinks to just 20-40% of its original value based on the active materials only.[23,24,36] As the specific energy loss from the mass contribution of the inactive components could be greatly reduced during the last decades, the optimization of the active materials now offers the largest lever to improve the specific energy of future lithium-ion batteries.

There exist two options to increase the specific energy of an active material: (i) Extend the cell cutoff voltages to higher/lower values to increase the utilization of the theoretical capacity of the selected cathode/anode active materials. (ii) Modify the cathode/anode active material composition to obtain a higher/lower mean potential (V$_{mean}$ vs. Li$^+$/Li) and/or a higher specific capacity (mAh g^{-1}). Staying with the cell cutoff voltage for a moment, Figure 1.2 shows typical galvanostatic potential profiles of a blended silicon-graphite (SiG) negative electrode (blue dots) and an NMC811 positive electrode (brown dashes) as a function of the areal capacity during the first charge-discharge cycle at 0.1 h^{-1} (~0.2 mA cm^{-2}). Initially, the open-circuit potential of both electrodes is about 3.0 V vs. Li^+/Li. Once an oxidative current is applied, upon which lithium ions migrate through the electrolyte and get reduced at the SiG electrode (e.g., $Si + x\,Li^+ + x\,e^- \rightarrow Li_xSi$), the anode potential immediately drops to values below 0.3 V vs. Li^+/Li. At the same time, the cathode is oxidized and its potential rises to above 3.6 V vs. Li^+/Li (e.g., $LiNi_{0.8}Mn_{0.1}Co_{0.1}O_2 \rightarrow Li_{1-x}Ni_{0.8}Mn_{0.1}Co_{0.1}O_2 + x\,Li^+ + x\,e^-$). The more lithium ions are extracted from the cathode and inserted into the anode, the higher becomes the difference between the two electrode potentials and thus the cell voltage (marine line). In other words, the cell voltage of a lithium-ion battery increases with an increasing state-of-charge until a certain cutoff voltage is reached (here: 4.4 V_{cell}).

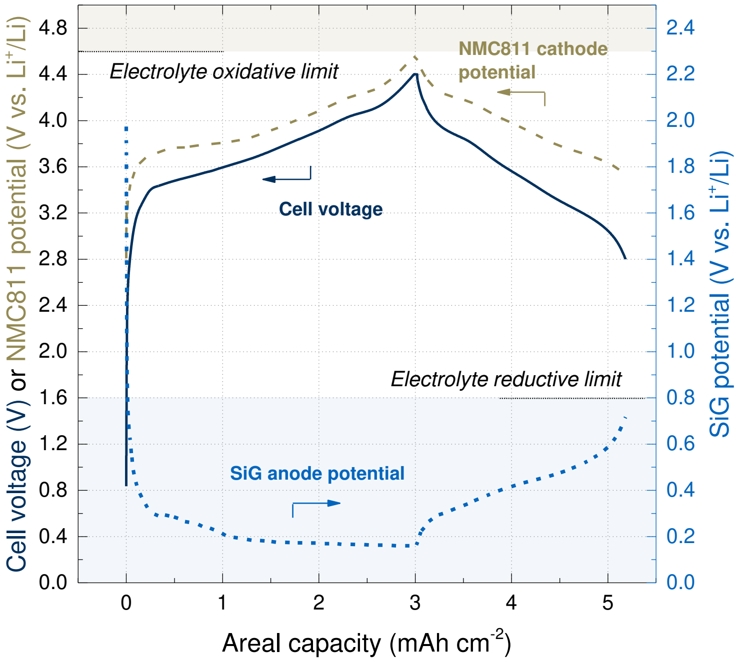

Figure 1.2 Typical galvanostatic potential profiles of a silicon-graphite negative electrode (blue dots) and an NMC811 positive electrode (brown dashes) during the first charge-discharge cycle at 0.1 h^{-1} (~0.2 mA cm^{-2}). The cell voltage (marine line) describes the difference between the two electrode potentials. While lithium-ion batteries are commonly controlled by the cell voltage, a reference electrode, e.g., lithium metal, can be used to separate the individual electrode potentials and reference them against the Li^+/Li potential. The shaded areas describe the potentials below the reductive stability limit (blue area) and above the oxidative stability limit (brown area) of commonly used carbonate-based electrolyte solutions. Image taken from Wetjen et al.[229]

During the subsequent discharge, the direction of the current and the flow of lithium ions are inverted, resulting in an oxidation of the anode, i.e., lithium extraction from silicon and graphite, respectively, and a reduction of the cathode, i.e., lithium re-insertion into the transition metal oxide. Nonetheless, increasing the specific energy by extending the cell cutoff voltages is a delicate endeavor. In accordance with the brown shaded area in Figure 1.2, the positive electrode remains mostly within the oxidative stability limit of the electrolyte solution and approaches the threshold only at high state-of-charge. Yet, although it seems to be attractive to increase the upper cutoff voltage because of only minor oxidative side reactions at the positive electrode at potentials below ~4.5 V vs. Li^+/Li (depending on the cathode active material), most of the battery producers are hesitant to allow too high upper cutoff voltages. While the electrochemical electrolyte oxidation increases only slowly with an increasing cutoff voltage,[37] the major concern are discrete parasitic reactions of the active materials at higher state-of-charge. The latter are caused by an increasing structural instability of the cathode active materials at low lithium contents, which deteriorates the cycling stability and risks the safety of the battery.[38,39] As a result, commercial lithium-ion batteries are nowadays limited to a cathode potential of ~4.3 V vs. Li^+/Li (except for the low voltage $LiFePO_4$).[7]

In accordance with the blue shaded area in Figure 1.2, the negative electrode is almost entirely operated at potentials below the reductive stability limit of the electrolyte solution. From a thermodynamic perspective, the electrolyte solution should therefore get continuously reduced at the lithiated negative electrode. The reason why lithium-ion batteries nevertheless operate for more than thousands of cycles (depending on the cell chemistry) is that during the first cycles a passivating layer forms at the interface of the electrode particles and the electrolyte solution. This so-called solid-electrolyte-interphase (SEI) was first introduced by Emanuel Peled in 1979 to describe the electrochemical behavior of alkali metals in nonaqueous electrolytes.[20] The SEI usually has a thickness of a few nanometers[40,41] and consists of a mixture of organic and inorganic electrolyte decomposition products, e.g., lithium fluoride (LiF), lithium carbonate (Li_2CO_3), lithium ethylene dicarbonate (LEDC), and lithium alkoxides (Li-OR), whose exact composition depends strongly on the electrolyte and the applied conditions.[42,43] For the operation of lithium-ion batteries, the two most important properties of the SEI include its selective permeability for lithium ions and at the same time its electrically insulating nature.[44] Thus, further decomposition of electrolyte compounds as well as the exfoliation of graphitic active materials caused by co-intercalation of solvated lithium ions is kinetically inhibited.[45,46] Ideally, the SEI would only form during the first reductive scan and remain stable upon continued cycling. However, volumetric changes of the active materials, thermal decomposition at elevated temperatures,[47] as well as the deposition and catalytic behavior of transition metals from the cathode[48,49] result in further decomposition of electrolyte compounds and a concomitant irreversible capacity loss. Lithium which is "consumed" by these side reactions is no longer available for the re-insertion into the cathode active material, thus leading to a so-called capacity fade, i.e., a gradual loss of capacity over cycling. For that reason, the coulombic efficiency (CE) is an extremely important measure to describe lithium-ion batteries. It is defined by the ratio of the discharge capacity and the charge capacity for a given cycle. For example, to achieve a capacity retention of 80% over 1000 cycles, a lithium-ion battery requires a CE of at least 99.98% (excl. the irreversible capacity of the 1st cycle). However, the CE is strongly influenced by several factors, including the type of active materials, the cutoff voltages, and the temperature. In addition, the electrolyte solution as well as the presence of additives also play a pivotal role that is interdependent with most of these factors.

Electrolyte solutions for lithium-ion batteries consist of a conducting salt which is dissolved in a mixture of aprotic organic solvents.[45] $LiPF_6$ is the most commonly used salt, because of its favorable transport properties and reasonable safety characteristics.[50] In contrast to other salts, it also passivates the aluminum current and thus prevents ongoing corrosion reactions at the cathode electrode. The aprotic organic solvents usually comprise a mixture of cyclic and linear alkyl carbonates. While the cyclic alkyl carbonates provide a high dielectric constant and thus a high lithium solubility, the linear alkyl carbonates are added to increase the ionic conductivity by reducing the viscosity.[45] In the last decades, ethylene carbonate (EC) has been be the cyclic alkyl carbonate of choice because of its high dielectric constant and good passivation of the negative electrode.[45,51] Yet, its limited oxidative stability recently raised concerns about its application at higher voltages, fueling research activities on EC-free electrolytes.[52,53] In terms of the linear alkyl carbonates, dimethyl carbonate (DMC), diethyl carbonate (DEC), and ethyl methyl carbonate (EMC) are the most widely used solvents. They are mixed in various ratios with cyclic carbonates and the lithium salt to optimize the properties of the resulting electrolyte solution.[54,55] To further improve the properties of these solutions with respect to the passivation of the negative electrode or stabilization of the positive electrode at high voltages, electrolyte additives (or enablers) are often added in small quantities.[56–58] Although there exists an abundance of different additives, most of them feature functional groups, e.g., a double bond or fluorine substituents. In the academic literature, vinylene carbonate (VC), fluoroethylene carbonate (FEC), and 1,3-propane sultone (PS) are among the most widely used additives.[41,59] Historically, the focus of researchers was more on the SEI-forming properties, however, nowadays the interest in additives is shifted towards the positive electrode to enable high-voltage applications in EC-free electrolytes.[60–62]

With respect to the optimization of the specific energy of lithium-ion batteries by substitution for active material compositions with more favorable properties, there exists an abundance of different families of suitable materials.[63] However, by evaluating these materials in terms of their combined properties, including energy, reversibility, lithium and electron transport, as well as cost, abundance, and safety, the selection is condensed to about 10-15 candidates which currently attract most of the attention from researchers and companies.[24] In the following, we summarize the most relevant state-of-the art and next-generation active materials for lithium-ion batteries and their properties, which are also depicted in the Figure 1.3.

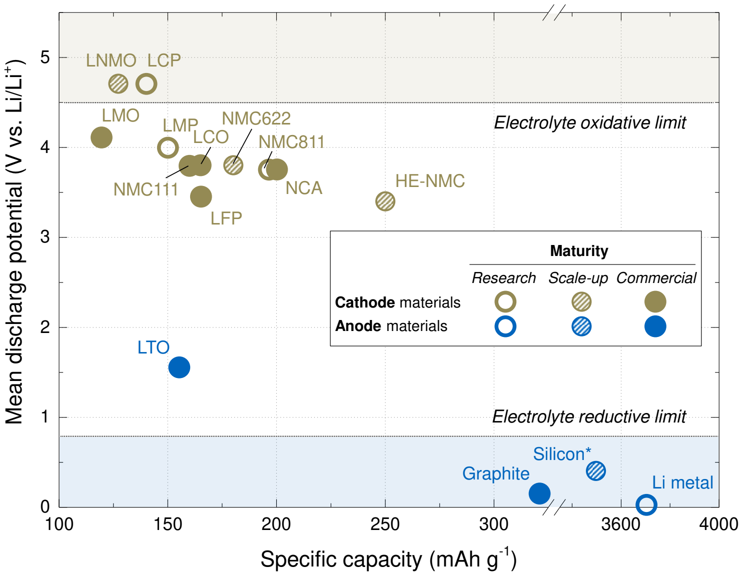

Figure 1.3 State-of-the-art and next-generation anode (blue) and cathode (brown) active materials for lithium-ion batteries plotted in accordance with their mean discharge potential (V vs. Li^+/Li), i.e., the mean delithiation potential for anodes and the mean re-lithiation potential for cathodes, respectively, and their accessible specific capacity (mAh g^{-1}). The maturity of these materials is indicated by the filling of the circles, including research (hollow), scale-up (patterned), and commercial (solid) stage. The shaded areas describe the potentials below the reductive stability limit (blue area) and above the oxidative stability limit (brown area) of commonly used carbonate-based electrolyte solutions.[24,64] The here assumed upper cutoff potentials vs. Li^+/Li for selected cathode active materials are 4.3 V (LMO, LCO, NMC111, NMC622, NMC811, and NCA), 4.7 V (HE-NMC), 4.9 V (LNMO), and 5.1 V (LCP).

For the negative electrode, graphite is the active material of choice in today's lithium-ion batteries because of its combined properties of a low and flat working potential of 0.1-0.2 V vs. Li^+/Li, high reversibility, high electrical conductivity, low cost, and abundant availability.[63] While its gravimetric capacity of 372 mAh g^{-1} (practically ~350 mAh g^{-1}) is notably higher than that of most cathode materials, its volumetric capacity of ~720 Ah L^{-1} is comparatively small, leaving room for improvement.[65] During charging, lithium-ions are intercalated reversibly in between the graphene layers, causing an uniaxial expansion of ~10% along the edge planes.[66] The concomitant staging behavior, as described in the Li_xC_6 phase diagram by Dahn *et al.*,[67] results in the characteristic step-like potential profile. While Stage II corresponds to a stoichiometry of LiC_{12} which correlates phenomenologically with two graphene layers separating one interstitial lithium layer, Stage I describes the maximum stoichiometry of LiC_6 and is characterized by an alternating pattern of one graphene layer and one interstitial lithium layer.[68]

Among the few alternative anode materials that are already commercially available, lithium titanium oxide ($Li_4Ti_5O_{12}$) is the most prominent. It has a practical specific capacity of ~155 mAh g^{-1} and a high potential plateau at ~1.55 V_{mean} vs. Li^+/Li which results in lithium-ion batteries with low specific energies.[69] Yet, its highly reversible zero-strain lithium insertion characteristics (i.e., only 0.2% change in volume) and the considerably lower level of side reactions still make LTO very attractive for niche applications with required prolonged cycle life, including medical devices and stationary battery storage systems.[70] In addition, its high mean potential offers further advantages. As surface passivation is not an issue, LTO can also be produced as nanoparticles which enable a high rate capability even though LTO has not a particularly high electrical conductivity or lithium diffusivity. In addition, LTO is also considered as an extremely safe material, because the potential of ~1.55 V_{mean} vs. Li^+/Li prevents the growth of lithium dendrites even at high currents. Nonetheless, surface reactions at the LTO particles cannot be entirely avoided, resulting in a gassing of organic electrolytes when in contact with LTO.[71] Apart from the insertion materials, lithium-alloys are another relevant but still immature class of anode active materials (e.g., silicon and tin) which promise future lithium-ion batteries with high specific energies.[72,73] As they follow a different (de-)lithiation chemistry, they are discussed in detail in the next section.

For the positive electrode, transition metal oxides (LiM_aO_b) are the most commonly used active materials in today's lithium-ion batteries, because of their favorable balancing between capacity, voltage, and rate capability.[10] During charging, lithium ions are extracted from the host structure resulting in an oxidation of the transition metal ions. Although lithium cobalt oxide (LCO, $LiCoO_2$, ~160 mAh g^{-1}, ~3.8 V_{mean} vs. Li^+/Li)[17] and lithium manganese oxide (LMO, $LiMn_2O_4$, ~120 mAh g^{-1}, ~4.1 V_{mean} vs. Li^+/Li)[16,74] were among the first materials to be discovered by researchers, they are still widely used in consumer electronic devices, e.g., smartphones.[7] Nonetheless, the increasing demand of automotive applications for higher energies at lower cost promotes the commercialization of alternative cathode active materials.

The layered lithium nickel manganese cobalt oxides ($LiNi_xMn_yCo_zO_2$) are the most promising class, combining the beneficial properties of higher specific capacities and lower stoichiometric amounts of the expensive cobalt. While NMC111 ($LiNi_{0.33}Co_{0.33}Mn_{0.33}O_2$, ~160 mAh g^{-1}, ~3.8 V_{mean} vs. Li^+/Li) is already well established and commonly used in blended cathodes with LMO, e.g., in the BMW i3 and the Nissan Leaf,[24] other stoichiometries with higher nickel contents are about to emerge soon.[75] Although the theoretical specific capacity of ~275 mAh g^{-1} is similar for all compositions, the combination of different transition metals allows to balance their properties. Nickel is the main redox active species (Ni^{2+}/Ni^{4+}) which provides a high capacity but suffers from a poor thermal stability.[76] Cobalt contributes less capacity (Co^{3+}/Co^{4+}) but increases the structural stability and improves the electronic conductivity, thus increasing the rate capability.[10] Manganese is electrochemically inactive but improves the cycle life and safety by stabilizing the structure.[77] NMC622 ($LiNi_{0.6}Co_{0.2}Mn_{0.2}O_2$, ~180 mAh g^{-1}, ~3.8 V_{mean} vs. Li^+/Li) is the first candidate of the nickel-rich materials that is expected to be commercialized soon. However, as both the advantages and disadvantages of these materials scale mostly with the nickel content, NMC's with even higher nickel stoichiometries, e.g., the NMC811 ($LiNi_{0.8}Co_{0.1}Mn_{0.1}O_2$, ~200 mAh g^{-1}, ~3.75 V_{mean} vs. Li^+/Li), still suffer from side reactions at oxidative potentials >4.3 V vs. Li^+/Li and a lower thermal stability.[39,78] The reason for this lies in an increasing structural instability of the layered oxides at low degrees of lithiation, which causes the release of lattice oxygen[38,39] and subsequent formation of a disordered spinel-type layer at the NMC particle surface.[79,80] The surface layer results in a rapid increase of the interfacial resistance and a reduced cycle life (see Section 3.3.1). Strategies to overcome these side reactions include *inter alia* the partial aluminum substitution for transition metal ions, as it is applied in the lithium nickel cobalt aluminum oxide ($LiNi_{1-y-z}Co_yAl_zO_2$) with $z < y < 0.20$ (~200 mAh g^{-1}, ~3.75 V_{mean} vs. Li^+/Li), which is used in the Tesla Model S.[7,81] Apart from the nickel-rich materials there exist two other interesting types of transition metal oxides, namely the high-energy lithium-rich materials (HE-NMC) and the high-voltage spinel (LNMO).

The HE-NMC is a layered-layered composite material, in which parts of the transition metal ions are substituted by lithium ions. It follows the general formula $x Li_2MnO_3 \bullet (1-x) LiMO_2$ (M = Ni, Co, Mn), whereby the layered $LiMO_2$ has been thought to be stabilized by the incorporation of the structurally compatible Li_2MnO_3.[82] By cycling between 2.0 and 4.4 V vs. Li^+/Li, $LiMO_2$ is the only redox active species, because the tetravalent manganese ions of the Li_2MnO_3 remain inactive. Nonetheless, the structural stabilization allows to achieve much higher degrees of delithiation compared to conventional layered oxides, e.g., $Li_{1-x}CoO_2$ with $x \leq \sim 0.5$, leading to a reversible capacity as high as ~250 mAh g^{-1} (at ~3.4 V_{mean} vs. Li^+/Li).[83] By increasing the voltage range to 4.7-4.8 V vs. Li^+/Li during the first charge, Li_2MnO_3 is also activated which results in the removal of the excess lithium ions from the transition metal layer, yielding a capacity of >300 mAh g^{-1}.[38] Yet, despite its promising properties, the commercialization of HE-NMC is still hindered by its poor cycling stability, particularly by the voltage decay during prolonged cycling (often referred to as "voltage fading"), as well as its low packing density.[24]

The high-voltage spinel (LNMO) originates from a partial substitution of manganese for nickel in the $LiMn_2O_4$ spinel.[84] It operates at a comparatively high voltage of ~4.7 V_{mean} vs. Li^+/Li and provides in full-cells a specific capacity of ~130 mAh g^{-1}.[85] Although its practical energy offers only minor improvements compared to state-of-the-art cathode materials, LNMO continues to attract attention because of its inexpensive and environmentally benign constituents.[24] Furthermore, the material convinces with good safety characteristics and an extremely high rate capability, which originates from the three-dimensional lithium-ion conduction pathways in the spinel structure. The stable framework mitigates the variation in the lattice parameters upon extraction and insertion of lithium which often compromises the long-term stability of layered oxides. In addition, the large availability of lithium diffusion channels makes this material less sensitive to structural defects and vacancies. Nonetheless, the hurdles LNMO still has to overcome concern its poor cycling stability at elevated temperatures and the need for suitable high-voltage electrolytes.[86]

Polyanionic compounds are another interesting class of cathode active materials which emerged from the work of Padhi and Goodenough.[87,88] Compared to the transition metal oxides, they offer improved safety characteristics due to the strong covalent character of the polyanionic clusters, e.g., $(PO_4)^{3-}$, which results in a higher thermal stability.[89] In addition, these materials also convince with lower costs and a better environmental compatibility due to abundant and non-toxic constituents, including iron, manganese, and phosphorus. Another interesting feature of these so-called “on demand cathodes” is the possibility to tailor their working potential by modifying the ionic character of the M-O bond through the electronegativity of the non-transition metal element (e.g., phosphorus, sulfur, and silicon).[24,87] The olivine lithium iron phosphate $LiFePO_4$ (LFP, ~160 mAh g^{-1}, ~3.45 V_{mean} vs. Li^+/Li)[24] is the most widely used polyanionic cathode active material. Due to its good cycle life and high-power capability, LFP is mostly used in power tools and stationary energy storage applications.[7] For automotive applications, however, lithium manganese phosphate $LiMnPO_4$ (LMP, ~150 mAh g^{-1}, ~4.0 V_{mean} vs. Li^+/Li)[24] is the most promising candidate because of its higher energy density. Yet, this advantage comes at the expense of a lower thermal stability in its delithiated state[90] and inferior cycling stability,[91] requiring further research activities.

1.3 Silicon as Anode Active Material

To achieve the goal of fully electrified BEV's with a driving range of 500 km, cell-level specific energies of 300 Wh kg^{-1} and energy densities of 700 Wh L^{-1} are required.[64] Although graphite is an excellent anode active material, its specific energy and energy density are not sufficient to meet these target values (see Table 1.1), which motivates the search for suitable alternatives. Nonetheless, to find a promising candidate which is characterized by a similar combination of favorable properties, including minimal structural changes during (de-)lithiation, a low working voltage, high coulombic efficiency, and excellent densification properties in electrode coatings, presents a challenging task.[92]

Table 1.1 Characteristics of selected anode active materials (graphite, silicon, and lithium)[92] as well as calculated cell-level energies for a prismatic hard-case cell featuring a nickel-rich cathode (e.g., NMC or NCA with a nickel content of ~80%) and optimized 6 mAh cm^{-2} anode electrodes.[64] [a] The volumetric changes of metallic lithium depend strongly on the electrode design.

		Anode active materials		
	Units	**Graphite**	**Silicon**	**Lithium**
Active material characteristics [92]				
Maximum lithium uptake	-	LiC$_6$	Li$_{3.75}$Si	Li
Mean delithiation potential	*V vs. Li$^+$/Li*	0.1-0.2	0.4	0
Theoretical specific capacity	*mAh g^{-1}*	372	3579	3860
Theoretical volumetric capacity *(in fully lithiated state)*	*Ah L^{-1}*	719	2194	2062
Volume expansion	*Percent*	+10%	+280%	- [a]
Calculated energies on a cell level (against a nickel-rich cathode) [64]				
Specific energy	*Wh kg$^{-1}_{cell}$*	230	280	340
Improvement *(ref. to graphite)*	*Percent*	-	+22%	+48%
Energy density	*Wh L$^{-1}_{cell}$*	575	750	900
Improvement *(ref. to graphite)*	*Percent*	-	+30%	+56%

In accordance with Figure 1.4, three types of anode active materials can be differentiated.[64] These include (i) intercalation/insertion materials, e.g., graphite and LTO, (ii) single-phase conversion materials, also described as *alloy* materials which include silicon, tin, and lithium,[93,94] as well as (iii) multi-phase conversion materials, usually referred to as *conversion* materials, including iron oxide and tin oxide.[63] While there exist excellent reviews on intercalation anodes[95,96] and conversion materials,[94] this PhD thesis is aimed to investigate silicon as the most promising representative of alloy-based active materials. In contrast to conversion materials, alloy-based electrodes are more attractive for the application in battery electric vehicles, because of their lower working voltage (0.2-1.0 instead of 1.0-2.2 V vs. Li$^+$/Li), higher gravimetric capacities (400-3500 instead of

650-1000 mAh g^{-1}), as well as better electronic and ionic transport properties.[63,64] Nonetheless, both types also share some disadvantages compared to insertion materials, including significant structural changes during (de-)lithiation, a larger voltage hysteresis between the lithiation and the delithiation potential (which is even larger for conversion materials), a low coulombic efficiency, and poor cycling stability. Most of the alloy materials are from the IIIa, IVa, and Va group and form intermetallic or Zintl-phases with lithium.[64,92] Although the maximum lithium uptake does not differ considerably, the molecular volume and the delithiation potential increase towards heavier elements.[65] Therefore, lighter elements, such as silicon, show the highest gravimetric and volumetric energy densities. Yet, it remains difficult to realize these theoretical values in practical lithium-ion batteries. While on a material level, silicon has an almost 3-times larger volumetric capacity compared to graphite, the practical improvement in a prismatic hard-case cell with a nickel-rich NMC622 cathode amounts to just +30% (compare Table 1.1).[64] The reason for this lies in the nature and the design of the alloy electrodes, which suffer from a lower coulombic efficiency, from the generally required higher electrode porosity, as well as from a typically higher content of inactive components in the electrode (viz., binder and conductive additive). It is to note, that lithium metal anodes offer even larger specific energies because of their high theoretical specific capacity and their low electrochemical potential.[97] However, their commercialization in rechargeable lithium batteries has been prevented over the past 40 years by a poor coulombic efficiency during lithium deposition/stripping and serious safety concerns, arising from the unpredictable and uncontrollable growth of lithium dendrites.[97]

The most challenging drawback of alloy active materials remains their large volume expansion between the delithiated and the lithiated state.[98] For silicon, the volumetric changes amount to +280% in its fully lithiated state (i.e., $Li_{15}Si_4$),[99] which results in detrimental consequences on all levels. On a cell level, this includes a distortion of the Cu-foil current collector and the separator, while on an electrode level, the volume expansion can lead to mechanical deformation and loss of interparticle contact pressure (see Section 3.1.1).[100–102] On a particle level, the repeated volumetric changes during (de-)lithiation are especially critical because of two reasons: First, they prevent the formation of a stable passivating layer, leading to a continuous rupture and renewal of the SEI. This coincides with an ongoing decomposition of electrolyte constituents and depletion of cyclable lithium from the cathode (see Section 3.3.3).[103,104] Second, they result in significant morphological changes of the silicon particles, which deteriorate electrical contact and cause an increased irreversible capacity loss (see Section 3.1.2).[73,105,106] The origin of these morphological changes are dealloying reactions during the delithiation of silicon, which are strongly dependent on the particle size, temperature, and the applied current.[107–111]

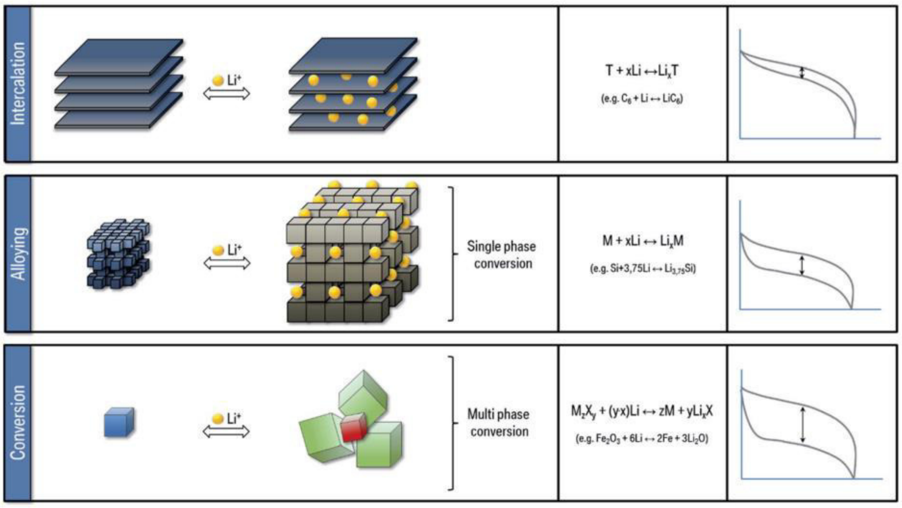

Figure 1.4 Schematic illustration of the three types of anode active materials, including intercalation, alloying, and conversion materials. Image taken from Andre *et al.*[64] Reprinted with permission from the Royal Society of Chemistry (Copyright 2017).

In their seminal work from 2007, Obrovac *et al.*[65] demonstrated that the lithiation of binary alloys follows Vegard's law. They calculated the volume of the lithiated alloy per mole of host atoms as a function of the number of inserted lithium atoms per mole of host atoms, which is shown in Figure 1.5a. Considering the similar slopes for the different elements, they concluded that the partial molar volume of lithium in these alloys is nearly the same in any lithium alloy (8.9 ± 0.5 mL mol^{-1} or 14.8 Å^3 per lithium), except for graphite which follows a different mechanism (4.2 mL mol^{-1}, 7.0 Å^3 per lithium). This relationship shows that at a given volume expansion, e.g., +100%, all alloy active materials have nearly the same impact on the resulting volumetric cell energy density (see Figure 1.5b). Minor deviations are mostly caused by the different mean delithiation potentials. As a corollary, any additional capacity exchanged by silicon compared to other alloy anode materials is only obtained at the expense of a further volume expansion. To manage the trade-off between the gain in capacity and the concomitant volumetric changes, researchers started to deploy capacity-limited cycling procedures.[112,113] However, this approach needs to be evaluated carefully (see Section 3.3.1), because the higher content of active materials and the larger first cycle irreversible capacity reduce the practical energy density. Alternatively, Obrovac *et al.*[65] demonstrated that the use of active-inactive alloys offers another promising approach to increase the energy density at a given volume expansion. For these materials, the addition of electrochemically inactive iron or aluminum has a diluting effect, which results in a reduced volume expansion and improved cycling stability.[114–116]

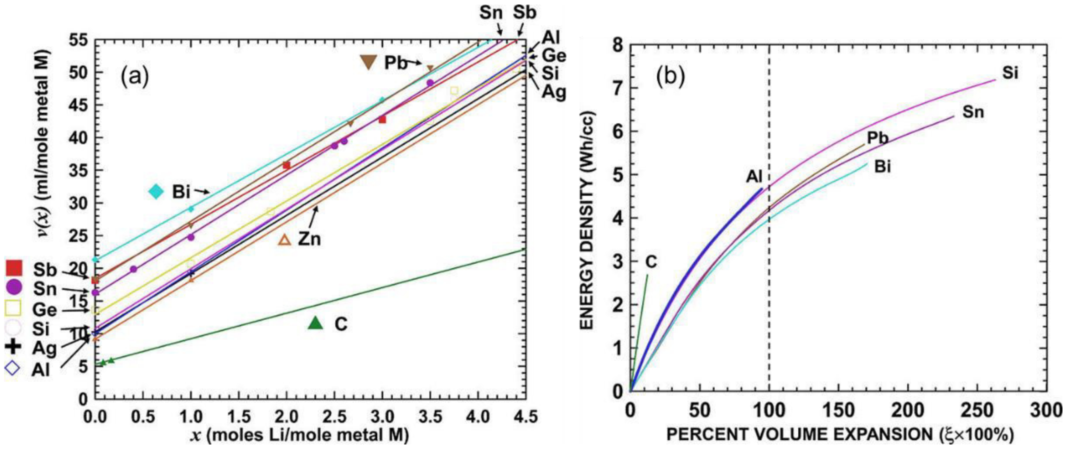

Figure 1.5 (a) Volume of the lithiated alloy per mole of host atoms plotted as a function of the number of inserted lithium atoms per mole of host atoms. (b) Energy density vs. volume expansion curves (referenced to a cathode mean voltage of 3.75 V) for various active metal elements calculated from their voltage curves. Images taken from Obrovac *et al.*[65] Reproduced with permission from The Electrochemical Society (Copyright 2007).

The first studies on the electrochemical lithiation of silicon were conducted in the late 1970's by Sharma and Seefurth from General Motors.[117,118] A few years later, Wen and Huggins[119] observed at temperatures around 400°C the formation of four crystalline Li-Si phases, with $Li_{22}Si_5$ as the most lithium-rich phase, which was in good agreement with the Li-Si phase diagram. However, when in the 1990's Wilson and Dahn[120] studied the insertion of lithium into nano-dispersed silicon using half-cells at room temperature, they obtained a significantly different voltage profile (see Figure 1.6). In contrast to the equilibrium voltage profile at high temperatures, the electrochemical lithiation of silicon at room temperature is feature-rich and dependent on several factors, including the particle size, morphology and the applied current.[121] During the first lithiation of *crystalline* silicon (see Equation [2]), the voltage profile drops to ~0.17 V vs. Li^+/Li and is furtheron characterized by a gently sloping plateau.[122] The corresponding two-phase reaction results in an *amorphous* Li_ySi alloy whose front grows into the particle.[123] Once it reaches the core, the particle entirely consists of *amorphous* Li_xSi

in which some silicon atoms are paired as dimers, whereas others are surrounded by lithium atoms.[124–126] At potentials near 0.05 V vs. Li^+/Li, further lithiation results in a sudden formation of a new metastable Li-Si phase, viz., *crystalline* $Li_{15}Si_4$, which was confirmed by XRD and differential capacity analyses as the final state of lithiation at room temperature (equating to a capacity of 3579 mAh g^{-1}_{Si}).[127,128] During subsequent delithiation, the Li_zSi alloy returns to an *amorphous* state and remains *amorphous* upon continuous cycling (see Equation [3]) until the potential drops again below 0.07 V vs. Li^+/Li (see Equation [4]).[92] As the (de-)lithiation of *amorphous* silicon follows a solution-type reaction, it occurs homogenously throughout the particle and is characterized by a sloping voltage profile.[128] Therefore, the structure of silicon upon continued cycling is essentially independent of the initial structure and changes only with the lower cutoff potential.[122] Several *in situ* studies supported this interpretation by means of XRD,[127] NMR,[125] and TEM.[129–131] A more detailed analysis of the (de-)lithiation features of silicon as well as a comparison with graphite can be found in Section 3.1.1.

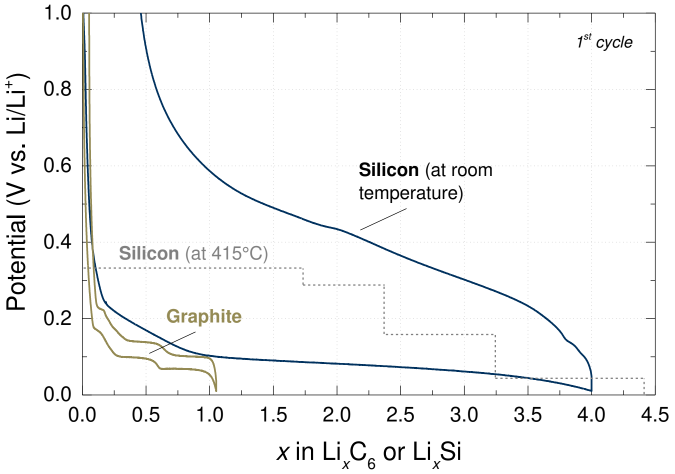

Figure 1.6 Galvanostatic potential profiles of crystalline silicon powder (marine line) and graphite (brown line) at room temperature. Dotted line: Coulombic titration curve for the Li-Si system at 415°C. High temperature data from Wen and Huggins.[119] Room temperature data from Wetjen et al.[132]

The formation of the *crystalline* $Li_{15}Si_4$ phase has another important implication for silicon as anode active material. Using acoustic emission measurements, Rhodes *et al.*[106] showed that the two-phase reactions during the first amorphization of *crystalline* silicon as well as during the delithiation from the *crystalline* $Li_{15}Si_4$ phase in subsequent cycles are accompanied by a massive fracturing of the silicon particles. They confirmed a long-standing theory according to which two-phase reactions cause internal stresses which have a detrimental effect on the cycle life of alloy materials.[92,133] To limit the fracturing and to avoid particle pulverization, researchers began to use nanometer-sized silicon with dimensions below the critical particle size of 150-300 nm.[72,129,130,134] Since then, numerous studies were conducted aiming to cope with the structural degradation of silicon active materials using nanoparticles,[110,135,136] nanowires,[137,138] or nanostructured silicon.[139,140] Alternatively, silicon nanoparticles were coated with a protective shell[141,142] or encapsulated in a carbon matrix.[143,144] Most of these approaches indeed resulted in a satisfying cycling stability in coin-cells with a lithium metal counter electrode and an excess of electrolyte.[145] However, their applicability in practical lithium-ion batteries with a limited amount of both electrolyte and cyclable lithium is yet to prove. Further concerns with nanometer-sized silicon include a significantly higher irreversible loss because of the larger surface area, higher contact resistances due to a larger number of interparticle contacts, as well as a lower volumetric packing density and a challenging manufacturing with respect to scalability and cost.

$$\textit{Lithiation:}\quad x\text{-}Si \xrightarrow{+Li} a\text{-}Li_ySi \xrightarrow{+Li} a\text{-}Li_xSi \xrightarrow{+Li} x\text{-}Li_{15}Si_4 \qquad [2]$$

$$\textit{Delithiation:}\quad x\text{-}Li_{15}Si_4 \xrightarrow{-Li} a\text{-}Li_zSi \xrightarrow{-Li} a\text{-}Si \qquad [3]$$

$$\textit{Subsequent cycling:}\quad a\text{-}Si \xrightarrow{+Li} a\text{-}Li_zSi \xrightarrow{+Li} x\text{-}Li_{15}Si_4 \qquad [4]$$

The last four decades of research on silicon as anode active material have generated a wealth of information about its electrochemical behavior and its structural changes. Nonetheless, the major challenges hampering its commercialization are still to be solved. This includes (i) a stable passivation of the silicon/electrolyte interface to prevent an ongoing consumption of electrolyte constituents and cyclable lithium, (ii) a further understanding and mitigation of the morphological degradation of silicon-based electrodes upon prolonged cycling both with respect to volume expansion and dealloying reactions, and (iii) a realization of the high theoretical gravimetric and volumetric energy density in practical lithium-ion batteries, using high-energy cathode materials, e.g., nickel-rich NMC.

The present PhD thesis is aimed to examine each of these challenges to derive implications and elucidate interdependencies which allow to develop a more fundamental understanding of silicon-based anodes. The first paper presented in Section 3.1.1 deals with blended silicon-graphite (SiG) anodes which are investigated with respect to the different degradation phenomena of intercalation and alloy active materials, respectively. Further, we introduce a new pseudo full-cell configuration to quantify the ongoing consumption of cyclable lithium and electrolyte compounds, and extrapolate our findings to practical lithium-ion batteries. Based on these results, our second paper (see Section 3.1.2) provides a detailed *post mortem* characterization of the morphological changes of the silicon active material and the electrode coatings upon prolonged cycling. To evaluate the consequences of these morphological changes, we apply for the first time neutron depth profiling (NDP) as a highly lithium-sensitive technique to derive depth- and quantity-resolved information on the uniformity of the aging phenomena across the thickness of SiG anode coatings. While the paper presented in Section 3.2.1 deals with the introduction of the method and the newly installed N4DP setup at the PGAA facility of Heinz Maier-Leibnitz Zentrum in Garching, the paper shown in Section 3.2.2 provides a detailed analysis and validation of the NDP results by complementary electrochemical and microscopy measurements. In Section 3.2.3, the application of NDP is expanded to other research questions concerning lithium-ion batteries, including the state-of-charge distribution in SiG anodes and the distribution of aqueous-based binders in graphite anodes. In the final part of this PhD thesis, we apply our newly developed analytical toolkit to evaluate the efficacy and applicability of different solution approaches to overcome the drawbacks associated with silicon in various full-cell configurations. This includes the prelithiation of SiG anodes for SiG//NMC811 full-cells (see Section 3.3.1), the use of lithium oxalate as sacrificial salt in SiG//LNMO full-cells (see Section 3.3.2), and the passivation of SiG anodes by use of differently fluorinated EC-derivatives as electrolyte additives (see Section 3.3.3).

2 Experimental Methods

2.1 Neutron Depth Profiling

Neutron depth profiling (NDP) is a non-destructive high energy-resolution nuclear analytical technique to monitor surface-near concentration profiles of specific elements in almost any material matrix. The method was introduced in 1972 by Ziegler *et al.*[146] to probe boron impurities in silicon wafers. Later, Biersack *et al.*[147] and Downing *et al.*[148] expanded its application to other light elements including ^{3}He, ^{6}Li, ^{7}Be, and ^{22}Na. Table 2.1 depicts a list of isotopes that are suitable for observation with thermal neutron induced $(\mathrm{n, p})$ or (n, α) reactions. While the group of isotopes with cross sections in the range of 1-48 kbarns can be detected with a very high sensitivity, isotopes with a thermal neutron cross section between 0.19 and 1.83 barns, i.e., $^{14}\mathrm{N(n, p)}$, $^{17}\mathrm{O}(\mathrm{n}, \alpha)$, $^{33}\mathrm{S}(\mathrm{n}, \alpha)$ and $^{35}\mathrm{Cl(n, p)}$, are only suitable for depth profiling at higher concentrations, depending on the neutron flux intensity. For all other known isotopes the corresponding nuclear $(\mathrm{n, p})$ or (n, α) reactions are endothermic, and thus cannot occur in the absence of fast neutrons.[147]

Table 2.1 Summary of the NDP reaction characteristics and example detection sensitivities for the 20 MW NIST reactor. The exponent *a* refers to radioactive species. The detection limit refers to 0.1 cps, a 0.013 Sr detector solid angle, and a neutron intensity of 6×10^{9} s^{-1}. Data from Downing *et. al.*[149]

Element	**Reaction**	**Abundance** (%) **or** (atoms mCi^{-1})^{a}	**Energy of emitted particles** (keV)		**Cross section** (barns)	**Detection limit** (atoms cm^{-2})
He	$^{3}\mathrm{He(n, p)}^{3}\mathrm{H}$	0.00014	572	191	5333	1.5×10^{12}
Li	$^{6}\mathrm{Li}(\mathrm{n}, \alpha)^{3}\mathrm{H}$	7.5	2055	2727	940	9.0×10^{12}
Be^{a}	$^{7}\mathrm{Be(n, p)}^{7}\mathrm{Li}$	(2.5×10^{14})	1438	207	48000	1.7×10^{11}
B	$^{10}\mathrm{B}(\mathrm{n}, \alpha)^{7}\mathrm{Li}$	19.9	1472	840	3837	2.1×10^{12}
N	$^{14}\mathrm{N(n, p)}^{14}\mathrm{C}$	99.6	584	42	1.83	4.5×10^{15}
O	$^{17}\mathrm{O}(\mathrm{n}, \alpha)^{14}\mathrm{C}$	0.038	1413	404	0.24	3.5×10^{16}
Na^{a}	$^{22}\mathrm{Na(n, p)}^{22}\mathrm{Ne}$	(4.4×10^{15})	2247	103	31000	2.3×10^{11}
S	$^{33}\mathrm{S}(\mathrm{n}, \alpha)^{30}\mathrm{Si}$	0.75	3081	411	0.19	6.0×10^{16}
Cl	$^{35}\mathrm{Cl(n, p)}^{35}\mathrm{S}$	75.8	598	17	0.49	1.7×10^{16}
K$^{(a)}$	$^{40}\mathrm{K(n, p)}^{40}\mathrm{Ar}$	0.012	2231	56	4.4	1.9×10^{15}
Ni^{a}	$^{59}\mathrm{Ni}(\mathrm{n}, \alpha)^{56}\mathrm{Fe}$	(1.3×10^{20})	4757	340	12.3	7.0×10^{14}

The use of thermal neutrons (in the meV regime) is essential to produce mono-energetic particles which are needed to correlate the observed energy loss with the depth origin of the nuclear reaction. NDP senses individual isotopes nearly independent of matrix effects and their chemical state.[148] Further, it provides a good depth resolution down to ±20 nm and a high concentration resolution of about 3 ppm, depending on the material matrix composition and the neutron flux intensity.[146] For the investigation of lithium-based energy storage systems, NDP is particularly interesting because of its extremely high sensitivity towards ^{6}Li (7.5% natural abundance).[149] In addition, the comparatively high energies of the emitted particles from the ^{6}Li(n, α)^{3}H reaction allow a reasonable energy resolution as well as maximum penetration depths of typically ~50 µm, depending on the composition and porosity of the material matrix.[150] Equation [5] summarizes the reaction of a thermal neutron with ^{6}Li, which results in the formation of an α-particle (^{4}He) and a triton particle (^{3}H). Due to the two-body kinematics, the ^{4}He and ^{3}H particles have well-defined energies at the moment of their formation and they are emitted back-to-back.

$$^{6}Li + n \rightarrow \; ^{4}He(2055\ \mathrm{keV}) + \; ^{3}H\ (2727\ \mathrm{keV}) \qquad [5]$$

On their path through the sample material towards the surface, the charged particles lose almost linearly energy by Coulombic interactions with adjacent atoms, which can be described by the Bethe-Bloch formalism.[151] The particle stopping power $S(E) = -dE/dx$ depends on the charged particle properties, as well as the elemental composition and the density of the surrounding matrix. In accordance with Equation [6],[152] the remaining particle energy $E(x)$ after leaving the sample surface can be correlated with the path length x, which yields a depth concentration profile of the investigated elements.

$$x = \int_{E(x)}^{E_0} dE/S(E) \qquad [6]$$

Figure 2.1 illustrates a top-view sketch of the N4DP (**N**eutron **4**-Dimensional **D**epth **P**rofiling) setup at the PGAA facility of the Heinz Maier-Leibnitz Zentrum (MLZ) in Garching, which is representative for a typical NDP setup.[148,150] The incoming cold neutron beam (mean energy: 1.8 meV) has a capture flux of 1.35×10^{9} cm^{-2} s^{-1} and is circularly collimated by boron-containing plates to an area of 12.6 mm^2 to irradiate only the investigated samples. It enters the vacuum chamber (10^{-4}-10^{-5} mbar) through a 100 µm thick aluminum window and hits the sample of a 45° angle, which increases the effective path length for the neutrons by a factor of $\sqrt{2}$. While most of the neutrons pass through the sample without interaction and exit the vacuum chamber through another aluminum window, some of the neutrons are captured by reactive isotopes, e.g., ^{6}Li, in proportion to their neutron cross section, yielding monoenergetic charged particles.[149] Two silicon surface-barrier detectors are installed perpendicular to the sample plane on both sides of the sample. The nominal sample-detector distances are about 53 mm (see Section 3.2.1) but need to be corrected for different sample thicknesses.[151] The high neutron flux can be reduced with three different attenuators (5.9%, 16%, and 47%) to keep signal rates of the detectors below 1 kHz, and thus mitigate pile-up effects.

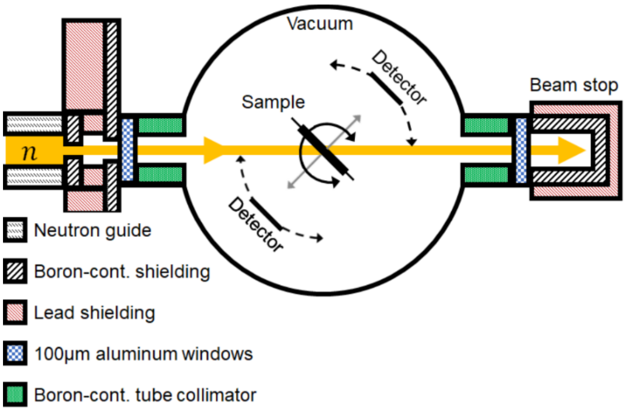

Figure 2.1 Schematic top-view sketch of the N4DP setup at the PGAA facility at MLZ. The cold neutron beam ***n*** (yellow arrow) is collimated by boron-containing plates. The beam enters and exits the N4DP vacuum chamber through 100 µm thick aluminum windows. Both, samples and detectors, can be rotated with respect to the center axis of the vacuum chamber (perpendicular to the drawing plane). Reproduced from Trunk *et al.*[151]

As the first tests of the N4DP setup at MLZ were started in 2017,[151] one of the main objectives of this PhD thesis was to design and validate NDP experiments with respect to material science investigations of lithium-ion batteries (see Section 3.2.1). Here, ^{6}Li acts as a key isotope to investigate a variety of different phenomena occurring in the electrodes, the electrolyte, and at the interfaces. Whitney *et al.*[153,154] and Nagpure *et al.*[155–157] were the first research groups who used NDP for the *post mortem* characterization of commercial lithium-ion batteries, *inter alia* to investigate lithium concentration gradients in aged graphite anodes and $LiFePO_4$ cathodes.[158] Later, Oudenhoven *et al.*[150] performed an *in situ* NDP study to monitor the lithium transport across thin-film solid-state microbatteries, consisting of a 1.5 µm thick nitrogen doped Li_3PO_4 (LiPON) solid-state electrolyte and a 500 nm thick $LiCoO_2$ cathode. With respect to alloy materials, Co and co-workers[159,160] recently reported an *in situ* setup that consisted of a lithium metal anode and a liquid electrolyte of 1 M $LiBF_4$ in EC:DMC to measure the lithium distribution in a tin-based thin-film electrode (12.5 μm thickness). More recently, Zhang *et al.*[161] used a similar *in situ* setup to investigate the rate-limiting charge transport phenomena in 12.5 μm thick $LiFePO_4$ cathode coatings in dependence on the electrode morphology and the C-rate.

In this PhD thesis, we focused on the investigation of graphite – and for the first time – also on silicon-based anodes. Emphasis is put on the generation of new insights using NDP that have not been accessible by other analytical techniques, e.g., the depth-resolved quantification of the SEI growth across SiG anodes (see Section 3.2.2) or the depth-distribution of aqueous-based binders in practical graphite electrode coatings (see Section 3.2.3). In contrast to other studies reported in the literature which deployed *in situ* setups, we conducted all measurements *ex situ*. Although *operando* measurements are planned in the future for the N4DP experiment, the use of *ex situ* samples offers several advantages, including (i) the use of electrodes with commercially relevant areal capacities between 2-3 mAh cm^{-2}, (ii) aging of the electrodes up to 140 cycles using established procedures in coin-cells, (iii) validation of the NDP spectra by complementary *post mortem* characterization, e.g., cross-sectional SEM images, and (iv) an abundance of reference data to support the interpretation of the NDP spectra.

There exist several factors that need to be considered for the design of NDP experiments. First, the stopping power of the ^3H and ^4He particles is strongly dependent on the elemental composition and the mass loading of the surrounding matrix. Thus, prior to the measurements, the maximum depth of emission should be calculated, e.g., by using the Stopping Range in Matter (SRIM) software written by Ziegler *et al.*[162] For SiG anodes this is very important, because during repeated (de-)lithiation these electrodes undergo significant changes in their mass loading and chemical composition, which is caused by the ongoing reductive decomposition of electrolyte compounds. Furthermore, thermal neutrons deployed by NDP react with any of the isotopes listed in Table 2.1, independent of their chemical state. Thus, the experiment needs to be designed carefully to derive meaningful information from the resulting NDP spectra. Although for lithium-ion batteries ^6Li and ^{10}B are the most relevant isotopes, their signal contributions can still get arbitrarily complex. For example, by only considering lithium there exist at least five different sources in commonly used SiG anodes,[102,115] including the lithium poly(acrylate) binder, lithium-containing electrolyte decomposition products, immobilized lithium in isolated active material particles, metallic lithium from plating, and cyclable lithium which is reversibly stored in the active material. In addition, boron-containing glass fiber residues from the frequently used glass separators lead to boron spectra which overlap with the signals from lithium (see Section 3.2.1). Therefore, the use of an adequate cell configuration, a defined cycling protocol, and suitable reference measurements are needed to separate and identify the individual signal contributions. In the following, we explain exemplarily the procedure for the investigation of the SEI growth in SiG anodes (see Section 3.2.2), however, the approach can be easily tailored to other research questions.

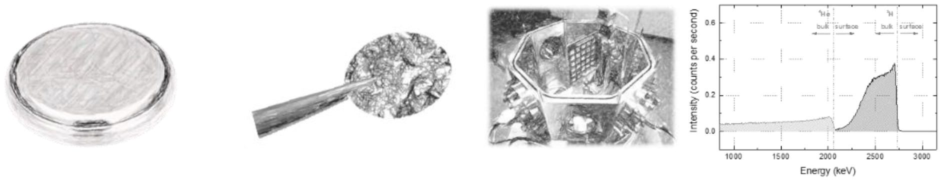

1. **Age** electrode in coin-cells and delithiate it to a **defined SOC**

2. Extract and wash **electrode** with DMC in **inert atmosphere**

3. Mount electrode on **sample holder** and transfer it into **vacuum** chamber

4. Measure **NDP** spectra using a **collimated neutron beam**

Figure 2.2 Schematic illustration of the sample preparation of an aged lithium-ion battery electrode for an NDP experiment.

In accordance with the schematic illustration shown in Figure 2.2, SiG anodes were first aged in coin-cells by galvanostatic charge/discharge cycling. In the last cycle, any residual active lithium was extracted from the active materials by applying a very low C-rate until an upper cutoff potential of 2.0 V vs. Li^+/Li. Thus, any lithium left in these electrodes originated either from the LiPAA binder, immobilized lithium or lithium-containing electrolyte decomposition products. While the signal contribution from the binder could be easily corrected by reference measurements with pristine electrodes, the amount of immobilized lithium was reduced to a minimum by the low C-rate (see Section 3.1.1), which left the SEI as the major variable source of lithium. In the next step, the electrodes were harvested from the coin-cells without exposure to ambient atmosphere and were carefully rinsed with dimethyl carbonate (DMC) to remove any residues from the $LiPF_6$ salt and the electrolyte solution. After determining the mass loading and the sample thickness, the electrodes were sealed in pouch-bags and transported to the PGAA facility at MLZ. Prior to the measurements, the electrodes were removed from the pouch-bags and mounted on the NDP sample holder before being transferred into the vacuum chamber. During this step, an exposure to ambient atmosphere for a few minutes could not be avoided while the samples were mounted on the NDP sample holder. Although the chemical state of some of the lithium-containing compounds might have been altered during this period, their depth-distribution should remain unchanged. Highly air-sensitive samples can alternatively be transferred into small pouch-bags with a thin Kapton® foil window, however, this design only works at the expense of the α-particle signal and results in a lower energy resolution of the ^{3}H particles (see Section 3.2.1).[163]

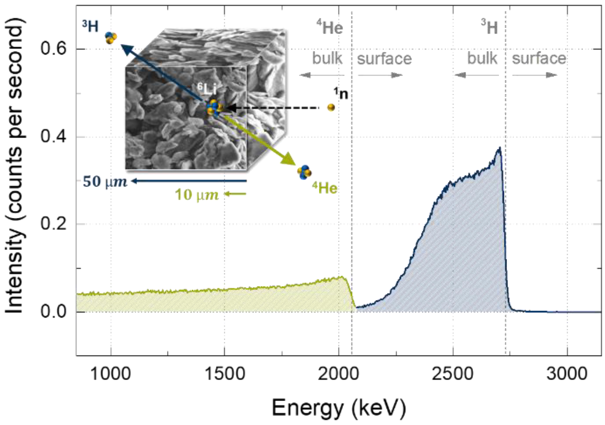

Figure 2.3 NDP spectrum, comprising signals from ^{3}H particles (blue line) and ^{4}He particles (green line) measured from the lithium poly(acrylate) (LiPAA) binder of a pristine SiG anode with an electrode mass loading of ~1.4 mg cm^{-2}, a porosity of ~60%, and a thickness of ~19 µm. Insert: Schematic illustration of the thermal neutron induced $^{6}Li(n, \boldsymbol{\alpha})^{3}H$ reaction in a graphite-based anode.

Figure 2.3 shows the NDP spectrum of an uncycled SiG anode with an electrode mass loading of ~1.4 mg cm^{-2}, a porosity of ~60%, and a thickness of ~19 µm. The ^{3}H (blue line) and the ^{4}He particle profiles (green line) originate entirely from the lithium poly(acrylate) (LiPAA) binder, which is distributed across the electrode coating thickness. As the charged particles lose energy on their way from the bulk towards the sample surface, the particle count vs. energy profile can be understood by going from the right- to the left-hand side of the *x*-axis. The well-defined formation energies of the two particles, i.e., 2727 keV for the ^{3}H and 2055 keV for the ^{4}He particles represent the lithium concentration at the upper sample surface, while lower energies correspond to particles originating from a greater depth. The shape of the spectrum shows the lithium concentration profile across the electrode coating thickness.[164] The profiles of the two particles can be understood as a superposition of Gaussian distributions around the respective energies of the emerging particles.[165] Yet, due to the higher stopping power of the α-particles, their maximum emission depth is lower compared to that of the ^{3}H particles.[166] Thus, the ^{4}He particles can only emerge from the surface-near ~10 µm thick region of the investigated electrode, whereas the ^{3}H signal reflects the entire electrode coating (up to a maximum accessible depth of ~50 µm) (see Section 3.2.1). At the same time, the higher stopping power of the ^{4}He particles results in an increased depth resolution. Thus, for some applications such as thin-film batteries with a total thickness of ~1 µm, the ^{4}He particles provide a better resolution of the lithium depth profile, as previously demonstrated by Oudenhoven *et al.*[150] In contrast, for samples with high mass loadings, e.g., aged SiG anodes, the ^{3}H signals broaden towards lower energies (corresponding to greater depth) and eventually overlap with the ^{4}He particle signal. In order to separate the ^{3}H signal, which intrinsically contains the profile shape of the full electrode, the ^{4}He particle signal can be subtracted analytically, which was recently demonstrated by Trunk *et al.*[151] (see Section 3.2.1). This is an alternative approach to the use of particle separation foils, e.g., Mylar® or Kapton®,[163] which would change the absolute quantity calibration. As the ^{3}H and the ^{4}He particles originate from the same concentration profile, the shape of the ^{4}He particle profile can be determined from the ^{3}H signal and vice versa.

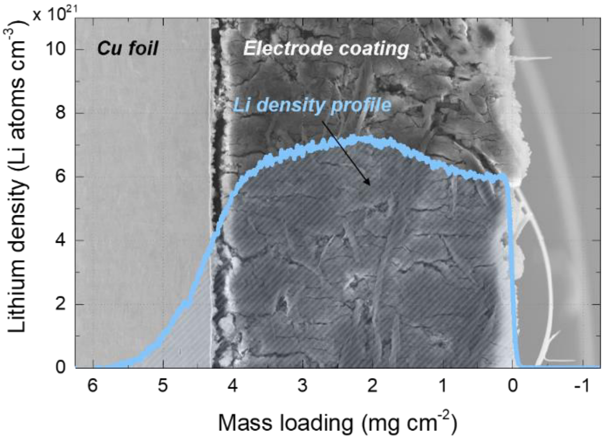

Figure 2.4 Lithium density profile of a SiG anode after 60 charge/discharge cycles as function of the electrode mass loading (blue line), exemplarily shown in front of the corresponding cross-sectional SEM image. The profile is a convolution of the density with the material-dependent resolution, which includes an energy spread due to the statistical process of the energy loss and possibly also because of a slight variation in the local mass loading of the electrode. Thus, there is no lithium in the Cu current collector. Reproduced from Wetjen *et al.*[167] with permission from The Electrochemical Society (Copyright 2018).

In the final step, the signal intensities from the NDP energy spectra are converted into an absolute lithium concentration (or density), considering the capture cross section and the natural abundance of the ^{6}Li isotope. To render the NDP analysis quantitative, the spectra intensities need to be normalized to the reference material SRM2137, a NIST standard which features a well-defined ^{10}B implantation profile with a systematic uncertainty of 3.4%.[168] Considering the chemical composition of the sample further allows to convert the energy loss of the charged particles into an electrode mass loading (see Section 3.2.1), which at a given density is proportional to the sample thickness. Figure 2.4 shows exemplarily the lithium density as a function of the electrode mass loading for a fully delithiated SiG anode after 60 charge/discharge cycles. To complement the NDP profile, a cross-sectional SEM image of the same electrode is placed into the background, which shows the surface of the electrode as well as the interface towards the Cu-foil current collector. In contrast to the uncycled sample shown in Figure 2.3, the lithium density of the aged electrode depicted in Figure 2.4 comprises not only the contribution from the LiPAA binder but also a significant signal contribution from the lithium-containing solid-electrolyte-interphase (SEI).

To sum up, NDP can provide depth- and quantity-resolved information concerning the distribution of light elements, such as lithium and boron, which is difficult to access by conventional analytical techniques. Yet, like other neutron-based methods, NDP is a complementary technique that requires an additional characterization, e.g., of the elemental composition or morphology, to adequately separate and interpret the profile shapes. In this PhD thesis, we applied NDP for the first time to investigate the SEI growth of practical silicon-based anodes for lithium-ion batteries that were aged over an extended period of 140 charge/discharge cycles (see Section 3.2.2). Hence, we designed and validated the first experiments at the newly installed N4DP setup at the PGAA facility at MLZ. Further, we complemented the analysis of the NDP spectra by electrochemical measurements, electron microscopy, and other *post mortem* characterization methods (see Section 3.2.1). Finally, we conducted a series of feasibility studies to expand the application of NDP to evaluate *inter alia* the state-of-charge distribution in SiG anodes as well as the distribution of aqueous-based binders in graphite anodes (see Section 3.2.3).

2.2 Pseudo Full-Cells

In the previous two decades, silicon-based anodes were mostly investigated in half-cells against metallic lithium.[120,169–171] While this cell configuration is favorable in terms of the cycling performance of the silicon-based anodes, it lacks important information concerning the constraints in practical lithium-ion batteries. The latter include a limited amount of electrolyte and cyclable lithium from the cathode. The relevance of this topic was recently highlighted by Trask *et al.*,[172] who stressed the need for more full-cell studies on silicon-based anodes with realistic areal capacities between 2-3 mAh cm^{-2}. Indeed, studies on full-cells with $LiCoO_2$ and NMC-based cathodes offer a more realistic evaluation of the performance of silicon-based anodes.[114,116,172–174] However, it is to note that there also exists a downside, because the superposition of different degradation phenomena in these setups (e.g., loss of cyclable lithium and cross-diffusion of side products) hinders a thorough analysis of their individual root causes. For that reason, this PhD thesis introduced a new cell configuration for the investigation of SiG anodes with an application-relevant areal capacity of ~2.0 mAh cm^{-2} (see Section 3.1.1).[102] This setup features a capacitively largely oversized $LiFePO_4$ cathode (~3.5 mAh cm^{-2}) and an FEC-containing electrolyte solution (here: LP57 with 5 wt% FEC), which offers several advantages over practical full-cells, namely: (i) A stable reference potential of 3.45 V vs. Li^+/Li of the $LiFePO_4$ counter electrode, allowing to monitor the silicon-graphite potential even in a two-electrode coin-cell configuration, and (ii) it provides a defined lithium reservoir, which allows to investigate the total irreversible capacity loss of the SiG anode without an additional capacity fade due to the depletion of cyclable lithium. While these conditions would also be satisfied in a half-cell configuration featuring a lithium metal electrode, the third advantage is that (iii) side reactions at the counter electrode are reduced to a minimum, because most electrolyte solutions are stable around the reversible potential of $LiFePO_4$. Therefore, any changes in the electrolyte (and the FEC concentration), which are obtained from *post mortem* characterization, e.g., by ^{19}F-NMR or gas chromatography,[103,175] can be directly related to the processes at the SiG anode. As a corollary, the pseudo full-cell configuration allows to investigate the individual degradation phenomena of SiG anodes in two-electrode coin-cells without sacrificing information concerning their application in practical lithium-ion batteries.

However, this setup also received some criticism because upon prolonged cycling the potential plateau of the $LiFePO_4$ starts to deviate from 3.45 V vs. Li^+/Li both at higher C-rates (i.e., >1.0 h^{-1}) and also towards lower lithium contents. Therefore, the potential profiles of the individual electrodes should be tested first in presence of a reference electrode for the intended C-rate and balancing ratio, respectively. This allows to refine the cell cutoff voltages and reliably determine the electrode potentials also in a two-electrode configuration. In a recently published independent study, Dose *et al.*[176] used a similar concept featuring a $LiFePO_4$ cathode with a 4-times higher areal capacity to investigate the irreversibility and the lithium inventory of a SiG anode. The fact that other research groups are also increasingly engaged in the development of such setups underlines the relevance of this research. In the present PhD thesis, the pseudo full-cell configuration was deployed in several studies, including the investigation of the degradation phenomena in SiG anodes (see Sections 3.1.1 and 3.1.2), the characterization of SiG anodes by neutron depth profiling (see Section 3.2.2), and the evaluation of new electrolyte additives for SiG anodes (see Section 3.3.3).

2.3 Nuclear Magnetic Resonance Spectroscopy

Nuclear magnetic resonance (NMR) spectroscopy is an analytical tool that is widely used in battery research to identify compounds in liquid electrolyte solutions,[177,178] to analyze changes in the local environment of individual electrode components,[125,179,180] or to investigate side reactions at the electrode/electrolyte interface.[41,181] The method exploits the magnetic properties of certain isotopes whose nucleus spin is unequal to zero, e.g. ^{1}H, ^{7}Li, ^{13}C or ^{19}F, to investigate their electronic environment and their interactions with adjacent atoms. This allows to derive qualitative information about the structure and the dynamics of the molecules as well as quantitative information about their concentrations.

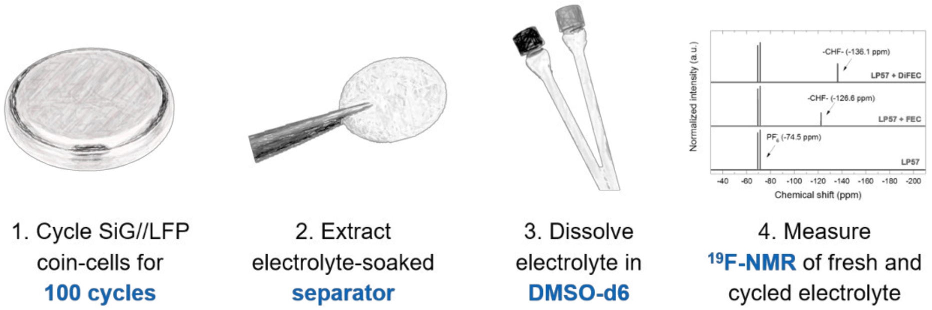

Figure 2.5 Schematic illustration of the *post mortem* electrolyte consumption measurement of a lithium-ion battery by integral analysis of the PF_6^- and FEC peaks in the ^{19}F-NMR spectra of the fresh and cycled electrolytes.

Recently, Jung *et al.*[103] introduced ^{19}F-NMR spectroscopy as an *ex situ* tool to characterize the electrolyte consumption in presence of silicon-based anodes during battery cycling by measuring *post mortem* the depletion of a fluorine-containing electrolyte compound (here: fluoroethylene carbonate, FEC). Figure 2.5 schematically illustrates the procedure, which involves the extraction of the electrolyte-soaked separator from a coin-cell after cycling, subsequent dissolution of the residual electrolyte in DMSO-d6, and finally an integral analysis of the PF_6^- and FEC peaks in the ^{19}F-NMR spectra of the fresh and cycled electrolytes. The concentration of the electrolyte salt (here: $LiPF_6$) is used as an internal standard, which assumes that its concentration remains almost constant upon cycling. Petibon *et al.*[104] indirectly confirmed the validity of this method by demonstrating the same preferential reduction and the same number of electrons for the reduction of FEC in $LiCoO_2$/Si-alloy Graphite cells using *post mortem* gas chromatography.

In this PhD thesis, we did not only confirm the results obtained by Jung *et al.*[103] for blended SiG anodes (see Section 3.1.1) but also expanded the use of this technique to other fluorine-containing electrolyte compounds, e.g., difluoroethylene carbonate (DiFEC) (see Section 3.3.3) and other cell configurations, e.g., SiG//LNMO full-cells (see Section 3.3.2). Further, we demonstrated that a comparison of the electrochemical data, e.g., the total charge+discharge capacity, and the additive consumption determined by ^{19}F-NMR, allows to calculate electrolyte consumption rates (e.g., in mAh μmol^{-1}_{FEC}) which can be used to forecast the cycle life of practical lithium-ion batteries with a given amount of electrolyte (see Section 3.1.1). Finally, we showed that this method does not only provide additional information about the reduction mechanism, e.g., in terms of the number of electrons (see Section 3.1.1 and 3.3.3), but also with respect to the efficacy of different electrolyte additives (see Sections 3.3.2 and 3.3.3).

2.4 Further Experimental Techniques

In addition to the methods described before, a variety of further experimental techniques was deployed in this PhD thesis. On-line electrochemical mass spectrometry (OEMS)[61,182] was used to analyze the gases that evolve during the electrochemical lithiation or delithiation of the investigated battery materials. Our studies included the first reductive scan of SiG anodes in presence of different electrolyte additives (see Section 3.3.3) as well as the first oxidative scan of NMC811 and LNMO cathodes, respectively (see Sections 3.3.1 and 3.3.2).

Electroanalytical methods such as cyclic voltammetry (CV) or galvanostatic cycling with constant voltage steps (CCCV) were applied (*inter alia* see Sections 3.1.1, 3.2.2, and 3.3.1) to investigate the electrochemical behavior of battery materials or to deliberately age electrode materials for subsequent *post mortem* characterizations. Depending on the procedure, the electrochemical measurements were evaluated using a variety of analyses to interpret the different cell or electrode characteristics as a function of the cycle number or state-of-charge. For example, we used differential capacity analysis (see Section 3.1.1 and 3.1.2) to evaluate the polarization of SiG anodes because this method is particularly powerful for blended electrodes to separate the contributions from the individual active materials. Further, we calculated the total irreversible capacity (see Sections 3.1.1, 3.2.2, and 3.3.3), which reflects the cumulative loss of cyclable lithium and serves as an indicator to forecast the cycle life of lithium-ion full-cells. For selected studies, we analyzed the open-circuit-potential relaxation (see Section 3.3.3) and the relative capacity contribution from the constant voltage step (see Section 3.1.1) to evaluate the build-up of resistances either in the electrolyte solution or the electrode.

For more sophisticated impedance analyses, we used a gold-wire micro-reference electrode in selected full-cells featuring either a $LiFePO_4$ (see Sections 3.1.2 and 3.3.3) or an NMC811 cathode (see Section 3.3.1). The micro-reference electrode was recently introduced by Solchenbach *et al.*[183] and offers an elegant tool to separately monitor the impedance contributions of the individual electrodes in a lithium-ion battery either as a function of the state-of-charge or the number of cycles, which generates valuable insights into the respective degradation mechanisms.

Throughout this PhD thesis, we extensively used electron microscopy to characterize the morphological degradation of SiG anodes and the individual active materials. In collaboration with JEOL (Germany) GmbH, we performed scanning electron microscopy (SEM), using various instruments, including the JEOL JSM-7800F PRIME (see Section 3.1.1,), the JEOL JSM-IT100 (see Section 3.1.2), and the JEOL JSM-IT300HR (see Section 3.2.2). Prior to the measurements, electrode cross-sections were prepared by means of argon ion beam polishing, using either a JEOL IB-09010CP (see Section 3.1.1) or a JEOL IB-19510CP cross-section polisher (see Sections 3.1.2 and 3.2.2). For selected studies on the thickness changes of the SiG anodes, we prepared the cross-sections in-house, following a resin-embedding and sand-paper polishing procedure first reported by Mittermeier *et al.*[184] The resulting SEM images were obtained using a JEOL JCM-6000 NeoScope.

In a collaboration with Vasiliki Tileli from the EPFL (Lausanne, Switzerland), we also deployed scanning transmission electron microscopy (STEM) and energy dispersive X-ray spectroscopy (EDS) to analyze the morphological changes and elemental composition of individual silicon nanoparticles (see Section 3.1.2). A detailed description of the instrumentation and the preparation procedures can be found in the Experimental part of our articles and manuscripts in the next section.

3 Results

The following Section summarizes the peer-reviewed journal articles and manuscripts originating from this PhD thesis, which are grouped along three core topics. Section 3.1 describes the characterization of silicon and graphite as active materials in blended silicon-graphite (SiG) anodes for lithium-ion batteries. Emphasis is put on the individual aging behavior of the intercalation and alloy materials, as well as on the differentiation of the degradation phenomena of the active material particles and the entire electrode coating during charge/discharge cycling.

Section 3.2 describes the application of neutron depth profiling (NDP) as a new analytical technique to characterize the uniformity of the aging phenomena in lithium-ion battery electrodes by means of a depth-resolved quantification of the lithium concentration. First, the method and the setup of the newly installed N4DP setup at the PGAA facility at the Heinz Maier-Leibnitz Zentrum in Garching are introduced. Afterwards, the distribution of lithium-containing species in blended SiG anodes is investigated, providing new insights into the growth of the solid-electrolyte-interphase (SEI) upon prolonged cycling. Finally, the method is expanded to other research questions concerning battery electrodes, including the state-of-charge distribution in SiG anodes and the distribution of aqueous-based binders in graphite anodes.

Section 3.3 evaluates three solution approaches aiming to overcome the inherent drawbacks of silicon-based anodes, including a lithium inventory established either by prelithiation or by addition of a sacrificial salt. Afterwards, a new electrolyte additive is evaluated with respect to the stabilization of the interface between the silicon particles and the electrolyte solution. The discussion provides a comprehensive assessment of these approaches both in terms of their efficacy and applicability, considering practical constraints of state-of-the-art lithium-ion batteries.

3.1 Characterization of Silicon as Anode Material

Despite its high theoretical specific capacity of 3579 mAh g^{-1}, the use of silicon as anode active material in commercial lithium-ion batteries is still limited to very few weight percent. The reason for this lies in the large volumetric changes of the silicon particles and the continuously proceeding side reactions at the silicon/electrolyte interface which negatively affect the safe and long-term operation of silicon-based full-cells, particularly of large-scale cells where the amount of electrolyte is limited.[104,112,174] Although the investigation of the underlying degradation phenomena continues to receive considerable attention both in the academic literature and in industrial research labs,[185,186] their identification and quantification remains a huge challenge. The latter is driven by the complexity of the degradation phenomena and the lack of suitable analysis tools to deconvolute their interdependencies.

In the following articles, this PhD thesis introduces a new cell configuration to separate, analyze, and quantify the degradation phenomena of SiG anodes. Beginning with a differentiation of the degradation of the individual active materials and the electrode coating, our new approach is expanded to address other relevant research questions which are currently discussed in the literature on silicon-based anodes, *inter alia* the morphological changes of the silicon nanoparticles[109,121,129] and the influence of the cutoff potentials.[173,178,187] Finally, the implications of the underlying mechanisms on the design of practical silicon-based anodes are discussed and recommendations for improved operating conditions of commercially relevant lithium-ion batteries are presented.

3.1.1 Degradation Phenomena in Silicon-Graphite Electrodes

This section presents the article “Differentiating the Degradation Phenomena in Silicon-Graphite Electrodes for Lithium-Ion Batteries”,[102] which was published in September 2017 in the *Journal of The Electrochemical Society*. It is an *open access* article distributed under the terms of the Creative Commons Attribution 4.0 License. The paper was also presented on international conferences, for example at the PRiME Meeting of The Electrochemical Society in Honolulu, Hawaii (October 2-7, 2016), Abstr. #280. The permanent web-link to the article is http://dx.doi.org/10.1149/2.1921712jes.

The article deals with the investigation of the degradation phenomena in blended SiG anodes with different active material ratios (20-60 wt% silicon) and an application-relevant areal capacity of ~2 mAh cm^{-2}. Although it is widely accepted that the cycling stability of silicon-based anodes usually improves upon the addition of graphite,[115,188,189] the relation between the silicon/graphite ratio and the SiG anode aging mechanisms still requires a more fundamental understanding. For example, the voltage profile evolution of blended SiG anodes as well as the extent of side reactions occurring at the individual active materials becomes increasingly important for the development of advanced battery management systems (BMS) and the optimal balancing of the anode and cathode capacity for high-energy density applications.[27,35,190] Although an abundance of articles discussing the degradation of silicon-based anodes exists in the literature,[100,169,170,178] most of these studies deploy electrochemical test cells using a lithium metal counter electrode in presence of a usually 10 times larger amount of electrolyte compared to what would be added to large-scale commercial cells (>50 μL cm^{-2} instead of ~5 μL cm^{-2}). Yet, in practical lithium-ion batteries both the amount of cyclable lithium as well as of the electrolyte solution are limited.[173]

In order to deconvolute lithium inventory limitations from aging effects due to particle/electrode morphological changes and electrolyte decomposition reactions at electrode surface, this PhD thesis introduced a new pseudo full-cell configuration to investigate the degradation phenomena of blended SiG anodes. It features a capacitively largely oversized $LiFePO_4$ cathode (~3.5 mAh cm^{-2}) which offers several advantages compared to conventional lithium-ion full-cells, namely: (i) a stable reference potential of ~3.45 V vs. Li^+/Li to monitor the potential of the SiG anode,[191] (ii) a defined lithium excess which allows to investigate exclusively the degradation of the SiG anode without an additional capacity loss due to the depletion of cyclable lithium, and (iii) minimized side reactions at the cathode due to the comparatively low potential of $LiFePO_4$.[102] In addition, an FEC-containing electrolyte (LP57 with 5 wt% FEC) is used which is known to significantly improve the cycling stability of silicon and at the same time allows to quantify the electrolyte consumption (here: mainly FEC) by *post mortem* ^{19}F-NMR measurements.[103,178]

This study generated four important insights: (i) There exist two major degradation phenomena in blended SiG anodes. The first is caused by a roughening of the silicon nanoparticles upon repeated (de-)lithiation, whereas the second can be ascribed to a mechanical deterioration of the entire electrode coating. (ii) The irreversible capacity loss at the interface between the silicon particles and the electrolyte solution depends only on the capacity exchanged by the silicon particles and is independent of the active material ratio. (iii) The reversible capacity, however, is mainly determined by the loss of interparticle contact pressure and thus strongly dependent on the silicon/graphite ratio. (iv) The comparatively low molar quantity of FEC in commercial electrolyte solutions is the most critical factor in determining the cycle life of SiG anodes in practical lithium-ion batteries.

To analyze the morphology of the SiG anodes, this PhD thesis initiated a collaboration with the JEOL (Germany) GmbH in Freising, which provided valuable insights into the dependence of the electrode morphology on the active material ratio.

Author contributions

M.W. prepared the electrodes and performed the electrochemical testing. M.W. and H.G. developed the pseudo full-cell configuration. M.W. and R.J. conducted the ^{19}F-NMR experiments. R.G. and M.W. prepared the samples for the cross-sectional SEM images and performed the microscopy measurements. M.W. analyzed the data. M.W., S.S., and H.G. wrote the manuscript. All authors discussed the results and commented on the manuscript.

Journal of The Electrochemical Society, **164** (12) A2840-A2852 (2017)

Differentiating the Degradation Phenomena in Silicon-Graphite Electrodes for Lithium-Ion Batteries

Morten Wetjen,[a,*,z] Daniel Pritzl,[a,*] Roland Jung,[a,*] Sophie Solchenbach,[a,*] Reza Ghadimi,[b] and Hubert A. Gasteiger[a,]**

[a]*Chair of Technical Electrochemistry, Department of Chemistry and Catalysis Research Center, Technical University of Munich, D-85748 Garching, Germany*
[b]*JEOL (Germany) GmbH, D-85356 Freising, Germany*

Silicon-graphite electrodes usually experience an increase in cycling performance by the addition of graphite, however, the relation of the silicon/graphite ratio and the aging mechanisms of the individual electrode and electrolyte compounds still requires a more fundamental understanding. In this study, we present a comprehensive approach to understand and quantify the degradation phenomena in silicon-graphite electrodes with silicon contents between 20-60 wt%. By evaluating the cycling performance and total irreversible capacity of silicon-graphite electrodes vs. capacitively oversized $LiFePO_4$ electrodes in presence of a fluoroethylene carbonate (FEC)-containing electrolyte, we demonstrate that the aging of silicon-based electrodes can be distinguished into two distinct phenomena, which we describe as silicon particle degradation and electrode degradation. Cross-sectional scanning electron microscopy (SEM) images and a detailed analysis of the electrode polarization upon cycling complement our discussion. Further, we deploy post-mortem ^{19}F-NMR spectroscopy to (i) quantify to loss of moles of FEC in the electrolyte and correlate this with the amount of charge that was exchanged by the silicon-graphite electrodes, (ii) estimate the pore volume of the silicon-graphite electrodes that is occupied by FEC decomposition products, and (iii) derive implications for the relation of the electrolyte volume and cycle life of commercial silicon-based Li-ion batteries.

Manuscript submitted June 26, 2017; revised manuscript received September 5, 2017. Published September 19, 2017. This was Paper 280 presented at the Honolulu, Hawaii, Meeting of the Society, October 2–7, 2016.

Silicon-based electrodes are very promising candidates to enable the next generation of Li-ion batteries with energy densities on the cell level beyond 350 Wh kg^{-1}.[1,2] In contrast to conventional intercalation anode materials, such as graphite (LiC_6, 372 mAh g^{-1}, 890 Ah L^{-1}), the specific capacity of silicon alloy electrodes is significantly higher ($Li_{15}Si_4$, 3579 mAh g^{-1}, 2194 Ah L^{-1}).[3] Nonetheless, commercialization of silicon-based electrodes is still hampered because of two major challenges:[4]

(i) Large volume expansions up to 280% upon repeated (de-)lithiation of silicon particles deteriorate the electrode integrity, thus causing isolation of active material.[5–7] The formerly reported pulverization of micron-sized silicon particles due to mechanical stress upon repeated volume expansion has been partially solved by using nanometer-sized particles. However, reduction of the silicon particle size also leads to inferior electronic conduction due to more numerous interparticle contacts, and higher solid-electrolyte-interphase (SEI) losses due to the larger relative surface area.[8–10]

(ii) Continuous side reactions at the silicon/electrolyte interface caused by repeated volume expansion and contraction result in ongoing electrolyte decomposition and in a gradual loss of active lithium.[8] In the course of this, SEI-forming additives in the electrolyte, e.g., FEC, are depleted, which was shown to result in a significant increase in cell polarization and a concomitant rapid capacity drop.[8,11]

Various strategies have been proposed to overcome the detrimental effects associated with the volume expansion during (de-)lithiation of silicon and to reduce concomitant irreversible capacity losses, including preparation of silicon thin-films with a significantly reduced silicon/electrolyte interface,[6,12–14] Si-Al-Fe active/inactive alloy electrodes that reduce the volume expansion of the active phase,[5,15,16] and design of nanostructured silicon materials with carbonaceous compounds, such as graphite, to improve the electrical conductivity within the electrode and to better accommodate the volume expansion of silicon.[17–20] Although the surface area per capacity usually increases for nanostructured silicon materials with decreasing diameter,[21] which leads to a higher first cycle irreversible capacity loss, silicon nanowires offer the advantage of a smaller relative surface area change upon (de-)lithiation and in addition usually reveal less morphological changes, due to a reduced mechanical stress within the materials.[22] Therefore, irreversible capacity losses upon cycling are expected to be lower compared to conventional nanoparticles.

Further studies on the degradation mechanisms of silicon-based electrodes were performed with respect to the actual conditions in commercial Li-ion batteries. While some research groups, including those from Obrovac,[15] Guyomard,[23,24] and Abraham,[25–27] already reported studies on full-cell configurations, the majority of the academic literature still refers to half-cell measurements, using lithium metal counter electrodes and an excess of electrolyte. However, side reactions at the lithium metal/electrolyte interface and the usually 10 times larger amount of electrolyte (i.e. >50 μL cm^{-2} instead of 5 μL cm^{-2} in commercial cells)[11] make it difficult to evaluate the degradation phenomena occurring at the silicon-based electrode, including the loss of active lithium and depletion of the electrolyte.[28–30]

In this study, we present a comprehensive approach to understand the degradation mechanisms in silicon-graphite electrodes. Hence, we prepare silicon-graphite electrodes with practical areal capacities between 1.8 and 2.3 mAh cm^{-2}, composed of physical mixtures of different silicon/graphite active material ratios, with silicon contents between 20–60 wt%.[31] By use of cyclic voltammetry, we investigate the electrochemical (de-)lithiation of silicon and graphite as a function of the active material ratio. To evaluate the electrode degradation upon cycling, we introduce pseudo-full cells, comprising silicon-graphite negative electrodes and capacitively oversized $LiFePO_4$ positive electrodes. This cell configuration offers several advantages over practical full-cells, namely: (i) a stable reference potential of 3.45 V vs. Li/Li$^+$ to monitor the silicon-graphite potential in a two-electrode coin-cell configuration, and (ii) to provide a defined lithium reservoir, which allows to investigate exclusively the degradation of the silicon-graphite electrode without an additional capacity loss due to the depletion of cyclable lithium. While these conditions would also be satisfied by a lithium metal electrode, the third reason is (iii) to minimize side reactions of the electrolyte at the positive electrode (here: $LiFePO_4$), which would alter the electrolyte (and FEC) decomposition and thus influence its quantification. As electrolyte we use 1 M $LiPF_6$ in EC:EMC (LP57) with 5 wt% of the widely used fluoroethylene carbonate (FEC) as additive, which is known to significantly improve the cycling stability of the silicon-graphite

---

*Electrochemical Society Student Member.
**Electrochemical Society Fellow.
[z]E-mail: morten.wetjen@tum.de

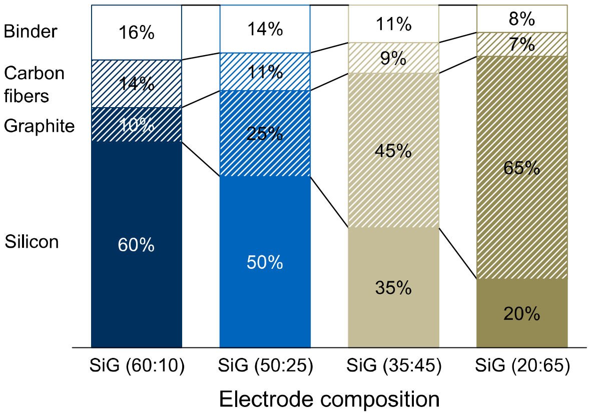

Scheme 1. Silicon-graphite electrode compositions (in wt%) that were investigated in this study.

electrode.[32] We also added a comparably large amount of electrolyte to the coin cells (130 μL or 84 μL cm^{-2}; ~15 times larger compared to large-scale cells), because it allows for a more precise quantification of the FEC consumption via ^{19}F-NMR.[11] From the analysis of the differential capacity curves and the electrode polarization upon cycling, we deconvolute the different degradation mechanisms arising from silicon-graphite electrodes. In addition, we evaluate the consumption of FEC as primary source for electrolyte decomposition through ^{19}F-NMR analysis of the electrolyte harvested from coin-cells after 120 cycles. Finally, we discuss the implications of these results on commercial Li-ion batteries with silicon-based electrodes by estimating the volume of the electrolyte decomposition products and forecasting cycle lifetimes, taking into account practical electrolyte amounts.

Experimental

Electrode preparation.—Silicon-graphite (SiG) electrodes, consisting of silicon nanoparticles (~200 nm, silicon, Wacker Chemie AG, Germany) and graphite (~20 μm, T311, SGL Carbon GmbH, Germany), were prepared through an aqueous ink procedure. Hence, silicon and graphite were thoroughly mixed with vapor grown carbon fibers (VCGF-H, Showa Denko, Japan) and lithium poly(acrylate) (LiPAA, MW = 250,000 g mol^{-1}, Sigma-Aldrich, Germany) in a planetary ball mill (Pulverisette 7, Fritsch, Germany) with ZrO_2 balls (10 mm diameter) under stepwise addition of 18 MΩ cm Milli-Pore water (final solid content ~30 wt%). The resulting ink was cast onto Cu-foil (thickness 25 μm, Goodfellow, USA), using a gap bar coater (RK PrintCoat Instruments, UK). Electrode discs of 14 mm in diameter were punched out and were subsequently dried in a Büchi oven for at least 12 h at 100°C, before being transferred into an Ar atmosphere MBraun glove box (H_2O and O_2 concentration <0.1 ppm) without exposure to air. The areal capacity of the resulting SiG electrodes ranged from 1.8 to 2.3 mAh cm^{-2}, which corresponds to a silicon-graphite active material loading of 0.71–1.84 mg_{SiG} cm^{-2}, depending on the active material ratio.

Scheme 1 summarizes the electrode compositions that were investigated in this study. As one can see, the weight contribution of the active materials (silicon and graphite) accounted for 70–85 wt% of the total electrode mass. Herein, the fraction of silicon was stepwise decreased from 60 to 20 wt%, while the fraction of graphite was simultaneously increased from 10 to 65 wt%. To accomplish adequate electrode integrity and to maintain sufficient electrical conductivity upon cycling, the amount of conductive additive and binder were adjusted to the amount of silicon in the electrode. In accordance with Marks et al.,[33] we adjusted the binder coverage to ~6.3 mg $m_{BET}{}^{-2}$ in all compositions, considering a BET surface area of ~40 m^2 g^{-1} for silicon in the delithiated state, ~5 m^2 g^{-1} for graphite, and ~13 m^2 g^{-1} for the carbon fibers. During the optimization of the electrode compositions, we explored different binder and conductive carbon contents that affected the integrity and cycling stability of the electrodes to a certain extent; yet they did not impact the relation of the FEC consumption and the exchanged capacity, as will be explained in detail in the Discussion section. As the theoretical electrode capacities ranged from 960 to 2,200 mAh $g^{-1}{}_{el}$ (taking theoretical active material capacities of 372 mAh $g^{-1}{}_{C}$ and 3579 mAh $g^{-1}{}_{Si}$),[21] the electrode coating thicknesses were adjusted to 15-31 μm (measured by Mitutoyo *Litematic VL-50*, Japan), thus providing a consistent areal capacity of 1.8–2.3 mAh cm^{-2}.

Electrolyte and test cell assembly.—Electrochemical characterization was performed in coin-cells (CR2032, Hohsen, Japan) that were assembled in an Ar-filled glove box (MBraun, Germany) by sandwiching two porous glass fiber separators (Ø 16 mm, thickness 250 μm, VWR, USA) soaked with 130 μL electrolyte solution (i.e., 84 μL cm^{-2}) between a silicon-graphite electrode (Ø 14 mm, 1.8–2.3 mAh cm^{-2}) and either a lithium metal electrode (Ø 15 mm, 450 μm thickness, Rockwood Lithium, USA) for cyclic voltammetry or a capacitively oversized $LiFePO_4$ (LFP) electrode (Ø 15 mm, 3.5 mAh cm^{-2}, Custom cells, Germany) for cell cycling. As electrolyte solution, 1 M $LiPF_6$ dissolved in a mixture of ethylene carbonate (EC) and ethyl methyl carbonate (EMC) (3:7 w:w; LP57, BASF, Germany) and 5 wt% of fluoroethylene carbonate (FEC, BASF, Germany) was used.

Electrode morphology.—The morphology of the pristine silicon-graphite electrodes was investigated by scanning electron microscopy (SEM). First, electrode cross-sections were prepared by Argon ion beam polishing, using a JEOL Cross Section Polisher IB-09010CP (JEOL, Japan). Afterwards, SEM images were measured by use of a JEOL JSM-7800F PRIME (JEOL, Japan) with a field-emission electron source and a secondary electron detector.

Cyclic voltammetry.—The electrochemical (de-)lithiation of the SiG electrodes was characterized by cyclic voltammetry in a Li//SiG coin-cell setup. Alternating linear potentiodynamic sweeps with a scan rate of 25 μV s^{-1} were applied, forcing the cell potential from open circuit potential (typically ~2.6 V vs. Li/Li^+) to 0.01 V vs. Li/Li^+ (lower vertex potential) and then back to 1.5 V vs. Li/Li^+ (upper vertex potential). All measurements were performed in a climate chamber (Binder, Germany) at 25°C (±0.5°C), using a multi-channel potentiostat VMP3 (BioLogic, France).

Cell cycling.—Electrode polarization and cycling performance of SiG electrodes were investigated through galvanostatic cycling of $SiG//LiFePO_4$ coin-cells. Initially, a formation cycle between 0.01 and 1.25 V vs. Li/Li^+ (corresponding to 3.44 and 2.2 V cell voltage) was applied to all cells using a C-rate of 0.05 h^{-1} (~0.1 mA cm^{-2}). Two constant voltage (CV) steps were performed at the end of SiG lithiation/delithiation (i.e., at 0.01/1.25 V vs. Li/Li^+) with a current limit of 0.02 h^{-1}. For the subsequent cycles, the C-rate was increased to 0.5 h^{-1} (~1.0 mA cm^{-2}). All measurements were performed in a climate chamber (Binder, Germany) at 25°C (±0.5°C), using a battery cycler (Series 4000, Maccor, USA).

Electrolyte consumption.—Consumption of fluoroethylene carbonate (FEC) during galvanostatic cycling was investigated by ^{19}F-NMR spectra which were obtained post-mortem from the electrolyte solutions. For this, $SiG//LiFePO_4$ coin-cells were disassembled after 120 cycles and the glass fiber separators were subsequently dipped into deuterated dimethyl sulfoxide (DMSO-d6, anhydrous, Sigma-Aldrich, USA). The resulting solutions were then filled into air-tight NMR tubes and ^{19}F-NMR spectra were measured using a Bruker Ascend 400 (400 MHz). As described by Jung et al., the resulting ^{19}F-NMR spectra show only peaks that can either be ascribed to PF_6^- or FEC, i.e., no additional peaks from $PO_2F_2^-$ or PO_3F^{2-} can be observed that originate from salt decomposition or separator

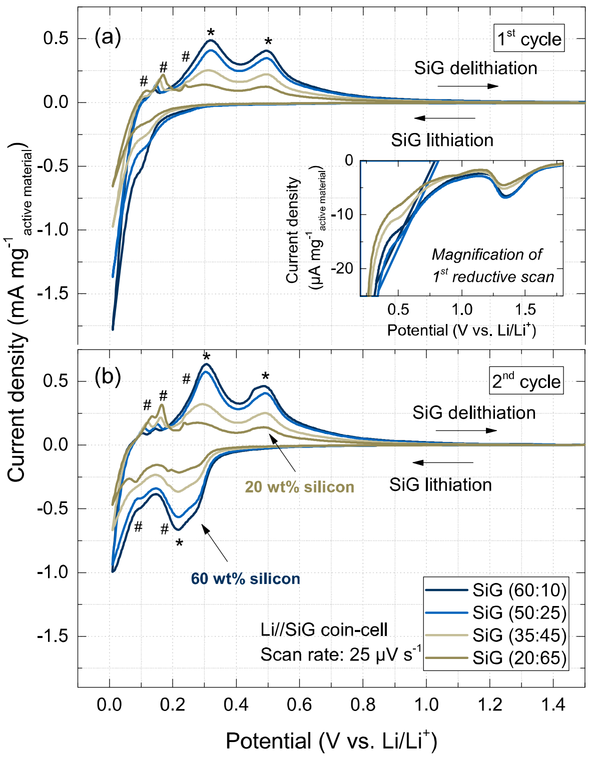

Figure 1. Cyclic voltammetry responses of the first (panel a) and the second cycle (panel b) of Li//SiG coin-cells, incorporating silicon-graphite electrodes with different active material ratios. Characteristic features are labelled either by star (silicon) or hash (graphite). Electrolyte: 130 μL LP57 with 5 wt% FEC, scan rate: 25 μV s^{-1}, vertex potentials: 0.01 and 1.5 V, electrode area: 1.54 cm^2, areal capacities ranged from 1.8 to 2.3 mAh cm^{-2}, temperature: 25°C.

decomposition by HF.[11,34] As a result, the concentration of PF_6^- in the electrolyte solution shows no quantitative changes upon cycling and can thus be defined as an internal standard. For that reason, changes in the ratio of PF_6^- peak integrals to FEC peak integrals allow to monitor the consumption of FEC after a selected number of cycles. A previous work from our group,[11] which deployed this method provided the same four-electron mechanism for the reduction of FEC as an independently conducted analysis via gas chromatography coupled with mass spectrometry (GC-MS) by Petibon et al.[35]

Results

Electrode characterization.—Table I summarizes the properties of the silicon-graphite electrodes that were investigated in this study. Based on measured areal loadings of the electrode coatings, the known electrode composition, and the measured electrode thicknesses, the calculated electrode densities of all electrodes range between ~0.6–0.7 g cm^{-3}$_{el}$, corresponding to electrode porosities ranging in between ~67–73%, were obtained for all compositions. We ascribe this characteristic to a combination of the similar bulk densities of silicon (~2.3 g cm^{-3}) and graphite (~2.2 g cm^{-3}) and of the large and well dispersed carbon fibers (diameter: 150 nm, length: 10–20 μm) that create a substantial amount of void spaces.

The electrochemical (de-)lithiation of the silicon-graphite electrodes was investigated by cyclic voltammetry. Figure 1 shows the current responses of (a) the first and (b) the second cycle obtained from the different SiG electrode compositions. While the lithiation features of silicon and graphite are largely superimposed during the first reductive scan at potentials below 0.18 V vs. Li/Li$^+$, the oxidative scan clearly reveals two characteristic delithiation peaks of silicon at 0.31 and 0.50 V vs. Li/Li$^+$,[36] as well as three delithiation peaks of graphite at 0.11, 0.16, and 0.24 V vs. Li/Li$^+$, which correspond to the voltage plateaus of lithium-graphite intercalation compounds LiC_x.[37] The silicon features appear more pronounced in the 60 wt% and 50 wt% silicon electrodes (blue curves), whereas the graphite peak currents decrease, according to the lower graphite content in these electrodes. As expected, the lithiation behavior of silicon changes between the first and second cycle (see Figure 1b). Once the silicon has become amorphous after the first reductive scan, lithiation in subsequent scans starts at more positive potentials of about 0.21 V and continues below 0.11 V vs. Li/Li$^+$. In agreement with Fuchsbichler et al.,[17] graphite is lithiated (<0.19 V vs. Li/Li$^+$) and delithiated (<0.24 V vs. Li/Li$^+$) step-wise at slightly more negative potentials compared to silicon.

The inset in Figure 1a shows a magnification of the first reductive scan. The feature at about 1.3 V vs. Li/Li$^+$ can be assigned to the reductive decomposition of FEC.[38] As it was reported earlier in the literature, FEC is reduced at more positive potentials than EC and EMC, thereby forming an SEI layer on the active material particles, which significantly reduces further electrolyte decomposition.[39–41]

Cycling performance in SiG//LFP cells.—The cycling performance of the silicon-graphite electrodes (1.8–2.3 mAh cm^{-2}) was investigated vs. capacitively oversized $LiFePO_4$ electrodes (~3.5 mAh cm^{-2}). To fully utilize the theoretical specific capacity of the different silicon-graphite electrodes, the cutoff potentials were set to 0.01 V vs. Li/Li$^+$ during lithiation (3.44 V cell voltage) and 1.25 V vs. Li/Li$^+$ during delithiation (2.2 V cell voltage). In addition, constant voltage steps were applied at the end of lithiation and delithiation. Figure 2 shows (a) the coulombic efficiency (in %) and (b) the gravimetric delithiation capacities normalized to the entire electrode mass (in mAh g^{-1}$_{el}$) as a function of the cycle number. Table I summarizes relevant data of the first cycle and the capacity retention upon

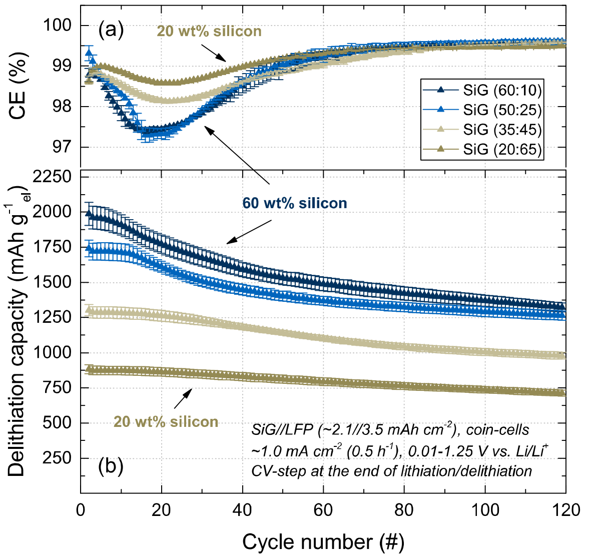

Figure 2. Galvanostatic cycling of SiG//LFP coin-cells, with different silicon-graphite electrode compositions. Areal capacities: SiG (1.8-2.3 mAh cm^{-2}), LFP (~3.5 mAh cm^{-2}), electrolyte: 130 μL LP57 with 5 wt% FEC, applied currents: ~0.1 mA cm^{-2} (0.05 h^{-1}) during formation cycle and ~1.0 mA cm^{-2} (0.5 h^{-1}) during consecutive cycles, SiG electrode cutoff potentials of 0.01 and 1.25 V vs. Li/Li$^+$, constant voltage steps at 0.01/1.25 V vs. Li/Li$^+$ at the end of (de-)lithiation with a current limit of 0.02 h^{-1}. Panel (a): Coulombic efficiency obtained from the ratio of delithiation/ lithiation capacity, and panel (b): Delithiation capacity in mAh g^{-1}$_{el}$ per silicon-graphite electrode. The error bars represent the standard deviation of at least two independent repeat measurements.

Table I. Properties of the silicon-graphite electrodes that were investigated in this study. Selected data from the first galvanostatic cycle at 0.05 h^{-1} between 0.01 and 1.25 V vs. Li/Li^+ and from ^{19}F-NMR FEC consumption measurements after 120 cycles. The ± values represent the standard deviation of at least two independent repeat measurements.

		Electrode composition			
Electrode properties	Units	SiG (60:10)	SiG (50:25)	SiG (35:45)	SiG (20:65)
Theoretical electrode capacity	$mAh\ g^{-1}{}_{el}$	2,185	1,883	1,420	958
Capacity contribution from silicon	%	98.3	95.1	88.2	74.7
Areal capacity	$mAh\ cm^{-2}$	2.3 ± 0.2	1.8 ± 0.2	1.8 ± 0.2	2.1 ± 0.2
Electrode mass loading	$mg\ cm^{-2}$	1.06	0.94	1.30	2.17
Active material loading	$mg_{SiG}\ cm^{-2}$	0.74	0.71	1.04	1.84
Electrode thickness	µm	15 ± 2	16 ± 2	21 ± 2	31 ± 2
Electrode density	$g\ cm^{-3}{}_{el}$	0.71	0.59	0.62	0.70
Electrode porosity	%	67	73	72	68
Electrode BET area (delithiated)	$m^2{}_{BET}\ g^{-1}$	26	23	17	12
Binder coverage	$mg\ m^{-2}{}_{BET}$	6.1	6.2	6.3	6.6
1st cycle coulombic efficiency	%	87.6 ± 0.8	86.1 ± 0.7	86.3 ± 0.5	87.1 ± 0.5
1st cycle irreversible capacity	$mAh_{irr}\ g^{-1}{}_{el}$	272	272	201	128
1st cycle delithiation capacity	$mAh\ g^{-1}{}_{el}$	1,933	1,685	1,265	860
Capacity retention in cycle 120	$mAh\ g^{-1}{}_{el}$	1,323	1,264	979	713
Capacity retention cycle 3–120	%	67	74	76	82
cycle # at 80% capacity retention	#	44	58	87	>120
Total irreversible capacity after 120 cycles	$Ah_{irr}\ g^{-1}{}_{el}$	2.47	2.17	1.62	0.93
	$mAh_{irr}\ cm^{-2}$	2.62	2.04	2.11	2.02
Capacity per FEC after 120 cycles	$mAh_{tot}\ \mu mol^{-1}$	11.5	12.9	14.5	15.7
	$mAh_{tot,\ Si}\ \mu mol^{-1}$	11.3	12.2	12.8	11.7
FEC per irreversible capacity after 120 cycles	$\mu mol\ mAh^{-1}{}_{irr}$	13.0	12.3	11.5	13.1

cycling. As can be seen from Figure 2b, the different electrode compositions demonstrate delithiation capacities between 860 mAh $g^{-1}{}_{el}$ (20 wt% silicon, dark brown curve) and 1,930 mAh $g^{-1}{}_{el}$ (60 wt% silicon, dark blue curve) during the first cycle (see also Table I). Interestingly, all electrodes indicate a very similar first cycle capacity utilization and coulombic efficiency, both in the range of ~85–88%, independent of the electrode composition (i.e., all electrodes reveal a similar areal irreversible capacity loss of 0.28 ± 0.02 mAh cm^{-2} in the first cycle). These first cycle coulombic efficiencies of the SiG electrodes are very similar as for the silicon electrodes without graphite but using the same silicon particles (40 wt% silicon, 20 wt% VGCF, 20 wt% LiPAA) with 85–86% (data not shown), and are only slightly lower compared to the ~92% for pure graphite electrodes (95 wt% graphite, 5 wt% PVdF). We explain this behavior by the similar BET surface area per capacity of both active materials (11–13 $m^2{}_{BET}$ Ah^{-1}) in the delithiated state, suggesting that the initial SEI formation process is similar at silicon and graphite. As the irreversible capacity loss of the first cycle, which is commonly associated with SEI formation, is proportional to the BET surface area of the active material, the amount of SEI loss per delivered capacity, and thus the coulombic efficiency, must consequently be the similar for all compositions.[42] Thus, contrary to common perception, the first cycle coulombic efficiencies of silicon and graphite are actually quite similar in this case. As a corollary, for silicon particles with a lower BET area (i.e., with a lower $m^2{}_{BET}$ Ah^{-1} value), one would expect them to exhibit equal or even superior coulombic efficiency compared to graphite, as the first-cycle coulombic efficiency seems to scale with $m^2{}_{BET}$ Ah^{-1} value. Consistent with this assumption, Yoon et al. recently reported a coulombic efficiency of ~91.5% for silicon particles with a diameter of 700 nm, which is higher than that of graphite.[30]

Within the first 60 cycles, all electrodes reveal a distinct capacity decay (see Figure 2b), which occurs earlier and increases in extent with increasing silicon content. Here we would like to note that this loss of reversible capacity is not related to the depletion of FEC as described by Jung et al.,[11] because our ^{19}F-NMR analysis after 120 cycles revealed a residual FEC concentration of at least ~1.2 wt% in the electrolyte (originally 5 wt%). The cycling stability notably improves after the initial capacity decays, leading to similar capacity fading rates for all compositions. The resulting capacity retentions between the 3rd (i.e., after formation) and the 120th cycle at 0.5 h^{-1} lie between 67% for the 60 wt% silicon electrode and 82% for the 20 wt% silicon electrode (see Table I), meaning that the silicon/graphite ratio displays a trade-off between the initial delithation capacity and subsequent cycling stability. In addition, all electrode compositions show a minimum in the coulombic efficiency around the 20th cycle (see Figure 2a), followed by a gradual increase to values above 99.5%. Like the capacity decay, the minimum coulombic efficiency value at ~20 cycles decreases with increasing silicon content. At this point we would like to note that the capacity fade in Figure 2b is not related to a depletion of active lithium, i.e. the capacity of the LFP positive electrode after 120 cycles is still large enough to avoid a limitation in cyclable lithium. The same cycling behavior was also obtained in preliminary experiments in half-cells vs. lithium metal.[31]

Irreversible capacity loss upon cycling.—To understand the irreversible processes taking place in the silicon-graphite electrodes at different stages of cycle life, the total irreversible capacity $\sum Q_{irr}$ as a function of the cycle number is shown in Figure 3. Here, $\sum Q_{irr}$ was calculated as described by Equation 1, with $Q_i^{lithiation}$ and $Q_i^{delithiation}$ being the specific lithiation and delithiation capacities in Ah_{irr} $g^{-1}{}_{el}$, while the index i stands for the respective cycle number.

$$\sum Q_{irr} = \sum_{i}^{120} \left(Q_i^{lithiation} - Q_i^{delithiation}\right) \qquad [1]$$

As can be seen in Figure 3, the $\sum Q_{irr}$ evolution of all electrode compositions is characterized by a sigmoidal shape. The first part consists of an initial offset in $\sum Q_{irr}$ of about 0.13–0.27 Ah_{irr} $g^{-1}{}_{el}$, corresponding to the first cycle irreversible capacity described in Table I, and subsequent sigmoidal increase in $\sum Q_{irr}$, with a maximum in the slope after ~20 cycles, whereby the slope increases with increasing silicon content. The second part after about ~45 cycles, however, is characterized by a less steep and nearly linear growth of $\sum Q_{irr}$ with cycle number. Interestingly, the sigmoidal increase of $\sum Q_{irr}$ within the first ~45 cycles implies that the irreversible processes go through a maximum after ~20 cycles, which also corresponds to the minimum in coulombic efficiency in Figure 2a. We

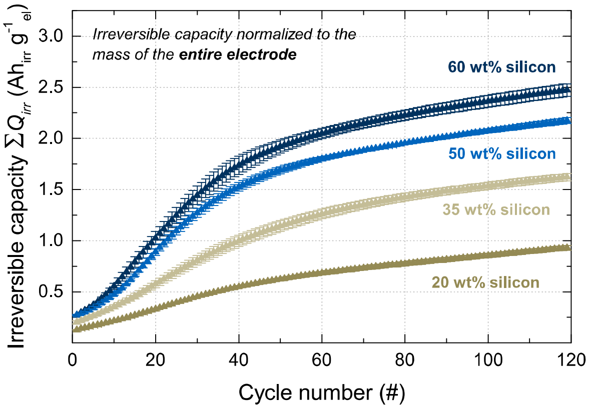

Figure 3. Total irreversible capacity $\sum Q_{irr}$ in units of $\text{Ah}_{\text{irr}}\ \text{g}^{-1}{}_{\text{el}}$ (defined by Equation 1) as a function of the cycle number, obtained from the galvanostatic cycling data of the SiG//LFP coin-cells shown in Figure 2. The error bars represent the standard deviation of at least two independent repeat measurements.

expect that this behavior is caused by the degradation of the silicon particles, which will be explained in more detail in the Discussion section. In contrast to the first phase, the $\sum Q_{irr}$ slopes in the second phase are almost constant and very similar for all electrode compositions (see Figure 3). In this stage, residual irreversible capacity losses are significantly reduced and mainly scale with the delivered capacity, but seem to be independent of the electrode composition.

Silicon-graphite electrode capacity decay.—Figure 4 shows cyclic voltage profiles of the 20 wt% silicon electrode as a function of the exchanged capacity for the 2nd, 20th, 60th, and 120th cycle. For this electrode with the highest graphite content of 65 wt%, the capacity contribution from the graphite active material can be most clearly distinguished from the contributions by silicon. In addition, we plotted the differential capacity curve of the same electrode in Figure 5a, which allows a direct identification of the (de-)lithiation potentials of silicon and graphite (highlighted by hash signs). Accordingly, the cyclic voltage profiles in Figure 4 are increasingly compressed in x-direction upon continued cycling, reflecting a decrease in the reversible capacity of the silicon-graphite electrode. To identify the origin of this capacity decay, we first consider that the delithiation capacity contribution in Figure 4 at potentials below 0.25 V vs. Li/Li$^+$ stays constant at about 250 mAh $\text{g}^{-1}{}_{\text{el}}$. Taking into account the graphite delithiation potentials obtained from cyclic voltammetry in Figure 1 and the theoretical capacity contribution of ~25% from graphite in the 20 wt% silicon electrode (~75% of the total theoretical capacity of 960 mAh $\text{g}^{-1}{}_{\text{el}}$ are contributed by silicon; see Table I), we can conclude that the loss of reversible capacity is mainly associated with the silicon active material at delithiation potentials above 0.25 V vs. Li/Li$^+$. This conclusion is additionally confirmed by the differential capacity curve shown in Figure 5a, which clearly shows that the integral of the peaks associated with the delithiation from graphite (see hash signs) remain almost constant.

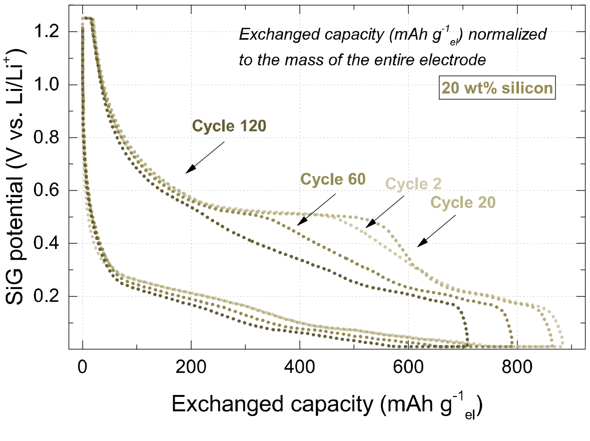

Figure 4. Cyclic voltage profiles of the 20 wt% silicon electrode plotted as a function of the exchanged capacity ($\text{mAh g}^{-1}{}_{\text{el}}$), obtained from galvanostatic cycling of SiG//LFP coin-cells. The SiG electrode potential was calculated from the SiG//LFP cell voltage, referring to a constant LFP electrode potential of 3.45 V vs. Li/Li$^+$.

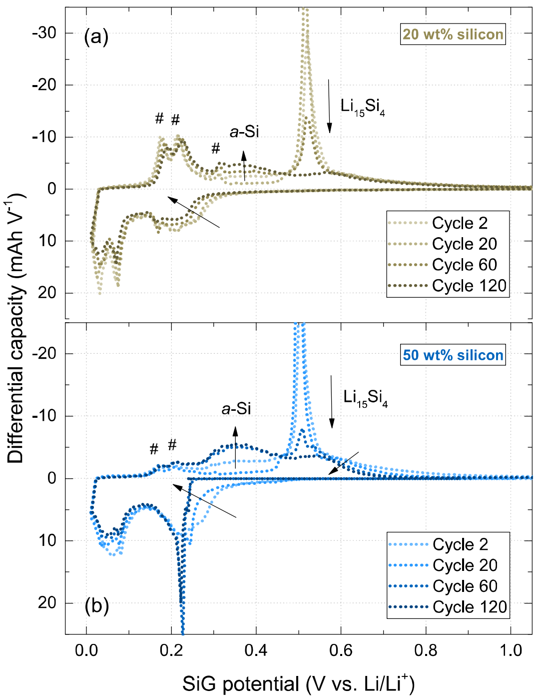

Figure 5. Differential capacity curves of the (a) 20 wt% silicon electrode and (b) 50 wt% silicon electrode plotted as a function of the silicon graphite potential (V vs. Li/Li$^+$). The data were obtained from galvanostatic cycling of SiG//LFP coin-cells. The SiG electrode potential was calculated from the SiG//LFP cell voltage, referring to a constant LFP electrode potential of 3.45 V vs. Li/Li$^+$.

In addition, Figure 5b shows the differential capacity profile of the 50 wt% silicon electrode for the 2nd, 20th, 60th, and 120th cycle as a function of the silicon-graphite potential. Both electrodes reveal almost no polarization during the lithiation at potentials below 0.2 V vs. Li/Li$^+$ upon cycling, however, a distinct potential drop after 60 cycles for the 50 wt% silicon electrode can be observed at low degrees of lithiation, i.e., at potentials above 0.2 V vs. Li/Li$^+$. As a result, the loss of reversible capacity must be largely caused by an incomplete lithiation of the silicon active material, which can be clearly seen by the disappearance of the lithiation shoulder in the 0.25-0.5 V vs. Li/Li$^+$ region. Analogously, during delithiation both electrodes reveal significant changes at potentials above 0.25 V vs. Li/Li$^+$ upon cycling. Between the 2nd and the 20th cycle, a distinct peak at about 0.45 V vs. Li/Li$^+$ can be seen, which is ascribed to the two-phase delithiation reaction from crystalline $Li_{15}Si_4$ to amorphous $Li_{\sim 2}Si$.[43] As expected, the extent of this peak is larger in the 50 wt% electrode. Several studies on different alloy electrodes indicated that these two-phase boundaries cause additional particle damage due to inhomogeneous volume changes compared

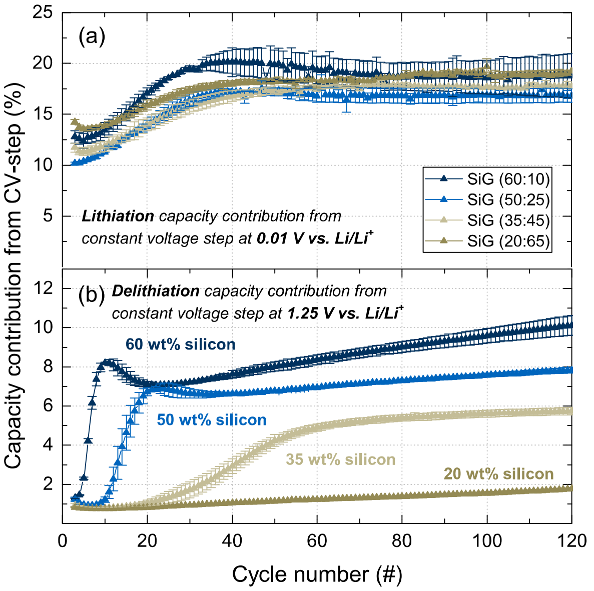

Figure 6. Capacity contribution (in %) from constant voltage steps at the end of (a) lithiation at 0.01 V vs. Li/Li$^+$ and (b) delithiation at 1.25 V vs. Li/Li$^+$, obtained from galvanostatic cycling at 0.5 h^{-1} of SiG//LFP coin-cells shown in Figure 2. The first two cycles were omitted to exclude any effects that may result from the lower C-rate of 0.05 h^{-1} during the first cycle. The error bars represent the standard deviation of at least two independent repeat measurements.

to single-phase reactions and that they often coincide with a capacity fade of the respective electrodes.[7,44] For silicon-based electrodes, Iaboni and Obrovac demonstrated recently that the formation of $Li_{15}Si_4$ during cycling can be used as a sensitive indicator for weakly bound silicon regions and coincides with the detachment of silicon particles, leading to a capacity decay.[6] In agreement with their report, the extent of the $Li_{15}Si_4$ peak shown in Figure 5 increases within the first 20 cycles, which corresponds to a simultaneous decrease of the delithiation from amorphous silicon-lithium alloy (*a*-Si). In other words, during lithiation within the first cycles more silicon is reduced to form the highly lithiated crystalline $Li_{15}Si_4$ phase. However, analogous to the cycling data shown in Figure 2b after 60 cycles a continuous decrease of the $Li_{15}Si_4$ peak can be observed, which, though it is partially compensated by a smaller increase of the delithiation capacity from amorphous silicon-lithium alloy (*a*-Si), indicates that the silicon particles no longer reach the highly crystalline $Li_{3.75}Si$ stoichiometry. Although this effect is more pronounced in electrodes with higher silicon content and can be explained by an incomplete lithiation, the decay of the delithiation capacity at potentials above 0.6 V vs. Li/Li$^+$, i.e. at low degrees of lithiation, is even more severe and the main source for the loss of reversible capacity, which agrees with the disappearance of the shoulder during lithiation at potentials between 0.25 and 0.5 V vs. Li/Li$^+$. This phenomenon is most likely caused by insufficiently connected silicon particles, which suffer either from incomplete lithiation or, more likely, incomplete delithation because of a higher contact and interfacial resistance during particle shrinkage.[30]

Figure 6 shows the capacity contributions $Q_{CV,\%}$ from the constant voltage steps at the end of (a) the lithiation step at 0.01 V vs. Li/Li$^+$ and (b) the delithiation step at 1.25 V vs. Li/Li$^+$ for the different electrode compositions. The contributions for each cycle were calculated according to Equation 2,

$$Q_{CV,\%} = \frac{Q_{CV}}{Q_{CC} + Q_{CV}} \cdot 100 \qquad [2]$$

where Q_{CC} is the capacity from the constant current step and Q_{CV} is the capacity from the constant voltage step. As can be seen in Figure 6a, the lithiation of the silicon-graphite electrodes is characterized by a continuous increase of $Q_{CV,\%}$ by ~6%-points before stabilizing between 17–19% across all electrode compositions. In other words, after ~45 cycles approximately one fifth of the lithiation capacity is derived from the constant voltage step at 0.01 V vs. Li/Li$^+$. The slope of $Q_{CV\%}$ vs. cycle number reaches a maximum after ~20 cycles before it decreases to essentially zero after about ~45 cycles. The occurrence of this inflection point seems to be independent of the electrode composition and again coincides with the minimum in the coulombic efficiency in Figure 2a. We assume that the initial rise in $Q_{CV,\%}$ results from a minor increase in electrode polarization (as shown in Figure 5, the voltage polarization increase for the lithiation process is rather small), which we believe originates from enhanced electrolyte decomposition in the initial cycles due to silicon particle degradation (i.e., surface growth) and subsequent growth of the SEI layer. Upon continued cycling (i.e., after ~45 cycles), the increase in $Q_{CV,\%}$ is only minor across all electrode compositions. As it is known that the SEI layer mainly consists of electrically insulating electrolyte decompositions products, e.g., inorganic LiF and Li_2CO_3 compounds as well as organic alkyl carbonates and alkoxides, its growth is limited to a certain thickness.[45,46] Hence, we expect that the silicon surface does not change significantly after cycle 45.

As the electrode polarization during lithiation does not seem to depend on the electrode composition, there must exist a second degradation phenomenon during delithiation that leads to the observed composition-dependent capacity drop shown in Figure 2. To further investigate this, the capacity contribution from the CV-step at 1.25 V vs. Li/Li$^+$ during delithiation is shown Figure 6b. Initially, $Q_{CV,\%}$ is in the range of ~1% across all electrode compositions and thus much smaller compared to that of the lithiation CV step. This can be explained by considering exemplarily the differential capacity curves in Figure 5, according to which the delithiation cutoff potential of all silicon-graphite electrodes, independent of the silicon content, is significantly higher than the average delithiation potential of ~0.5 V vs. Li/Li$^+$. However, for the silicon-rich SiG electrode with 60 wt% silicon, $Q_{CV,\%}$ rises rapidly after the first cycle, reaching ~8% within less than 10 cycles, which indicates an increased difficulty to completely delithiate the silicon particles. The same is observed for the 50 wt% and the 35 wt% SiG electrodes, which display a sharp increase of the $Q_{CV,\%}$ value after ~10 and ~20 cycles, respectively. While also for the Si-poor SiG electrode with 20 wt% silicon a gradual increase of $Q_{CV,\%}$ is observed after ~30 cycles, the magnitude of this increase is substantially smaller than for the electrodes with higher silicon content. In summary, the higher the silicon content of the SiG electrodes, the earlier initiates the observed increase in $Q_{CV,\%}$ and the higher is the magnitude of the $Q_{CV,\%}$ increase. Remarkably, the onset and the extent of the increase of $Q_{CV,\%}$ during the delithiation cycles shown in Figure 6b coincides with the onset and the extent of the distinct capacity decay within the first 60 cycles as shown in Figure 2. The origin of this phenomenon will be further examined in the Discussion section.

Electrolyte consumption.—Besides the capacity decay, continuous consumption of the electrolyte constitutes a severe challenge to silicon-based electrodes. To quantify the loss of electrolyte caused by side reactions at the silicon/electrolyte interface, we harvested the electrolyte-soaked separators from the cycled SiG//LFP coin-cells after 120 cycles and measured ^{19}F-NMR of the extracted electrolytes. As FEC is reduced at more positive potentials than EC or EMC, Jung et al. demonstrated by on-line electrochemical mass spectrometry (OEMS) that FEC almost entirely suppresses the decomposition of EC as long there is FEC present in the electrolyte.[11] Hence, we consider in the following the change in the ratio of the FEC and PF_6^- peak integrals as a sensitive indicator for the electrolyte consumption upon cycling.

Figure 7a shows the total charge+discharge capacity per mole of FEC obtained from the SiG//LFP coin-cells depicted in Figure 2 after 120 cycles. This consumption rate was calculated by Equation 3,

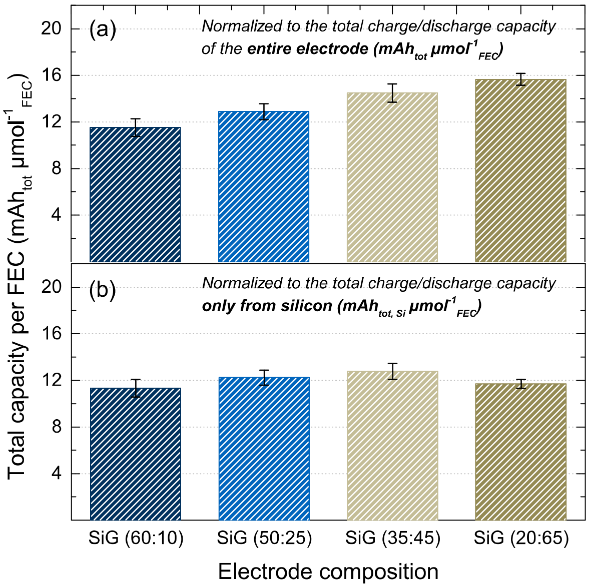

Figure 7. Total charge+discharge capacity (as defined by Equation 4) per mole of FEC after 120 cycles, using the cycling procedure described in Figure 2. The consumed amount of FEC was determined by ^{19}F-NMR spectroscopy from electrolytes that were harvested from SiG//LFP coin-cells after 120 cycles. (a) Total capacity of the entire electrode (mAh$_{tot}$ µmol^{-1}$_{FEC}$), (b) Total capacity contributed only from the silicon active material (mAh$_{tot, Si}$ µmol^{-1}$_{FEC}$). The error bars represent the standard deviation of at least two independent repeat measurements.

where $\sum Q_{tot}$ is the total charge exchanged during charging and discharging in mAh$_{tot}$ (see Equation 4) and n_{FEC} is the FEC consumption in µmol$_{FEC}$ as determined from integral analysis of the ^{19}F-NMR spectra. In other words, this thus determined capacity per FEC describes the amount of charge that can be exchanged by the silicon active material until 1 µmol of FEC is consumed by concomitant side reactions.

$$Capacity\ per\ FEC = \frac{\sum Q_{tot}}{n_{FEC}} \qquad [3]$$

$$\sum Q_{tot} = \sum_{i}^{120} \left(Q_i^{lithiation} + Q_i^{delithiation}\right) \qquad [4]$$

As can be seen, the total capacity per mole of FEC increases gradually with decreasing silicon content from 11.5 mAh$_{tot}$ µmol^{-1}$_{FEC}$ in the 60 wt% silicon electrode to 15.7 mAh$_{tot}$ µmol^{-1}$_{FEC}$ in the 20 wt% silicon electrode. Taking into account a density of 1.41 g cm^{-3} for FEC, this would correspond to a total capacity per µL FEC of 150–210 mAh$_{tot}$ µL^{-1}$_{FEC}$. Interestingly, this difference is comparatively small, especially when considering that the 60 wt% silicon electrode contains nominally three times more silicon compared to the 20 wt% silicon electrode. For that reason, we applied Equation 5 to correct the total exchanged capacity by the capacity contribution from graphite to obtain the capacity that results only from the (de-)lithiation of silicon (mAh$_{tot, Si}$ µmol^{-1}$_{FEC}$) as shown in Figure 7b,

$$\sum Q_{tot,\,Si} = \sum Q_{tot} \cdot \frac{x_{Si} \cdot Q_{Si}^{theo}}{x_{Si} \cdot Q_{Si}^{theo} + x_C \cdot Q_C^{theo}} \qquad [5]$$

where $\sum Q_{tot,Si}$ is the total capacity from silicon, $\sum Q_{tot}$ is the total capacity from the entire electrode (see 1st and 2nd rows in Table I), Q_{Si}^{theo} is the theoretical capacity of silicon, Q_C^{theo} is the theoretical capacity of graphite, x_{Si} is the relative amount of silicon, and x_C is the relative amount of graphite. It is to note that for reasons of simplicity, we make the approximation that the ratio of the capacity contributions of silicon and graphite remains constant throughout cycling. As the silicon accounts for the majority of the capacity (>75%) in any case, the error arising from this assumption should be low, even if the capacity of graphite and silicon in the SiG electrodes would fade at different rates. Using Equation 5 to quantify the charge+discharge capacity contribution from silicon and dividing its value by the measured FEC consumption, it can be seen in Figure 7b that the thus calculated total capacity from silicon per mole of FEC falls within a very narrow range, with mean values for each SiG electrode composition which differ from each other by less than one standard deviation, so that the overall capacity per consumed FEC can be averaged for all four SiG electrode compositions to 12.0 ± 0.8 mAh$_{tot, Si}$ µmol^{-1}$_{FEC}$. From this, we conclude that the total capacity exchanged by silicon causes the same FEC consumption across all SiG electrode compositions, suggesting that the graphite content has no influence on the FEC consumption rate.

$$FEC\ per\ irreversible\ capacity = \frac{n_{FEC}}{\sum Q_{irr}} \qquad [6]$$

$$Electrons\ per\ FEC = \frac{\sum Q_{irr}}{n_{FEC} \cdot F} \qquad [7]$$

To further support our conclusion, we applied Equation 6 to normalize the FEC consumption n_{FEC} after 120 cycles to the total irreversible capacity $\sum Q_{irr}$ (see Equation 1). As a result of the repeated volume expansion of silicon (~280%) and the resulting cracking and continuous renewal of the SEI layer, we assume that the irreversible capacity losses after 120 cycles can be almost fully ascribed to the side reactions at the silicon/electrolyte interface. In accordance with that, the normalization reveals a similar ratio of 11.5-13.1 µmol$_{FEC}$ mAh^{-1}$_{irr}$ across all electrode compositions (shown in Table I), which is in good agreement with the results obtained by Jung et al. and additionally confirms their hypothesis according to which there is only one major source of irreversible capacity loss on silicon when using FEC containing electrolytes, namely the reduction of FEC.[11] However, by use of Equation 7, the conversion of the µmol$_{FEC}$ mAh^{-1}$_{irr}$ into the number of electrons that are consumed by the reduction of FEC reveals a slightly lower value of 3.0 ± 0.2 compared to the proposed four-electron mechanism of Jung et al.[11] We ascribe this discrepancy to the influence of the two constant voltage steps at 0.01 and 1.25 V vs. Li/Li$^+$ in the present study, as result of which our silicon-graphite electrodes experienced these limiting potentials for a much longer time compared to the constant current procedure of Jung et al.,[11] which in turn seem to affect the reduction processes at the silicon/electrolyte interface.

Building up on the relation of the FEC consumption and the irreversible capacity of 11.5–13.1 µmol$_{FEC}$ mAh$_{irr}$, we can now compare the silicon-graphite electrodes with a standard graphite:PVdF (95:5) electrode with the same graphite particles in a conventional graphite//LFP full-cell cycling procedure (~1.7 mAh cm^{-2}, CCCV cycling between 2.0–4.0 V at 1 C), which shows a total irreversible capacity of ~0.34 mAh per 550 mAh total charge-discharge capacity (after ~200 cycles). By multiplying the total irreversible capacity with the FEC consumption rate (here: 13.1 µmol$_{FEC}$ mAh$_{irr}$), we obtain an absolute FEC consumption of 4.45 µmol$_{FEC}$ (see Equation 6). Subsequent normalization of the total charge-discharge capacity of 550 mAh to the absolute FEC consumption in accordance with Equation 3 results in a total capacity per FEC of ~124 mAh µmol$_{FEC}$. Comparing this value to the capacities per FEC for the different silicon-graphite electrodes of 11.5–15.7 mAh µmol$_{FEC}$ (see Figure 7a) clearly shows that the FEC consumption caused by the (de-)lithiation of graphite is more than one order of magnitude smaller as for silicon and likely mainly results from the initial SEI formation during the first cycles.

Discussion

Differentiating the degradation phenomena in silicon-graphite electrodes.—A close inspection of the galvanostatic cycling data

(Figure 2) and the two different regions in the corresponding total irreversible capacity vs. cycle number plot (Figure 3) suggest that our silicon-graphite electrodes undergo two distinct degradation phenomena. There seems to be one degradation mechanism common to all SiG electrodes, which results in an initial dip in the coulombic efficiency over the first ~45 cycles, which goes through a minimum after ~20 cycles (see Figure 2a), and which results in a rapid initial increase in the CV-step lithiation capacity (see Figure 6a). Although the extent of the coulombic efficiency minimum increases with the silicon content in the electrodes, it occurs after the same number of charge/discharge cycles across all electrode compositions, independent of the silicon/graphite active material ratio. In contrast, there seems to be another degradation mechanism which depends on the silicon/graphite ratio, namely the initially rapid and distinct capacity decay (see Figure 2b) as well as the clearly different increase in the delithiation capacity during the CV-step (see Figure 6b). As will be outlined in the following, we propose that the first phenomenon is mostly related to the intrinsic properties of the silicon active material such as particle size and morphology (furtheron referred to as *silicon particle degradation*), whereas the second phenomenon depends not only on the silicon material but also on the electrode composition, viz., the silicon/graphite ratio (furtheron described as *electrode degradation*).

Our hypothesis that the first degradation mechanisms, i.e., the silicon particle degradation mechanism indeed mostly depends on the intrinsic properties of the silicon particles can be illustrated by normalizing the accumulated irreversible capacity $\sum Q_{irr}$ (in $\mathrm{Ah_{irr}\,g^{-1}{}_{el}}$) shown in Figure 3 by the silicon content of the respective silicon-graphite electrodes and plotting the resulting $\sum Q_{irr,Si}$ (in $\mathrm{Ah_{irr}\,g^{-1}{}_{Si}}$) as a function of the cycle number, as shown in Figure 8a, as well as a function of the total charge-discharge capacity (see Figure 8b). The most important finding of this analysis is that all four SiG electrode compositions now show an essentially identical behavior, thus revealing that the total irreversible capacity only depends on the amount of silicon in the electrodes, with apparently negligible contributions from the silicon/graphite ratio or from the graphite content. Furthermore, by plotting $\sum Q_{irr,Si}$ versus the total amount of exchanged charge (see Equation 4), Figure 8b shows that $\sum Q_{irr,Si}$ is identical for all SiG electrodes, consistent with the observation that the FEC consumption of all SiG electrodes only depends on the total charge+discharge capacity (see Figure 7b).

To explain the initial sigmoidal increase of the accumulated irreversible capacity losses ($\sum Q_{irr}$), we consider that alloy electrode materials suffer from an enhanced particle roughening and from the formation of nanoporous particle morphologies as a consequence of the repeated volume changes during lithiation/delithiation, as was reported for tin[7] and silicon[10] (analogous to the structures formed during dealloying reactions).[47] Assuming that nanoporous silicon particles are being created during the early phase of the charge/discharge cycling, the sigmoidal behavior of the accumulated irreversible capacity versus cycle number (see Figure 8a) can easily be rationalized: the associated rapid initial increase in silicon particle surface area would lead to an initial steep increase in the accumulated irreversible capacity due to enhanced SEI formation, which subsequently would slow down once a fully developed nanoporous particle morphology has been reached. As this phenomenon would only depend on the silicon particle size and morphology, its effect would have to be independent of the silicon/graphite ratio of the SiG electrodes, as long as the electrodes are cycled between identical potential limits (i.e., between identical degrees of silicon lithiation/delithation), as indeed is observed in Figure 8. Furthermore, this hypothesis is consistent with the fact that the characteristic dip in the coulombic efficiency with a minimum after the same number of cycles is the same for all SiG electrode compositions, independent of the silicon/graphite ratio (see Figure 2a).

As can be seen in Figure 8, the silicon particle degradation is significantly decreased after ~ 45 cycles, leading to a much reduced slope of the accumlated irreversible capacity versus cycle number or total exchanged charge. This would be consistent with the assumption that a steady-state morphology of the silicon particles is reached after the initial ~45 cycles, i.e., that the silicon surface area has reached a final steady-state value. We explain this behavior by a reduction of the mechanical stress during insertion and extraction of lithium in the nano-sized silicon features, resulting from the initial morphological changes. In addition, this may also be related to the fact that the hypothesized increased surface area and porosity of the silicon particles would lead to a decrease of the effective surface-normalized current density, which in turn would reduce the mechanical stresses due to volume changes during cycling. In other words, the degradation of the silicon particles results in morphological changes that simultaneously diminish the root cause for their mechanical degradation, namely the mechanical stress upon insertion and extraction of lithium.[22] Once the surface growth of silicon has reached a minimum and the silicon particles are fully covered by an electronically insulating SEI layer, further irreversible capacity losses at a now much lower rate would mainly originate from ongoing electrolyte decomposition due to cracking and repair of the existing SEI layer, which is caused by the repeated volume changes upon cycling.

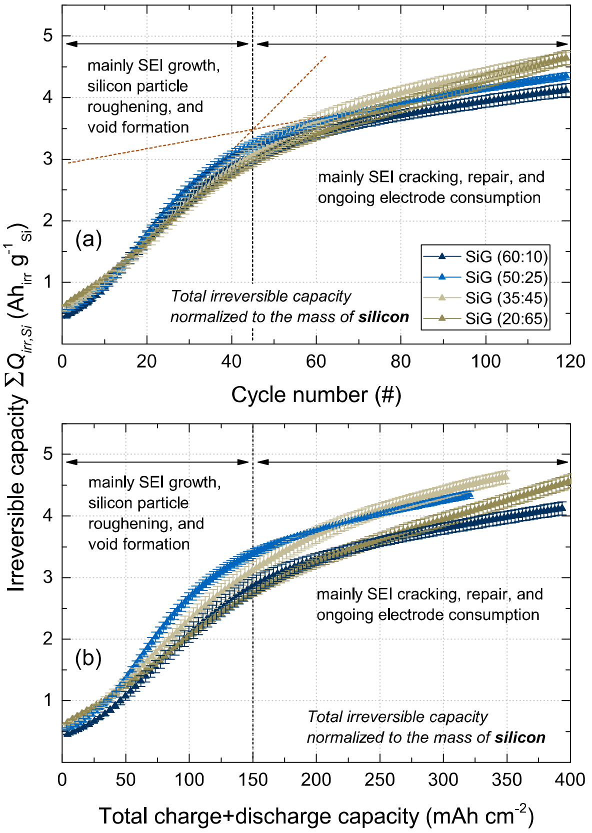

Figure 8. Total irreversible capacity $\sum Q_{irr,Si}$ ($\mathrm{mAh_{irr}\,g^{-1}{}_{Si}}$) normalized to the mass of silicon in the SiG electrodes compositions (same color codes as in Figure 3) and plotted (a) as a function of the cycle number, and (b) as a function of the total charge+discharge capacity. The data were obtained from galvanostatic cycling of SiG//LFP coin-cells, as shown in Figure 2.

While the here given hypothesis is consistent with the literature, we are currently seeking to provide microscopic proof for the proposed relationship between nanoporous particle formation and the behavior of the accumulated irreversible capacity versus cycle number.[48]

In contrast to the silicon particle degradation mechanism, the electrode degradation mechanism is highly dependent on the electrode composition, with an observed earlier (in terms of cycle number) and more severe decay of the reversible capacity with increasing silicon

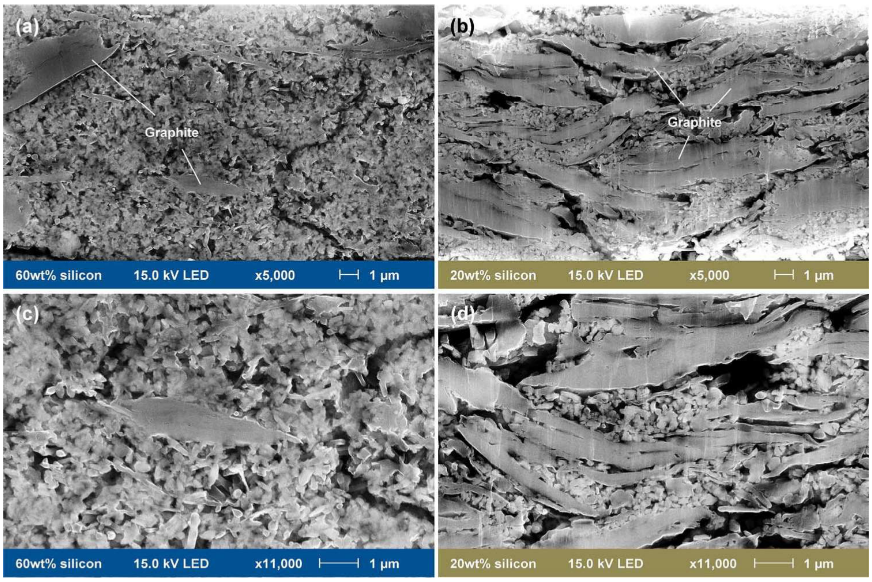

Figure 9. Scanning electron microscope cross-sectional images of (a, c) the 60 wt% silicon electrode, and (b, d) the 20 wt% silicon electrode. Secondary electron detector (SE), 15.0 kV electron acceleration voltage, magnification x5,000 (upper panels) and x11,000 (lower panels). Cross-sections were prepared with an Ar-ion beam cross-section polisher.

content as shown in Figure 2b. Similarly, the delithiation capacity contribution of the CV-step at 1.25 V vs. Li/Li$^+$ in Figure 6b strongly increases with increasing silicon content, indicating an increasingly significant polarization of the delithiation reaction of the silicon particles. To understand how the electrode composition might lead to these observations, Figure 9 shows representative cross-sectional scanning electron microscope (SEM) images of (a, c) the 60 wt% silicon electrode and (b, d) the 20 wt% silicon electrode. The lower SEM images (c, d) depict magnifications of the upper electrodes (a, b) at 11,000x. As can be seen in (a) and (c), the 60 wt% silicon electrode consists of a dense matrix of nanometer-sized silicon particles into which a few graphite flake-like particles are widely dispersed. Therefore, electronic conduction through this silicon-rich electrode involves the contribution of a large number of silicon/silicon and silicon/carbon fiber contact junctions, with the associated electronic contact resistances. In contrast, the 20 wt% silicon electrode in (b) and (d) consists of a nearly contiguous graphite backbone structure, whose interspaces are partially filled by silicon particles, leading to a much smaller average distance between the individual silicon particles and adjacent graphite particles. Therefore, the electronic conductivity of the SiG electrodes is expected to be significantly improved with increasing graphite content.

Although the SEI growth is largely driven by the above described silicon particle degradation mechanism, the mean electron conduction path length from the individual silicon particles to the graphite particles is crucial to maintain sufficient electronic conductivity throughout the electrode, which we tried to capture by Scheme 2. Based on this, one would expect that the progressive surface roughening of the silicon particles in the early stages of SEI growth would lead to a substantial loss of electrode integrity and subsequent increase of the electrode resistance. This, however, seems to be only partially consistent with the analysis of the potential profiles (see Figure 5) over extended charge/discharge cycling: while the gradual disappearance of the $Li_{15}Si_4$ phase is consistent with an electronic conduction resistance induced electrode polarization, the observed overpotential increase during charge and discharge is rather small and there are no obvious differences between the different SiG composites. On the other hand, our hypothesis of increased local electronic resistance contributions with increasing silicon content seems to hold when examining the capacity contribution during the delithiation CV step (at 1.25 V vs. Li/Li$^+$, see Figure 6b), which rapidly rises for silicon-rich electrodes in contrast to SiG electrodes with low silicon content. This can be easily explained by the silicon particle shrinkage during delithiation, resulting in a temporary particle isolation and incomplete delithiation, as was shown previously by Yoon et al.[30] Consistent with this hypothesis is the observation that the capacity contribution during the lithiation CV step (at 0.01 V vs. Li/Li$^+$, see Figure 6a) is similar for all SiG composites, as the expanded volume of the lithiated silicon particles will reduce the effect of inter-particle electronic contact resistances. The fact that the electrode polarization effects only set in toward the end of the delithiation process now also explains why it is not apparent in the overall differential capacity curves (Figure 5). In summary, we believe that the increasing capacity decay rate with increasing silicon content is due to silicon particle detachment and loss of electrical contact, particularly during the delithiation step, caused by the increasingly long mean electron conduction

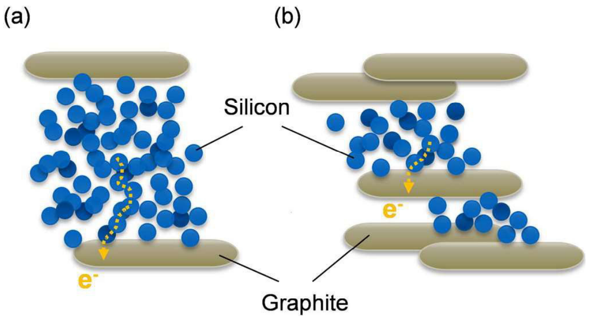

Scheme 2. Illustration of the difference in the mean electron conduction path length from the individual silicon particles to the electronically conductive graphite particles as a function of the silicon/graphite ratio sketched for (a) an Si-rich electrode (based on Figures 9a and 9c) and (b) an Si-poor electrode (based on Figures 9b and 9d). The different path lengths for electron conduction are illustrated by the yellow dotted line.

path length with increasing silicon content (see Scheme 2). Thus, in contrast to the silicon particle degradation mechanism, the electrode degradation mechanism and the concomitant capacity decay of the SiG electrodes is largely determined by the silicon/graphite active material ratio.

To estimate the contribution from the incomplete delithiation to the total irreversible capacity, we first considered that the loss of reversible capacity of the 60 wt% silicon electrode between the 3rd and the 120th cycle accounted for 634 mAh $g^{-1}{}_{el}$ (see Figure 2b). Taking into account that the incomplete delithiation mainly affects silicon particles at low degrees of lithiation, i.e., below roughly 25% state-of-charge (compare Figure 5b), the maximum amount of immobilized lithium in these particles is 159 mAh $g^{-1}{}_{el}$ (= 0.25 × 634 mAh $g^{-1}{}_{el}$). Comparing this number to the total irreversible capacity of 2.47 Ah $g^{-1}{}_{el}$ after 120 cycles shown in Figure 3 yields a contribution of less than ~6.4%. With decreasing silicon content and improved electrical conductivity within the electrodes (compare Figure 6b) this value is expected to decrease further. As a result, despite its harmful impact on the reversible capacity, the irreversible capacity caused by incomplete delithiation of the silicon particles displays only a minor contribution compared to irreversible capacity caused by the continuous electrolyte decomposition at the silicon/electrolyte interface.

***Estimation of the electrode pore clogging upon cycling.*—**The sheer extent of the electrolyte consumption shown in Figure 7 suggests that the SEI on silicon is less a conformal surface layer formed in the initial cycles that evenly surrounds the silicon particles, but instead an increasingly thick and electrically insulating matrix (see above discussion and Figure 6b) that penetrates the entire porous electrode structure. For that reason, we decided to modify the approach of calculating the number of monolayers that are formed on the electrode's surface, which was recently reported by Jung et al.[11] and Pritzl et al.,[49] and characterize the electrolyte decomposition products by an average density rather than an average area defined by a C-C single bond length and thus also take into account the reduction of previously evolved CO_2 gas. To quantify how much SEI volume the SiG electrodes could accommodate before being entirely clogged by electrolyte decomposition products, we will present in the following an estimate of the relative SEI volume after 120 cycles and compare it to the pore volume of the pristine electrodes. Starting from the electrode properties shown in Table I, we first calculate the absolute pore volumes V_{pore} of the different electrode compositions, according to Equation 8,

$$V_{pore} = d \cdot A \cdot \varepsilon \qquad [8]$$

where d is the pristine electrode thickness (see Table I), A is the electrode area (1.54 cm^2), and ε is the electrode porosity (see Table I). As can be seen from Table II, the resulting pore volumes increase with decreasing silicon content from 1.54 μL (~1.00 μL cm^{-2}) for the 60 wt% electrode to 3.26 μL (2.21 μL cm^{-2}) for the 20 wt% silicon electrode, due to the increase of the electrode thickness from ~15 to ~30 μm at nearly similar electrode porosities (~67–73%, see Table I).

In the next step, we approximate the mass of the SEI m_{SEI} from Equation 9 by taking into account the FEC consumption n_{FEC} determined by post-mortem ^{19}F-NMR analysis. Herein, we assume that the SEI has an equivalent mass as the preceding FEC decomposition product m_{FEC*}. In addition, we correct the molar mass of FEC (M_{FEC} = 106.05 g mol^{-1}) by the molar mass of four lithium atoms (M_{Li} = 6.84 g mol^{-1}) that are also incorporated into the SEI compounds (e.g., LiF or Li_2O),[11] leading to an effective molar mass M_{FEC*} of the FEC decomposition product of 133.41 g mol^{-1}.

$$m_{SEI} \equiv m_{FEC*} = n_{FEC} \cdot M_{FEC*} \qquad [9]$$

Building up on this, we can further calculate the SEI volume V_{SEI}, as described by Equation 10, thereby assuming an average density ρ_{SEI} of 1.4–1.8 g cm^{-3} for the SEI. This value is a very rough zero order estimate based on the densities of the different SEI compounds, including ~50% of inorganic compounds, inter alia LiF (2.64 g cm^{-3}), Li_2CO_3 (2.11 g cm^{-3}), Li_2O (2.01 g cm^{-3}), and ~50% organic compounds, such as lithium alkoxides (~1.0 g cm^{-3}), which are typically observed via for cycled silicon electrodes in FEC-containing electrolyte by XPS spectroscopy.[50–52]

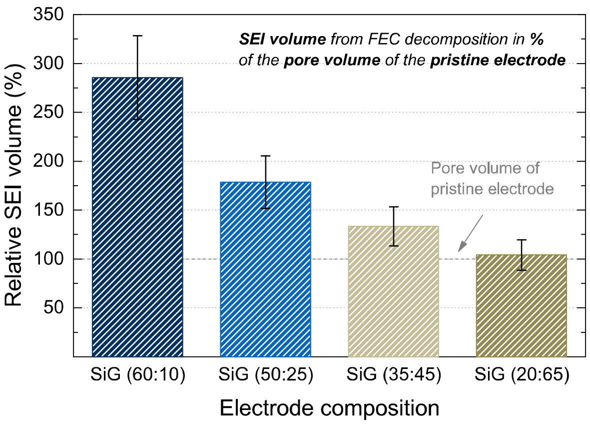

Figure 10. Estimated relative SEI volume defined by the fraction of pore volume of the pristine silicon-graphite electrodes which is occupied by FEC decompositions products. The values were calculated from a zero-order estimate based on the FEC consumption from ^{19}F-NMR. The SEI volume was calculated based on an average density of 1.6 g cm^{-3} for the FEC decomposition products. The error bars represent a variation in the density between 1.4–1.8 g cm^{-3}.

$$V_{SEI} = \frac{m_{SEI}}{\rho_{SEI}} \qquad [10]$$

Finally, we divide the SEI volume V_{SEI} by the pore volume V_{pore} of the pristine electrodes by using Equation 11 to obtain the relative SEI volume v_{SEI}, which gives us an impression of the fraction of the original pore volume that would be occupied by electrolyte decomposition products after 120 cycles.

$$v_{SEI} = \frac{V_{SEI}}{V_{pore}} \qquad [11]$$

Figure 10 shows the resulting zero order estimates of the relative SEI volumes normalized to the pore volume of the pristine electrodes. While this very simple approximation does not include the swelling of the electrodes over the course of cycling, it nonetheless provides a semi-quantitative measure of the volume of the electrolyte decomposition products and how it compares to the initially available void volume of the SiG electrodes. A comparison of the different electrode compositions in Figure 10 reveals a strong dependence of the relative SEI volume after 120 cycles on the silicon/graphite ratio, decreasing with decreasing silicon content from ~280% to ~100%. This grantedly simple estimate provides a reasonably convincing argument that the FEC decomposition products after 120 cycles would have to lead to an essentially complete pore blocking in the case of the 20 wt% silicon electrode and could not even be accommodated in the 60 wt% silicon electrode. Therefore, considering that about three quarters of the accumulated irreversible capacity occur within the first ~45 cycles (see Figure 8a), and given that the SEI formation is proportional to irreversible capacity, we can assume that without any changes in electrode morphology and thickness, all ionic pathways would be filled by electrolyte decomposition products after less than 45 cycles. However, as our results from galvanostatic cycling clearly prove a residual reversible capacity of ~70% after 120 cycles for the 60 wt% silicon electrode (see Figure 2), we conclude that the electrodes must significantly swell upon cycling in order to increase the available pore volume and thus facilitate the accommodation of the FEC decomposition products while simultaneously conserving the ionic conduction pathways. These conclusions agree well with the thickness

Table II. Pore volumes of the pristine electrodes and calculated SEI volumes after 120 cycles, based on the FEC consumption after 120 cycles n_{FEC} determined by post-mortem ^{19}F-NMR. The SEI volume was calculated based on an average density of 1.6 g cm^{-3} for the FEC decomposition products.

		Electrode composition			
Measures	Units	SiG (60:10)	SiG (50:25)	SiG (35:45)	SiG (20:65)
Electrode pore volume V_{pore}	µL	1.54	1.79	2.32	3.26
FEC consumption after 120 cycles n_{FEC}	µmol	53	38	37	41
Mass of FEC* precipitates m_{FEC*}	mg	7.1	5.1	4.9	5.4
Absolute SEI volume V_{SEI}	µL	4.4	3.2	3.1	3.4
Relative SEI volume	%	285	179	133	104

measurements and cross-sectional SEM images of cycled silicon electrodes reported by Mazouzi et al.[53]

Obrovac and co-workers measured the coating thickness of Si-alloy/graphite composite electrodes in their fully lithiated state and found that the entire coating expanded by about ∼96%, which was very similar to the expected expansion of the lithiated Si-alloy (∼115%).[15] Interestingly, the porosity of these electrodes remained nearly the same as in the delithiated state, leading them to the conclusion that the pore size expands by the same amount as the silicon particles. Transferring these observations to our electrodes, the silicon particle volume increase of about 280% upon full lithiation would result in an additional pore volume of 60–170% (e.g., 60 wt% silicon x 280% expansion = ∼170% additional pore volume), depending on the electrode composition. As the pores are increasingly filled by decomposition products upon cycling, they likely cannot shrink back to their initial volume when silicon is delithiated. Hence, the electrode thickness will increase continuously, in particular during the silicon particle degradation phase, where electrolyte decomposition and subsequent SEI growth are strongest. In contrast, a higher graphite content of the composite electrodes increases the total pore volume and simultaneously improves the electrode conductivity with graphite acting as an electrically conductive backbone.

Cycle life dependence on the electrolyte amount.—Besides the electrode morphology, the amount of SEI-forming additives in the electrolyte also plays a crucial role for the cycling performance of silicon-based electrodes. Thus it was shown that a rapid capacity drop can be observed for silicon based anodes at the point where the capacity-stabilizing FEC additive was found to be depleted quantitatively.[11,35] As in commercial-scale Li-ion batteries the electrolyte amount is in the order of ∼5 µL cm^{-2} and thus much smaller compared to typical lab-scale measurements (∼85 µL cm^{-2} for our coin cells), the available moles of FEC per mass of silicon are substantially lower in commercial-scale cells, so that the expected cycle life of silicon-based electrodes in commercial-scale cells should consequently be much shorter.[11] To quantify this difference, we approximate the number of cycles prior to FEC depletion of SiG electrodes in lab-scale versus commercial-scale cells by considering the constant ratio of the FEC consumption n_{FEC} and the irreversible capacity loss $\sum Q_{irr}$ (see Table I). Assuming a commercial-scale cell using 5 µL cm^{-2} electrolyte with 20 wt% FEC additive and our lab-scale cells using 85 µL cm^{-2} electrolyte with 5 wt% FEC additive, we use Equation 12 to first determine the absolute amount of FEC n_{FEC}^{tot} in the two electrolytes.

$$n_{FEC}^{tot} = \frac{V_{el} \cdot \rho_{el} \cdot x_{FEC}}{M_{FEC}} \qquad [12]$$

where V_{el} is the electrolyte volume, ρ_{el} is the electrolyte density (∼1.19 g cm^{-3}), x_{FEC} is the mass fraction of FEC in the electrolyte, and M_{FEC} is the molar mass of FEC (106.05 g mol^{-1}). Accordingly, the commercial-scale cell would contain ∼11 µmol cm^{-2} of FEC, whereas the lab-scale cells tested in this work contain ∼48 µmol cm^{-2} of FEC, i.e, the ∼5-fold amount. In the next step, we use the inverse of the constant ratio of the FEC consumption n_{FEC} to irreversible capacity loss $\sum Q_{irr}$ (in units of µmol$_{\mathrm{FEC}}$ Ah$^{-1}{}_{\mathrm{irr}}$, calculated by Equation 6, shown in Table I) to calculate the maximal irreversible capacity $\sum Q_{irr}^{max}$ that corresponds to a total depletion of FEC from the respective electrolytes, according to Equation 13,

$$\sum Q_{irr}^{\max} = n_{FEC}^{tot} \cdot \frac{\sum Q_{irr}}{n_{FEC}} \cdot \frac{1}{m_{Si}} \qquad [13]$$

where m_{Si} is the mass of silicon in the electrode (in mg$_{\mathrm{Si}}$ cm^{-2}), and n_{FEC}^{tot} is the total amount of FEC per cm^2 electrode area (µmol$_{\mathrm{FEC}}$ cm^{-2}). Table III summarizes the maximal irreversible capacities $\sum Q_{irr}^{max}$ of the various silicon-graphite electrodes in either lab-scale cells or in commercial-scale cells. To forecast the number of cycles until the depletion of FEC, we can compare the accumulated irreversible capacity versus cycle number in Figure 8a with the maximal irreversible capacity until FEC depletion (in units of Ah$_{\mathrm{irr}}$ g$^{-1}{}_{\mathrm{Si}}$) listed in Table III for both cell formats. For the commercial-scale cells, this analysis suggests that FEC would already be consumed within the first ∼20–30 charge/discharge cycles. In contrast, the number of cycles prior to FEC depletion predicted for our lab-scale cells substantially exceeds the here tested 120 cycles (at this point, $\Sigma Q_{\mathrm{irr,Si}}$ in Figure 8a is still much below the projected estimated maximal irreversible capacity given in Table III). That FEC, as predicted, is not depleted after 120 cycles in our lab-scale experiments is confirmed by our post-mortem ^{19}F-NMR measurements, which show a residual FEC content of >1.2 wt% in the electrolyte (originally 5 wt%) after the 120 cycles.

Thus, we conclude that the lifetime of silicon-graphite electrodes in commercial-scale cells with a reasonably sized positive electrode would be limited by the amount of FEC in the electrolyte, rather than by the degradation of the electrode structure. These findings highlight again the importance of an effective SEI on silicon-based electrodes and the need for a proper quantification of the electrolyte consumption. Therefore, we recommend that future investigations of silicon-based electrodes in lab-scale cells should take into account the actual FEC consumption in µmol$_{\mathrm{FEC}}$ and to compare this to the FEC inventory in commercial-scale cells. As our results from ^{19}F-NMR analysis reveal an almost constant ratio of the consumed FEC n_{FEC} to cumulative irreversible capacity $\sum Q_{irr}$ of 11.5-13.1 µmol$_{\mathrm{FEC}}$ mAh$^{-1}{}_{\mathrm{irr}}$, Equation 14 can be used as an approximation to assess the FEC consumption from battery cycling. We would like to note that this relation is only valid for cell chemistries that do not have further electrolyte decomposition reactions at the positive electrode, e.g., LiFePO$_4$, and involve two constant voltage steps. If the cycling protocol does not include any constant voltage steps, the ratio r_{FEC} of the consumed FEC n_{FEC} to total irreversible capacity $\sum Q_{irr}$ approaches the four electron reduction mechanism of FEC, which was reported by Jung et al.,[11] corresponding to a value of 9.4 ± 0.4 µmol$_{\mathrm{FEC}}$ mAh$^{-1}{}_{\mathrm{irr}}$.[54]

$$n_{FEC} = r_{FEC} \cdot \sum Q_{irr} \qquad [14]$$

Conclusions

In this study, we presented a comprehensive approach to understand the degradation phenomena in silicon-graphite electrodes with different graphite/silicon ratios (20–60 wt% silicon) and areal

Table III. Maximal irreversible capacity and forecasted cycle life of silicon-graphite electrodes calculated for typical lab-scale and commercial-scale cells. The upper segments provide the specifications of the various SiG electrodes as well as the measured FEC consumption per accumulated irreversible capacity over 120 cycles (taken from Table I). The middle and the lower segments provide the estimated number of cycles for lab-scale and commercial-scale cells by which the available amount of FEC will be consumed.

		Electrode composition			
Measures	Units	SiG (60:10)	SiG (50:25)	SiG (35:45)	SiG (20:65)
Silicon-graphite electrode specifications					
Silicon content	%	60	50	35	20
Silicon loading	mg$_{Si}$ cm^{-2}	0.64	0.47	0.46	0.43
FEC consumption per irr. capacity	µmol mAh$^{-1}_{irr}$	13.0	12.3	11.5	13.1
Lab-scale cell (85 µL cm^{-2} electrolyte with 5 wt% FEC additive)					
Maximal irreversible capacity	Ah$_{irr}$ g$^{-1}_{Si}$	5.8	8.3	9.1	8.4
Cycle lifetime acc. Figure 8a	#	>120	>120	>120	>120
Commercial-scale cell (5 µL cm^{-2} electrolyte with 20 wt% FEC additive)					
Maximal irreversible capacity	Ah$_{irr}$ g$^{-1}_{Si}$	1.4	1.9	2.2	2.0
Cycle lifetime acc. Figure 8a	#	20	25	30	25

capacities of 1.8–2.3 mAh cm^{-2}. By use of an FEC-containing electrolyte and capacitively oversized $LiFePO_4$ cathodes, we could clearly distinguish two degradation phenomena, which we described as silicon particle degradation and electrode degradation. While the former is mainly determined by the intrinsic properties of the silicon active material, such as particle size and morphology, as well as the amount of charge that is exchanged by the silicon particles, the electrode degradation mechanism depends not only on the silicon material but also on the electrode composition, i.e., the silicon/graphite ratio. Increasing the silicon content results in an increase of the number of interparticle contacts, e.g., silicon-silicon, which leads to a higher contact resistance. During discharge, i.e., in delithiated silicon electrodes, this phenomenon is even more pronounced because of a reduced contact pressure at these interfaces.

Based on our results from ^{19}F-NMR analysis we could demonstrate that the consumption of FEC after 120 cycles is independent of the graphite/silicon ratio and only depends on the total accumulated exchanged charge (i.e., sum of charge and discharge) experienced by the silicon. Based on this, we could show that: (i) the irreversible capacity loss correlates linearly with the decomposition of FEC on silicon, and can thus be used to estimate the extent of FEC consumption from the cycling data; (ii) the estimated volume of the FEC decomposition products increases with the silicon content and for all investigated SiG compositions largely exceeds the pore volume of the pristine electrodes, explaining the commonly observed swelling of silicon electrodes upon cycling; and (iii) the comparatively low molar quantity of FEC in commercial electrolytes is the most critical factor in determining the cycle life of silicon-based electrodes.

Acknowledgments

The German Federal Ministry for Economic Affairs and Energy is acknowledged for funding (Project "LiMo", funding number 03ET6045D). Wacker Chemie AG is kindly acknowledged for providing the silicon nanoparticles. Susanne Cornfine and JEOL (Germany) GmbH are kindly acknowledged for supporting the SEM measurements. The authors also kindly thank Yelena Gorlin, Manu Patel, Qi He, and Anne Berger (all TUM) for fruitful discussions.

References

1. D. Andre, S.-J. Kim, P. Lamp, S. F. Lux, F. Maglia, O. Paschos, and B. Stiaszny, *J. Mater. Chem. A*, **3**(13), 6709 (2015).
2. O. Gröger, H. A. Gasteiger, and J.-P. Suchsland, *J. Electrochem. Soc.*, **162**(14), A2605 (2015).
3. V. L. Chevrier, L. Liu, D. B. Le, J. Lund, B. Molla, K. Reimer, L. J. Krause, L. D. Jensen, E. Figgemeier, and K. W. Eberman, *J. Electrochem. Soc.*, **161**(5), 783 (2014).
4. D. Ma, Z. Cao, and A. Hu, *Nano-Micro Lett*, **6**(4), 347 (2014).
5. M. N. Obrovac, L. Christensen, D. B. Le, and J. R. Dahn, *J. Electrochem. Soc.*, **154**(9), A849 (2007).
6. D. S. M. Iaboni and M. N. Obrovac, *J. Electrochem. Soc.*, **163**(2), 255 (2016).
7. M. N. Obrovac and V. L. Chevrier, *Chem. Rev.*, **114**, 11444 (2014).
8. R. Petibon, V. Chevrier, C. P. Aiken, D. S. Hall, S. Hyatt, R. Shunmugasundaram, and J. R. Dahn, *J. Electrochem. Soc.*, **163**(7), 1146 (2016).
9. J. O. Besenhard, J. Yang, and M. Winter, *J. Power Sources*, **68**, 87 (1997).
10. M. T. McDowell, S. W. Lee, J. T. Harris, B. A. Korgel, C. Wang, W. D. Nix, and Y. Cui, *Nano Lett*, **13**(2), 758 (2013).
11. R. Jung, M. Metzger, D. Haering, S. Solchenbach, C. Marino, N. Tsiouvaras, C. Stinner, and H. A. Gasteiger, *J. Electrochem. Soc.*, **163**(8), A1705 (2016).
12. V. Baranchugov, E. Markevich, E. Pollak, G. Salitra, and D. Aurbach, *Electrochem. commun.*, **9**(4), 796 (2007).
13. E. Markevich, K. Fridman, R. Sharabi, R. Elazari, G. Salitra, H. E. Gottlieb, G. Gershinsky, A. Garsuch, G. Semrau, M. A. Schmidt, and D. Aurbach, *J. Electrochem. Soc.*, **160**(10), A1824 (2013).
14. E. Markevich, G. Salitra, and D. Aurbach, *J. Electrochem. Soc.*, **163**(10), 2407 (2016).
15. Z. Du, R. A. Dunlap, and M. N. Obrovac, *J. Electrochem. Soc.*, **161**(10), 1698 (2014).
16. M. D. Fleischauer, M. N. Obrovac, J. D. Mcgraw, R. A. Dunlap, J. M. Topple, and J. R. Dahn, *J. Electrochem. Soc.*, **153**(3), 484 (2006).
17. B. Fuchsbichler, C. Stangl, H. Kren, F. Uhlig, and S. Koller, *J. Power Sources*, **196**(5), 2889 (2011).
18. C.-H. Yim, F. M. Courtel, and Y. Abu-Lebdeh, *J. Mater. Chem. A*, **1**(5), 8234 (2013).
19. T. Yim, S. J. Choi, J.-H. Park, W. Cho, Y. N. Jo, T.-H. Kim, and Y.-J. Kim, *Phys. Chem. Chem. Phys.*, **17**(4), 2388 (2014).
20. M. Ko, S. Chae, and J. Cho, *ChemElectroChem*, **2**(11), 1645 (2015).
21. F. Luo, B. Liu, J. Zheng, G. Chu, K. Zhong, H. Li, X. Huang, and L. Chen, *J. Electrochem. Soc.*, **162**(14), A2509 (2015).
22. M. T. McDowell, S. W. Lee, W. D. Nix, and Y. Cui, 4966 (2013).
23. N. Dupré, P. Moreau, E. De Vito, L. Quazuguel, M. Boniface, A. Bordes, C. Rudisch, P. Bayle-Guillemaud, and D. Guyomard, *Chem. Mater.*, **28**(8), 2557 (2016).
24. N. Delpuech, N. Dupre, P. Moreau, J. S. Bridel, J. Gaubicher, B. Lestriez, and D. Guyomard, *ChemSusChem*, **9**(8), 841 (2016).
25. M. Klett, J. A. Gilbert, S. E. Trask, B. J. Polzin, A. N. Jansen, D. W. Dees, and D. P. Abraham, *J. Electrochem. Soc.*, **163**(6), A875 (2016).
26. M. Klett, J. A. Gilbert, K. Z. Pupek, S. E. Trask, and D. P. Abraham, *J. Electrochem. Soc.*, **164**(1), 6095 (2017).
27. S. E. Trask, K. Z. Pupek, J. A. Gilbert, M. Klett, B. J. Polzin, A. N. Jansen, and D. P. Abraham, *J. Electrochem. Soc.*, **163**(3), A345 (2016).
28. C. Erk, T. Brezesinski, H. Sommer, R. Schneider, and J. Janek, *ACS Appl. Mater. Interfaces*, **5**(15), 7299 (2013).
29. J. H. Ryu, J. W. Kim, Y. Sung, and S. M. Oh, *Electrochem. Solid State Lett.*, **7**(10), 306 (2004).
30. T. Yoon, C. C. Nguyen, D. M. Seo, and B. L. Lucht, *J. Electrochem. Soc.*, **162**(12), A2325 (2015).
31. M. Wetjen, R. Jung, D. Pritzl, and H. A. Gasteiger, *ECS Meet*, **230** (2016), Abstr. #280.
32. E. Markevich, K. Fridman, R. Sharabi, R. Elazari, G. Salitra, H. E. Gottlieb, G. Gershinsky, A. Garsuch, G. Semrau, M. a Schmidt, and D. Aurbach, *J. Electrochem. Soc.*, **160**(10), A1824 (2013).
33. T. Marks, S. Trussler, A. J. Smith, D. Xiong, and J. R. Dahn, *J. Electrochem. Soc.*, **158**(1), A51 (2011).
34. A. V Plakhotnyk, L. Ernst, and R. Schmutzler, *J. Fluor. Chem.*, **126**(1), 27 (2005).
35. R. Petibon, V. L. Chevrier, C. P. Aiken, D. S. Hall, S. R. Hyatt, R. Shunmugasundaram, and J. R. Dahn, *J. Electrochem. Soc.*, **163**(7), A1146 (2016).
36. K. W. Schroder, H. Celio, L. J. Webb, and K. J. Stevenson, *J. Phys. Chem. C*, **116**, 19737 (2012).
37. T. Ohzuku, Y. Iwakoshi, and K. Sawai, *J. Electrochem. Soc.*, **140**(9), 2490 (1993).
38. T. Swamy and Y.-M. Chiang, *J. Electrochem. Soc.*, **162**(13), A7129 (2015).

39. C. Xu, F. Lindgren, B. Philippe, M. Gorgoi, F. Björefors, K. Edström, and T. Gustafsson, *Chem. Mater.*, **27**(7), 2591 (2015).
40. T. Jaumann, J. Balach, M. Klose, S. Oswald, U. Langklotz, A. Michaelis, J. Eckert, and L. Giebeler, *Phys. Chem. Chem. Phys.*, **17**(38), 24956 (2015).
41. D. Aurbach, *J. Power Sources*, **89**, 206 (2000).
42. T. Placke, S. Rothermel, O. Fromm, P. Meister, S. F. Lux, J. Huesker, H. Meyer, and M. Winter, *J. Electrochem. Soc.*, **160**, A1979 (2013).
43. M. N. Obrovac and L. Christensen, *Electrochem. Solid-State Lett.*, **7**(5), A93 (2004).
44. J. Li and J. R. Dahn, *J. Electrochem. Soc.*, **154**(3), A156 (2007).
45. D. Aurbach, E. Zinigrad, Y. Cohen, and H. Teller, *Solid State Ionics*, **148**, 405 (2002).
46. M. Gauthier, T. J. Carney, A. Grimaud, L. Giordano, N. Pour, H. Chang, D. P. Fenning, S. F. Lux, O. Paschos, C. Bauer, F. Maglia, S. Lupart, P. Lamp, and Y. Shao-horn, *J. Phys. Chem. Lett.*, **6**, 4653 (2015).
47. J. Erlebacher, M. J. Aziz, A. Karma, N. Dimitrov, and K. Sieradzki, *Nature*, **410**, 450 (2001).
48. M. Wetjen, S. Solchenbach, D. Pritzl, J. Hou, V. Tileli, and H. A. Gasteiger, Manuscript in preparation.
49. D. Pritzl, S. Solchenbach, M. Wetjen, and H. A. Gasteiger, *J. Electrochem. Soc.*, **164** (12), A2625 (2017).
50. X. Cheng, R. Zhang, C. Zhao, F. Wei, J. Zhang, and Q. Zhang, *Adv. Sci.*, **3**, 1 (2016).
51. E. Peled, D. Golodnitsky, and G. Ardel, *J. Electrochem. Soc.*, **144**(8), 208 (1997).
52. K. Schroder, J. Alvarado, T. A. Yersak, J. Li, N. Dudney, L. J. Webb, Y. S. Meng, and K. J. Stevenson, *Chem. Mater.*, **27**(16), 5531 (2015).
53. D. Mazouzi, N. Delpuech, Y. Oumellal, M. Gauthier, M. Cerbelaud, J. Gaubicher, N. Dupré, P. Moreau, D. Guyomard, L. Roué, and B. Lestriez, *J. Power Sources*, **220**, 180 (2012).
54. M. Wetjen, G. Hong, S. Solchenbach, D. Pritzl, and H. A. Gasteiger, Manuscript in preparation.

3.1.2 Morphological Changes of Silicon Nanoparticles

This section presents the article "Morphological Changes of Silicon Nanoparticles and the Influence of Cutoff Potentials in Silicon-Graphite Electrodes",[132] which was published in May 2018 in the *Journal of The Electrochemical Society*. It is an open access article distributed under the terms of the Creative Commons Attribution 4.0 License. This paper was also presented on international conferences, for example at the 232nd Meeting of The Electrochemical Society in National Harbor, Maryland (October 1-5, 2017), Abstr. #424. The permanent web-link to the article is http://dx.doi.org/10.1149/2.1261807jes.

The article addresses two important characteristics of silicon-based anodes, namely (i) the roughening of the silicon nanoparticles upon repeated (de-)lithiation, and (ii) the dependence of the electrode's cycling stability on the applied cutoff potentials. Originally, silicon nanoparticles were introduced to mitigate the large mechanical strain and subsequent pulverization which occurs with μm-sized particles.[121,133] Yet, there still exists no consensus on the critical particle diameter.[109,129] Moreover, our previous work on SiG anodes with silicon particle lengths of ~200 nm even indicated a severe increase of the irreversible capacity within the first 60 cycles, which we ascribed to a roughening of the silicon particles.[102] This phenomenon has a significant impact on lithium-ion batteries, because the morphological changes of the silicon particles lead to increased side reactions at the silicon/electrolyte interface and a subsequent partial electrical isolation of the silicon particles, which further reduces the reversible capacity of SiG anodes. Therefore, this article investigates the morphological changes of silicon nanoparticles as a function of the cycle number using *post mortem* scanning transmission electron microscopy (STEM) and energy dispersive X-ray spectroscopy (EDS). In contrast to previous studies,[121] which often used model electrodes, the particles in the present paper were harvested from application-relevant SiG anodes with an areal capacity of 1.7-1.8 mAh cm^{-2} and a reasonable cycling stability over more than 100 cycles.[102] Thus, our STEM-EDS analysis was not restricted to the first cycles but also included electrodes that were aged up to 60 cycles, which provided valuable insights into the morphological changes upon prolonged cycling.

The second question this paper attempts to answer is the dependence of the cycling stability on the upper and lower cutoff potentials. Previous studies have repeatedly demonstrated that a limitation of the delithiation of silicon (by the upper cutoff potential) is more favorable than a limitation of the lithiation (by the lower cutoff potential),[178,192] yet the underlying mechanisms are still subject to discussion.[173,187] Therefore, we cycled SiG anodes using different cutoff conditions before characterizing them with respect to their electrochemical performance, electrode morphology, and impedance evolution.

This study generated two important insights into silicon-based anodes: (i) While to date dealloying reactions and the associated changes of the particle morphology were only reported in the field of heterogeneous catalysis[193,194] and for selected alloy materials with µm-sized particles,[107,108] this PhD thesis demonstrated that silicon nanoparticles can also undergo dealloying reactions upon repeated (de-)lithiation in lithium-ion batteries. The dealloying reactions result in the formation of expanded bicontinuous networks consisting of nanometer-sized silicon branches with a significantly increased surface area as well as in enhanced electrolyte decomposition reactions leading to solid products that accumulate in the porous structures. Furthermore, the dealloying reactions lead to a permanent volume change of the silicon particles up to +700%, which by far exceeds the commonly reported volume expansion of ~300% upon full-lithiation ($Li_{15}Si_4$).[185] (ii) Limiting the upper (delithiation) cutoff potential to 0.65 V vs. Li^+/Li leads to a notably improved coulombic efficiency of the SiG anodes, which was reflected not only by a reduced electrode swelling and impedance increase upon cycling but also by a higher cycling stability. Based on theoretical considerations of perfect spheres, we demonstrated in this article that the relative surface area changes of delithiation-limited silicon particles are much lower compared to fully delithiated particles. This reduces the lateral stress and thus the cracking and renewal of the SEI at the silicon/electrolyte interface. As a corollary, our results offer an explanation for the often observed[173] improvement of the cycling stability of silicon-based full-cells with increasing lower cell cutoff voltage (which corresponds to the delithiation cutoff potential of silicon).

To analyze the morphological changes of the silicon nanoparticles, this PhD thesis initiated a collaboration with Prof. Vasiliki Tileli at the École Polytechnique Fédérale de Lausanne (EPFL), which provided valuable insights into the dealloying reactions of lithium silicides (Li_xSi) upon repeated (de-)lithiation as well as the resulting changes of their elemental composition caused by ongoing electrolyte decomposition.

Author contributions

M.W. prepared the electrodes, performed the electrochemical testing, and characterized the electrodes *post mortem*. M.W. and D.P. conducted the impedance measurements. V.T., J.H., and M.W. prepared the samples for the STEM-EDS analysis and performed the measurements. Sonja Gürster (JEOL) and M.W. prepared the samples for the cross-sectional SEM images and performed the microscopy measurements. M.W. and S.S. analyzed the data. M.W., V.T., and H.G. wrote the manuscript. All authors discussed the results and commented on the manuscript.

Journal of The Electrochemical Society, **165** (7) A1503-A1514 (2018)

Morphological Changes of Silicon Nanoparticles and the Influence of Cutoff Potentials in Silicon-Graphite Electrodes

Morten Wetjen,[1,*,z] Sophie Solchenbach,[1,*] Daniel Pritzl,[1,*] Jing Hou,[2] Vasiliki Tileli,[2] and Hubert A. Gasteiger[1,]**

[1] *Chair of Technical Electrochemistry, Department of Chemistry and Catalysis Research Center, Technische Universität München, D-85748 Garching, Germany*
[2] *Institute of Materials, École Polytechnique Fédérale de Lausanne, CH-1015 Lausanne, Switzerland*

Silicon-graphite electrodes usually exhibit improved cycling stability when limiting the capacity exchanged by the silicon particles per cycle. Yet, the influence of the upper and the lower cutoff potential was repeatedly shown to differ significantly. In the present study, we address this discrepancy by investigating two distinct degradation phenomena occurring in silicon-graphite electrodes, namely (i) the roughening of the silicon particles upon repeated (de-)lithiation which leads to increased irreversible capacity losses, and (ii) the decay in the reversible capacity which mainly originates from increased electronic interparticle resistances between the silicon particles. First, we investigate the cycling stability and polarization of the silicon-graphite electrodes in dependence on different cutoff potentials using pseudo full-cells with capacitively oversized $LiFePO_4$ cathodes. Further, we characterize post-mortem the morphological changes of the silicon nanoparticles by means of scanning transmission electron microscopy (STEM) and energy dispersive spectroscopy (EDS) as a function of the cycle number. To evaluate the degradation of the entire electrode coating, we finally complement our investigation by impedance spectroscopy (EIS) with a gold-wire micro-reference electrode and post-mortem analyses of the electrode structure and coating thickness by cross-sectional SEM.

[DOI: 10.1149/2.1261807jes]

Manuscript submitted February 23, 2018; revised manuscript received May 10, 2018. Published May 18, 2018. This was Paper 424 presented at the National Harbor, Maryland Meeting of the Society, October 1–5, 2017.

Silicon is among the most promising anode materials for future lithium-ion batteries.[1,2] For example, a prismatic hard case cell comprising a silicon-carbon anode with 1000 mAh $g^{-1}{}_{electrode}$ and an NMC811 cathode would offer a specific energy of up to ~280 Wh $kg^{-1}{}_{cell}$.[3] In contrast to state-of-the-art graphite electrodes, where lithium is inserted into the interlayers between the graphene sheets, silicon reacts with lithium and forms Li_xSi alloys.[4–6] Because the (de-)alloying reaction allows a higher lithium uptake per silicon atom (3579 mAh $g^{-1}{}_{Si}$, $Li_{15}Si_4$) compared to the intercalation of lithium into the graphite host structure (372 mAh $g^{-1}{}_{C}$, LiC_6), silicon offers an about ~10 times larger theoretical specific capacity.[7] However, while the intercalation chemistry reveals excellent cycling stability with only minor irreversible changes of the graphite's morphology (ca. +10%),[8] the (de-)alloying reaction causes significant morphological and chemical changes to the silicon particles, including (i) a large volume expansion of up to +280% and (ii) repeated breakage and formation of Si-Si bonds, which leads to severe mechanical stress and particle fracturing.[9–12] Upon continued cycling, these morphological changes cause a rapid capacity decay of silicon-based electrodes, which is largely driven by the electrical isolation of the fractured silicon particles.[13–17] Nanometer-sized structures, including nanoparticles and nanowires, were shown to mitigate the mechanical stress which results from volumetric changes during the (de-)alloying reaction.[12,18–20] However, there exists a trade-off, because the reduction of the particle size also leads to a lower volumetric energy density and an inferior electrical conductivity across the electrode.[21,17] Possibly equally important and detrimental for the long-term stability of nanometer-sized silicon is its high specific surface area, which leads to a significantly increased irreversible capacity.[22]

Inspired by the early work on lithium-alloys in nonaqueous electrolyte solutions by Dey[23] and by Nicholson,[24] the coulombic efficiency and rate of the alloying reactions have been subject to numerous studies. Especially, lithium-alloys with silicon[25] and aluminum[26] attracted the interested of researchers because of their high specific capacity, good reversibility and mitigation of lithium dendrites. The morphological changes of silicon caused by (de-)alloying have been investigated, e.g., by means of in situ lab or synchrotron based X-ray diffraction (XRD),[27–30] nuclear magnetic resonance spectroscopy (NMR),[11,31–34] and in situ transmission electron microscopy (TEM),[12,35–38] which provided valuable insights into the phase transition of crystalline silicon as well as the volumetric expansion and strain-induced fracture of silicon particles within the first cycles. As pointed out by McDowell et al.,[13] most of the these studies either deal with the degradation of individual particles or investigate primarily the first few cycles. However, to derive implications for practical applications of silicon-based batteries, it is important to examine the degradation of silicon particles also as part of the entire electrode structure, by considering (i) the electronic interparticle resistances between silicon particles, (ii) the mechanical integrity of the electrode, (iii) the impact of repeated (de-)lithiation on the morphology of the silicon particles, as well as (iv) the electrolyte decomposition and solid-electrolyte-interphase (SEI) formation at the silicon/electrolyte interface over longer cycling periods.

In the present study, we investigate the degradation of silicon-graphite (SiG) electrodes with 35 wt% of silicon nanoparticles (particle length scales of ~200 nm) and an areal capacity of 1.7–1.8 mAh cm^{-2}. Based on our previous work,[39] where we differentiated two distinct degradation phenomena occurring in silicon-graphite electrodes, namely (i) the roughening of the silicon particles upon repeated (de-)lithiation which leads to increased irreversible capacity losses (furtheron described as silicon particle degradation), and (ii) the decay in the reversible capacity which mainly originates from increased interparticle contact resistances between the silicon particles (furtheron described as electrode degradation), we now focus on the underlying morphological changes of the silicon particles and of the electrode structure that occur upon repeated (de-)lithiation. Inspired by recent publications of the groups of Aurbach,[40] Abraham,[41] and Kobayashi,[42] who independently reported a significant difference in the cycling stability of silicon-based electrodes depending on a capacity or potential limitation either during lithiation or delithiation, we extend our analysis of the different degradation phenonema by two cutoff potential-limited cycling protocols. While it is widely accepted in the literature[8] that limiting the capacity of silicon reduces its degradation and irreversible capacity loss, the differences between limiting either the lower or the upper cutoff potential still require further understanding.

By use of scanning transmission electron microscopy (STEM) and energy dispersive spectroscopy (EDS), we investigate the morphology and chemical composition of the silicon particles post

---

[*] Electrochemical Society Student Member.
[**] Electrochemical Society Fellow.
[z] E-mail: morten.wetjen@tum.de

mortem after different number of charge-discharge cycles in a SiG//$LiFePO_4$ pseudo-full cell setup (i.e., with a capacitively largely oversized cathode of ∼3.5 mAh cm^{-2}) and a fluoroethylene carbonate (FEC)-based electrolyte.[39] Combining the microscopic characterization with the electrochemical analysis of the cycling stability, the electrode polarization, and the irreversible capacity losses upon cycling allows us to correlate the morphological changes of the silicon particles and the electrode with the observed cycling stability of the SiG electrodes. Electrochemical impedance spectroscopy (EIS) and cross-sectional scanning electron microscopy (SEM) images further complement the discussion by providing additional information about the electrode impedance and the morphological changes of the entire electrode structure as a function of the cycle number. A fully (de-)lithiated SiG electrode (0.01–1.25 V vs. Li^+/Li, ∼89% utilization of its theoretical capacity at a C-rate of 0.33 h^{-1}) is used as baseline in this study, the degradation of which will be compared to a lithiation-limited SiG electrode (0.05–1.25 V vs. Li^+/Li) and a delithiation-limited SiG electrode (0.01–0.65 V vs. Li^+/Li), both with a lower utiliztation of ∼76% of their theoretical capacity at 0.33 h^{-1}. Finally, we conclude our analysis with a detailed discussion of the impact of the upper/lower cutoff potentials on the morphological changes of silicon nanoparticles and the integrity of the SiG electrode.

Experimental

Silicon-graphite (SiG) electrode preparation.—Silicon-graphite (SiG) electrodes, consisting of 35 wt% silicon nanoparticles (∼200 nm dimensions, Wacker Chemie AG, Germany), 45 wt% graphite (∼20 μm, T311, SGL Carbon, Germany), 10 wt% vapor grown carbon fibers (VGCF-H, Showa Denko, Japan), and 10 wt% lithium poly(acrylate) binder (LiPAA) were prepared through an aqueous ink procedure, which is described in detail in our previous publication.[39] The LiPAA was prepared by diluting a 35 wt% poly(acrylic acid) solution (PAA, MW = 250,000 g mol^{-1}, Sigma-Aldrich, Germany) with deionized water and neutralizing it with lithium hydroxide (LiOH, Sigma-Aldrich, Germany) to a pH-value of ∼8.[43] The theoretical areal capacity of these electrodes was 1.8–1.9 mAh cm^{-2} (referenced to the theoretical specific capacities of 3579 mAh $g^{-1}{}_{Si}$ and 372 mAh $g^{-1}{}_{C}$, respectively, for the full potential range of 0.01–1.25 V vs. Li^+/Li), which corresponds to a mass loading of ∼1.4 $mg_{electrode}$ cm^{-2}. Practically, first cycle delithiation capacities of 1.7–1.8 mAh cm^{-2} (∼1280 mAh $g^{-1}{}_{electrode}$) could be utilized at a C-rate of 0.1 h^{-1}. This discrepancy can be rationalized by considering Figure 1b which shows the potential profiles of the first cycle for the individual active materials at 0.05 h^{-1} (viz., silicon:VGCF–H:LiPAA 37.5:37.5:25 wt% or graphite:LiPAA 95:5 wt%). The electrodes were prepared analogously to the procedure described above. Accordingly, the graphite electrode shows a first cycle delithiation capacity of 343 ± 2 mAh $g^{-1}{}_{C}$ (i.e., ∼92% of the theoretical capacity of 372 mAh g^{-1}), while the silicon electrode delivers 3273 ± 16 mAh $g^{-1}{}_{Si}$ (i.e., ∼91% of the theoretical capacity of 3579 mAh $g^{-1}{}_{Si}$). By considering a small capacity contribution of the carbon fibers (∼80 mAh $g^{-1}{}_{VGCF}$),[48] the practical capacity utilization of silicon shrinks to ∼89%. Transferring these values to the SiG electrodes results in an accessible electrode capacity of 1277 mAh $g^{-1}{}_{electrode}$, which is in a good agreement with the practical first cycle delithiation capacity of ∼1280 mAh $g^{-1}{}_{electrode}$. As a corollary, about ∼11 wt% of the silicon nanoparticles do not contribute the reversible capacity, likely because of the formation of electrochemically inactive SiO_2 during the aqueous ink procedure.

Test cell assembly.—Electrochemical characterization was performed in Swagelok T-cells (Swagelok, Germany), incorporating a lithiated gold-wire micro-reference electrode as described in detail by Solchenbach et al.[44] For post-mortem characterization of the SiG electrodes via STEM and SEM, CR2032 coin-cells (Hohsen, Japan) were prepared using the same electrode configuration. All cells were assembled in an Ar atmosphere MBraun glove box (H_2O and O_2 concentration <0.1 ppm), by sandwiching two porous glass fiber separators (thickness 250 μm, VWR, USA) that were soaked with electrolyte solution between a silicon-graphite anode (1.7–1.8 mAh cm^{-2} at 0.1 h^{-1}) and a capacitively oversized $LiFePO_4$ (LFP) cathode (3.5 mAh cm^{-2}, Custom cells, Germany). As electrolyte solution, a mixture of 1 M $LiPF_6$ in ethylene carbonate:ethyl methyl carbonate (EC:EMC, 3:7 w:w) with 5 wt% fluoroethylene carbonate (FEC) was used. Capacitively oversized LFP electrodes were selected for three reasons: (i) a capacitively oversized LFP cathode excludes the loss of active lithium as cause for cell polarization for the number of cycles conducted in this work; (ii) LFP forms a potential plateau at about 3.45 V vs. Li^+/Li during (de-)lithiation, which was used to reference the SiG electrode potential to the Li^+/Li potential; and, (iii) the low potential of the LFP cathode minimizes detrimental side reactions between the electrolyte and the cathode.[39]

Battery cycling.—The electrode polarization and cycling performance of the SiG electrodes was investigated by constant current cycling of SiG//LFP Swagelok T-cells. The C-rate was always referenced to the full theoretical capacity, independent of the cutoff potential (i.e., a C-rate of 1.0 h^{-1} corresponds to 1.8–1.9 mA cm^{-2}). The cell voltage was controlled between the silicon-graphite and the LFP electrode, whereby the SiG potential was calculated from the SiG//LFP cell voltage, based on the constant LFP potential of 3.45 V vs. Li^+/Li for the here used capacitively oversized LFP electrode. Initially, two formation cycles were performed of all electrodes between 0.01–1.25 V vs. Li^+/Li at a low C-rate of 0.1 h^{-1} (∼0.2 mA cm^{-2}) to achieve a similar passivation. The data of these first two cycles are omitted from the following figures and cycle number one in cycle-life tests refers to the first cycle after these initial two formation cycles. Cycle life tests at a C-rate of 0.33 h^{-1} (∼0.6 mA cm^{-2}) were conducted using three different voltage ranges: (i) full lithiation/delithiation between 0.01–1.25 V vs. Li^+/Li, (ii) partial lithiation between 0.05–1.25 V vs. Li^+/Li (furtheron referred to as lithiation-limited), and (iii) partial delithiation between 0.01–0.65 V vs. Li^+/Li (furtheron referred to as delithiation-limited). Every 1st, 32nd, and 63rd cycle (after formation), one cycle was applied to all electrodes in the full potential range: starting from the upper cutoff potential of the preceding cycle, the SiG electrodes were first lithiated to 0.01 V vs. Li^+/Li at 0.1 h^{-1} (∼0.2 mA cm^{-2}) and then delithiated to 2.0 V vs. Li^+/Li at 0.02 h^{-1} (∼0.04 mA cm^{-2}), before switching back to the respective set cutoff potentials and the higher C-rate of 0.33 h^{-1}. All measurements were performed in a climate chamber (Binder, Germany) at 25°C (±0.1°C), using either a battery cycler (Series 4000, Maccor, USA) or in case of the impedance measurements a multi-channel potentiostat VMP3 (BioLogic, France).

Electrochemical impedance spectroscopy.—Impedance measurements were performed during the slow intermediate cycles (1st, 32nd, and 63rd), using the lithiated gold-wire micro-reference electrode of the Swagelok T-cell setup described above.[44] Hence, the SiG electrodes were first delithiated to 0.65 V vs. Li^+/Li (∼15% SOC) and kept at this potential for 30 min by applying a constant voltage step. Afterwards, potentiostatic electrochemical impedance spectroscopy (PEIS) was measured in the frequency range of 100 kHz – 500 mHz, using a perturbation of 15 mV.

Transmission electron microscopy.—The morphology and relative composition of the silicon particles from an uncycled electrode and after 1, 5, 20, 40, and 60 cycles was investigated by scanning transmission electron microscopy (STEM) and energy dispersive spectroscopy (EDS), using a FEI Titan Themis (FEI, USA) at 200 kV. Prior to these measurements, the SiG electrodes were slowly delithiated at 0.02 h^{-1} to 2.0 V vs. Li^+/Li, then harvested from the cells and carefully washed with 50 μL dimethyl carbonate (DMC), and finally dried in an inert atmosphere. Afterwards, the coatings were scratched and a TEM lacey carbon Cu 200 grid (EMS, USA) was directly pressed onto the surface to collect the powder before being

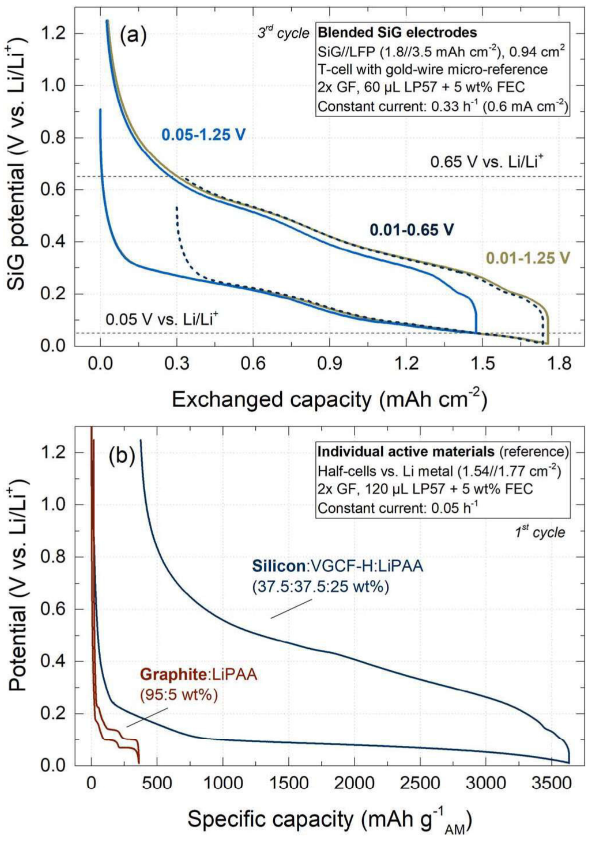

Figure 1. (a) Potential profiles of silicon-graphite electrodes vs. capacity during galvanostatic cycling at 0.33 h^{-1} (3^{rd} cycle) of SiG//LFP Swagelok T-cells at different cutoff potentials: 0.01–1.25 V vs. Li^+/Li (brown), 0.05–1.25 V vs. Li^+/Li (blue), and 0.01–0.65 V vs. Li^+/Li (marine). The SiG potential was calculated from the SiG//LFP cell voltage, based on the constant LFP potential of 3.45 V vs. Li^+/Li for the here used capacitively oversized LFP electrodes. (b) Potential profiles of the individual active materials during the first galvanostatic cycle at 0.05 h^{-1} in half-cells against lithium metal between 0.01–1.25 V vs. Li^+/Li (marine: silicon/VGCF-H/LiPAA 37.5/37.5/25 wt%, red: graphite/LiPAA 95:5 wt%).

transferred into the instrument. During that period, the samples were exposed to air for a time interval of ~10 min.

Scanning electron microscopy.—The morphology of the SiG electrodes prior to cycling and after 60 cycles at different cutoff potentials was investigated by cross-sectional scanning electron microscopy (SEM). First, electrode cross-sections were prepared by Argon ion beam polishing, using a JEOL Cross Section Polisher IB-09010CP (JEOL, Japan). Afterwards, SEM images were measured by use of a JEOL JSM-IT100 (JEOL, Japan) with a tungsten electron source and a secondary electron detector. Both the preparation of the cross-sections and the subsequent measurement of the SEM images were conducted by the JEOL (Germany) GmbH in Freising, Germany. Prior to the measurement, the samples were exposed to ambient atmosphere for less than an 30 minutes.

Quantification of electrode thickness changes.—The changes in the electrode thickness were measured by cross-sectional SEM with the aid of a JEOL JCM-6000 Neoscope (JEOL, Japan), using a modification of the method described by Mittermeier et al.[45] For each cutoff condition, two SiG//LFP coin-cells were aged for 60 cycles, using the same cycling procedure as described above, yet without the intermediate cycles at low C-rate. Afterwards, the SiG electrodes were harvested from the cells and embedded into a resign solution with a hardener, hereupon evacuated repeatedly in a desiccator to remove gas bubbles, and subsequently dried in an oven at 40°C overnight. The solid polymer block was then polished stepwise to obtain a mirror finished cross-section. For each cutoff condition, two electrodes were evaluated at fifteen positions along the entire cross-section, resulting in ~30 measurements to obtain an average thickness and its standard deviation (represented by the error bars).

Results and Discussion

Influence of the cutoff potentials on the electrochemical performance of SiG electrodes.—Figure 1a shows the potential profiles of the silicon-graphite (SiG) electrodes at different cutoff potentials during the 3^{rd} cycle at 0.33 h^{-1}. Full (de-)lithiation of the electrodes between 0.01 and 1.25 V vs. Li^+/Li (brown line) provides a reversible capacity of ~1.7 mAh cm^{-2} at 0.33 h^{-1} which corresponds to a capacity utilization of ~89% (referenced to the theoretical value of ~1.9 mAh cm^{-2} for this electrode). The sloped profile of the potential curves shown in Figure 1a is characteristic for the (de-)lithiation of amorphous silicon, which contributes most of the electrode's capacity (~88% based on the theoretical capacities, graphite accounts for ~12%). While the formation of the lithium-graphite compounds LiC_x starts not until potentials below 0.19 V vs. Li^+/Li and is therefore largely overlapped by the lithiation of silicon, it can be distinguished during the delithiation process by the small plateau at potentials below 0.24 V vs. Li^+/Li (see Figure 1a).[39] By limiting either the lithiation to 0.05 V vs. Li^+/Li (blue line) or alternatively the delithiation to 0.65 V vs. Li^+/Li (dashed marine line), the reversible capacity at 0.33 h^{-1} drops to a similar value of ~1.45 mAh cm^{-2}, i.e., to ~76% of the theoretical capacity. It is noted that a partial delithiation presupposes a previous full lithiation of the SiG electrode, which means that at least 0.25 mAh cm^{-2} (~15%) excess capacity remains in the electrode.

Obrovac and Christensen demonstrated that limiting the lithiation of silicon-based electrodes to potentials above 0.05 V vs. Li^+/Li avoids the formation of the metastable crystalline $Li_{15}Si_4$ phase and results in a better cycling performance due to the absence of the two-phase reaction of crystalline $Li_{15}Si_4$ to amorphous $Li_{\sim 2}Si$, which has been associated with detrimentally high internal stress in the silicon particles.[7] For the here investigated SiG electrodes, we observed the characteristic delithiation plateau of the $Li_{15}Si_4$ phase around 0.45 V vs. Li^+/Li only during the two formation cycles at a low C-rate of 0.1 h^{-1} (data not shown). However, during subsequent cycling at a higher C-rate of 0.33 h^{-1} (see Figure 1a) the feature disappeared, indicating that $Li_{15}Si_4$ formation did not occur at the here applied C-rate at any of the investigated cutoff potentials.[16] The reason for this lies in the high overpotential of the SiG electrodes during lithiation, which prevents the formation of the $Li_{15}Si_4$ phase at the expense of lowering the achievable capacity. If, on the other hand, as in our previous study with the same SiG electrodes,[39] a constant potential hold step at 0.01 V vs. Li^+/Li is applied, a distinct peak at about 0.45 V vs. Li^+/Li can be observed during delithiation even upon continued cycling. Therefore, we conclude that the following results recorded without potential hold are not influenced by additional stress arising from the $Li_{15}Si_4$ two-phase boundary at potentials below 0.05 V vs. Li^+/Li.

Figure 2 shows (a) the coulombic efficiency (defined as the first cycle delithiation capacity divided by the first cycle lithiation capacity) and (b) the areal delithiation capacity of the SiG electrodes at different cutoff potentials as a function of the cycle number. The delithiation capacity reveals a distinct decay within the first 60 cycles, which occurs not only during full (de-)lithiation (brown symbols) but also during the lithiation-limited cycling (blue symbols), i.e., during the two cycling conditions at which the electrodes are nominally fully delithiated to 1.25 V vs. Li^+/Li. As recently reported by Yoon et al.,[15] this decay can be associated with the degradation of the SiG electrode and is caused by the buildup of interfacial resistances (electronic and/or charge transfer resistances) for upper cutoff voltages which allow for a complete delithiation of the silicon. In contrast,

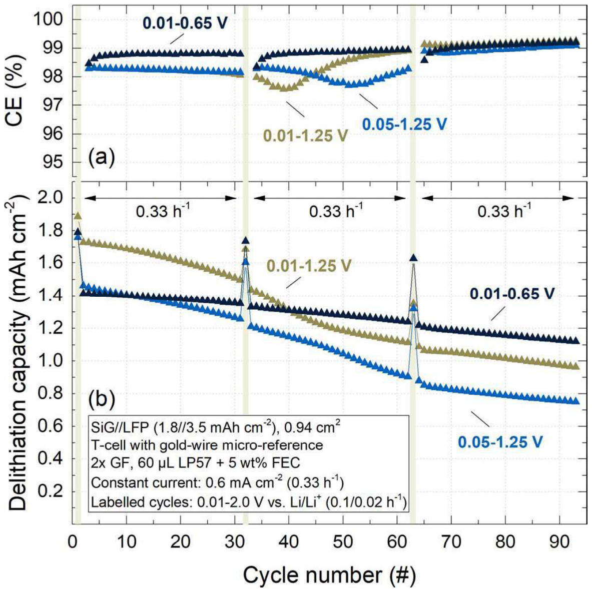

Figure 2. (a) Coulombic efficiency and (b) delithiation capacity obtained from constant current cycling (0.33 h^{-1}) of SiG//LFP Swagelok T-cells at different cutoff potentials: 0.01–1.25 V vs. Li$^+$/Li (brown), 0.05–1.25 V vs. Li$^+$/Li (blue), and 0.01–0.65 V vs. Li$^+$/Li (marine). The yellow bars indicate intermediate cycles (1st, 32nd, and 63rd), which were performed at lower C-rates (lithiation: 0.1 h^{-1}, delithiation: 0.02 h^{-1}) and the capacities of which are summarized in Table I; for these single cycles evaluation of the coulombic efficiency is not meaningful and is thus not shown.

for delithiation-limited SiG electrode cycling (0.01–0.65 V; marine symbols), only a comparatively small capacity fade upon cycling is observed. In this case, ~15% (~0.25 mAh cm^{-2}) of active lithium remain in the silicon, which according to Kimura et al.[42] reduces the formation of electronically insulated silicon particles. We would like to stress that although the capacity contribution from graphite is likely smaller for the lithiation-limited electrode (0.05–1.25 V; blue symbols), a similar behavior was also reported in the literature for silicon-based electrodes which did not contain any graphite.[40,42]

Next, we wanted to understand whether the improved cycling stability at the delithiation-limited cutoff potential results really from an improved electrode integrity and decreased overpotential or results just from a reduced lithium immobilization in poorly connected silicon particles due to the deliberate incomplete lithiation. Hence, the delithiation capacity of the intermediate cycles which were performed similarly for all electrodes in the full potential range with a deep delithiation (0.01–2.0 V vs. Li$^+$/Li) at very low C-rates is summarized in Table I. The delithiation-limited electrode reveals a high capacity retention of ≥91% even after 60 cycles, whereas the electrodes that were delithiated to 1.25 V vs. Li$^+$/Li demonstrate only a residual reversible capacity of 72–75%. Therefore, these results demonstrate that at the selected cycling conditions a higher upper cutoff potential not only reduces the cycling stability of the SiG electrode (irrespective of the overall exchanged capacity), but also lowers the amount of cyclable lithium due to the formation of inaccessible lithium. Note that the capacitively largely oversized LFP cathode provides a non-limiting lithium inventory in the cell and remains at a stable reference potential of 3.45 V vs. Li$^+$/Li with only a marginal potential upward shift of 20–25 mV over the examined ~100 cycles. Considering the potential profiles shown in Figure 1a, this corresponds to a reversible capacity loss of 0.1–0.2 mAh cm^{-2} for each of the cutoff conditions. As a corollary, we slightly underestimate the residual capacity of our SiG electrodes after 100 cycles compared to measurements in half-cells.

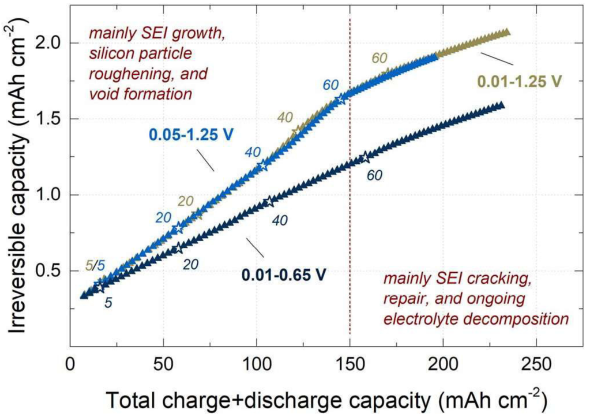

Figure 3. Total irreversible capacity $\sum Q_{irr}$ (in mAh cm^{-2}) of silicon-graphite electrodes as a function of the total exchanged charge+discharge capacity (in mAh cm^{-2}), obtained from the constant current cycling data of the SiG//LFP (1.8//3.5 mAh cm^{-2}) Swagelok T-cells shown in Figure 2 (i.e., over 90 cycles at 0.33 h^{-1}). The irreversible capacity contribution from the intermediate cycles (0.1/0.02 h^{-1}) were omitted to mitigate the influence of the different C-rates. The hollow stars label the number of the respective charge-discharge cycles. Electrolyte: LP57 + 5 wt% FEC.

The coulombic efficiency of the SiG electrodes shown in Figure 2a further supports the observation that electrodes which were delithiated to 1.25 V vs. Li$^+$/Li (brown and blue symbols) behave more alike than electrodes that were cycled at the same reversible capacity but at different cutoff potentials (blue and marine symbols). Clearly, the delithiation-limited electrode (marine symbols) indicates on average a 0.7% higher coulombic efficiency within the first 60 cycles, which increases steadily upon cycling. In contrast, the fully delithiated electrodes (brown and blue symbols) do not only start at a lower value of 98.3% but also show a slight decline during the same period that is followed by a minimum at ~97.7% after 40 cycles for the full (de-)lithiation (brown symbols) and after 50 cycles during the lithiation-limited cycling (blue symbols), respectively. After 60 cycles, however, a rapid increase can be observed in the coulombic efficiency across all cutoff potentials, which results in a similar value of 99.2% after 90 cycles for all electrodes.

To understand the origin of the differences in the coulombic efficiency when cycling with different cutoff potentials, Figure 3 illustrates the total irreversible capacity, i.e., the summation of the irre-

Table I. Delithiation capacity and capacity retention of selected intermediate cycles performed at a lower cutoff potential of 0.01 V vs. Li/Li at a lithiation rate of 0.1 h^{-1} and a deep delithiation to 2.0 V vs. Li$^+$/Li at delithiation rate of 0.02 h^{-1}.

	Delithiation capacity/mAh cm^{-2}			Capacity retention/%	
Cutoff potentials	1st cycle	32nd cycle	63rd cycle	cycle 1–32	cycle 1–63
0.01–1.25 V (full (de-)lithiation)	1.88	1.68	1.35	89	72
0.05–1.25 V (lithiation-limited)	1.76	1.60	1.32	91	75
0.01–0.65 V (delithiation-limited)	1.79	1.74	1.62	97	91

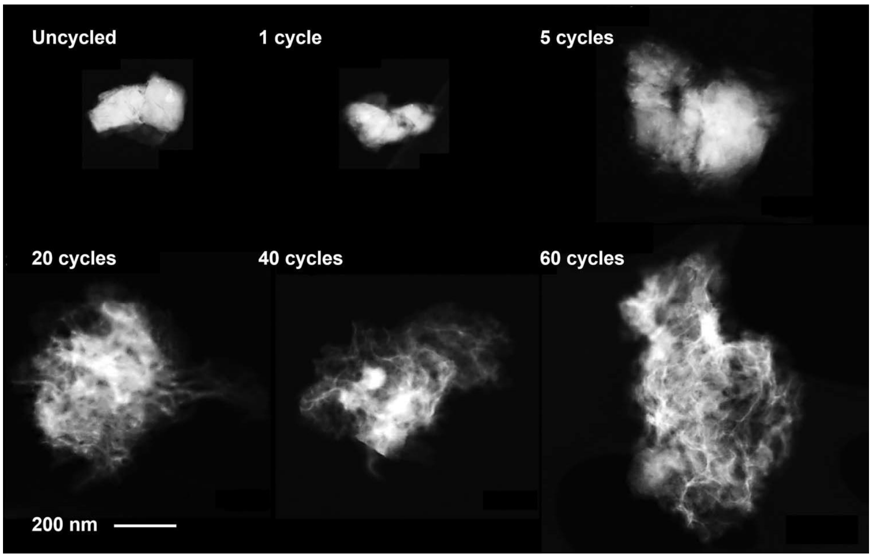

Figure 4. Scanning transmission electron microscopy (STEM) images of silicon particles from an uncycled electrode (upper left panel) and after different number of full (de-)lithiation cycles using the standard cutoff potentials of 0.01–1.25 V vs. Li^+/Li (1, 5, 20, 40, and 60 cycles; 60 cycles corresponds to a total charge+discharge capacity of ~170 Ah cm^{-2} in Figure 3). High-angle annular dark field (HAADF) detector, acceleration voltage: 200 kV.

versible capacity for each cycle, as a function of the total exchanged charge+discharge capacity. In contrast to plotting the accumulated irreversible capacity vs. the cycle number, plotting it vs. the total exchanged capacity takes into account the differences in the reversible capacity obtained over the different charge/discharge protocols, and allows thus to better compare the effect of the different cutoff potentials. Furthermore, for the interpretation of Figure 3 it is important to note that the irreversible capacity can almost be fully ascribed to the silicon particles, because graphite is almost completely passivated after the two formation cycles preceding the charge/discharge cycling test, so that its contribution to the accumulated irreversible capacity after formation is negligible compared to silicon.[39]

Two distinct slope regions can be differentiated in Figure 3 (see red dashed vertical line), very distinct for the electrodes that were delithiated to 1.25 V vs. Li^+/Li (brown and blue symbols), and somewhat less pronounced for the delithiation-limited electrodes delithiated to 0.65 V vs. Li^+/Li (marine symbols). The steep increase of the irreversible capacity within the first 60 cycles was previously ascribed to an enhanced growth of the solid-electrolyte-interphase (SEI) due to silicon particle roughening and void formation.[39] After ~60 cycles, however, the curves become much flatter, which we interpreted to indicate that a steady-state silicon particle morphology was reached, so that the lower rate of irreversible capacity gains would result mainly from SEI cracking and electrolyte decomposition caused by the ongoing volumetric changes upon repeated (de-)lithiation.[39] In this latter stage of aging (i.e., after ~60 cycles), the total irreversible capacity gain rate vs. total exchanged capacity of the electrodes delithiated to 1.25 V vs. Li^+/Li (brown and blue symbols) approaches the same value (i.e., the flatter slope) of the delithiation-limited electrodes (marine symbols). In order to verify that this persists over more than the 90 cycles shown in Figure 3, we also performed an extended cycling procedure up to 150 cycles (data not shown), which confirmed that the total irreversible capacity gain rates at the different cycling conditions indeed converge to nearly identical values after 60–80 cycles. In other words, after ~60 cycles, the coulombic efficiency shows only a minor dependence on the investigated cutoff potentials (see Figure 2a). From this point onwards, ongoing SEI cracking and renewal only depends on the amount of charge which is exchanged by the silicon particles upon cycling.

Silicon particle degradation upon repeated (de-)lithiation.— Throughout our previous studies on SiG electrodes[39,46] as well as in the literature,[32,41,43,47] it has been observed that electrodes based on silicon nanoparticles typically show a significantly lower coulombic efficiency in comparison to conventional graphite. However, it can often be seen that the coulombic efficiency upon extended cycling goes through a minimum between ~20–80 cycles before recovering to higher values again (see Figure 2a and references[39,43,48]). Our explanation for this phenomenon is that the silicon nanoparticles undergo dealloying reactions during the extraction of lithium, which result in a roughening of the particle surface and formation of void spaces, as recently shown for tin.[49] Dealloying is a common corrosion process which involves the selected dissolution of the more electrochemically active element, here lithium, from an alloy and results in the formation of a nanoporous structure of the more noble alloy constituent, here silicon.[50,51] The resulting surface area increase drives further electrolyte decomposition and SEI growth on the freshly exposed silicon/electrolyte interface, which results in the steeper increase of the irreversible capacity (compare Figure 3). To confirm our hypothesis, we aged SiG electrodes for a different number of cycles, using the standard cutoff potentials of 0.01–1.25 V vs. Li^+/Li (see brown curve in Figure 2). Afterwards, we slowly delithiated the electrodes to ~2.0 V vs. Li^+/Li to extract any residual lithium from the active materials and prepared lacey carbon TEM grids as described in the Experimental section. Figure 4 shows representative STEM images of a silicon particle from an uncycled electrode and of aged silicon particles after 1, 5, 20, 40, and 60 cycles.

Prior to cycling, the silicon particles reveal an irregular shape, consisting of a dense, crystalline structure with a mean size of ~200 nm (see top left panel). After the first cycle (top center panel), the shape and the dimensions remain very similar, whereas the silicon surface is less smooth and the edges are less defined, suggesting an amorphous structure without crystalline order and with a decreased density. From the literature it is known that crystalline silicon becomes amorphous upon the insertion of lithium and the formation of Li_xSi alloys; only at high degrees of lithiation a metastable crystalline $Li_{15}Si_4$ phase is formed.[7] During the subsequent extraction of lithium, the resulting silicon phase remains amorphous and no crystalline phases are observed anymore if silicon is either cycled at potentials above 0.05 V vs. Li^+/Li

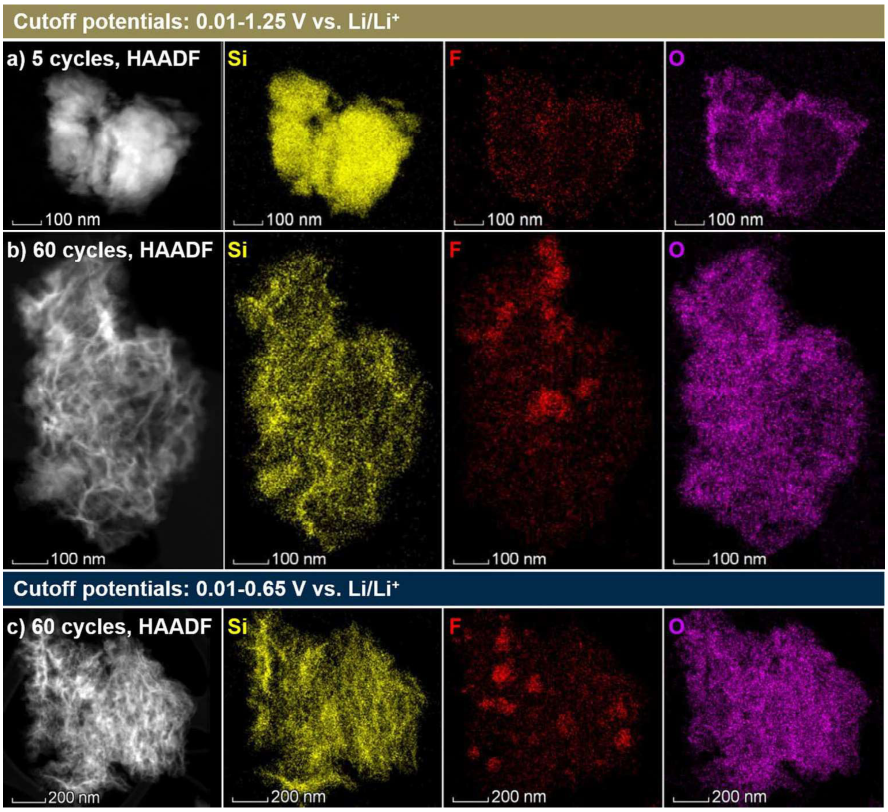

Figure 5. HAADF images and EDS spectra of the silicon particles, obtained after cycling to different cutoff potentials: 0.01–1.25 V vs. Li^+/Li a) after 5 and b) after 60 cycles (particles as shown in Figure 4); and, c) 0.01–0.65 V vs. Li^+/Li after 60 cycles. From left to right: HAADF image (white) and EDS spectra of silicon (yellow), fluorine (red), and oxygen (purple). Carbon was not considered, because the silicon particles were prepared on TEM carbon grids, which contributes significantly to the measurement.

or, as is the case in the present study, an increased electrode overpotential suppresses the formation of the $Li_{15}Si_4$ phase even at lower cutoff voltages of 0.01 V vs. Li^+/Li. Although the silicon particles undergo a large volume expansion up to +280% during the insertion of lithium, our STEM investigation indicates that after the first cycle the silicon particles return almost entirely to their initial dimensions in their delithiated state, with only minor deviation from the appearance of the uncycled silicon particle, which is in agreement with previous in situ atomic force microscopy measurements by Beaulieu et al.[52] However, Figure 4 also demonstrates that after 5 (top right panel) and even more after 20 cycles (bottom left panel), the silicon particles transform into an increasingly nanoporous structure with a high surface area and large void spaces, resulting in a considerable expansion with mean diameters up to 400 nm (in their delithiated state), which corresponds to a permanent volume expansion of approximately +700% (estimated from the ~2-fold expansion in each dimension). These morphological changes are accompanied by the formation of a continuous network of nanometer-sized silicon branches, which is presumably driven by a phase separation process at the solid/electrolyte interface, as described by Erlebacher et al.[50,53] The appearance of the silicon particles after 20 and more cycles (bottom panels of Figure 4) very much resembles the structures obtained upon the delithiation of Li–Sn alloys reported by Chen and Sieradzki.[49] Comparing the STEM images for 20, 40, and 60 cycles, one can notice that the change in the morphology of the silicon particles become less and less significant with increasing cycle number.

The progressive and large increase of the silicon surface area and the associated electrolyte decomposition at the newly formed silicon/electrolyte interface also explains the steep increase of the accumulated irreversible capacity over the first 60 cycles shown in Figure 3. Nonetheless, as indicated by the gradual decrease of the accumulated irreversible capacity gain rate (i.e., the slope in Figure 3) after ~60 cycles, the expansion of the silicon matrix by the dealloying process seems to approach a steady-state. Accordingly, the bottom center and right panel in Figure 4 show that already existing nanometer-sized silicon branches indicate less dramatic changes after 40 and 60 cycles, while few remaining dense areas expand further to also form a nanoporous silicon network. This can be explained by the fact that the increase of the silicon particle surface area and porosity leads to a decrease of the effective surface-normalized current density, which lowers the driving force for the formation of finer silicon filaments, as it was shown for Li–Sn alloys.[49] In other words, the morphological changes caused by dealloying of the silicon particles diminish their own root cause, namely the internal stress resulting from the repeated insertion and extraction of lithium.

Although the high-angle annular dark-field (HAADF) images shown in Figure 4 suggest that the silicon particles continuously transform into a continuous network of nanometer-sized highly branched silicon filaments, these structures are indeed not hollow. Instead, the freshly exposed silicon surface formed by these morphological changes of the silicon particles results in a further decomposition of electrolyte compounds at the silicon/electrolyte interface, leading to SEI growth and concomitant filling of the porous silicon structure. In fact, it is likely that the porous silicon structure is additionally stabilized by the SEI precipitates, which counteract the contraction of the high-surface area silicon structures during delithiation steps. Figure 5 shows the energy dispersive spectroscopy (EDS) spectra of silicon (yellow), fluorine (red), and oxygen (purple) of silicon

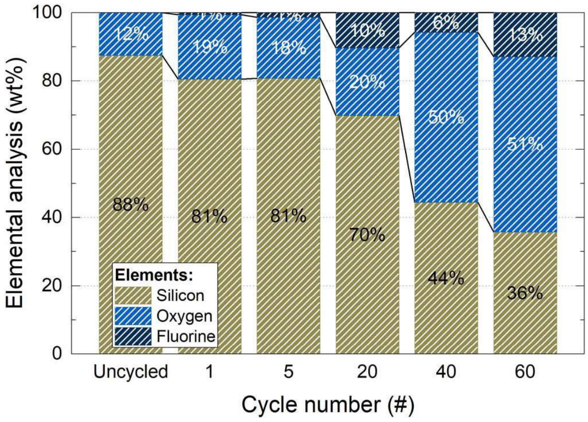

Figure 6. Relative weight composition determined by EDS analysis of silicon particles from uncycled electrodes and after different number of full (de-)lithiation cycles between 0.01–1.25 V vs. Li^+/Li, based on the data shown in Figure 4 and Figures 5a/5b.

particles (a) after 5 and (b) after 60 deep (de-)lithiation cycles between 0.01–1.25 V vs. Li^+/Li. The silicon spectrum (yellow) confirms the considerable decrease of the density of silicon within the expanded silicon particles and the formation of a nanoporous network upon cycling, whereas the fluorine and oxygen spectra reveal an inverse trend. Accordingly, only minor amounts of fluorine and oxygen can be seen after 5 cycles (panel a) at the edges of the particles, which mainly stem from the initial SEI formation and, in the case of oxygen, also from the initial native SiO_2 and additional SiO_2 formed during the aqueous ink processing. After 60 cycles (panel b), however, the spectra indicate much larger amounts of fluorine and oxygen that penetrate the entire nanoporous silicon structure.[54,55]

Figure 6 summarizes the relative weight composition of the silicon particles from uncycled electrodes and after different number of cycles. The uncycled particles show mostly silicon (~88 wt%) and small amounts of oxygen (~12 wt%). Considering that about 11% of the theoretical capacity of silicon are not accessible, likely because of SiO_2 which forms during the aqueous ink procedure, this would correspond to a silicon:oxygen mass ratio of 94:6 wt%. As a corollary, the oxygen content for the here investigated particles is slightly higher compared to values obtained by the electrochemistry for the entire electrode. Yet, given the sample size of few individual particles as well as the accuracy of EDS they are in a reasonable agreement. After several charge-discharge cycles, the relative contribution from silicon decreases continuously at the expense of larger amounts of the electrolyte decomposition products (here represented by fluorine and oxygen). In agreement with the increasing porosity within the silicon particle shown by the HAADF images (Figure 4 and Figure 5b), silicon accounts for only one third of the entire structure after 60 cycles. This number can be easily rationalized based on the electrolyte decomposition during the same period. Taking into account a total irreversible capacity loss of 1.79 mAh cm^{-2} after 60 cycles (marked for the brown curve in Figure 3), which is mainly caused by the reductive decomposition of FEC ($M_W = 106.05$ g mol^{-1}) and follows a four-electron reduction mechanism (i.e., 9.4 μmol_{FEC} mAh^{-1}), as indicated by our previous electrolyte consumption studies using ^{19}F-NMR,[39,48] the total amount of the reduced FEC amounts to 1.78 mg_{FEC} cm^{-2}. Assuming as a zero order approximation that all FEC decomposition species transform into SEI products as well as considering further that fluorine and oxygen contribute about 57% to the molecular mass of FEC (i.e., 0.57×1.78 mg cm^{-2}) and that the initial silicon mass loading of the electrodes was ~0.5 mg_{Si} cm^{-2} (=0.35×1.4 mg cm^{-2}), the relative weight contribution of silicon after 60 cycles would be roughly 33 wt% and is thus in good agreement with the EDS spectra. Therefore, both the NMR and STEM investigation consistently demonstrate that the silicon-graphite electrodes are increasingly filled by electrolyte decomposition products, which do not only cover the active materials but also penetrate the increasingly nanoporous structure of the silicon particles.

After this discussion of the morphological transformation of the silicon particles upon extended deep delithiation to 1.25 V, the open question is whether this can also be observed under delithiation-limited condition, i.e., upon extended cycling with an upper cutoff potential of 0.65 V. At first glance, the flatter initial slope of the accumulated irreversible capacity within the first 60 cycles under delithiation-limited conditions (see marine symbols in Figure 3) suggests that the extent of silicon particle expansion may be reduced under these conditions. Hence, Figure 5c shows the HAADF image and the EDS spectra for the silicon-graphite electrodes after 60 cycles between 0.01–0.65 V vs. Li^+/Li. Analogous to the electrodes that were fully (de-)lithiated (compare Figure 5b), the delithiation-limited silicon particles reveal the same formation of a continuous network consisting of nanometer-sized silicon branches, which indicates that the investigated silicon particles undergo the same dealloying reactions, despite the lesser degree of delithiation at this lower cutoff potential. No significant differences could be observed for the two cutoff conditions during several repeat measurements after 60 cycles (compare Figures 5b and 5c) as well as after 40 cycles (data not shown), which demonstrates that the here investigated upper cutoff potentials do not affect the extent of the permanent silicon particle expansion. This demonstrates that a residual amount of about ~15% active lithium at 0.65 V upper cutoff potential (in contrast to essentially 0% for an upper cutoff potential of 1.25 V) does not prevent the morphological changes of the silicon particles caused by the dealloying mechanism. As a result, the flatter slope of the accumulated irreversible capacity loss curve for the delithiation-limited cycling procedure shown in Figure 3 cannot be explained by differences in silicon particle expansion and the concomitant formation of additional surface area. Instead, there must exist another reason for the differences in the total irreversible capacity curve within the first 60 cycles, which is related to the cutoff potentials and explains why the slope for the delithiation-limited cycling is already lower over the initial ~60 cycles (compare Figure 3).

In order to explain this apparent discrepancy, we propose that this phenomenon is related to the differences in the relative surface area change of the silicon particles, $\Delta S_{Si}/S_{Si,0}$, with ΔS_{Si} being the surface area differences between the lower and the upper cutoff potential, and with $S_{Si,0}$ being the surface area at the upper cutoff potential (i.e., at the lowest degree of lithiation). This is because the relative change in silicon surface area over the course of one lithiation/delithiation cycle should be directly proportional to the in-plane mechanical stress on the SEI layer at the silicon surface and, in turn, to the extent of the SEI cracking and re-formation.[8] In other words, although the total surface area of the silicon particles is continuously increasing as a consequence of the above described morphological changes, the repeated volume changes upon (de-)lithiation over the course of every single lithiation/delithiation presents an additional irreversible capacity contribution. It is known from the literature that silicon particles expand almost linearly as a function of the lithium content.[52] However, based on simple geometric considerations of the volume-surface relation of a sphere, which are shown in Figure 7a, it can be demonstrated that the concomitant increase of the surface area (see dotted red line) of a sphere is larger during the initial stages of lithiation (indicated by the steeper slope of the dotted read line for small x-values) compared to the lower relative increase of the surface area at higher degrees of lithiation (reflected by the lower slope at high x-values). While our silicon particles are clearly not spherical, we are using this analysis based on spherical particles as a zero-order approximation to describe the processes occurring at the silicon/electrolyte interface. The goal is merely to demonstrate based on simple geometric considerations that depending on the degree of lithiation the relative surface area changes of silicon vary in their extent. This has an important implication on the in-plane mechanical stress on the SEI layer and thus the resulting coulombic efficiency. As the extent of the differences depends

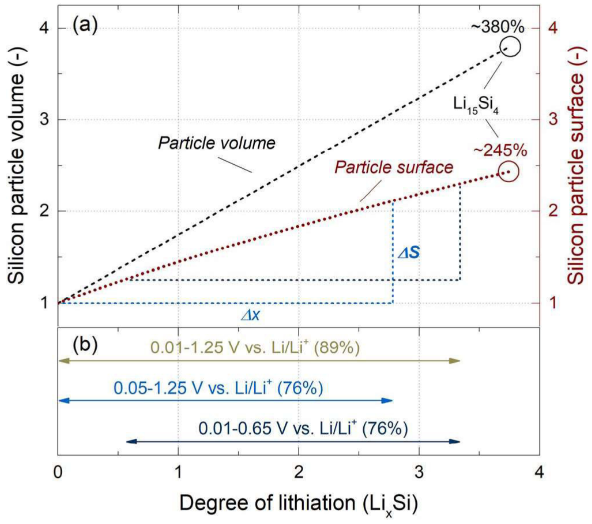

Figure 7. Illustration of (a) the relative volume $V_{Si,rel} \equiv V_{LixSi}/V_{si}$ (dashed black line, left axis) and the relative surface area $S_{Si,rel} \equiv S_{LixSi}/S_{si}$ (dotted red line, right axis) of a spherical silicon nanoparticle as a function of the degree of lithiation x in Li_xSi. b) Initial degree of lithiation ranges for the three investigated cutoff conditions. which were calculated based on their reversible capacity at 0.33 h^{-1} as obtained from the constant current cycling shown in Figure 2b. The blue and the marine dashed triangles represent the surface area changes for the lithiation- and delithiation-limited cutoff conditions, respectively.

strongly on the morphology of the silicon active material (as well as their changes upon cycling), this will not enable a prediction of the exact values of ΔS_{Si} during lithiation/delithiation. Yet, we think that it will allow a semi-quantitative assessment of the different behavior of silicon depending on the applied cutoff potentials.

Based on the initial capacities of the SiG electrodes at 0.33 h^{-1} (see Figure 2b) and under the assumption of the same theoretical capacity utilization for silicon and graphite (i.e., ~89% at 0.01–1.25 V), the range of the degrees of lithiation x (referring to Li_xSi) of the silicon particles for the different cycling protocols can be estimated and is indicated in Figure 7b: (i) x ≈ 0–3.34 for the deep (de-)lithiation cycling (0.01–1.25 V cutoff potentials); (ii) x ≈ 0–2.85 for lithiation-limited cycling (0.05–1.25 V cutoff potentials); and, (iii) x ≈ 0.49–3.34 for the delithiation-limited cycling (0.01–0.65 V cutoff potentials). Upon continued cycling, the ranges of the degree of lithiation change, because of the capacity fade and disconnection of silicon particles. Therefore, the total volume expansion and the total surface area will also decrease, resulting in a lower capacity fade upon extended cycling across all cutoff potentials (see Figure 2b). Nonetheless, at least over the first 20–30 cycles, i.e., during the period of the largest degradation (see Figure 3), these changes are reasonably small, which allows a fair comparison of the different degree of lithiation ranges. While, the surface area of conceptual silicon spheres over a lithiation-limited (blue arrow in Figure 7b) and a deep (de-)lithiation cycle (brown arrow) changes by ~113% (derived from $\frac{S_{Si,rel\ (x=2.85)}}{S_{Si,rel\ (x=0)}} - 1 = \frac{2.13}{1} - 1$) and ~128% (froam $\frac{S_{Si,rel\ (x=3.34)}}{S_{Si,rel\ (x=0)}} - 1 = \frac{2.28}{1} - 1$), respectively, the silicon particle surface area over a delithiation-limited cycle (see marine arrow) changes by only ~82% (from $\frac{S_{Si,rel\ (x=3.34)}}{S_{Si,rel\ (x=0.49)}} - 1 = \frac{2.28}{1.25} - 1$). Normalizing these values to the number of inserted/extracted lithium atoms x (as defined by Li_xSi) per half-cycle reveals that the delithiation-limited silicon experiences a relative surface area change of ~30% per exchanged lithium atom (i.e., ~82% divided by $\Delta x = 2.85$), whereas the lithiation-limited (i.e., ~113% divided by $\Delta x = 2.85$) and the fully (de-)lithiated electrodes (i.e., ~128% divided by $\Delta x = 3.34$) experience almost the same but notably higher relative surface area change of 38–40% per lithium atom. Considering that a larger relative change in the silicon surface area during a (de-)lithiation cycle should lead to increased cracking and renewal of the SEI on the silicon surface, the results from this admittedly rather rough estimate of relative surface area changes for hypothetical silicon spheres provide a feasible explanation for the lower slope in the initial total irreversible capacity gain of the delithiation-limited cycling (see Figure 3) compared to cycling to full delithiation.

In summary, the initially high slope of the total irreversible capacity curves (Figure 3) is largely governed by the formation of nanoporous silicon particles with increasingly higher surface area, whereby this morphology evolution is not significantly affected by the here examined cutoff potentials (see Figure 5). The more subtle differences in the initial slopes are likely due to the above described relative surface area changes over a lithiation/delithiation cycle depending on the cutoff voltages. After an extended number of cycles, quasi steady-state silicon nanostructures are obtained and the flatter slope of the total irreversible capacity curves seems to be mostly controlled by the relative silicon surface area changes per cycle. The observed similar slopes for all cycling protocols suggest that the higher remaining capacity of the delithiation-limited cycled electrodes compensates for its lower value of relative surface area change per exchanged capacity. As a corollary, the silicon particle degradation can be considered as the root cause for the aging of SiG electrodes and an intrinsic property of the silicon particles. The underlying dealloying reactions likely depend on the initial size and shape of the silicon particles as well as their chemical composition (e.g., oxygen content). Although the dealloying induced roughening of the here studied silicon particles is almost independent of the chosen cutoff potentials (within the range studied here), it is conceivable that different particle morphologies, the use of active-inactive alloys, and a significantly reduced capacity utilization may help to mitigate the extent of this phenomenon. For example, Krause et al.[56] reported in a recent publication a very stable BET surface area over 80 cycles for silicon-graphite electrodes, featuring 15 wt% of ~5 μm particles of a silicon alloy. In these alloys, nano-domains of silicon are immersed in an alloy matrix which suppresses the morphological changes of silicon and decreases the surface area exposed to the electrolyte.[43]

Electrode degradation upon repeated (de-)lithiation.—While the coulombic efficiency of the SiG electrodes shown in Figure 2a is largely determined by the morphological changes of the silicon nanoparticles and subsequent electrolyte decomposition, the discrepancy in the cycling stability (see Figure 2b) at the different cutoff potentials requires to consider the entire electrode structure.[39] Figure 8 shows the differential capacity curves of the SiG electrodes of the 5th, 20th, 40th, and 60th cycle for the different cutoff potentials. The electrodes that were delithiated to 1.25 V vs. Li^+/Li (panel a and b) reveal a severe capacity decay at low degrees of lithiation (i.e., at high potentials), whereas the delithiation-limited electrode (panel c) indicates only a minor fading. From previous studies it is known that the distinct potential drop to 0.2 V vs. Li^+/Li at the beginning of lithiation (see Figures 8a and 8b) is mainly caused by an incomplete delithiation from the silicon nanoparticles during the preceding cycle, which is reflected by the disappearance of the delithiation capacity contribution at potentials above 0.55 V vs. Li^+/Li.[15,39] Further, it can be seen in panel a) and b) that the nominally fully delithiated electrodes show an increasingly growing polarization of the (de-)lithiation from silicon during lithiation at ~0.15 V vs. Li^+/Li as well as during delithiation at ~0.35 V vs. Li^+/Li, indicating higher charge transfer overpotentials and resulting in an additional capacity loss. Again, this behavior is notably less pronounced for delithiation-limited cycling of silicon (see Figure 8c). The discrepancy in the electrode polarization is in good agreement with the SiG electrode impedances at the different cutoff potentials, which are shown in Figure 9. After formation, i.e., before switching to the individual cutoff potential ranges, all electrodes reveal a distorted semicircle with a similar overall impedance of ~2.4 Ω cm^2. The values were extracted from the Nyquist plot shown in the insert in Figure 9, by fitting with two R/Q elements which cor-

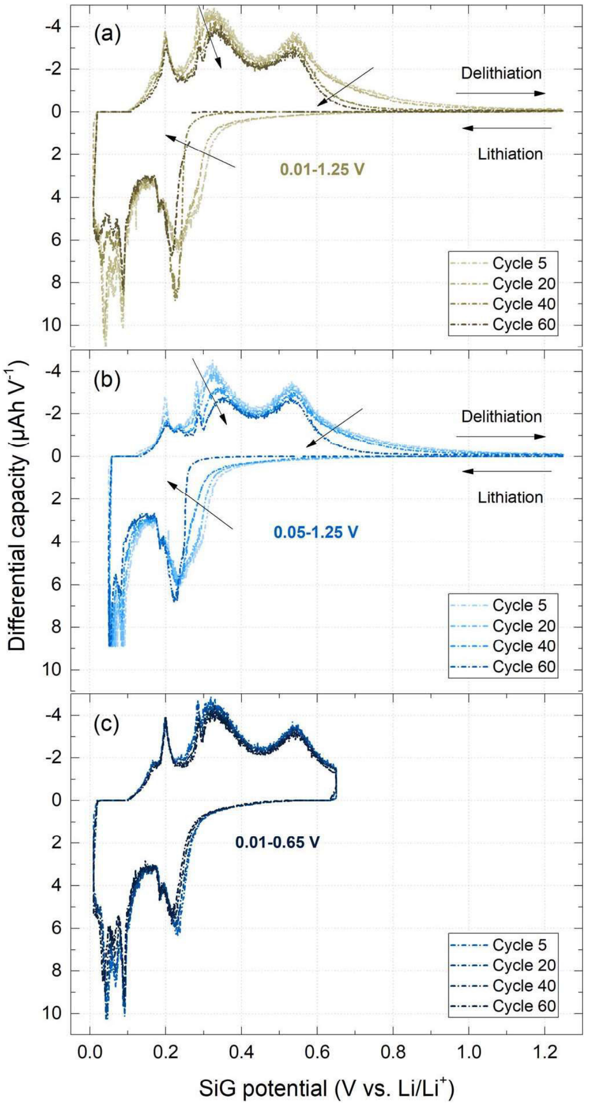

Figure 8. Differential capacity curves of selected cycles, obtained from constant current cycling (0.33 h^{-1}) of SiG//LFP Swagelok T-cells at different cutoff potentials: 0.01–1.25 V vs. Li^+/Li(brown), 0.05–1.25 V vs. Li^+/Li (blue), and 0.01–0.65 V vs. Li^+/Li (marine). These plots are derived from the measurements shown in Figure 2.

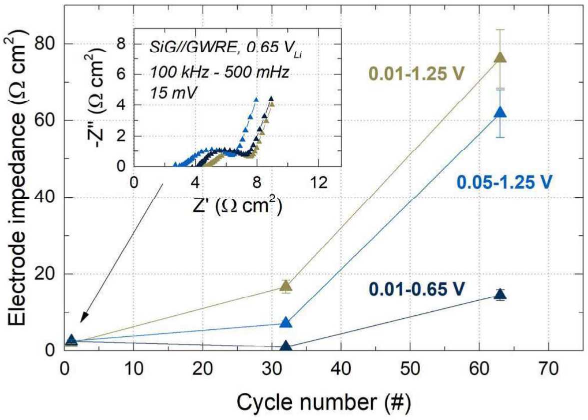

Figure 9. Electrode impedance of the silicon-graphite electrodes as a function of the cycle number, obtained at several cycles during the constant current cycling of SiG//LFP Swagelok T-cells at different cutoff potentials: 0.01–1.25 V vs. Li^+/Li(brown), 0.05–1.25 V vs. Li^+/Li (blue), and 0.01–0.65 V vs. Li^+/Li (marine). Potentiostatic impedance spectroscopy was measured at 0.65 V vs. Li^+/Li after a 30 min constant voltage step during the delithiation of the intermediate cycles at low currents (0.02 h^{-1}). Perturbation 15 mV. frequency range: 100 kHz – 500 mHz, temperature: 25°C. Insert: Nyquist spectra of the silicon-graphite electrodes during the 1st cycle after formation.

respond to the charge-transfer and the initial SEI layer on the active materials.[57] After 60 cycles, however, the two electrodes that were fully delithiated to 1.25 V vs. Li^+/Li (brown and blue symbols) show a significant impedance increase up to ~62 Ω cm^2 and ~76 Ω cm^2, respectively. At the same time, the delithiation-limited electrode reveals only a small increase up to ~14 Ω cm^2, which supports the lower polarization shown in the differential capacity analysis and agrees with a better silicon particle connectivity as indicated by the higher capacity retention shown in Figure 2b.

To examine whether there are any changes in electrode morphology which could be ascribed to the differences in the cycling stability and electrode impedance as a function of cutoff potentials, Figure 10 shows representative cross-sectional scanning electron microscopy (SEM) images of (a) an uncycled silicon-graphite electrode, as well as after 60 cycles (b) at full (de-)lithiation (0.01–1.25 V), and (c) at the delithiation-limited conditions (0.01–0.65 V). While in the uncycled electrode the well dispersed silicon nanoparticles and the flake-like graphite particles can be distinguished easily, the two cycled electrodes are largely filled by electrolyte decomposition products that penetrate a large share of the pores and additionally cover the active material particles. In agreement with the STEM-EDS analysis of cycled silicon particles shown in Figure 5, the original silicon nanoparticles can be barely identified in panels b) and c). Instead, a variety of differently sized agglomerates can be seen (see white arrow in Figure 10b), likely resulting from the expansion of the silicon particles and subsequent formation of large continuous networks of nanometer-sized silicon branches, which are extensively penetrated by SEI precipitates. Furthermore, the graphite particles are no longer predominantly aligned parallel to the current collector surface, but rather display random orientations across the electrode thickness, which in principle could originate from a substantial expansion of the electrode in a direction normal to the current collector surface, driven, e.g., by the large expansion of the silicon particles. A visual comparison of the SEM cross sections of the electrodes which were cycled under delithiation-limited conditions (Figure 10c) versus under conditions of full (de-)lithiation (Figure 10b) indicates that the SEI precipitates of the former are still more macro-porous and less agglomerated in feature size compared to the latter, which is in line with the improved cycling stability (see Figure 2b and Figure 8) of the electrodes cycled under delithiation limited conditions.

In order to describe the morphological changes between these electrodes more quantitatively, we determined the thickness of the coatings after 60 cycles between the different cutoff potentials and compared it to the uncycled electrodes, which is shown in Figure 11. Accordingly, the SiG electrodes that were fully (de-)lithiated upon cycling reveal a considerable thickness increase of +163% from ~18 to ~45 µm after 60 cycles, at which point the total irreversible capacity amounts to 1.79 mAh cm^{-2} (see Figure 3). Similarly, the lithiation-limited electrodes, which over the course of 60 cycles remains at a ~15% lower delithiation capacity (Figure 2b) and accumulates a somewhat lower irreversible capacity up to this point (1.63 mAh cm^{-2}, see Figure 3), still shows an increase of +143% to 41 µm. The by fare lowest increase of electrode thickness is observed for the delithiation-limited electrode (+98% to 34 µm), which is in line with its lowest total irreversible capacity after 60 cycles (1.24 mAh cm^{-2}, see

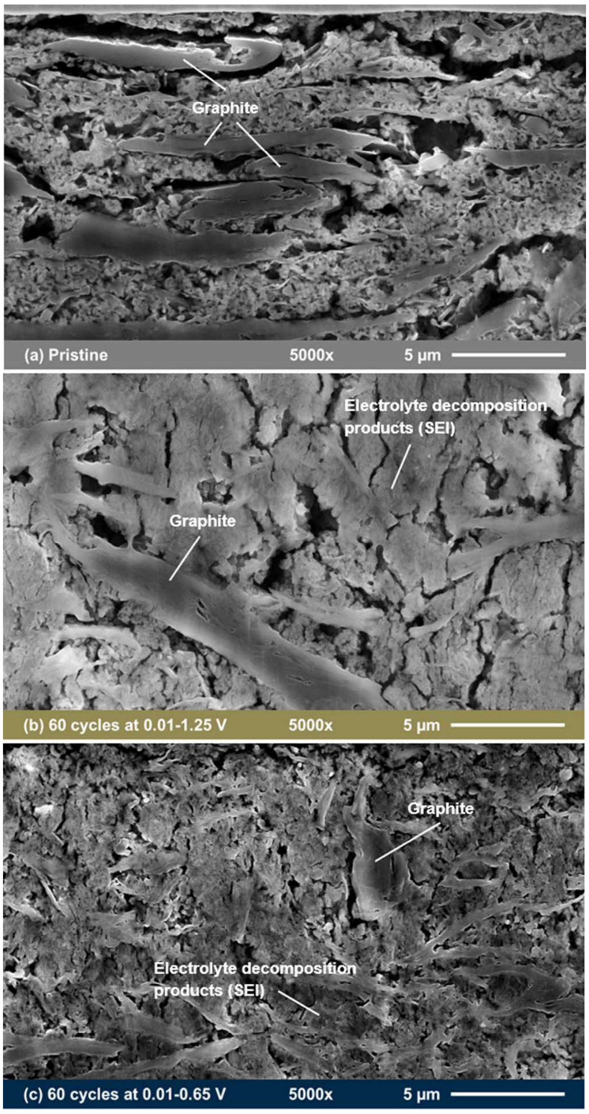

Figure 10. Scanning electron microscopy (SEM) cross-sectional images of (a) an uncycled electrode, (b) after 60 cycles between 0.01–1.25 V vs. Li^+/Li, and (c) after 60 cycles between 0.01–0.65 V vs. Li^+/Li. SEM specifications: secondary electron detector (SE), 10.0 kV electron acceleration voltage, magnification x5,000. Cross-sections were prepared with an Ar-ion beam cross-section polisher and the horizontal direction of the images is parallel to the current collector surface.

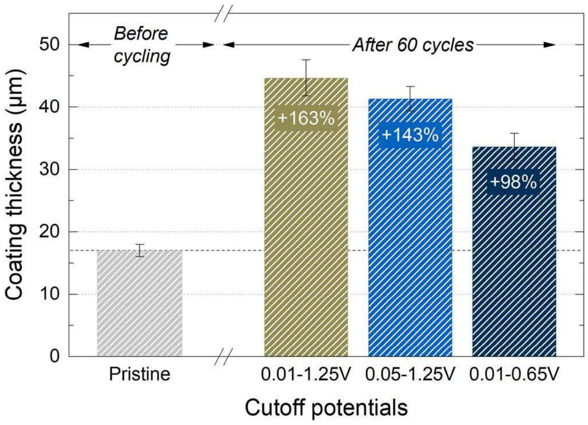

Figure 11. Silicon-graphite electrode coating thickness in pristine state and after 60 cycles, obtained from constant current cycling (0.33 h^{-1}) of SiG//LFP Swagelok T-cells at different cutoff potentials: 0.01–1.25 V vs. Li^+/Li(brown), 0.05–1.25 V vs. Li^+/Li (blue), and 0.01–0.65 V vs. Li^+/Li (marine).

Figure 3), despite the fact that the total exchanged charge+discharge capacity at this point is in between that of the electrodes which underwent lithiation-limited and deep (de-)lithiation cycling (see Figure 3). To further examine these trends, it is instructive to determine whether the amount of SEI products formed can be related directly to the gain in electrode thickness, i.e., whether the electrode thickness gain is directly proportional to the total irreversible capacity: (i) ~15 $\mu m_{\Delta t}$ $(mAh_{\Sigma Qirr}\ cm^{-2})^{-1}$ for the deep (de-)lithiation cycling, (ii) ~15 $\mu m_{\Delta t}$ $(mAh_{\Sigma Qirr}\ cm^{-2})^{-1}$ for lithiation-limited cycling, and (iii) ~13 $\mu m_{\Delta t}$ $(mAh_{\Sigma Qirr}\ cm^{-2})^{-1}$ for the delithiation-limited cycling. The approximately constant value of $\mu m_{\Delta t}$ $(mAh_{\Sigma Qirr}\ cm^{-2})^{-1}$ indicates that there is a good correlation between thickness gain and total irreversible capacity, which suggests that the electrode thickness expansion by the formation of porous silicon nanostructures has approximately the same contribution for all cycling protocols (which is consistent with Figure 5), and that the buildup of SEI does not only occur inside the silicon nanostructures but also on their outside, thus leading to the differences in thickness between the electrodes.

As a corollary, the electrode degradation can be considered as consequence of the silicon particle degradation, which additionally depends on the electrode composition, including its electrical conductivity and mechanical integrity.[39] For that reason, we observe a very similar degradation for the fully (de-)lithiated and the lithiation-limited electrodes (both with an upper cutoff potential of 1.25 V), both in terms of electrode swelling and impedance increase, which causes the immobilization of lithium within the first 60 cycles and results in a similarly poor cycling stability. In contrast, the delithiation-limited electrode reveals a considerably smaller swelling and impedance increase, which mainly results from the smaller relative surface area changes and the consequently lower total amount of electrolyte decomposition products across the electrode coating. Therefore, the beneficial effect of a limited delithiation of silicon-based electrodes on the cycling stability is considerably larger compared to a limited lithiation, at least as long as the initial reversible capacity is kept constant for both conditions (here: ~1.45 mAh cm^{-2}, ~76%). Once the capacity utilization of the lithiation-limited protocol is reduced further, e.g., to 50%, it also decreases the irreversible capacity and eventually becomes on par with the delithiation-limited protocol, however, only at the expense either of a smaller reversible capacity or alternatively an oversized electrode.

Finally, we would like to note that although the delithiation-limited cycling of silicon-based electrodes is more favorable not only in terms of the cycling stability but also because of the lower average electrode potential and the full utilization of graphite, it also requires a higher initial investment of active lithium (here: ~0.25 mAh cm^{-2}) that needs to be provided either by a larger positive electrode or suitable prelithiation of the silicon-based electrode. Therefore, a comprehensive evaluation of this cycling protocol in practical lithium-ion full cells also requires a careful consideration of the electrode balancing and the effective energy density.

Conclusions

In this study, we investigated the degradation of silicon-graphite electrodes with respect to the morphological changes of the silicon nanoparticles and the entire electrode structure in dependence on the applied cutoff potentials. Based on our recent classification of (i) the silicon particle degradation and (ii) the electrode degradation, we

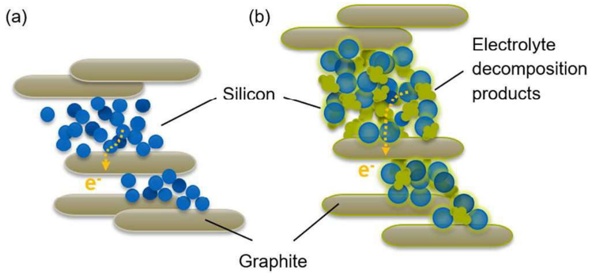

Scheme 1. Illustration of the difference in the mean electron conduction path length from individual silicon particles to the electrically conductive graphite particles in (a) an uncycled and (b) an aged silicon-graphite electrode.

summarized the underlying mechanisms as follows: Within the first 60 cycles, the silicon nanoparticles undergo severe morphological changes caused by dealloying reactions that result in (i) the expansion of initially solid silicon particles into porous networks of nanometer-sized silicon branches, (ii) a large concomitant increase of the silicon surface area which causes further SEI growth and leads to an increase of the irreversible capacity, and (iii) a significant volume expansion of the silicon particles not only reversibly over the course of a single lithiation/delithiation cycle but also permanently of up to +700% as indicated by STEM measurements. Driven by the increasing amount of electrolyte decomposition products and the volumetric changes of silicon, the SiG electrodes substantially increase in thickness during the same period, which we try to capture by Scheme 1. Both the insulating electrolyte decomposition products and the particle disconnection during electrode swelling result in a continuous impedance growth upon cycling that leads to an incomplete delithiation from electrically poorly connected silicon particles and thus to a distinct decay of the reversible capacity However, at some point the dealloying reactions reach a steady-state at which the silicon surface growth over cycling gradually diminishes.[39] At the same time, irreversible capacity losses and electrode swelling also approach a minimum after ~60 cycles, resulting in a stabilization of the reversible capacity with minor ongoing capacity fade. Although this degradation occurs in all investigated potential ranges, we conclude that the occurrence and the consequences can be delayed and reduced by limiting the delithiation of silicon to 0.65 V vs. Li^+/Li, which reduces the initially accessible capacity by ~15%, but owing to the lower capacity fade rate, the delithiation-limited cycling results in a superior absolute capacity after 40 cycles compared to the other cycling protocols. Our simplified theoretical consideration of a perfectly spherical silicon particle shows that by deliberately leaving ~15% of the reversible capacity in the particle, the relative surface area changes between end-of-lithiation and end-of-delithiation can be effectively reduced, thus mitigating the lateral stress at the particle surface and reducing SEI growth.

Acknowledgments

The German Federal Ministry for Economic Affairs and Energy is acknowledged for funding (funding number 03ET6045D). S.S and D.P acknowledge BASF SE for funding through its Scientific Network on Electrochemistry and Batteries. The authors kindly acknowledge Dr. Sonja Gürster and Dr. Susanne Cornfine (both JEOL Germany GmbH) for the preparation and measurement of the cross-sectional SEM images. Wacker Chemie AG is kindly acknowledged for providing the silicon nanoparticles.

ORCID

Morten Wetjen https://orcid.org/0000-0002-2357-1151
Sophie Solchenbach https://orcid.org/0000-0001-6517-8094
Daniel Pritzl https://orcid.org/0000-0002-9029-107X

References

1. O. Gröger, H. A. Gasteiger, and J.-P. Suchsland, *J. Electrochem. Soc.*, **162**(14), A2605 (2015).
2. K. G. Gallagher, S. Goebel, T. Greszler, M. Mathias, W. Oelerich, D. Eroglu, and V. Srinivasan, *Energy Environ. Sci.*, **7**, 1555 (2014).
3. S.-T. Myung, F. Maglia, K.-J. Park, C. S. Yoon, P. Lamp, S.-J. Kim, and Y.-K. Sun, *ACS Energy Lett.*, **2**, 196 (2017).
4. C. J. Wen and R. A. Huggins, *J. Solid State Chem.*, **37**, 271 (1981).
5. R. N. Seefurth and R. A. Sharma, *J. Electrochem. Soc.*, **124**(8), 1207 (1974).
6. R. A. Sharma and R. N. Seefurth, *J. Electrochem. Soc.*, **123**(12), 1763 (1976).
7. M. N. Obrovac and L. Christensen, *Electrochem. Solid-State Lett.*, **7**(5), A93 (2004).
8. M. N. Obrovac and V. L. Chevrier, *Chem. Rev.*, **114**, 11444 (2014).
9. J. Christensen and J. Newman, *J. Solid State Chem.*, **10**, 293 (2006).
10. Z. Du, R. A. Dunlap, and M. N. Obrovac, *J. Electrochem. Soc.*, **161**(10), A1698 (2014).
11. B. Key, R. Bhattacharyya, M. Morcrette, V. Sezne, J. Tarascon, and C. P. Grey, *J. Am. Chem. Soc.*, **131**, 9239 (2009).
12. M. T. McDowell, S. W. Lee, J. T. Harris, B. A. Korgel, C. Wang, W. D. Nix, and Y. Cui, *Nano Lett.*, **13**, 758 (2013).
13. M. T. McDowell, S. W. Lee, W. D. Nix, and Y. Cui, *Adv. Mater.*, **25**, 4966 (2013).
14. M. N. Obrovac and L. J. Krause, *J. Electrochem. Soc.*, **154**(2), A103 (2007).
15. T. Yoon, C. C. Nguyen, D. M. Seo, and B. L. Lucht, *J. Electrochem. Soc.*, **162**(12), A2325 (2015).
16. D. S. M. Iaboni and M. N. Obrovac, *J. Electrochem. Soc.*, **163**(2), A255 (2016).
17. T. Kasukabe, H. Nishihara, S. Iwamura, and T. Kyotani, *J. Power Sources*, **319**, 99 (2016).
18. D. Ma, Z. Cao, and A. Hu, *Nano-Micro Lett.*, **6**(4), 347 (2014).
19. C. K. Chan, H. Peng, G. A. O. Liu, K. Mcilwrath, X. F. Zhang, R. A. Huggins, and Y. I. Cui, *Nat. Nanotechnol.*, **3**, 31 (2008).
20. M. T. McDowell, I. Ryu, S. W. Lee, C. Wang, W. D. Nix, and Y. Cui, *Adv. Mater.*, **24**, 6034 (2012).
21. U. Kasavajjula, C. Wang, and A. J. Appleby, *J. Power Sources*, **163**, 1003 (2007).
22. F. Béguin, F. Chevallier, C. Vix-Guterl, S. Saadallah, V. Bertagna, J. N. Rouzaud, and E. Frackowiak, *Carbon N. Y.*, **43**, 2160 (2005).
23. A. N. Dey, *J. Electrochem. Soc.*, **118**(10), 1547 (1971).
24. M. M. Nicholson, *J. Electrochem. Soc.*, **121**(6), 734 (1974).
25. A. M. Wilson and J. R. Dahn, *J. Electrochem. Soc.*, **142**(2), 326 (1995).
26. B. M. L. Rao, R. W. Francis, and H. A. Christopher, *J. Electrochem. Soc.*, **124**(10), 1490 (1977).
27. T. D. Hatchard and J. R. Dahn, *J. Electrochem. Soc.*, **151**(6), A838 (2004).
28. J. Li and J. R. Dahn, *J. Electrochem. Soc*, **154**(3), A156 (2007).
29. S. Tardif, E. Pavlenko, L. Quazuguel, M. Boniface, M. Maréchal, J. S. Micha, L. Gonon, V. Mareau, G. Gebel, P. Bayle-Guillemaud, F. Rieutord, and S. Lyonnard, *ACS Nano*, **11**, 11306 (2017).
30. X. Q. Yang, J. McBreen, W. S. Yoon, M. Yoshio, H. Wang, K. Fukuda, and T. Umeno, *Electrochem. commun.*, **4**, 893 (2002).
31. B. Key, M. Morcrette, J.-M. Tarascon, and C. P. Grey, *J. Am. Chem. Soc.*, **133**, 503 (2011).
32. Y. Oumellal, N. Delpuech, D. Mazouzi, N. Dupré, J. Gaubicher, P. Moreau, P. Soudan, B. Lestriez, and D. Guyomard, *J. Mater. Chem.*, **21**, 6201 (2011).
33. N. Delpuech, N. Dupre, P. Moreau, J. S. Bridel, J. Gaubicher, B. Lestriez, and D. Guyomard, *ChemSusChem*, **9**, 841 (2016).
34. A. L. Michan, G. Divitini, A. J. Pell, M. Leskes, C. Ducati, and C. P. Grey, *J. Am. Chem. Soc.*, **138**, 7918 (2016).
35. X. H. Liu, L. Zhong, S. Huang, S. X. Mao, T. Zhu, and J. Y. Huang, *ACS Nano*, **6**(2), 1522 (2012).
36. H. Wu, G. Chan, J. W. Choi, I. Ryu, Y. Yao, M. T. McDowell, S. W. Lee, A. Jackson, Y. Yang, L. Hu, and Y. Cui, *Nat. Nanotechnol.*, **7**, 310 (2012).
37. M. Nie, D. P. Abraham, Y. Chen, A. Bose, and B. L. Lucht, *J. Phys. Chem. C*, **117**, 13403 (2013).
38. X. H. Liu and J. Y. Huang, *Energy Environ. Sci.*, **4**, 3844 (2011).
39. M. Wetjen, D. Pritzl, R. Jung, S. Solchenbach, R. Ghadimi, and H. A. Gasteiger, *J. Electrochem. Soc.*, **164**(12), A2840 (2017).
40. E. Markevich, K. Fridman, R. Sharabi, R. Elazari, G. Salitra, H. E. Gottlieb, G. Gershinsky, A. Garsuch, G. Semrau, M. A. Schmidt, and D. Aurbach, *J. Electrochem. Soc.*, **160**(10), A1824 (2013).
41. M. Klett, J. A. Gilbert, K. Z. Pupek, S. E. Trask, and D. P. Abraham, *J. Electrochem. Soc.*, **164**(1), A6095 (2017).
42. K. Kimura, T. Matsumoto, H. Nishihara, T. Kasukabe, T. Kyotani, and H. Kobayashi, *J. Electrochem. Soc.*, **164**(6), A995 (2017).
43. V. L. Chevrier, L. Liu, D. B. Le, J. Lund, B. Molla, K. Reimer, L. J. Krause, L. D. Jensen, E. Figgemeier, and K. W. Eberman, *J. Electrochem. Soc.*, **161**(5), A783 (2014).
44. S. Solchenbach, D. Pritzl, E. J. Y. Kong, J. Landesfeind, and H. A. Gasteiger, *J. Electrochem. Soc.*, **163**(10), A2265 (2016).
45. T. Mittermeier, A. Weiß, F. Hasché, G. Hübner, and H. A. Gasteiger, *J. Electrochem. Soc.*, **164**(2), F127 (2017).
46. S. Solchenbach, M. Wetjen, D. Pritzl, K. U. Schwenke, and H. A. Gasteiger, *J. Electrochem. Soc.*, **165**(3), 512 (2018).
47. S. E. Trask, K. Z. Pupek, J. A. Gilbert, M. Klett, B. J. Polzin, A. N. Jansen, and D. P. Abraham, *J. Electrochem. Soc.*, **163**(3), A345 (2016).
48. R. Jung, M. Metzger, D. Haering, S. Solchenbach, C. Marino, N. Tsiouvaras, C. Stinner, and H. A. Gasteiger, *J. Electrochem. Soc.*, **163**(8), A1705 (2016).

49. Q. Chen and K. Sieradzki, *Nat. Mater.*, **12**, 1102 (2013).
50. J. Erlebacher, M. J. Aziz, A. Karma, N. Dimitrov, and K. Sieradzki, *Nature*, **410**, 450 (2001).
51. H. W. Pickering, *Corros. Sci.*, **23**, 1107 (1983).
52. L. Y. Beaulieu, T. D. Hatchard, A. Bonakdarpour, M. D. Fleischauer, and J. R. Dahn, *J. Electrochem. Soc.*, **150**(11), A1457 (2003).
53. I. McCue, E. Benn, B. Gaskey, and J. Erlebacher, *Annu. Rev. Mater. Res.*, **46**, 263 (2016).
54. K. W. Schroder, H. Celio, L. J. Webb, and K. J. Stevenson, *J. Phys. Chem. C*, **116**, 19737 (2012).
55. K. Schroder, J. Alvarado, T. A. Yersak, J. Li, N. Dudney, L. J. Webb, Y. S. Meng, and K. J. Stevenson, *Chem. Mater.*, **27**, 5531 (2015).
56. L. J. Krause, T. Brandt, V. L. Chevrier, and L. D. Jensen, *J. Electrochem. Soc.*, **164**(9), A2277 (2017).
57. M. Wetjen, G. Hong, S. Solchenbach, D. Pritzl, and H. A. Gasteiger, (2018), in preparation.

3.2 Investigation of Silicon-Graphite Anodes by Neutron Depth Profiling

In lithium-ion batteries, a safe and reversible operation of the anode is determined by several phenomena that involve the distribution of lithium across the electrode coating. For example, during fast-charging, lithium ion concentration gradients form in the electrolyte-filled pores across the anode electrode thickness that can cause plating of highly reactive metallic lithium at the surface of the anode.[195–197] Alternatively, cross-diffusion of products from side reactions at the cathode, e.g., from transition metal dissolution,[198–200] can lead to a non-uniform growth of the solid-electrolyte-interphase (SEI) and eventually to a rapid rollover capacity loss.[201,202] In silicon-based anodes, the SEI plays a pivotal role because its ongoing growth can lead to a blocking of ion-conducting pathways and a partial electrical isolation of active material particles.[203,204] In the previous two decades, numerous techniques were applied to characterize the side reactions occurring in silicon-based anodes, *inter alia* nuclear magnetic resonance spectroscopy (NMR),[125,205–207] X-ray photoelectron spectroscopy (XPS),[43,208] and focused ion beam scanning electron microscopy (FIB-SEM),[203,204,209] which provided valuable insights into the growth and composition of the SEI. However, most of these methods either provide only local information or are not capable of quantifying the distribution of lithium across the entire electrode coating. Therefore, this PhD thesis applied for the first time neutron depth profiling (NDP) for a depth-resolved quantification of lithium concentration gradients in SiG anodes. NDP is a non-destructive technique with a very high sensitivity towards the ^{6}Li isotope,[147] allowing to determine the distribution of lithium across electrode coatings with thicknesses up to ~50 μm.[150]

In the following articles, this PhD thesis demonstrated that NDP is a powerful analytical technique to derive depth- and quantity-resolved information on lithium concentration profiles in battery anodes. It starts with presenting the first measurements at the recently installed N4DP setup at the PGAA facility at the Heinz Maier-Leibnitz Zentrum (MLZ) in Garching.[151] Based on these results, the second article provides a thorough analysis of the uniformity of the SEI growth in application-relevant SiG anodes over prolonged cycling over up to 140 cycles.[167] Finally, further applications of NDP for the characterization of battery electrodes are discussed with respect to the state-of-charge distribution in SiG anodes and the distribution of aqueous-based binders in graphite anodes.

3.2.1 Material Science Applications of Neutron Depth Profiling

This section presents the article “Materials Science Applications of Neutron Depth Profiling at the PGAA facility of Heinz Maier-Leibnitz Zentrum”.[151] At the time of the submission of this PhD thesis, this article has still been in the peer-review process for publication. The article describes the first experiments at the recently installed N4DP setup at the Prompt Gamma-ray Activation Analysis (PGAA) facility at MLZ in Garching.[210] As a first application, a lithium-containing single crystal thin film was examined to validate the uniformity of the $LiNbO_3$ phase across the film thickness of ~400 nm. Its unique nonlinear optical and refractive index properties in the visible and near-infrared light regime make $LiNbO_3$ a highly attractive material for photonic waveguide transport. However, to be suitable for optical applications, the single crystals must be highly homogeneous and free of vacancies, which is difficult to prove by means of conventional analytical techniques. In this study, NDP was used to investigate the stoichiometry of the $LiNbO_3$ thin film, thereby demonstrating a uniform lithium distribution and only insignificant fluctuations in the mass loading, which confirmed the high quality of the $LiNbO_3$ film.

As a second application, the solid-electrolyte-interphase (SEI) growth in SiG anodes with an application-relevant areal capacity of ~1.7 mAh cm^{-2} was monitored for the first time using NDP. In contrast to previous studies on the distribution of electrolyte decomposition products in silicon-based electrodes, the use of *ex situ* NDP provided depth- and quantity-resolved information about the growth and the profile of the SEI across the thickness of the electrode coatings as a function of the cycle number up to 140 cycles. In addition, the NDP spectra also allowed to calculate the increase in the mass loading and the thickness of the electrode, which was confirmed by *post mortem* cross-sectional scanning electron microscopy (SEM) images. The measurements indicated a large accumulation of lithium-containing electrolyte decomposition products within the first 60 cycles, which agrees with the electrochemical results from our previous work[102] (see Section 3.1.1). Furthermore, the NDP spectra also revealed a uniform SEI growth across the thickness of the investigated SiG anodes even upon extended cycling. This finding would not have been quantitatively accessible by conventional analytical techniques. A more detailed analysis of the underlying morphological changes of the SiG anodes is provided in a separate article[167] (see Section 3.2.2).

To deconvolute the signals from the ^{3}H and the ^{4}He particles, which overlap with increasing mass loading of the SiG anodes, a new analytical evaluation method to separate the signal contributions from the two particles was introduced and experimentally validated. The method offers an alternative to the common experimental approach of using thin separator foils, e.g., Kapton®, to block the ^{4}He particles.[163,211] However, as these separator foils also deteriorate the resolution and prohibit the detection of particles from below a certain depth, the here presented analytical approach expands the application of NDP to samples with higher mass loadings.

Author contributions

M.T., L.W., R.G., B.M., Zs.R., and R.G. designed and installed the new N4DP setup. M.T. and L.W. conducted the NDP measurements of the $LiNbO_3$. M.W. and M.T. developed the concept for the silicon-graphite study and wrote the beamtime proposals. M.W. prepared the SiG anodes and performed the electrochemical measurements. M.W. carried out the *post mortem* characterization of the SiG anodes. M.T., L.W., and M.W. conducted the NDP measurements of the SiG anodes. M.T. and L.W. developed the analytical evaluation and signal correction method. M.T. and M.W. carried out the data analysis. M.T. and M.W. wrote the manuscript. All authors discussed the data and commented on the results.

Materials Science Applications of Neutron Depth Profiling at the PGAA facility of Heinz Maier-Leibnitz Zentrum

M. Trunk[a,*], M. Wetjen[c,*], L. Werner[a], R. Gernhäuser[a], B. Märkisch[a], Zs. Révay[b], H. A. Gasteiger[c], R. Gilles[b]

[a] *Physics Department, Technical University of Munich, D-85748 Garching, Germany*
[b] *Heinz Maier-Leibnitz Zentrum, Technical University of Munich, D-85748 Garching, Germany*
[c] *Chair of Technical Electrochemistry, Chemistry Department and Catalysis Research Center, Technical University of Munich, D-85748 Garching, Germany*

Abstract

Lithium is widely used for different materials science applications as ceramics, optical waveguides or energy-storage systems. In the present work, the lithium formations within lithium niobate thin films for optical waveguide applications and in newly developed silicon-graphite electrodes for lithium-ion batteries are studied *ex situ* for the first time by the method of Neutron Depth Profiling (NDP) at the recently developed instrument N4DP at MLZ. Due to its high theoretical capacity these electrodes are promising candidates for the use in next-generation Li-ion batteries. However, accumulation of inactive lithium in these electrodes during extensive charge-discharge cycling hampers their long-term performance. NDP as non-destructive profiling technique provides information of the material where the lithium is passivated in these electrodes and thus complements other electronic and microscopic characterization measurements as coulombic efficiency measurements or SEM.

Keywords: Neutron Depth Profiling, MLZ, Lithium, Lithium-ion batteries, Thin Film

---

1. Introduction

Neutron Depth Profiling (NDP) is a well established non-destructive nuclear analytical technique to quantitatively probe the concentration profile of specific elements in different matrices [1]. When the material is irradiated by a neutron beam, certain nuclides emit charged particles after neutron capture: ^{3}He, ^{6}Li, ^{10}B, ^{14}N, ^{17}O, ^{33}S, ^{35}Cl, and ^{40}K, as well as a few radioactive nuclides: ^{7}Be, ^{22}Na and ^{59}Ni [1]. Due to the low energy of the cold neutron beam and the two-body kinematics of the nuclear reaction, the energies of these charged particles are well-defined and are ranging from 100 keV to 5 MeV. These charged particles are detected using high-energy-resolution detectors in an evacuated chamber. In this way, even traces of elements can be measured.

The charged particles lose energy almost linearly while reaching the surface. More precisely, the stopping power $S(E) = -dE/dx$ in matter depends on the particle type, its energy, as well as on the composition and the density of the matrix and can be described by the Bethe-Bloch formalism [2]. After the particles leave the surface, their residual energies $E(x)$ are related to the path length x by

$$x = \int_{E(x)}^{E_0} \frac{1}{S(E)} dE \quad , \tag{1}$$

from which a depth concentration profile of the investigated element can be determined. Due to its high sensitivity, NDP can be applied in many research areas, from brain research [3], to implantation profile tracking and energy-storage research, especially lithium-ion batteries [1, 4, 5]. In this contribution measurements on optical waveguide materials and silicon-graphite electrodes for Li-ion batteries are presented and discussed. Here, NDP provides insight into the homogeneity of the lithium distribution within these waveguides and allows the tracking of passivated lithium concentration profiles in the electrodes with respect to depth. The measurements were performed at the recently established NDP instrument at the MLZ PGAA, referred to as 'N4DP'. It accounts for the **N**eutron **4**-Dimensional Isotope-Sensitive Material **D**epth **P**rofiling, which is planned in future. A method is developed and demonstrated to isolate signals of different particles, substituting the use of particle-filter foils.

2. Theory

Assuming a straight travel path of the charged particles to the surface, the energy loss corresponds to the depth of the emission according to Eq. 1. The energy loss and energy straggling was calculated using the Stopping Range in Matter (SRIM) software [6]. Particles emitted in a depth x are detected at energies E statistically distributed around the mean residual energy $E(x)$, given by

---

[*] These authors contributed equally to this study.
Email address: `markus.trunk@ph.tum.de` (M. Trunk)

the response function [7]

$$f(E) = \frac{1}{\sqrt{2\pi}\sigma_{E(x)}} \exp\left(-\frac{1}{2}\left(\frac{E(x)-E}{\sigma_{E(x)}}\right)^2\right) \quad . \quad (2)$$

It is a normalized Gaussian distribution and has to be weighted with the number of particles from each surface layer at depth x. The measured depth profile is then given by the sum of the response functions of the individual layers. $\sigma_{E(x)}$ sums quadratically the individual uncertainties σ_i of the different statistical processes [7].

The signal broadening arises from the intrinsic noise of the detector (σ_{det}) and the electronic noise of the signal readout (σ_{el}). A particle-dependent broadening σ_{ion} accounts for statistical processes in the detector, like charge-carrier statistics of electron-hole pair production, as well as energy straggling by the dead-layer of the detector [8]. Both, energy straggling (σ_{stragg}) and multiple small-angle scattering (σ_{scatt}) depend on the charged particle and the traveled path-length through the material.

In the N4DP setup, the σ_{ion} contribution is experimentally determined from the difference between the particle signals and the equivalent noise charge (ENC) of well-defined LiF calibration targets to σ = 5 keV and 7 keV for ^{3}H (2727 keV) and ^{4}He (2055 keV), respectively. Longitudinal ($\sigma_{stragg}(x)$) and transversal ($\sigma_{scatt}(x)$) energy stragglings are sample and particle specific and were calculated for each case using SRIM.

3. Experimental

3.1. N4DP setup

At the Prompt Gamma Activation Analysis (PGAA) facility of the MLZ a cold neutron beam with a mean energy of 1.8 meV (6.7 Å) is used. It provides a collimated neutron beam with a capture-flux of 1.35×10^9cm^{-2}s^{-1}, which can be increased to 2.7×10^{10}cm^{-2}s^{-1} using focusing [9]. If not stated otherwise, the collimated beam without focusing was used. Three attenuators with different reduction factors (5.9 %, 16 % and 47 %) can be placed into the beam, in order to keep the signal rates below 10^3 s^{-1} to avoid pile-up. The N4DP setup is shown in Fig. 1. The neutron beam is collimated using apertures made of boron-containing plastic plates with a circular opening with the area of 12.6 mm^2.

The neutron beam enters and exits the target chamber through 100 μm-thick aluminum windows, while the flanges are shielded with boron-containing glass-tubes which suppress the background signal from scattered neutrons [10].

The samples are positioned at an angle of 45° with respect to the incoming neutron beam increasing the illuminated area to 17.8 mm^2. This arrangement also increases the effective target layer thickness for the neutron path with a factor of $\sqrt{2}$, while the charged particles reach the detectors on a straight path perpendicular to the sample surface. There are two surface-barrier detectors, one faces the front and the other the backside of the sample both at a distance of 53 mm. The detector signals are preamplified[1], shaped[2] and read-out by a standard VME-based digital data-acquisition system using a MADC-32 peak-sensing ADC and the software MARABOU [11].

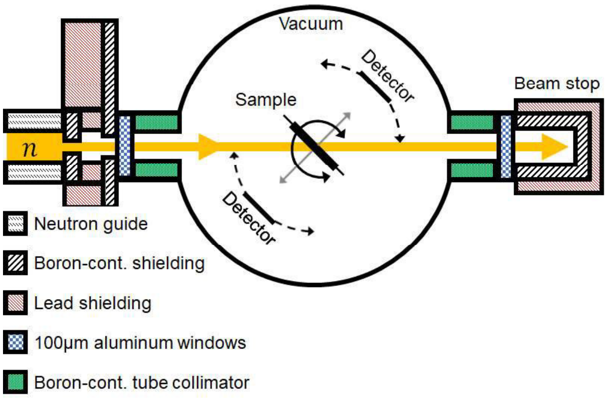

Figure 1: Schematic top-view sketch of the N4DP setup. The cold-neutron beam n (yellow arrow) is collimated with boron-containing plates. The beam enters and exits the N4DP vacuum chamber through 100-μm aluminum windows. Both, samples and detectors, can be rotated independently with respect to the axis in the center of the vacuum chamber (perpendicular to the drawing plane). The chamber was obtained from NIST.

3.2. Calibration

The thickness of targets influences the effective sample to detector distance, since only the sample's front or back surface is mounted at a fixed distance to the detectors. In the present setup, the backside was fixed. Thus, thick targets shorten the distance to the front detector (on the incoming neutron beam side), and the solid angle of the sample seen by the detector is increased leading to different correction factors $\Delta(r)$:

$$\Delta(r) = \frac{(r)^2}{(r_0)^2} \quad (3)$$

for a point-like source, where r_0=53mm is the original distance between sample and detector. This is not negligible, since a 1 mm thick sample already causes a geometry correction of Δ(1 mm)≈ 4 %. (It is to note that this correction applies for the backside detector when the sample's surface is fixed and it is negligible for thin samples which can be measured with both detectors in coincidence.)

In order to convert the signal to an absolute quantity, the SRM2137 standard reference material from the National Institute of Standards and Technology (NIST) was measured as calibration sample, and all count rates were normalized to it. It has a well-known ^{10}B implantation profile in silicon with a systematic uncertainty of 3.4 % [12].

---

[1] MMPR1 by Mesytec

[2] STM 16+ by Mesytec

Taking into account the capture cross-sections, the signal intensities of different nuclides could be converted to element concentrations.

4. Results and Discussion

4.1. Lithium Niobate Thin Films

A single crystal lithium niobate thin film on an insulating layer (LNOI) on a 2 cm×2 cm silicon wafer was provided by an industrial company[3]. Lithium niobate is used for photonic waveguide transport and resonator applications due to its unique nonlinear optical and refractive-index properties in visible and near-infrared light regimes [13]. In order to ensure the characteristics for optical applications, the LNOI single crystal must be highly homogeneous and vacancy-free which enables its use as a reference material for NDP, too. The optical thickness of the film was previously determined by the company to be 403.1 nm using non-contact optical measurements.

The nuclear reaction ^{6}Li(n,^{3}H)^{4}He was utilized to quantify the lithium distribution by NDP. The energy spectrum from the LNOI layer is shown in Fig. 2. It shows two distinct signals for the two emitted particles. They can be described as the mapping of the lithium depth distribution with the respective response function. Signals at lower energy correspond to particles produced at greater depth. Due to its higher atomic number, the stopping power for ^{4}He is stronger, therefore the ^{4}He signal of the film is broader than the ^{3}H signal. The ^{4}He signal has a better depth resolution for the same reason and both signals were confirmed to have the same integral within the measurement accuracy. In order to check the spatial homogeneity of the sample, the wafer was probed at two different spots 1 cm apart. A natural isotopic abundance of 7.59 % for ^{6}Li was assumed to derive the lithium concentration.

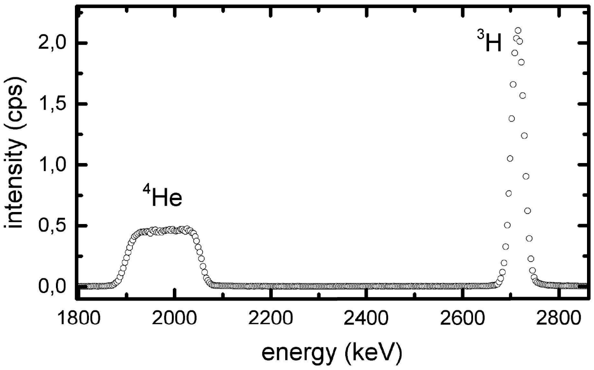

Figure 2: Energy spectrum from the NDP measurements of a 403.1 nm thick LNOI film. Signals of the charged particles from the reaction ^{6}Li(n,^{3}H)^{4}He are well separated. Due to the higher stopping power of ^{4}He particles, the signal is broadened producing greater depth resolution.

The mass loading of the thin film was then determined in two ways: the ^{4}He-signal counts were summed, which equals as average of both spots 6.90×10^{17} Li/cm^{2} with a total uncertainty of 3.6 % (composing of the systematic uncertainty of the standard and counting statistics). Taking into account the molar mass of 147.85 g/mol for LiNbO$_3$, this corresponds to a mass loading of (169±8) μg/cm^{2}. Independently, the mass loading was determined from the energy loss of the charged particles using SRIM, assuming an uniform film density with LiNbO$_3$ composition. The uncertainty of the mass loadings were based on the deviation of the modeled mean mass-loading value. The loadings were found to be (173±4) μg/cm^{2} and (172±4) μg/cm^{2} for the two spots. The difference is within the uncertainty limits which confirms the homogeneity of the film with an average mass loading of (172.5±5) μg/cm^{2} and it agrees well with the above value calculated by summing. Thus the relative uncertainty of the mass loading was found to be ~3 %.

Assuming the 403.1 nm thickness accurate, this mass load corresponds to a density of (4.28±0.17) g/cm^{3}. Our data are in agreement with typical energy loss predictions of lithium niobate proposed by the SRIM database [14]. We note that this density deviates from other reported values of 4.63 g/cm^{3} by about 7.5 % [15, 16], which could possibly stem from the thin film preparation, as well as further systematic uncertainties of the measurement or energy loss calculation uncertainties using SRIM.

The magnified ^{4}He signal is shown versus energy and depth in Fig. 3, with red and blue dots showing the profile of the two spots. The previously determined density of 4.28 g/cm^{3} was assumed. The error bars compose of the systematic uncertainty of the calibration sample together with statistical uncertainties of the measurement. The dashed, purple box represents a 403.1 nm thick layer with homogeneous lithium concentration corresponding to the com-

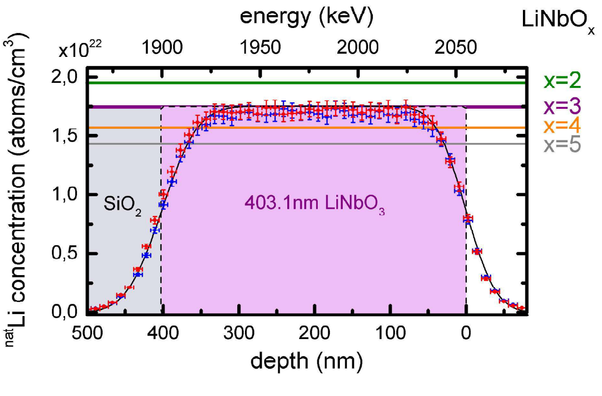

Figure 3: Magnified section of the ^{4}He signal regime. 403.1 nm thick LNOI film on SiO$_2$ insulator was probed. The thickness was determined by the NanoLN company.

---

[3] Company: NanoLN Jinan Jingzheng Electronics Co. Ltd.

position of $LiNbO_3$. The insulating SiO_2 layer at greater depths, on which the $LiNbO_3$ layer is deposited, is indicated in gray. The modeled profile based on the nominal lithium distribution is mapped by the depth-dependent response function and is drawn in black. Due to statistical energy loss in $LiNbO_3$, the resolution of detecting a single lithium layer worsens from $\sigma = 10.6\,\text{keV}$ at the upper surface to $\sigma = 13.2\,\text{keV}$ at the bottom layer. These correspond to broadenings of 28 nm and 34 nm in the 403.1 nm film, respectively. The relative uncertainty of the total thickness is equal to that of the mass loading (3 %), and that is smaller than these broadening values (~8 %). The calculated profile agrees well with the measured data, indicating a homogeneous rectangular function as the depth profile.

Due to the single-crystal properties, the elemental composition of the film is defined and can be probed using NDP. The horizontal lines in Fig. 3 depict the expected lithium concentrations for elemental $LiNbO_x$ compositions ranging from x=2 to x=5. The experimental data (red and blue dots) indicate a pure $LiNbO_3$ phase and no formations of $LiNbO_x$ with $x\neq3$ were observed. Insignificant lithium concentration fluctuations <3 % were seen, though.

In summary, we could investigate the uniformity of the layer thickness as well as the stoichiometry of a lithium niobate thin film with NDP. We observed an uniform lithium distribution across its depth within the measurement accuracy. The high quality of the LNOI film motivates further use of these films as lithium-based reference materials for NDP.

4.2. Lithium aggregation in silicon-graphite electrodes

Extensive and continuous accumulation of electrochemically inactive lithium in the solid-electrolyte-interphase (SEI) on the surface of silicon-based anodes in lithium-ion batteries currently hampers the introduction of silicon anodes envisaged for the next generation of lithium ion batteries [17, 18]. The nuclear reaction $^6Li(n,^3H)^4He$ was utilized to quantify the distribution of inactive lithium across the silicon-graphite (SiG) anodes and the concomitant mass loading increase of SiG-anode electrode coatings.

The SiG electrodes were coated onto a 20-μm thick copper current collector and they consist of porous silicon-graphite coatings with 35 wt% silicon nanoparticles (~200 nm diameter), 45 wt% graphite particles (~20 μm diameter), 10 wt% carbon fibers and 10 wt% lithium poly(acrylate) binder (LiPAA). Details on the materials and SiG electrode preparation are given in [19, 20, 21]. The nominal areal capacity of the SiG electrodes was (2.05±0.06) mAh/cm^2 based on the total mass loading of the electrode ((1.44±0.04) mg/cm^2) as well as the theoretical capacities of silicon (3579 mAh/g_{Si}) and graphite (372 mAh/g_{C}). The SiG electrodes were cycled in coin cells, containing 1 M $LiPF_6$ dissolved in a carbonate-based electrolyte (EC:EMC, 3:7 wt:wt) with 5 wt% fluoroethylene carbonate (FEC) as additive and a capacitively oversized $LiFePO_4$ cathode (3.5 mAh/cm^2) at C/2 rate (referenced to the theoretical capacity of the anode, i.e., 1C equals 2.0 mA/cm^2). Details of the electrochemistry and the cell performance of these electrodes are presented elsewhere [20, 21]. The focus here is to demonstrate the suitability of NDP to quantify the distribution of inactive lithium captured in the SEI which is building up over the course of extended charge-discharge cycling of SiG electrodes.

Hence, the electrodes were either pristine or harvested from cycled SiG/LFP coin-cells in their fully discharged state (i.e., fully delithiated to a cutoff potential of 2.0 V vs. Li/Li^+) after 1, 5, 20, 40, 60, 80, 100, 120, and 140 charge-discharge cycles, which were then examined *ex situ* by NDP. Since the thus harvested SiG electrodes do not contain any intercalated lithium, the residual lithium in the electrodes could be assigned to both the lithium from LiPAA binder and to the inactive lithium incorporated into the SEI formed by the decomposition of the FEC containing electrolyte (for the pristine SiG electrodes, the lithium only derives from the LiPAA binder).

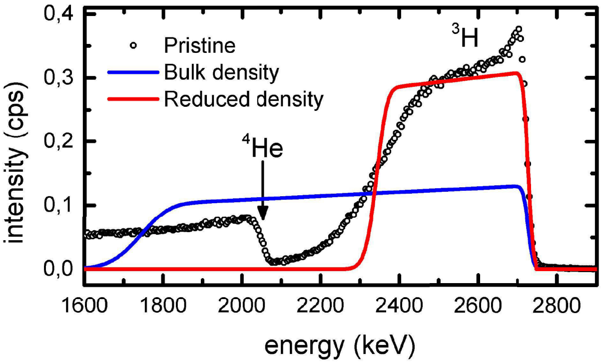

Figure 4: Energy spectrum measured from a pristine SiG anode (black circles) and two simulated ^3H signals for 18.7-μm thick SiG anodes with conceptionally zero porosity (bulk, blue line) and with a mean density corresponding to a porosity of 0.58 (red line). Around 2 MeV the onset of the ^4He signal can be observed.

The energy spectrum obtained with NDP of the pristine SiG electrode coating is shown in black circles in Fig. 4. It resembles the profile in Fig. 2 with broader signals meaning thicker layers. The sharp edge at 2.7 MeV corresponds to ^3H particles emitted by lithium at the surface of the electrode, where they did not undergo energy loss. The energy resolution statistically worsens towards lower energies, meaning greater depths. At 2 MeV, the ^4He signal rises and repeats the lithium depth profile with a higher resolution. Due to its higher stopping power, it only probes the surface of the film down to 1.3 mg/cm^2 mass loading. In contrast, the ^3H signal reveals the complete depth profile through the (18.7±0.3) μm thick SiG electrode coating. Since NDP is only sensitive to the mass loading (i.e. product of thickness and density), the SiG electrode coating thicknesses were measured using a scanning electrode microscope (SEM), which is described elsewhere [20]. The blue line in Fig. 4 depicts the expected profile of an 18.7-μm thick, isotropic and "dense" electrode coating without vacancies, i.e. zero porosity. Its density was calculated to be 2.08g/cm^3 considering the individual densities of silicon, graphite and 1.5 g/cm^3 for the LiPAA binder [20]. It lasts down until 1.7 MeV, thus the accessible range of NDP would be sufficient to probe even a dense coating and verifies that the full depth profile of the actual porous SiG electrode is accessible.

In the pristine electrode, the ^{3}H signal does not broaden as much as the signal of the simulated "dense" SiG electrode coating. This indicates that its mean density is reduced caused e.g. by a porous structure. In the next step, the mass loading was calculated from the ^{3}H signal until the inflection point of the signal at around 2.3 MeV to be (1.65±0.34) mg/cm^2, assuming a homogeneous material composition. Taking into account the coating thickness obtained from SEM, this corresponds to a packing density of (0.88±0.18) g/cm^3 which equals the bulk density reduced by a factor of 0.58±0.12. This agrees well with the electrode porosity of 0.61 measured complementary [20]. Therefore the inflection point of the signal at around 2.3 MeV represents the end of the SiG electrode at the depth of about 18.7 μm, i.e. where the Cu current collector begins, and is not caused by lithium depletion at the backside.

The calculated ^{3}H signal of a 18.7-μm thick and homogeneous lithium distribution in an isotropic matrix with a density of 0.88 g/cm^3 is shown in Fig. 4 in red. Its shape deviates from the measured depth profile (black circles) in two aspects. 1) A higher lithium concentration at the free surface (corresponding to the electrode/separator interface prior to cell disassembly) is observed in the measurements compared to the model using the mean density. This lithium enrichment could possibly be attributed to the rough and porous SiG electrode surface, which increases the effective surface compared to the layers within the electrode. However, this effect is indistinguishable from any true lithium enrichment at the surface. 2) The measured energy broadening at an energy value corresponding to the current collector position (~2.3 MeV) is more pronounced than what would be predicted by the model (red curve). The SiG electrode coating consists of a porous structure based on randomly distributed particles rather than a homogeneous material with fixed density. Charged particles penetrating entirely through the solid phase of the coated electrode materials will follow the profile shown in Fig. 4 in blue, whereas particles traveling only through pores do not lose energy. Both of these extreme cases are rather unlikely but the distribution of the randomly oriented silicon and graphite particles modifies the path-lengths of the charged particles perpendicular to the surface. Thus, the additional energy broadening depends on the silicon and graphite particle distribution in the electrodes and on the electrode porosity (i.e. for zero porosity, the distribution of path-length variation would vanish).

In Fig. 5, the spectra of SiG electrodes after different numbers of charge-discharge cycles from the pristine state (purple, lowermost) up to 140 cycles (brown, uppermost) are shown. The spectra were acquired for 1 h each, and that ensured sufficient counting statistics. Apart from the lithium signals in form of ^{4}He (below 2.0 MeV) and ^{3}H (below 2.7 MeV), further signals at 1.47 MeV from boron were also detected, which we ascribe to residues of the glass-fiber separator at the surface of the harvested cycled SiG electrodes. These impurities were neither observed for the pristine electrodes, nor when using a polymer-based separator [20]. Over the course of charge-discharge cycling, the amount of lithium in the electrode was observed to rapidly increase (particularly over the first 60 cycles), as indicated by the increasing signal intensities that gradually approach a constant value after ~100 cycles. In addition, the ^{3}H signals last to lower energies with increasing cycle number indicating an increasing mass loading of the electrode coatings. Previous works have shown that during charge-discharge cycling of SiG electrodes, fluoroethylene carbonate (FEC) molecules are reduced preferentially at the surface of the silicon because of the large volumetric changes between its charged and discharged state, resulting in a continuous growth of SEI [21, 22, 23]. The changing elemental composition of the SiG electrode caused by the SEI growth was thus considered for the energy-loss calculations of the charged particles.

The ^{3}H signals which represent the embedded lithium in the SiG electrode matrix broaden to lower energies due to the increased mass loadings of the SiG electrode coatings and overlap with the ^{4}He for which the number of charge-discharge cycles increases. The ^{4}He and ^{3}H signals arise from the same depth profile but with different resolutions, thus the shape of the ^{4}He signal can be determined from that of the ^{3}H signal and vice versa. The principle is presented on the spectrum for the electrode with 60

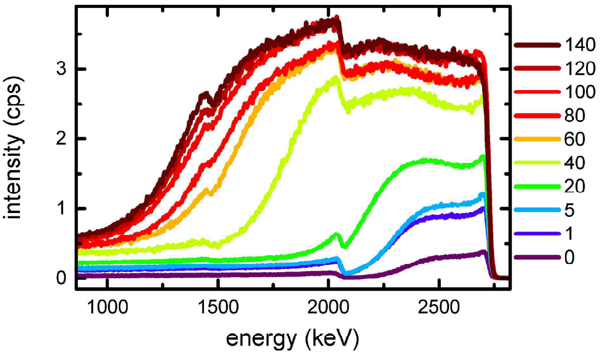

Figure 5: Spectra of SiG electrodes in pristine state (purple line) and harvested in their fully delithiated state after different numbers of charge-discharge cycles. With cycling, the amount of residual lithium in the discharged SiG electrode coatings increases, which in turn increases the measured ^{3}H and ^{4}He intensity. The SiG-electrode mass loadings increase with greater charge-discharge cycle number, which results in ^{3}H signal broadening to lower energies.

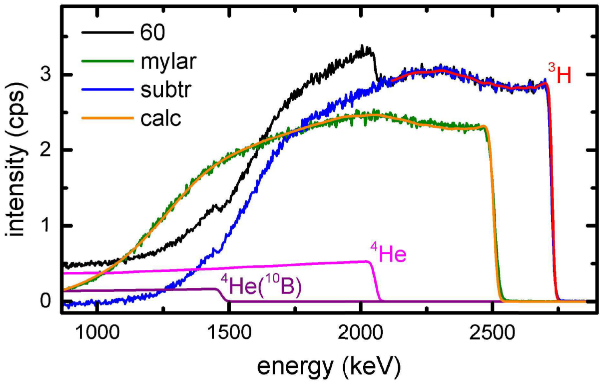

Figure 6: Spectrum of the discharged SiG electrode after 60 cycles (black). The purple (lower-most) line shows the signal of the boron contribution from the glass-fiber residuals on the electrode surface which then can be subtracted from the overall signal. From the onset of the ^{3}H signal (red line), the profile of the ^{4}He signal contribution is reconstructed, as shown by the pink line. The final ^{3}H profile from which the calculated boron and the ^{4}He contributions were subtracted is shown in blue. The green line shows the profile measured when using a 6-μm separator foil which suppresses the boron and ^{4}He signal contributions. Finally, the orange line represents the shape of the blue curve calculated through the separator foil, which agrees with the measurement (green).

cycles shown in Fig. 6. First, from the onset of the ^{3}H signal (shown in red) the depth profile is determined. Then, the profile is mapped with the response function of the ^{4}He particles yielding the expected ^{4}He distribution profile shown in pink, which then can be subtracted from the recorded spectrum shown in black. The ^{4}He signals deriving from boron (shown in purple) were also subtracted until the signal became continuous (blue spectrum).

To verify that the corrected ^{3}H signal still reflects the original profile shape prior to the subtraction of the ^{4}He and boron signals, the 60-cycles electrode was remeasured using a 6-μm Mylar foil (0.9 mg/cm^{2}) between the sample and the detector. The spectrum is shown in green, with ^{4}He particles being suppressed and the ^{3}H signal being lowered in energy and broadened. Thin foils are commonly used to suppress signals from the heavier charged particles [5]. However, they affect the measurement in the following ways: 1) Particles undergo further statistical energy loss, and so the signal resolution at the upper electrode surface worsens from 9 keV to 12 keV. 2) They can hamper the detection of charged particles from deep layers and thus restrict the maximum detection depth. 3) The additional particle scattering can affect the geometrical acceptance angle and thus also change the calibration for the absolute quantity. Thinner foils may have a smaller impact on the ^{3}H signal, yet, they also result in a less effective suppression of the ^{4}He particles. Thus the thickness and positioning of the separation foils should be adjusted to address the specific measurement. The form of the subtracted ^{3}H signal (blue) penetrating through the Mylar foil was calculated using SRIM (by taking into account the energy loss and energy broadening caused by it) and is shown as orange line. Only the height of the signals, stemming from change in detector acceptance angle, was used as free parameter. The signal shape is preserved, since it fits the spectrum measured with the Mylar foil (green line), thus confirming the validity of this calculation method.

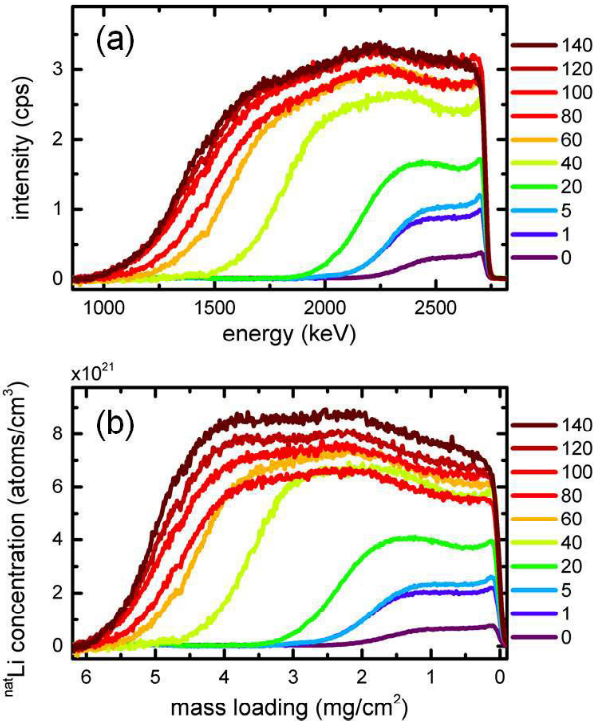

Figure 7: a) Energy spectra of separated ^{3}H signals of SiG electrode coatings in pristine state (purple line) and after different numbers of charge-discharge cycles. b) Lithium concentration is shown versus mass loading, assuming 1) natural lithium abundance and 2) constant material densities for electrodes after different cycle numbers.

The separated ^{3}H profiles are shown in Fig. 7 a. In the next step, the energy losses were determined from the inflection points of the signals at lower energies, and they were converted into mass loadings, considering the elemental composition and electrode density after the respective number of cycles. These mass loadings were calculated from the energy loss assuming the changing SiG-electrode composition. Their uncertainties were correlated to the FWHM values and they are listed together with the densities obtained from NDP (taking into account the electrode thicknesses measured via SEM) in Tab. 1.

Finally, the spectra were converted to concentration profiles, taking into account the non-linear stopping power of the ^{3}H particles and are shown in Fig 7 b versus mass loading. It depicts the amount of electrode material per area through which the charged particles traveled through towards the upper surface before they were detected. Constant electrode mass densities across the coatings were assumed, as well as a natural lithium abundance. Accordingly, the NDP profiles demonstrate that the lithium concentration increases across the entire electrode coating even upon extended charge-discharge cycling up to 140 cycles. That means the silicon particles all over the electrode are utilized even after a large number of cycles and no completely inactive layers are formed. Yet, the lithium distribution changes with depth: e.g., after 40 cycles an increase of about 15% can be seen in the lithium density from the electrode surface towards the bulk, leading to a lithium enrichment near the Cu current collector, which reaches a saturation level upon continued cycling.

The areas under the profiles display the total number of lithium stored in the full coating. The total lithium content in the electrodes (i.e., from the LiPAA binder and from passivated lithium in the SEI) was calculated by integrating the NDP spectra over the entire energy range and subsequent conversion into an irreversible capacity equivalent in units of $\mathrm{mAh/cm^2}$, assuming one electron per lithium atom. The resulting values are listed in Tab. 1.

The offset of $(0.058 \pm 0.002)\,\mathrm{mAh/cm^2}$ caused by the LiPAA binder was subtracted in order to consider only the capacity originating from the passivated lithium. The irreversible capacity rapidly increases during the first cycles and saturates above 100 cycles, which agrees well with the electrochemical capacity loss measured during cycling [21]. The measurements demonstrate the high depth- and quantity-resolution of NDP, which allows to monitor the SEI growth of silicon-graphite electrode as a function of the cycle number. A more detailed electrochemical interpretation is published in parallel by Wetjen et al. [20].

Cycle	Electrode thickness SEM (μm)	Mass loading NDP ($\mathrm{mg/cm^2}$)	Electrode density ($\mathrm{g/cm^3}$)	Irrev. Capacity NDP ($\mathrm{mAh/cm^2}$)
0	18.7 ± 0.3	1.65 ± 0.34	0.88 ± 0.18	(0.058 ± 0.002)
1	20.5 ± 1.4	1.96 ± 0.37	0.95 ± 0.18	0.138 ± 0.007
5	20.4 ± 0.9	1.90 ± 0.35	0.93 ± 0.17	0.164 ± 0.008
20	24.6 ± 0.8	2.40 ± 0.44	0.97 ± 0.16	0.380 ± 0.016
40	37.6 ± 1.2	3.63 ± 0.41	0.97 ± 0.10	1.02 ± 0.04
60	48.6 ± 0.8	4.39 ± 0.45	0.90 ± 0.09	1.42 ± 0.05
80	57.1 ± 5.0	4.64 ± 0.49	0.81 ± 0.12	1.51 ± 0.06
100	57.7 ± 1.2	4.86 ± 0.63	0.84 ± 0.12	1.75 ± 0.07
120	55.1 ± 1.7	4.93 ± 0.61	0.89 ± 0.11	1.79 ± 0.07
140	51.4 ± 1.9	4.97 ± 0.55	0.97 ± 0.12	1.83 ± 0.07

Table 1: Electrode coating thicknesses after different cycles measured by complementary SEM cross-section measurements. The obtained electrode mass loadings from energy loss calculations are shown (FWHM errors), as well as the resulting densities, which were calculated from the electrode thickness determined by SEM and the mass loadings determined by NDP. Irreversible capacities measured by the area under the ^3H profiles of the different electrodes are listed. For the pristine electrode, the equivalent capacity was calculated from the lithium atoms in the LiPAA binder.

5. Conclusion

The lithium concentration profile in a $\mathrm{LiNbO_3}$ thin film was examined by NDP. The lithium niobate was found to be homogeneous across the film and a pure $\mathrm{LiNbO_3}$ phase could be confirmed.

NDP was applied on silicon-graphite electrode coatings in order to study *ex situ* the growth of the SEI upon extended charge-discharge cycling. The spectra revealed by a higher energy loss an increase in mass loading, and that corroborates well with the thickness increase of the SiG electrode coating, which was directly observed using cross-sectional SEM measurements. Furthermore, NDP complements these mechanic images and reveals a saturation of the passivated lithium at the current collector side.

A method for the separation of different charged-particle signals was introduced and verified. This method replaces the use of separator foils, which if used, however, would restrict particle detection from greater depths. All NDP measurements were performed at the recently installed N4DP experiment at the PGAA facility of MLZ.

Acknowledgements

The authors gratefully thank Dr. Greg Downing from the National Institute of Standards and Technology (NIST) in Gaithersburg for sharing his knowledge and experience with us, especially during his visit at MLZ. Furthermore, we thank him for providing us the target chamber used for these first experiments.

We acknowledge the opportunity to use the neutron beam of the Heinz Maier-Leibnitz Zentrum at the PGAA facility.

We thank the NanoLN company for providing us with the lithium niobate thin films and for their permission of publication.

Wacker Chemie AG is kindly acknowledged for providing the silicon nanoparticles used in the Li-ion batteries.

The authors acknowledge the financial support by the Federal Ministry of Education and Research of Germany (project number 05K16WO1).

Data availability

The raw/processed data required to reproduce these findings cannot be shared at this time as the data also forms part of an ongoing study.

References

[1] R. Downing, G. Lamaze, J. Langland, S. Hwang, Neutron depth profiling: overview and description of NIST facilities, Journal of Research of the National Institute of Standards and Technology 98 (1) (1993) 109. `doi:10.6028/jres.098.008`.

[2] H. Bethe, Zur theorie des durchgangs schneller korpuskularstrahlen durch materie, Annalen der Physik 397 (3) (1930) 325–400. `doi:10.1002/andp.19303970303`.

[3] J. Lichtinger, R. Gernhäuser, A. Bauer, M. Bendel, L. Canella, M. Graw, R. Krücken, P. Kudejova, E. Mützel, S. Ring, et al., Position sensitive measurement of lithium traces in brain tissue with neutrons, Medical physics 40 (2). `doi:10.1118/1.4774053`.

[4] E. Portenkirchner, G. Neri, J. Lichtinger, J. Brumbarov, C. Rüdiger, R. Gernhäuser, J. Kunze-Liebhäuser, Tracking areal lithium densities from neutron activation–quantitative li determination in self-organized TiO2 nanotube anode materials for li-ion batteries, Physical Chemistry Chemical Physics 19 (12) (2017) 8602–8611. `doi:10.1039/C7CP00180K`.

[5] Y. He, R. G. Downing, H. Wang, 3D mapping of lithium in battery electrodes using neutron activation, Journal of Power Sources 287 (2015) 226–230. `doi:10.1016/j.jpowsour.2015.03.176`.

[6] J. F. Ziegler, M. D. Ziegler, J. P. Biersack, SRIM–the stopping and range of ions in matter (2010), Nuclear Instruments and Methods in Physics Research Section B: Beam Interactions with Materials and Atoms 268 (11) (2010) 1818–1823. `doi:10.1016/j.nimb.2010.02.091`.

[7] J. T. Maki, R. F. Fleming, D. H. Vincent, Deconvolution of neutron depth profiling spectra, Nuclear Instruments and Methods in Physics Research Section B: Beam Interactions with Materials and Atoms 17 (2) (1986) 147–155. `doi:10.1016/0168-583X(86)90077-7`.

[8] E. Steinbauer, P. Bauer, M. Geretschläger, G. Bortels, J. Biersack, P. Burger, Energy resolution of silicon detectors: approaching the physical limit, Nuclear Instruments and Methods in Physics Research Section B: Beam Interactions with Materials and Atoms 85 (1-4) (1994) 642–649.

[9] Z. Révay, P. Kudějová, K. Kleszcz, S. Söllradl, C. Genreith, In-beam activation analysis facility at MLZ, garching, Nucl. Instr. and Meth. A 799 (2015) 114–123. `doi:10.1016/j.nima.2015.07.063`.

[10] L. Werner, M. Trunk, R. Gernhäuser, R. Gilles, B. Märkisch, Z. Révay, The new neutron depth profiling instrument (n4dp) at the heinz maier-leibnitz zentrum (mlz), to be published.

[11] R. Lutter, O. Schaile, K. Schoeffel, K.Steinberger, C. Broude, MARaBOU: Mbs and root based online offline utility (2017). URL `http://www.bl.physik.tu-muenchen.de/marabou/htmldoc/`

[12] NIST, Certificate of analysis standard reference material 2137 (2010). URL `https://www-s.nist.gov/srmors/certificates/2137.pdf`

[13] C. Wang, M. J. Burek, Z. Lin, H. A. Atikian, V. Venkataraman, I.-C. Huang, P. Stark, M. Lončar, Integrated high quality factor lithium niobate microdisk resonators, Optics express 22 (25) (2014) 30924–30933. `doi:10.1364/OE.22.030924`.

[14] I. Paulini, W. Heiland, A. Arnau, E. Zarate, P. Bauer, Stopping cross section of protons and deuterons in lithiumniobate near the stopping power maximum, Nuclear Instruments and Methods in Physics Research Section B: Beam Interactions with Materials and Atoms 118 (1-4) (1996) 39–42.

[15] J. F. Ziegler, The stopping and range in compounds (2017). URL `http://www.srim.org/SRIM/Compounds.htm`

[16] R. Weis, T. Gaylord, Lithium niobate: summary of physical properties and crystal structure, Applied Physics A: Materials Science & Processing 37 (4) (1985) 191–203. `doi:10.1007/BF00614817`.

[17] D. Andre, S.-J. Kim, P. Lamp, S. F. Lux, F. Maglia, O. Paschos, B. Stiaszny, Future generations of cathode materials: An automotive industry perspective, Journal of Materials Chemistry A 3 (13) (2015) 6709–6732.

[18] K. G. Gallagher, S. Goebel, T. Greszler, M. Mathias, W. Oelerich, D. Eroglu, V. Srinivasan, Quantifying the promise of lithium–air batteries for electric vehicles, Energy & Environmental Science 7 (5) (2014) 1555–1563.

[19] M. Wetjen, S. Solchenbach, D. Pritzl, J. Hou, V. Tileli, H. A. Gasteiger, Morphological changes of silicon nanoparticles and the influence of cutoff potentials in silicon-graphite electrodes, submitted.

[20] M. Wetjen, M. Trunk, L. Werner, R. Gernhäuser, B. Märkisch, Z. Révay, R. Gilles, H. A. Gasteiger, Quantifying the distribution of electrolyte decomposition products (SEI) in silicon-graphite electrodes by neutron depth profiling, to be published.

[21] M. Wetjen, D. Pritzl, R. Jung, S. Solchenbach, R. Ghadimi, H. A. Gasteiger, Differentiating the degradation phenomena in silicon-graphite electrodes for lithium-ion batteries, Journal of The Electrochemical Society 164 (12) (2017) A2840–A2852. `doi:10.1149/2.1921712jes`.

[22] R. Petibon, V. Chevrier, C. Aiken, D. Hall, S. Hyatt, R. Shunmugasundaram, J. Dahn, Studies of the capacity fade mechanisms of LiCoO2/Si-alloy: graphite cells, Journal of The Electrochemical Society 163 (7) (2016) A1146–A1156.

[23] R. Jung, M. Metzger, D. Haering, S. Solchenbach, C. Marino, N. Tsiouvaras, C. Stinner, H. A. Gasteiger, Consumption of fluoroethylene carbonate (fec) on Si-C composite electrodes for li-ion batteries, Journal of The Electrochemical Society 163 (8) (2016) A1705–A1716. `doi:10.1149/2.0951608jes`.

3.2.2 Depth-Distribution of the SEI in Silicon-Graphite Electrodes

This section presents the article "Quantifying the Distribution of Electrolyte Decomposition Products in Silicon-Graphite Electrodes by Neutron Depth Profiling",[167] which was published in August 2018 in the *Journal of The Electrochemical Society*. It is an open access article distributed under the terms of the Creative Commons Attribution 4.0 License. The study was accepted for presentation at the AiMES Meeting of The Electrochemical Society in Cancun, Mexico (Sep 30 – Oct 4, 2018), Abstr. #427. The permanent web-link to the article is http://dx.doi.org/10.1149/2.1341810jes.

This article is a follow-up study on our previous NDP measurements reported in Trunk *et al.*[151] (see Section 3.2.1). While the first article focused on the introduction of the method, now we analyze and validate the NDP spectra in detail with respect to the electrochemical performance and the morphological changes of the SiG anodes. The lithium density profiles obtained from NDP were used (i) to quantify the amount of lithium-containing electrolyte decomposition products in the SiG anodes (35 wt% silicon, areal capacity ~1.7 mAh cm^{-2}), (ii) to monitor their depth distribution across the electrode coatings, and (iii) to determine the active material utilization across the electrodes after 140 charge-discharge cycles. In addition, the mass loading and the thickness increase of the electrodes were determined *post mortem* and used to validate the values calculated from the NDP measurements. Finally, high-resolution cross-sectional SEM images were taken to complement the interpretation of the morphological changes of the SiG anodes.

This study generated three important insights into the SEI growth in SiG anodes: (i) The aging of the SiG anodes is mainly determined within the first 60 cycles. During this period, the silicon nanoparticles undergo dealloying reactions which enhance side-reactions occurring at the silicon/electrolyte interface and result in the accumulation of large amounts of electrolyte decomposition products in the electrode. This accumulation coincides with a severe increase of the electrode mass loading and a swelling of the electrode coating. In contrast to reports in the literature, this study revealed that the porosity of the investigated SiG anodes shows only a minor decrease, which was rationalized by high-resolution SEM images that showed a micro-porosity in the agglomerates consisting of silicon and electrolyte decomposition products. (ii) Further, this study indicated an almost uniform distribution of the lithium-containing electrolyte decomposition products across the thickness of the SiG anodes, whose profile shape remained almost unchanged upon cycling. As a corollary, the silicon active material was uniformly utilized at different electrode depths even upon prolonged cycling, which excludes the presence of a dominating transport-limiting process across the thickness of the investigated SiG anodes. Instead, the findings suggested that the capacity decay of the SiG anodes stems from the loss of interparticle contact pressure and increases with an increasing mean path length between individual silicon particles and adjacent electrically well-conducting graphite particles, which occurs statistically in a homogeneous electrode coating. (iii) Finally, this study reinforced the need for an integral design of silicon-based electrodes, considering both (a) a suppression of the degradation of the silicon particles and subsequent side reactions at the silicon/electrolyte interface, and (b) a hierarchical electrode structure that maintains a sufficient electron and lithium ion transport not only across the thickness of the electrode coating but also between the individual silicon particles.

To analyze the morphology of the SiG anodes, this PhD thesis expanded the collaboration with JEOL (Germany) GmbH in Freising. Argon-polished cross-sections were prepared from the electrodes and measured using a high-resolution SEM instrument.

Author contributions

M.W. and M.T. developed the concept for the silicon-graphite study and wrote the beamtime proposals. M.T., L.W., and M.W. conducted the NDP measurements of the SiG anodes. M.W. prepared the SiG anodes and performed the electrochemical measurements. M.W. carried out the *post mortem* characterization of the SiG anodes. Tristan Harzer (JEOL) and M.W. prepared the samples for the cross-sectional SEM images and performed the microscopy measurements. M.W. and M.T. carried out the data analysis. M.W., M.T., and H.G. wrote the manuscript. All authors discussed the data and commented on the results.

Quantifying the Distribution of Electrolyte Decomposition Products in Silicon-Graphite Electrodes by Neutron Depth Profiling

**Morten Wetjen,[1,=,*,z] Markus Trunk,[2,=] Lukas Werner,[2] Roman Gernhäuser,[3]
Bastian Märkisch,[2] Zsolt Révay,[4] Ralph Gilles,[4] and Hubert A. Gasteiger[1,**]**

[1] *Chair of Technical Electrochemistry, Department of Chemistry and Catalysis Research Center, Technische Universität München, D-85748 Garching, Germany*
[2] *Professorship of Fundamental Particle Physics at Low Energies, Technische Universität München, D-85748 Garching, Germany*
[3] *Physics Department, Technische Universität München, D-85748 Garching, Germany*
[4] *Heinz Maier-Leibnitz Zentrum (MLZ), Technische Universität München, D-85748 Garching, Germany*

Silicon-based anodes for lithium-ion batteries exhibit severe volumetric changes of the active material particles during (de-)lithiation, resulting in continuously occurring side reactions at the silicon/electrolyte interface over extended charge/discharge cycling. The thus formed and accumulating electrolyte decomposition products lead to a growth of the solid-electrolyte-interphase (SEI) on the silicon particles. This results not only in an ongoing loss of electrolyte but also in a significant swelling and impedance increase of silicon-based anodes which significantly compromises their cycle-life. In the present study, neutron depth profiling (NDP) is used post mortem as a non-destructive, highly lithium-sensitive technique to (i) quantify the amount of lithium-containing electrolyte decomposition products in silicon-graphite (SiG) electrodes (35 wt% silicon, areal capacity ~1.7 mAh cm^{-2}), (ii) monitor their distribution across the SiG electrode thickness, and (iii) determine the active material utilization across the electrode over 140 cycles. Hence, SiG negative electrodes are aged and characterized by means of galvanostatic cycling in SiG//LiFePO$_4$ pseudo-full cells, using a capacitively oversized positive electrode and an electrolyte mixture consisting of 1 M LiPF$_6$ in EC:EMC with 5 wt% FEC. High-resolution cross-sectional SEM images and post-mortem characterization of the SiG electrodes with respect to changes in electrode mass thickness complement the analysis.

Manuscript submitted June 18, 2018; revised manuscript received July 23, 2018. Published August 1, 2018. This article is a version of Paper 427 from the Cancun, Mexico, Meeting of the Society, September 30–October 4, 2018.

Silicon is among the most promising anode materials for future lithium-ion batteries to achieve cell-level energy densities above 300 Wh kg^{-1}.[1–3] Yet, its commercialization is still hampered by the large morphological changes of the silicon particles upon repeated (de-)lithiation.[4,5] These changes result in (i) a continuous consumption of electrolyte with a concomitant accumulation of electrolyte decomposition products in porous silicon-based electrodes,[6–8] and (ii) a significant swelling of the entire electrode structure, leading to electrode polarization and a loss of reversible capacity.[9,10] Numerous research groups investigated the degradation of silicon-based electrodes, e.g., using in-situ X-ray diffraction (XRD),[11,12] nuclear magnetic resonance spectroscopy (NMR),[13–16] X-ray photoelectron spectroscopy (XPS),[17,18] and focused ion beam scanning electron microscopy (FIB-SEM).[19–21] These measurements provided valuable insights into the side-reactions of the silicon particles as well as the formation of electrolyte decomposition products which lead to a growth of the solid-electrolyte-interphase (SEI).[22] Nonetheless, most of these methods do not provide information on the extent of electrolyte decomposition products across the thickness of the electrode which would allow further insight into the degradation mechanism of silicon-based electrodes. This can be provided by neutron depth profiling (NDP), a non-destructive and highly lithium-sensitive technique which enables a depth-resolved quantification of the lithium concentration across the electrode thickness of up to ~50 μm.[23–25] In 2009, Whitney et al.[26,27] used NDP for the first time to determine the SEI growth on graphite anodes at different storage conditions. Later, Co and co-workers[28,29] applied NDP to measure the lithium distribution in a tin-based thin-film alloy electrode (12.5 μm thickness), using an in-situ setup that consisted of a lithium metal anode and an electrolyte mixture of 1 M LiBF$_4$ in EC:DMC. More recently, Zhang et al.[30] used a similar in-situ setup to investigate the influence of the electrode morphology and the C-rate on the lithium gradients across a 12.5 μm thick LiFePO$_4$ cathode coating.

Here, the degradation of silicon-graphite (SiG) electrodes (35 wt% silicon) with an areal capacity of ~1.7 mAh cm^{-2} is studied post mortem by ex-situ NDP to (i) quantify the amount of lithium-containing electrolyte decomposition products, (ii) monitor their distribution across the electrode coatings, and (iii) determine the active material utilization across the SiG electrodes over the course of 140 charge/discharge cycles. SiG electrodes were aged and characterized by means of galvanostatic cycling in SiG//LiFePO$_4$ pseudo-full cells, using a capacitively oversized positive electrode and an electrolyte mixture consisting of 1 M LiPF$_6$ in EC:EMC with 5 wt% fluoroethylene carbonate (FEC).[7] Over the course of charge/discharge cycling, side reactions occurring at the silicon/electrolyte interface result in the continuous preferential consumption of FEC which is accompanied by the accumulation of lithium-containing electrolyte decomposition products,[6,8] consisting of LiF, Li$_2$CO$_3$, Li$_2$O, and lithium alkoxides.[18,31,32] After different numbers of cycles, fully delithiated SiG electrodes were harvested from the cells and characterized by ex-situ NDP. In this case, residual lithium in the electrodes mainly originates from the lithium poly(acrylate) (LiPAA) binder and from the lithium-containing electrolyte decomposition products, independent of their chemical state.[7] The NDP analysis method was recently implemented and validated using pristine and aged SiG electrodes by Trunk et al.[33] at the newly constructed neutron depth profiling instrument (N4DP) at the Prompt Gamma-ray Activation Analysis (PGAA) facility of the Heinz Maier-Leibnitz Zentrum (MLZ) in Garching, Germany. In the present work, these NDP results are analyzed by taking into account the electrochemical performance and the morphological changes of the SiG electrodes. Hence, the mass loading and the thickness increase of the electrodes were determined post-mortem and compared to the NDP measurements. In addition, high-resolution cross-sectional SEM images were taken to further elucidate the morphological changes of the SiG electrodes. The study concludes with a detailed discussion of the degradation phenomena of SiG electrodes and the influence of the electrolyte decomposition products on cycling performance.

[=] These authors contributed equally to this work.
[*] Electrochemical Society Student Member.
[**] Electrochemical Society Fellow.
[z] E-mail: morten.wetjen@tum.de

Experimental

Electrode preparation.—Silicon-graphite (SiG) electrodes, consisting of 35 wt% silicon nanoparticles (~200 nm, Wacker Chemie AG, Germany), 45 wt% graphite (~20 μm, T311, SGL Carbon, Germany), 10 wt% vapor grown carbon fibers (VCGF-H, Showa Denko, Japan), and 10 wt% lithium poly(acrylate) binder (LiPAA) were prepared by an aqueous ink procedure, which is described in detail in our previous publication.[7] The LiPAA was prepared by diluting a 35 wt% poly(acrylic acid) solution (PAA, MW = 250,000 g mol^{-1}, Sigma-Aldrich, Germany) with deionized water and neutralizing it with lithium hydroxide (LiOH, Sigma-Aldrich, Germany) to a pH-value of ~8.[34] The mass loading of the electrodes was adjusted to 1.44 ± 0.04 $mg_{electrode}$ cm^{-2}, which corresponds to a theoretical areal capacity of 2.05 ± 0.06 mAh cm^{-2} (referenced to theoretical specific capacities of 3579 mAh $g^{-1}{}_{Si}$ and 372 mAh $g^{-1}{}_{C}$). During the first cycle at a C-rate of 0.1 h^{-1}, the SiG electrodes delivered a delithiation capacity of 1.69 ± 0.05 mAh cm^{-2}.

Test cell assembly.—Electrochemical characterization and aging of the SiG electrodes was conducted in coin-cells (Hohsen, Japan), by sandwiching two 250 μm thick glass fiber separators (VWR, USA) between a SiG anode (~1.7 mAh cm^{-2} at 0.1 h^{-1}, 14 mm diameter) and a capacitively oversized $LiFePO_4$ (LFP) cathode (~3.5 mAh cm^{-2} at 0.1 h^{-1}, 15 mm diameter, Customcells, Germany). As electrolyte, 100 μL of 1 M $LiPF_6$ in ethylene carbonate:ethyl methyl carbonate (EC:EMC, 30:70 wt%; also referred to as LP57), with 5 wt% fluoroethylene carbonate (FEC) was used.

Battery cycling.—The electrode polarization and cycling performance of the SiG electrodes was investigated by means of galvanostatic cycling of SiG//LFP coin-cells. As in our previous publication,[7] the cell voltage was controlled between the SiG and the LFP electrode, whereby the SiG potential was calculated from the SiG//LFP cell voltage, referring to a stable LFP electrode potential of 3.45 V vs. Li^+/Li. Initially, two formation cycles at a C-rate of 0.1 h^{-1} (~0.2 mA cm^{-2}) were performed between cell voltages of 3.44 and 2.2 V, corresponding to a SiG potential of ~0.01 and ~1.25 V vs. Li^+/Li. For consecutive cycling, the C-rate was increased to 0.5 h^{-1} (~1.0 mA cm^{-2}), whereby the C-rate is always referenced to the theoretical capacity of the electrodes, i.e., 1.0 h^{-1} equals ~2.0 mA cm^{-2}. During the last cycle of each procedure and prior to disassembly of the coin-cells, the SiG electrodes were again lithiated to 0.01 V vs. Li^+/Li at 0.5 h^{-1} and then delithiated to ~2.0 V vs. Li^+/Li at a very low C-rate of 0.02 h^{-1} (~0.04 mA cm^{-2}) in order to extract any residual active lithium from the SiG electrodes. All measurements were performed in a climate chamber (Binder, Germany) at 25°C, using a multi-channel potentiostat VMP3 (BioLogic, France).

Test cell disassembly.—Following the charge/discharge cycling and the slow delithiation in the last cycle, the SiG//LFP coin-cells were disassembled in their fully discharged state in an argon-filled glovebox (H_2O and O_2 concentration < 0.1 ppm; MBraun). The SiG electrodes were harvested from the cells and carefully rinsed with 50 μL of dimethyl carbonate (DMC) to remove any residues of the liquid electrolyte. Thus, remaining lithium in these electrodes mainly originated from the LiPAA binder and the lithium-containing electrolyte decomposition products, which can be ascribed to the irreversible capacity loss. Finally, the SiG electrodes were weighed and then sealed separately in pouch-foils before being opened again just before the transfer into the NDP vacuum chamber, whereby electrodes were exposed to ambient atmosphere only for a few minutes prior to NDP measurements.

Neutron depth profiling.—The NDP measurements of the SiG electrodes were conducted ex-situ using the N4DP setup at the PGAA facility of the MLZ in Garching, Germany.[33] The beamline provides a collimated cold neutron beam with an area of 12.6 mm^2 and a flux of 1.35×10^9 cm^{-2} s^{-1} which can be reduced by different attenuators (5.9%, 16%, and 47%) to mitigate pile-up effects at count rates above 10^3 s^{-1}.[35] The 14 mm diameter SiG electrodes were placed in the NDP vacuum chamber with the coating facing the incoming beam at an angle of 45°. The N4DP setup at the PGAA facility is described in more detail by Trunk et al.[33]

High-resolution cross-sectional SEM images.—The morphology of the SiG electrodes in their pristine state and after different numbers of cycles was investigated by high-resolution cross-sectional scanning electron microscopy (SEM). First, electrode cross-sections were prepared by argon ion beam polishing, using a JEOL Cross Section Polisher IB-19530CP (JEOL, Japan). Afterwards, SEM images were taken using a JEOL JSM-IT300HR (JEOL, Japan) with a field-emission electron source and a secondary electron detector. Both the preparation of the electrode cross-sections and the measurements of the cross-sectional SEM images were conducted by JEOL (Germany) GmbH in Freising, Germany.

Quantification of electrode thickness changes.—The changes in the SiG electrode thickness were measured by cross-sectional scanning electron microscopy (SEM) with the aid of a JEOL JCM-6000 NeoScope (JEOL, Japan), using a procedure described in detail elsewhere.[10] After the NDP measurements, the SiG electrodes were cut across the center of the electrodes. One half was polished by the argon ion beam and measured by high-resolution SEM as described above. The other half was embedded into a resin solution; after hardening of the resin, the samples were polished stepwise using different polishing papers down to 1 μm size to obtain a mirror finished cross-section of the electrodes. Each electrode was evaluated at fifteen positions along the entire cross-section to obtain an average thickness and its standard deviation.

Results and Discussion

Charge/discharge cycling and post-mortem characterization of SiG electrodes.—Figure 1a shows the areal delithiation capacity (brown symbols) and the total irreversible capacity (marine symbols) of the SiG electrode as a function of the cycle number, exemplarily shown for the cell cycled over 120 cycles (the total irreversible capacity after 120 cycles from two cells is reproducible within ±5%; see blue symbols at cycle 120 in Figure 4a). After two formation cycles at a C-rate of 0.1 h^{-1} where ~83% of the theoretical capacity of 2.05 mAh cm^{-2} are obtained, the initially delivered delithiation capacity at the subsequently higher C-rate of 0.5 h^{-1} amounts to ~1.4 mAh cm^{-2} (~68% of the theoretical capacity). The cycling stability of the SiG electrodes is characterized by a distinct capacity decay to ~0.9 mAh cm^{-2} within the first 60 cycles (~65% capacity retention, referenced to the 3rd cycle at 0.5 h^{-1}), perhaps more evident by the steep increase in the total irreversible capacity within the first 60 cycles (marine symbols in Figure 1a), which can be used as a measure for the accumulation of electrolyte decomposition products in the porous electrode. This behavior is also reflected by the differential capacity curves shown in Figure 1b which, within the first 60 cycles, reveal a distinct capacity fade at low degrees of lithiation, i.e., at potentials above 0.2 V vs. Li^+/Li during lithiation (see lower left segment in Figure 1b),[7] a characteristic feature observed if the delithiation during the preceding lithiation cycles is incomplete.[36] In our earlier work,[10] it was demonstrated that the increase in the electrode impedance and the loss of interparticle electrical contact is caused by the drastic expansion of the surface area of the silicon particles over the initial charge/discharge cycles, accompanied by an initially high formation rate of electrolyte decomposition products and high SEI growth as well as by a significant swelling of the SiG electrode. It is to note that although FEC is continuously reduced at the silicon/electrolyte interface, the total amount in the electrolyte solution is large enough to prevent a complete depletion and subsequent reductive decomposition of EC within the here investigated 140 cycles.[6,8]

Figure 2 shows (a) the mass loading and (b) the coating thickness of the SiG electrodes which were determined post-mortem after

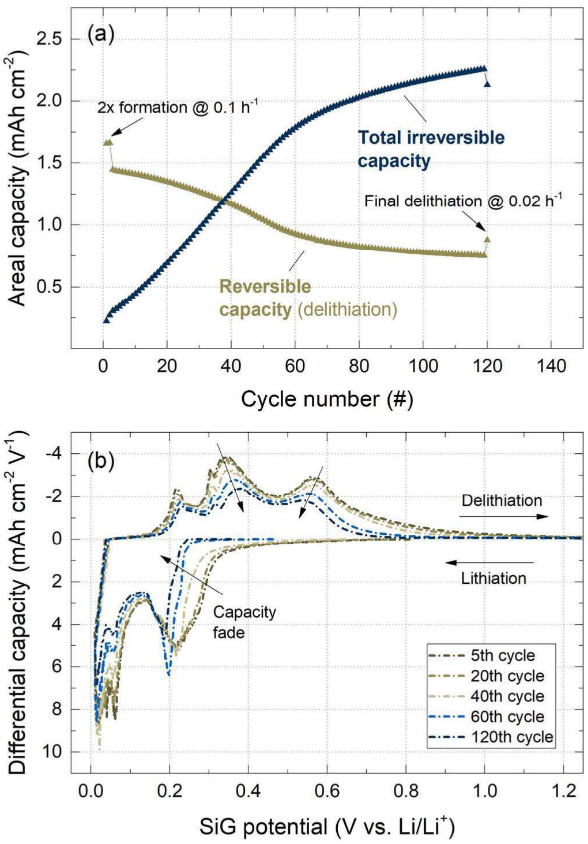

Figure 1. (a) Areal delithiation capacity (brown symbols) and total accumulated irreversible capacity (marine symbols) of a SiG electrode (~1.7 mAh cm^{-2} at 0.1 h^{-1}) cycled between SiG potentials of 0.01 and 1.25 V vs. Li$^+$/Li, obtained from galvanostatic cycling of SiG//LFP coin-cells at a C-rate of 0.5 h^{-1} with a capacitively oversized LFP electrode (~3.5 mAh cm^{-2} at 0.1 h^{-1}) in LP57 with 5 wt% FEC. (b) Differential capacity curves of selected cycles at 0.5 h^{-1} plotted vs. the SiG electrode potential (obtained by considering a stable LFP electrode potential of 3.45 V vs. Li$^+$/Li).

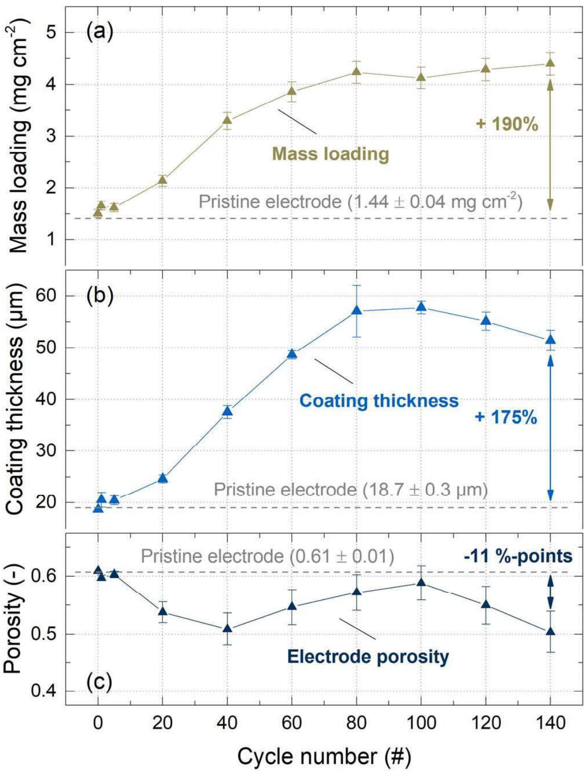

Figure 2. (a) Mass loading and (b) electrode thickness of the SiG electrodes measured post-mortem after different numbers of cycles, and (c) electrode porosity calculated from mass loading and electrode thickness. The error bars represent the following: (a) the standard error of ± 5% based on a larger number of electrodes from previous experiments, (b) the standard deviation of 15 repeat measurements along the cross-section of a single electrode, and (c) error propagation including the variance in the estimated density of the electrolyte decomposition products of ± 0.2 g cm^{-3}.

different numbers of cycles by weighing and by thickness measurements using cross-sectional SEM images. In (c), the electrode porosity was calculated based on the thickness and mass loading of the electrodes, using estimated average densities of 2.33 g cm^{-3} for silicon, 2.0 g cm^{-3} for graphite and the carbon fibers, 1.5 g cm^{-3} for the LiPAA binder, and 1.6 ± 0.2 g cm^{-3} for the electrolyte decomposition products (this calculation is outlined in detail in reference [7]). Analogous to the cycling data, these electrode properties undergo a drastic change within the first 60 cycles. While the mass loading increases from ~1.4 to ~3.9 mg cm^{-2}, the coating swells from ~19 μm to ~49 μm. In contrast, between 80 and 140 cycles, only minor changes can be observed, resulting in a final mass loading of 4.4 mg cm^{-2} and a coating thickness of ~51 μm, respectively. The ≈5-10% decrease in the measured electrode thickness for the electrodes aged for 120 and 140 cycles, likely originates from a slightly lower initial mass loading and thus also a smaller coating thickness prior to cycling. Yet, it is to note that the preparation of the electrodes is quite reproducible, yielding an average thickness and standard deviation for the pristine electrodes of 18.7 ± 0.3 μm.

Based on a recent TEM investigation,[10] it was indeed expected that after 60 cycles the further increase of the mass loading and the coating thickness would become very small, as the cycling induced structural changes to the silicon particle morphology and the concomitant surface area growth of the silicon particles approach a steady-state condition, which is accompanied by a much reduced increase of the total irreversible capacity per cycle and by a consequent stabilization of the reversible capacity (see Figure 1a). Interestingly, Figure 2c indicates that the electrode porosity undergoes only a minor decrease from 0.61 to 0.5 over 140 cycles, which is comparatively small considering that the electrode mass loading almost triples during the cycling experiment. This is related to the fact that the electrode thickness also increased by a factor of ~2.8. In other words, the increased electrode volume resulting from the electrode swelling largely compensates the increased mass loading, leading to only minor changes in the electrode's porosity and thus the electrolyte volume fraction in the pores. As a corollary, any conclusions about the clogging of the pores in SiG electrodes should consider not only the SEI formation but also the swelling of the electrodes and, equally important, the distribution of the electrolyte decomposition products across the electrode thickness.

Neutron depth profiling of SiG electrodes.—FEC consumption measurements from a recent ^{19}F-NMR study demonstrated that the decomposition of electrolyte compounds at the silicon/electrolyte interface increases proportionally with the capacity exchanged by the silicon particles.[7] The amount of these decomposition products can thus be used as a sensitive measure for the capacity utilization of the adjacent silicon active material. In other words, silicon particles that experience a larger change in their state-of-charge (SOC) during cycling, and thus also larger volumetric changes, consequently accumulate more electrolyte decomposition products. Since the SEI from the FEC-containing LP57 electrolyte consists mainly of

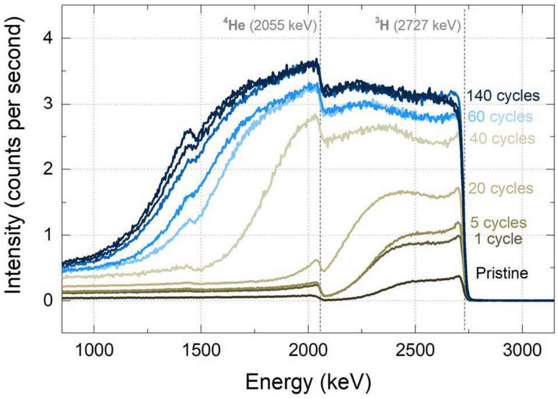

Figure 3. NDP energy spectra, showing the ^{3}H and ^{4}He intensity as a function of their energy for SiG electrodes measured ex-situ after different numbers of cycles (adapted from Trunk et al.[33]). The electrodes were aged according to the cycling protocol shown in Figure 1, whereby cycle number 1 represents the SiG electrode after the first formation cycle at a C-rate of 0.1 h^{-1}. The vertical dashed lines show the formation energy of ^{3}H and ^{4}He.

lithium-containing compounds from the reductive decomposition of FEC, e.g., Li_2CO_3, LiF, and Li_2O,[17,31,32] a quantification of the lithium concentration profile across aged SiG electrodes thus allows to determine the evolution of the depth-resolved silicon capacity utilization upon cycling. For this reason, the lithium distribution across pristine and cycled SiG electrodes was determined by neutron depth profiling measurements. A thickness-independent lithium concentration would indicate a homogeneous formation of electrolyte decomposition products, which in turn would indicate a depth-independent capacity utilization of the active materials. In contrast, differences in the accessibility of the SiG anode upon aging would be indicated by a non-homogeneous lithium distribution. For example, a clogging of the electrolyte-filled pores by electrolyte decomposition products could lead to a lithium ion concentration gradient in the electrolyte phase during (de-)lithiation, which would favor the (de-)lithiation of silicon particles near the SiG anode/separator interface, as reported by Radvanyi et al.[20] and Michan et al[21] for graphite-free silicon electrodes. On the other hand, an insufficient electrical conductivity across the electrode due to SEI build-up and electrode swelling would result in a higher active material utilization near the current collector/electrode interface, as shown by NDP for an electronically poorly conductive LFP electrode.[30]

Figure 3 shows the energy spectra obtained from NDP measurements of SiG electrodes which were aged for different numbers of cycles. In accordance with Equation 1, neutrons are absorbed by ^{6}Li to form an α (^{4}He) and a triton (^{3}H) particle which are detected by a surface-barrier detector facing the free top-surface of the SiG electrode (opposite the SiG electrode/current collector interface).[24] Due to the two-body kinematics, α and triton particles have well-defined energies at the moment of their formation and they are emitted back-to-back.[23,24,37] The energy loss experienced by these particles while traveling through the electrode can therefore be used to measure the depth where the nuclear reaction has taken place.[23,38] This energy loss can be described by the so-called stopping power, which is highly dependent on the nature of the charged particles, their energy, as well as on the properties of the material matrix through which they pass, namely its density and composition.

$$^6\text{Li} + \text{n} \rightarrow {}^4\text{He}\,(2055\text{ keV}) + {}^3\text{H}\;\;(2727\text{ keV}) \qquad [1]$$

Since the ^{4}He and ^{3}H particles are emitted isotropically, only one of them is detected at a time, but signals from both appear in the spectra. While the escape depth of ^{4}He particles through the porous SiG electrode is only ~15 μm, that of the ^{3}H particles is much larger,[39] having an escape depth of up to ~50 μm through the SiG electrode.[33] In other words, the energy distribution profile obtained for the ^{3}H signal starts at 2727 keV (corresponding to ^{3}H particles created at the top-surface of the SiG electrode) and continues to lower energy values for ^{3}H particles emanating from a greater depth in the SiG electrode; at an energy of 2055 keV, the ^{3}H signal will then overlap with the ^{4}He particle signal. A third signal was found to appear at 1472 keV and determined to originate from boron impurities of the glass fiber separator, pieces of which were stuck on the top-surface of the harvested SiG electrodes. It was observed to increase with the cycle number, caused by the stronger adhesion of the fibers on the aged and roughened surface of the SiG electrodes. This was confirmed by the fact that no such signals were observed for pristine SiG electrodes as well as in reference measurements with boron-free poly(olefin)-based Celgard separators (data not shown).

In the pristine electrode (the lowest, dark brown line in Figure 3), in which the LiPAA binder is the only source of lithium, the ^{4}He and ^{3}H signals still occur at distinctly different energies and do not overlap. The high-energy onset for each signal represents particles emanating from the top-surface of the electrode, while signals at lower energies correspond to particles emanating from a greater depth. At 2727 keV, the ^{3}H signal jumps to ~0.3 cps, followed by a slightly tilted plateau towards lower energies, which vanishes at ~2100 keV; here, the location of the interface between the Cu current collector and the SiG electrode is marked on this energy scale by the inflection point of the decaying signal at around 2340 keV.[33] The area below this signal can be ascribed to the total lithium content in the SiG electrode and the rather flat plateau of the ^{3}H signal vs. energy indicates a fairly uniform LiPAA distribution across the pristine electrode. At lower energies, the intensity jump at 2055 keV shows the onset of the ^{4}He particle signal.

The curve just above the lowest in the same graph, labeled "1 cycle", shows the intensity vs. energy profile after the first charge/discharge cycle (delithiated to 2.0 V vs. Li^+/Li at a very slow C-rate of 0.02 h^{-1}). The ^{3}H signal at ~2727 keV now increases from ~0.3 cps for the pristine electrode to ~0.9 cps at the plateau, indicating a considerable increase of the lithium content in the electrode. At the same time, however, the shape of the triton profile is still the same as in the pristine electrode, indicating that the distribution of the additional lithium containing species deposited in the SiG electrode is similarly uniform as that of the LiPAA binder.[33] In fact, there are two possible causes for the additional amount of lithium in the SiG electrode, whereby both of them would result in an irreversible capacity loss: (i) lithium-containing electrolyte decomposition and SEI products formed at the electrode/electrolyte interface, and (ii) immobilized lithium remaining in the silicon active material due to kinetic overpotentials.[40] As the SiG electrodes were measured in a fully discharged state after a very slow delithiation rate of 0.02 h^{-1} to a SiG electrode potential of 2.0 V vs. Li^+/Li, we conclude that the majority of the irreversible capacity loss must stem from the SEI rather than from immobilized lithium. This can be further supported by exemplarily considering the reversible capacity decay of the SiG electrode over 120 cycles (see Figure 1a). During the first cycle at 0.1 h^{-1}, the electrode delivered a capacity of 1.66 mAh cm^{-2}, whereas after 120 cycles the reversible capacity after a slow delithiation step to 2 V vs. Li^+/Li at 0.02 h^{-1} amounted to 0.88 mAh cm^{-2} ($\Delta = 0.78$ mAh cm^{-2}). Taking into account that the incomplete delithiation mainly affects silicon particles at low degrees of lithiation, i.e., below ~25% state-of-charge,[7] the estimated maximum contribution from immobilized lithium would be ~0.20 mAh cm^{-2}. This corresponds to just ~9% of the total irreversible capacity of 2.13 mAh cm^{-2}. Repeating this calculation for SiG electrodes after different number of cycles reveals the same fraction of 8–10%, thus confirming our assumption.

After 5 cycles, the uniform lithium distribution across the SiG electrode remains, while the lithium content slightly increases which we assign to cracking and renewal of the passivating layer at the silicon/electrolyte interface caused by the volumetric changes of the silicon particles upon repeated (de-)lithiation. Towards 20 cycles, the lithium content further increases to ~1.6 cps, while the shape of the signal remains essentially the same. In addition, the signal clearly broadens, shifting the inflection point of the ^{3}H signal towards lower energies, which indicates a further mass loading increase of the electrode; this also goes hand in hand with an increase in the lithium mass loading, as the total amount of lithium is proportional to the area under the curve in Figure 3. In agreement with the cycling data (see Figure 1a) and the electrode mass and thickness data (see Figure 2), the NDP spectra thus confirm that the largest changes in terms of the irreversible capacity loss as well as of the mass and thickness increase occur within the first 60 cycles.

Eventually, the ^{3}H signal overlaps with the onset of the ^{4}He signal, resulting in a shoulder at 2055 keV as shown in Figure 3. Therefore, the depth profiles from the ^{3}H signal become hard to interpret beyond 60 cycles. For separation of the ^{3}H and ^{4}He signals, a thin Mylar or Kapton foil is commonly used which blocks the ^{4}He particles; however, at the same time it would also worsen the energy resolution of the ^{3}H signal.[41] Instead, we performed a mathematical deconvolution of the ^{3}H and ^{4}He signal contribution to the recorded spectra: the two signals in Figure 3 were separated by describing the ^{4}He signal based on the distinct part of the triton signal above 2055 keV which originates from the same depth information near the surface, as introduced by Trunk et al.[33]

As the intensity of the triton signal is strictly proportional to the number of ^{6}Li isotopes and therefore the number of lithium atoms in the SiG electrodes (calculated using the natural ^{6}Li abundance of 7.59%), the latter was converted into an equivalent capacity (using 1 As of charge per mol of lithium). In the pristine electrode, the equivalent capacity of lithium in the LiPAA binder determined by the integrated lithium intensity from the NDP spectrum was found to be 0.058 ± 0.002 mAh cm^{-2}. Since the observed energy loss in combination with the Stopping Range in Matter (SRIM) approach[33,37] also allows to calculate an equivalent mass loading of the pristine SiG electrode of 1.65 ± 0.34 mg cm^{-2}, the equivalent capacity of lithium in the LiPAA binder can also be determined by multiplying the thus found mass loading with the LiPAA content of 10 wt% and dividing it by its molecular weight ($M_W = 77.9$ g mol^{-1}). This yields an equivalent capacity of ~0.057 mAh cm^{-2}, which is in excellent agreement with the above value from the integrated lithium signal intensity. Furthermore, while the NDP-derived mass loading of 1.65 ± 0.34 mg cm^{-2} for the pristine SiG electrode is ~15% larger than the value obtained by weighing of the pristine SiG electrode (1.44 ± 0.04 mg cm^{-2}, see Figure 2a), this agreement is reasonably good considering the overall rather low lithium mass loading (~10 μg/cm^{2}) in the pristine SiG electrode. From here on forward, the total irreversible capacity of the cycled electrodes was calculated from the NDP signal intensities by subtracting the initial lithium content from the LiPAA binder (i.e., 0.058 mAh cm^{-2}).

Figure 4a summarizes the total irreversible capacity obtained by the above outlined NDP analysis (marine symbols; assuming 1 As of total irreversible capacity per mol of lithium after subtraction of the LiPAA binder contribution) and the total irreversible capacity obtained from the electrochemical measurements of the respective electrodes (blue symbols; note the excellent agreement with the irreversible capacity vs. cycle number shown for one of the electrodes in Figure 1a). A rapid increase of the irreversible capacity is observed in the first 60 cycles, as was already seen in Figure 1a. Further cycling results in decreasing irreversible capacity gain per cycle (i.e., a "flattening" of the curve), indicating a decrease of the extent of side reactions at the silicon/electrolyte interface.[10] In general, the irreversible capacity values monitored by the two methods agree fairly. The ~20% lower total irreversible capacity values obtained by NDP may have two possible reasons: (i) The NDP signals derive only from the center of the electrode (~0.18 cm^{2} of 1.54 cm^{2}),[33] whereas the electrochemical method averages over the entire electrode surface, thus any inhomogeneities at the electrode edges are not considered by NDP. (ii) A partial mechanical removal of the coating and electrolyte decomposition products either by washing after disassembly or during the transport from the glovebox to the NDP experiment.

To determine the distribution of the lithium-containing electrolyte decomposition products across the thickness of the SiG electrodes, the mathematically separated ^{3}H spectra (removing the ^{4}He and ^{10}B contributions) were converted into a lithium density (in units of Li atoms cm^{-3}),[33] assuming natural ^{6}Li abundance and uniform electrode porosity, and plotted against the electrode mass loading (in mg cm^{-2}), which is shown in Figure 5a. The energy-loss model is based on the SRIM calculation and described elsewhere.[33,37] By this approach, the full depth evolution even for cycles where the signals were previously superimposed can now be studied. In accordance with the increasing fraction of electrolyte decomposition products which accumulate in the porous electrode upon cycling, the changing composition of the SiG electrode has to be taken into account for the SRIM calculation of each cycle. For that purpose, a recent publication by Petibon et al.[6] was considered, who, based on gas chromatography (GC) measurements, reported that FEC is the major electrolyte compound which gets reduced on silicon at potentials below 1.0 V vs. Li^{+}/Li, yielding electrolyte decomposition products with an overall stoichiometry of $C_3H_3O_3F$. Although initially gaseous carbon dioxide (CO_2) is evolved during FEC reduction,[6,8] Krause et al.[42] reported that CO_2 gets reduced at the silicon surface and thus also becomes part of the SEI. Because the overall FEC reduction was shown by Jung et al.[8] to consume a total of four electrons per FEC molecule, the stoichiometry of the final reduction products was complemented by four additional lithium ions to restore charge neutrality,

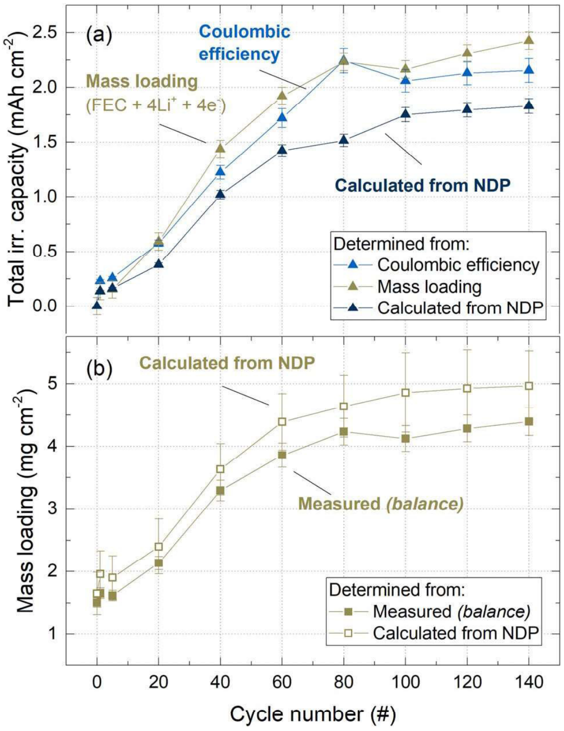

Figure 4. (a) Total irreversible capacity of the SiG electrode as a function of the cycle number determined from: (i) the integration of the coulombic efficiency over cycle number during galvanostatic cycling (blue symbols); (ii) the post-mortem electrode mass loading measurements and assuming a four-electron reduction mechanism of FEC described by Equation 2 (brown symbols); and, (iii) the lithium intensity measured by ex-situ NDP after correction for the lithium intensity originating from the LiPAA binder of 0.058 mAh cm^{-2} (marine symbols). (b) Mass loading of the SiG electrodes as a function of the cycle number measured with a balance (solid symbols, taken from Figure 2a) or computed from the NDP spectra (hollow symbols). For the mass loading and the coulombic efficiency, a standard error of ± 5% was used based on a larger number of electrodes and measurements in a previous study. For the NDP measurements, an error propagation was calculated considering the signal processing and the definition of the inflection points.

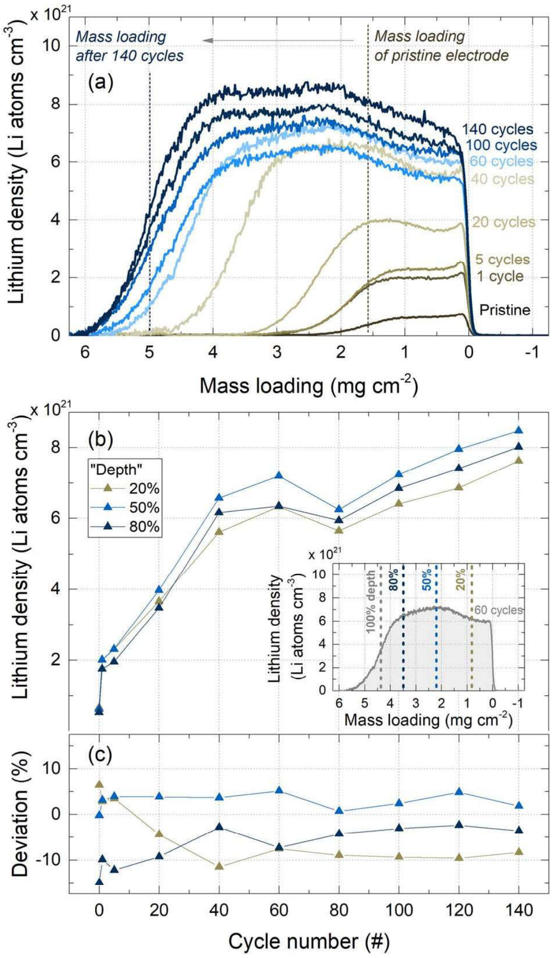

Figure 5. (a) Lithium density distribution as a function of the electrode mass loading (in mg cm^{-2}) of SiG electrodes measured ex-situ by NDP after different numbers of cycles. (b) Lithium density at 20, 50, and 80% of the electrode mass loading ("depth") referenced to the electrode top-surface as a function of the cycle number, obtained from the lithium density distribution shown in (a), which is illustrated in the inset in (b). (c) Deviation of the lithium density at 20, 50, and 80% from the mean lithium density.

yielding an overall stoichiometry of $C_3H_3O_3FLi_4$. To verify that this four-electron reduction mechanism can also be applied in the present work, Equation 2 was used to calculate the capacity Q_{SEI} which would correspond to the increase in electrode mass loading L_{SEI} shown in Figure 2a (determined by post-mortem weight measurements):

$$Q_{SEI} = \frac{L_{SEI}}{M_{SEI}} \times z \times F \qquad [2]$$

where M_{SEI} the molecular weight of the electrolyte decomposition products with the overall stoichiometry of $C_3H_3O_3FLi_4$ (M_W = 133.81 g mol^{-1}),[7] z the number of electrons (here: 4), and F is the Faradaic constant. Figure 4a shows the resulting total irreversible capacity Q_{SEI} (brown symbols), which is in good agreement with the values obtained by integrating the measured coulombic efficiency (blue symbols) and thus supports the above made assumptions on the overall SEI stoichiometry.

The electrode mass loadings shown in Figure 5a, as calculated from the NDP energy spectra, were also compared to the mass loadings which were measured by weighing of harvested SiG electrodes (compare Figure 2a). This is exemplarily shown by the vertical dashed lines, marking the NDP spectra inflection points for the pristine SiG electrode and the electrode after 140 cycles, respectively. Figure 4b summarizes the corresponding inflection points for all electrode mass loadings (hollow symbols) determined by NDP and the mass loadings obtained by weighing harvested electrodes (solid symbols) as a function of the cycle number, showing excellent agreement between the NDP-based and the weight measurement-based values.

The lithium density profiles shown in Figure 5a indicate the same two major trends that were previously discussed for the NDP energy spectra, namely (i) an increase in the local lithium density at any given electrode depth due to the accumulation of electrolyte decomposition products, and (ii) a concomitant mass loading increase of the entire electrode upon cycling. In addition, the lithium density profiles of the first 20 cycles indicate an almost uniform lithium distribution across the thickness of the SiG electrodes, while after more cycles a ~15% lower lithium density can be observed at the top-surface of the SiG electrodes. This phenomenon likely originates from the rapid swelling of the electrodes particularly after 20 cycles (see Figure 2a and Figure 6) which may cause that some of the already detached particles or electrolyte decomposition products remain in the inner layers of the electrodes. Overall, however, the lithium concentration across the cycled SiG electrodes, as revealed by Figure 5a is surprisingly homogeneous. This can be seen more clearly in Figure 5b, which summarizes the lithium density evolution over cycling at different electrode depths of 20, 50, and 80% referenced to the top-surface of the SiG electrode (100% equals the mass loading calculated from NDP which is shown in Figure 4b). In agreement with the capacity fading rates and the total irreversible capacity growth rates shown in Figure 1a, the largest increase in the lithium density from ~0.7 to ~6.0 × 10^{21} Li atoms cm^{-3} occurs within the first 60 cycles. However, continued cycling reveals a much smaller increase to ~8.0 × 10^{21} Li atoms cm^{-3} after 140 cycles. Remarkably, despite the slightly lower lithium density towards the surface of the electrode (i.e., at 20% electrode depth), the distribution of the lithium atoms remains widely constant across the electrode even upon extended cycling. This is illustrated more clearly by Figure 5c showing only small deviations of less than 15% from the mean lithium density across the electrode coatings.

From this it can be concluded that apart from the small deviation at the electrode top-surface, the lithium containing electrolyte decomposition products are almost uniformly distributed across the SiG electrode coatings even upon extended cycling. Since the amount of electrolyte decomposition products is proportional to the capacity exchanged by the silicon particles,[7] one can conclude that the silicon active material utilization over the 140 cycles must also be homogeneous across the SiG electrode thickness, so that the occurrence of significant transport-limitations which would lead to an inhomogeneous silicon utilization can be excluded for the here investigated aged SiG electrodes. This supports a previous work from our group,[7] according to which the incomplete delithiation from electronically poorly connected silicon particles in SiG electrodes is the main cause for the capacity decay within the first 60 cycles, presuming an excess of active lithium from the positive electrode. Because the network of graphite particles provides a reasonable electrode porosity and electrical conductivity even across substantially swollen SiG electrodes, the major capacity fading mechanism for these SiG electrodes are electronic contact resistances occurring between the silicon particles due to insufficient interparticle contact pressure at low degrees of lithiation. These contact resistances are expected to grow with cycling due to SEI build-up, and since this phenomenon is independent of the location of the silicon particles, this aging mechanism does predict the here observed homogeneous silicon utilization across the thickness of the electrode.

It must be noted, however, that this finding seems to contradict some results in the literature where clogging of electrode pores by SEI products was stated to lead to an inhomogeneous silicon utilization across the electrode.[15,20,21] However, the discrepancy to these studies from Oumellal et al.,[15] Radvanyi et al.,[20] and Michan et al.[21] likely originates from the absence of large graphite particles in the respective silicon-based electrodes (using either only carbon black

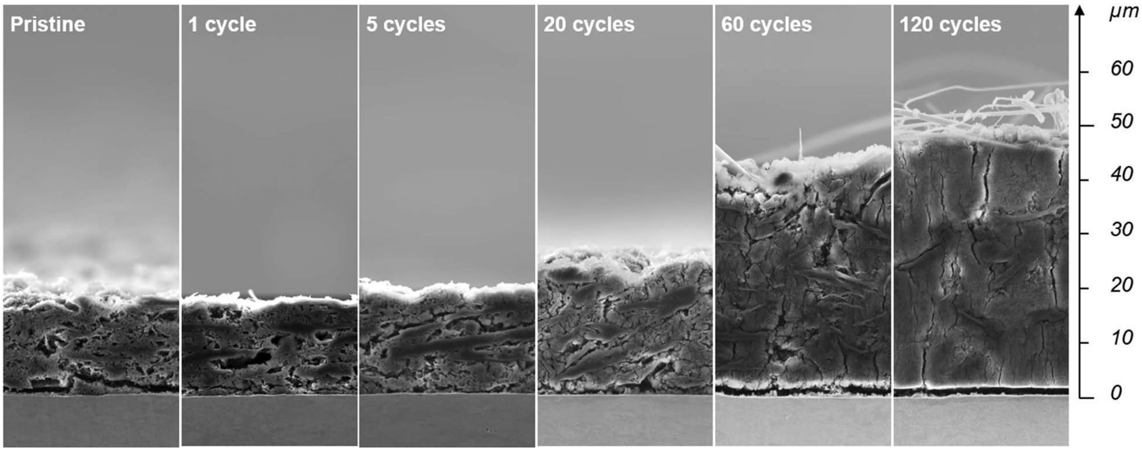

Figure 6. Cross-sectional SEM images of SiG electrodes in the pristine state and after different numbers of cycles at a magnification of 1000x. Recorded with a secondary electron detector and an acceleration voltage of 10 kV.

or carbon fibers), which increases the risk of a deterioration of the electronic conductivity across the thickness of the electrode upon extensive SEI formation as well as a loss of void volume in the vicinity of the sterically demanding graphite particles. In addition, Oumellal and Radvanyi also used capacity-limited cycling procedures which bear the risk of an inhomogeneous (de-)lithiation of silicon particles, because only a fraction of the available capacity is utilized during each cycle, likely resulting in more charge/discharge of well-connected particles compared to others.

Morphological changes of SiG electrodes upon cycling.—To support our above interpretation of the electrode property changes (see Figure 2) and the lithium density profiles across the electrode (see Figure 5) upon extended cycling, cross-sections of the SiG electrodes were investigated by means of scanning electron microscopy (SEM). Figure 6 shows representative sections of the SEM images (1000x magnification) of electrodes before and after a different number of charge/discharge cycles. The SEM cross-sections (Figure 6) show that the major increase in the thickness of the SiG electrode occurs between 20 and 60 cycles, analogous to what was shown in Figure 2b. It is to note that the values shown in Figure 2b represent the average of the entire cross-section of the resign-embedded halved pieces of the electrodes, whereas the argon ion beam polished images shown in Figure 6 only refer to a section of ~500 μm length from the center of the other piece of the electrode, from which only ~30 μm are shown in the images. The SEM cross-sections indicate that the SiG electrodes accumulate a large amount of electrolyte decomposition products upon cycling. As expected from the volumetric changes upon repeated (de-)lithiation, the silicon nanoparticles are increasingly covered by SEI products and thus not any more visible as single entities, whereas most of the large graphite particles can still be distinguished well. In accordance with the lithium depth profiles, the SEM cross-sections reveal a rather uniform distribution of the electrolyte decomposition products across the thickness of the SiG electrodes up to the shown 120 cycles.

Another striking observation from these images is that with an increasing cycle number the graphite particles are no longer horizontally aligned, but instead are partially displaced and become randomly oriented as the swelling of the SiG electrodes proceeds. This, we believe, is a consequence of the homogeneous growth of the SEI across the thickness of the SiG electrode: as each graphite particle faces the same forces which depend only on the statistical distribution of the silicon particles, a random orientation of the graphite particles results as the electrode thickness is increasing due to the irreversible expansion of the silicon particles over the first ~60 cycles and the accumulation of electrolyte degradation products.[10]

In summary, these cross-sectional SEM images further support our interpretation of the NDP spectra, according to which the silicon active material is utilized homogeneously across the entire SiG electrode, without any indication of a reduced silicon accessibility either near the current collector (driven by insufficient through-plane conductivity)[30] or near the electrode top-surface adjacent to the separator (driven by pore clogging).[15] Nonetheless, the similar utilization of the silicon particles is likely only sustained by the network of large graphite particles that maintains a sufficient porosity and electrical conductivity across the thickness of the electrode. As a corollary, further optimization of silicon-based electrodes in terms of the electrical conductivity requires not only a sufficient electrical connection of the individual silicon particles to overcome interparticle contact resistances, but also to ensure a contiguous network of well-conducting graphite particles to minimize the mean path length that electrons need to travel between the individual silicon particles and graphite. This finding is in good agreement with our previous publication[7] where we showed that a lower silicon/graphite ratio significantly improves the cycling stability of these electrodes.

Figure 7 shows cross-sectional images of the same SiG electrodes at a higher magnification of 5000x. By comparing the electrodes in the pristine state and after 5 cycles, it can be clearly seen that the SEI preferably accumulates near the silicon particles, which has also been reported by Michan et al.[21] In contrast, no SEI accumulation can be observed at the edges of the graphite particles, thus preserving some void space in the coating. Further, the precipitation of electrolyte decomposition products around the silicon particles seems to occur evenly across the thickness of the electrode, consistent with the NDP analysis. While initially individual silicon particles can still be discerned, this becomes increasingly difficult after 20 cycles, which in part is due to the fact that the silicon particles expand irreversibly into a network of nanometer-sized silicon branches interpenetrated by electrolyte decomposition products, as was shown in a previous TEM study.[10] After 60 and even more so after 120 cycles, the electrolyte decomposition products and silicon particles merge into apparently dense agglomerates that have also been observed by Radvanyi et al.[20] As a matter of fact, however, SEM images of the electrode after 120 cycles at higher magnification of 15’000x and 50’000x (see Figure 8), reveal that these agglomerates are not dense, but instead are porous, foam-like structures consisting of silicon covered by electrolyte decomposition products (more clearly visible in our previous TEM analysis).[10]

Because the remaining pores are still on the order of 10^1-10^2 nanometers, they can be easily penetrated by electrolyte; their presence also explains that the porosity of the electrodes even after 140 cycles remains as high as ~50% (see Figure 2c). An unexpected con-

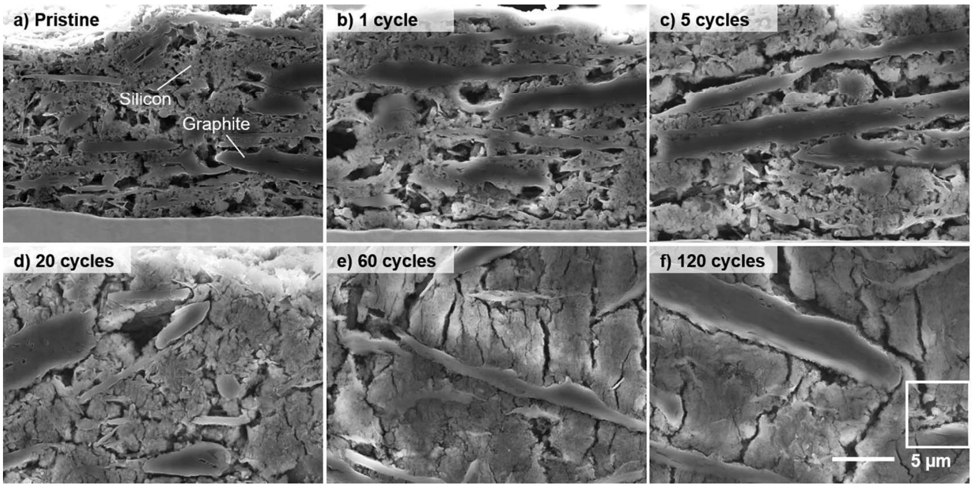

Figure 7. Cross-sectional SEM images of SiG electrodes in the pristine state and after different numbers of cycles at a magnification of 5000x. The white frame in (f) indicates the location of measurements taken with a higher magnification and shown in Figure 8. Recorded with a secondary electron detector and an acceleration voltage of 10 kV.

sequence of the high remaining porosity in combination with the substantial electrode swelling is that the total pore volume contained in the cycled SiG electrodes is increasing upon repeated charge/discharge cycling rather than decreasing. Considering a pristine SiG electrode with a coating thickness of ~19 μm and a porosity of ~60% (see Figure 2), the initial pore volume of the electrode equates to ~1.1 μL cm^{-2}, while it increases to ~2.6 μL cm^{-2} after 140 cycles (based on a thickness of ~51 μm and a porosity of ~50%; see Figure 2). While the higher pore volume in principle should allow for facile lithium ion transport across the electrode thickness in the electrolyte phase, it has a rather noteworthy corollary when comparing the capacity fading of battery cells with silicon-based anodes measured in coin-cells (or other lab-scale cell hardware) and large-scale cells. In coin-cells, the added amount of electrolyte typically exceeds the void volume provided by the electrodes and the separator(s) by ~10-fold, so that the increasing electrode void volume upon cycling can easily be replenished by the excess electrolyte. On the other hand, in large-scale cells, the electrolyte volume typically exceeds the total void volume of electrodes and separator by only ~20%, so that the here observed ~2.5-fold increase in anode void volume would lead to a partial dry-out of the electrodes, which in turn should result in a more accelerated capacity fading. Thus, one would expect that the typically much shorter cycle life of large-scale vs. lab-scale cells with silicon anodes is not only due to the more rapid consumption of stabilizing additives like FEC,[6,8] but also due to the electrode swelling induced dry-out of the electrodes.

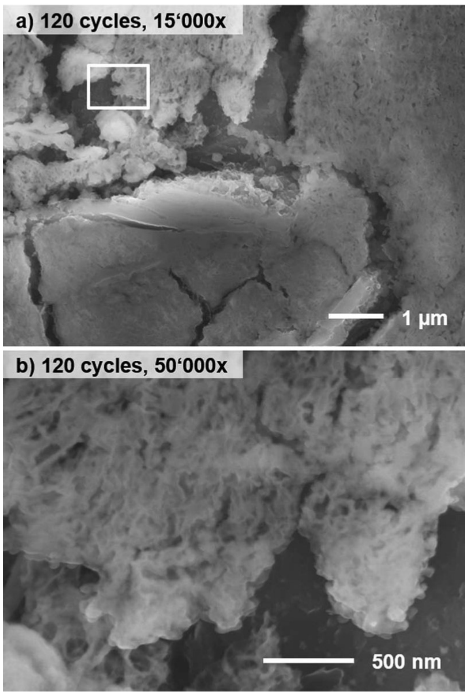

Figure 8. Cross-sectional SEM images of SiG electrodes after 120 cycles with a magnification of (a) 15’000x and (b) 50’000x. The white frame in (a) indicates the location of measurement taken with the higher magnification, which is shown in (b). Recorded with a secondary electron detector and an acceleration voltage of 10 kV.

In summary, the above discussed phenomena underline the need for an integral design of silicon-based electrodes, considering both (i) a suppression of the degradation of the silicon particles and subsequent side reactions at the silicon/electrolyte interface, and (ii) a hierarchical electrode structure that maintains sufficiently low electron and lithium-ion transport resistances not only across the thickness of the electrode but also between the individual silicon particles. While the NDP analysis indicates that the performance of the here investigated SiG electrodes is not significantly compromised by transport resistances across the thickness of the electrode even at a relatively high C-rate of 0.5 h^{-1}, the ongoing electrolyte decomposition at the silicon/electrolyte interface and the loss of interparticle contact pressure remain the major challenges for silicon-based electrodes.

Conclusions

In the present study, silicon-graphite (SiG) electrodes with an areal delithiation capacity of ~1.7 mAh cm^{-2} were investigated in terms of their morphological changes and the distribution of lithium-containing electrolyte decomposition products as a function of the cycle number. Using ex-situ neutron depth profiling (NDP) on pristine and cycled electrodes in the discharged state, it was demonstrated that the aging of the SiG electrodes is most pronounced within the first 60 cycles. During this period, the silicon nanoparticles undergo se-

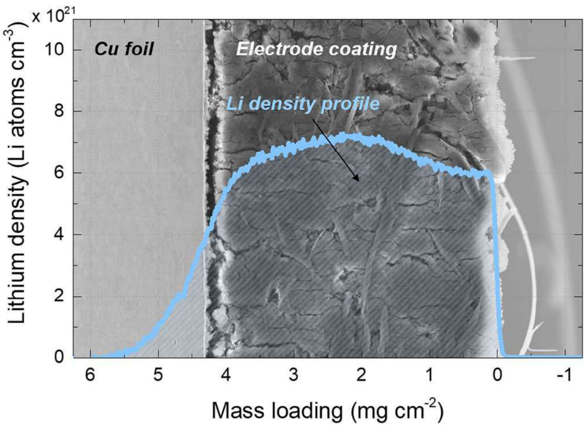

Figure 9. Lithium density profile of a SiG electrode after 60 charge/discharge cycles as a function of the electrode mass loading (blue line), exemplarily shown superimposed onto the corresponding cross-sectional SEM image. The profile is a convolution of the density with the material-dependent resolution, which includes an energy spread due to the statistical process of the energy loss and possibly also because of a slight variation in the local mass loading of the electrode. Thus, there is no lithium in the Cu current collector.

vere morphological changes which fuel side-reactions occurring at the silicon/electrolyte interface interface. The subsequent accumulation of large amounts of electrolyte decomposition products in the SiG electrodes could be followed quantitatively by NDP, which is exemplarily shown in Figure 9.

The depth-resolved lithium density profiles obtained in this way revealed a uniform distribution of the lithium-containing electrolyte decomposition products across the thickness of the SiG electrodes up to 140 charge/discharge cycles. As a corollary, the silicon active material was uniformly utilized across the SiG electrode thickness, demonstrating the absence of significant transport resistances (electronic or ionic) across the thickness of the investigated SiG electrodes even upon extended cycling. Instead, these findings suggest that the capacity decay of the SiG electrodes stems from the loss of interparticle contact pressure and increases with an increasing mean path length between individual silicon particles and adjacent electrically well-conducting graphite particles, which occurs statistically in a homogeneous electrode coating. High-resolution cross-sectional SEM images at different magnifications supported the interpretation of the uniform SiG electrode aging.

Finally, post-mortem weight, thickness and SEM cross-sectional studies of cycled SiG electrodes revealed that the electrode porosity remained almost unchanged over extended charge/discharge cycling. Owing to the significant swelling of the electrodes, the void volume of the pores even increased, which has important implications for the electrolyte amount in large-scale cells with SiG electrodes.

Acknowledgments

The authors kindly acknowledge Dr. Tristan Harzer and Dr. Susanne Cornfine (both JEOL Germany GmbH) for the preparation and measurement of the cross-sectional SEM images. Wacker Chemie AG is kindly acknowledged for providing the silicon nanoparticles. The Heinz Maier-Leibnitz Zentrum (MLZ) is kindly acknowledged for the possibility to use the high-quality neutron beam at the PGAA facility. The authors acknowledge the financial support by the Federal Ministry of Education and Research (project numbers 05K16WO1 "N4DP" and 03XP0081 "ExZellTUM II") as well as by the Federal Ministry for Economic Affairs and Energy (project number 03ET6045D "LiMo").

ORCID

Morten Wetjen https://orcid.org/0000-0002-2357-1151

References

1. O. Gröger, H. A. Gasteiger, and J.-P. Suchsland, *J. Electrochem. Soc.*, **162**(14), A2605 (2015).
2. K. G. Gallagher, S. Goebel, T. Greszler, M. Mathias, W. Oelerich, D. Eroglu, and V. Srinivasan, *Energy Environ. Sci.*, **7**, 1555 (2014).
3. D. Andre, S.-J. Kim, P. Lamp, S. F. Lux, F. Maglia, O. Paschos, and B. Stiaszny, *J. Mater. Chem. A*, **3**, 6709 (2015).
4. M. N. Obrovac and V. L. Chevrier, *Chem. Rev.*, **114**, 11444 (2014).
5. F. Luo, B. Liu, J. Zheng, G. Chu, K. Zhong, H. Li, X. Huang, and L. Chen, *J. Electrochem. Soc.*, **162**(14), A2509 (2015).
6. R. Petibon, V. Chevrier, C. P. Aiken, D. S. Hall, S. Hyatt, R. Shunmugasundaram, and J. R. Dahn, *J. Electrochem. Soc.*, **163**(7), A1146 (2016).
7. M. Wetjen, D. Pritzl, R. Jung, S. Solchenbach, R. Ghadimi, and H. A. Gasteiger, *J. Electrochem. Soc.*, **164**(12), A2840 (2017).
8. R. Jung, M. Metzger, D. Haering, S. Solchenbach, C. Marino, N. Tsiouvaras, C. Stinner, and H. A. Gasteiger, *J. Electrochem. Soc.*, **163**(8), A1705 (2016).
9. Z. Du, R. A. Dunlap, and M. N. Obrovac, *J. Electrochem. Soc.*, **161**(10), A1698 (2014).
10. M. Wetjen, S. Solchenbach, D. Pritzl, J. Hou, V. Tileli, and H. A. Gasteiger, *J. Electrochem. Soc.*, **165**(7), A1503 (2018).
11. T. D. Hatchard and J. R. Dahn, *J. Electrochem. Soc.*, **151**(6), A838 (2004).
12. M. N. Obrovac and L. Christensen, *Electrochem. Solid-State Lett.*, **7**(5), A93 (2004).
13. B. Key, R. Bhattacharyya, M. Morcrette, V. Sezne, J. Tarascon, and C. P. Grey, *J. Am. Chem. Soc.*, **131**, 9239 (2009).
14. B. Key, M. Morcrette, J.-M. Tarascon, and C. P. Grey, *J. Am. Chem. Soc.*, **133**, 503 (2011).
15. Y. Oumellal, N. Delpuech, D. Mazouzi, N. Dupré, J. Gaubicher, P. Moreau, P. Soudan, B. Lestriez, and D. Guyomard, *J. Mater. Chem.*, **21**, 6201 (2011).
16. N. Delpuech, D. Mazouzi, N. Dupre, P. Moreau, M. Cerbelaud, J. S. Bridel, E. De Vito, D. Guyomard, B. Lestriez, and B. Humbert, *J. Phys. Chem. C*, **118**, 17318 (2014).
17. K. W. Schroder, H. Celio, L. J. Webb, and K. J. Stevenson, *J. Phys. Chem. C*, **116**, 19737 (2012).
18. M. Nie, D. P. Abraham, Y. Chen, A. Bose, and B. L. Lucht, *J. Phys. Chem. C*, **117**, 13403 (2013).
19. S. Komaba, N. Yabuuchi, T. Ozeki, Z. J. Han, K. Shimomura, H. Yui, Y. Katayama, and T. Miura, *J. Phys. Chem. C*, **116**, 1380 (2012).
20. E. Radvanyi, W. Porcher, E. De Vito, A. Montani, S. Franger, and S. Jouanneau Si Larbi, *Phys. Chem. Chem. Phys.*, **16**, 17142 (2014).
21. A. L. Michan, G. Divitini, A. J. Pell, M. Leskes, C. Ducati, and C. P. Grey, *J. Am. Chem. Soc.*, **138**, 7918 (2016).
22. E. Peled and S. Menkin, *J. Electrochem. Soc.*, **164**(7), A1703 (2017).
23. J. P. Biersack, D. Fink, R. Henkelmann, and K. Müller, *Nucl. Instruments Methods*, **149**, 93 (1978).
24. R. G. Downing, G. P. Lamaze, J. K. Langland, and S. T. Hwang, *J. Res. Natl. Inst. Stand. Technol.*, **98**(1), 109 (1993).
25. J. F. M. Oudenhoven, F. Labohm, M. Mulder, R. A. H. Niessen, F. M. Mulder, and P. H. L. Notten, *Adv. Mater.*, **23**(35), 4103 (2011).
26. S. Whitney, S. R. Biegalski, Y. H. Huang, and J. B. Goodenough, *J. Electrochem. Soc.*, **156**(11), A886 (2009).
27. S. M. Whitney, S. R. F. Biegalski, and G. Downing, *J. Radioanal. Nucl. Chem.*, **282**, 173 (2009).
28. J. Wang, D. X. Liu, M. Canova, R. G. Downing, L. R. Cao, and A. C. Co, *J. Radioanal. Nucl. Chem.*, **301**, 277 (2014).
29. D. X. Liu, J. Wang, K. Pan, J. Qiu, M. Canova, L. R. Cao, and A. C. Co, *Angew. Chemie - Int. Ed.*, **53**, 9498 (2014).
30. X. Zhang, T. W. Verhallen, F. Labohm, and M. Wagemaker, *Adv. Energy Mater.* (2015), 1500498.
31. K. Schroder, J. Alvarado, T. A. Yersak, J. Li, N. Dudney, L. J. Webb, Y. S. Meng, and K. J. Stevenson, *Chem. Mater.*, **27**, 5531 (2015).
32. C. Xu, F. Lindgren, B. Philippe, M. Gorgoi, F. Björefors, K. Edström, and T. Gustafsson, *Chem. Mater.*, **27**, 2591 (2015).
33. M. Trunk, M. Wetjen, L. Werner, R. Gernhäuser, B. Märkisch, Z. Révay, H. A. Gasteiger, and R. Gilles (2018), submitted.
34. V. L. Chevrier, L. Liu, D. B. Le, J. Lund, B. Molla, K. Reimer, L. J. Krause, L. D. Jensen, E. Figgemeier, and K. W. Eberman, *J. Electrochem. Soc.*, **161**(5), A783 (2014).
35. Z. Révay, P. Kudějová, K. Kleszcz, S. Söllradl, and C. Genreith, *Nucl. Instruments Methods Phys. Res. Sect. A*, **799**, 114 (2015).
36. T. Yoon, C. C. Nguyen, D. M. Seo, and B. L. Lucht, *J. Electrochem. Soc.*, **162**(12), A2325 (2015).
37. J. F. Ziegler, M. D. Ziegler, and J. P. Biersack, *Nucl. Instruments Methods Phys. Res. Sect. B*, **268**, 1818 (2010).
38. J. F. Ziegler, G. W. Cole, and J. E. E. Baglin, *J. Appl. Phys.*, **43**(9), 3809 (1972).
39. D. J. Skyrme, *Nucl. Instruments Methods*, **57**, 61 (1967).
40. P.-K. Lee, Y. Li, and D. Y. W. Yu, *J. Electrochem. Soc.*, **164**(1), A6206 (2017).
41. Y. He, R. G. Downing, and H. Wang, *J. Power Sources*, **287**, 226 (2015).
42. L. J. Krause, V. L. Chevrier, L. D. Jensen, and T. Brandt, *J. Electrochem. Soc.*, **164**(12), A2527 (2017).

3.2.3 Evaluation of Lithium Density Profiles in Battery Electrodes

In addition to the published results, this PhD thesis featured numerous feasibility studies which were aimed to expand the application of NDP to further research questions concerning lithium-ion batteries. In the following, two NDP experiments are presented which offer insights into the lithium distribution in battery electrodes that are hardly accessible by conventional analytical techniques. At the time of the submission of this PhD thesis, one manuscript addressing the state-of-charge distribution across the thickness of SiG anodes has still been in preparation.[212]

(i) *State-of-charge (SOC)*-dependent experiments of SiG anodes (35 wt% silicon, ~1.8 mAh cm^{-2}) were conducted to investigate the lithium depth-distribution across the electrode coating during the first (de-)lithiation of the active materials. Figure 3.1 shows (a) *ex situ* NDP spectra and (b) the corresponding voltage profile of SiG anodes which were lithiated at 0.1 h^{-1} to different state-of-charge (SOC, blue lines) and delithiated to different depth-of-discharge (DOD, brown lines).

As expected, the lithium intensity as well as the mass loading increases notably during the lithiation and decreases again during the subsequent delithiation. Yet, a higher residual lithium concentration can be observed at nominally 100%$_{\text{DOD}}$ (darkest brown line) compared to the electrode after the initial SEI formation (i.e., between OCV and 0.25 V vs. Li$^+$/Li). This indicates an ongoing growth of SEI during the first cycle. Moreover, the electrodes reveal a reasonably uniform lithium depth-distribution at different SOC and DOD, respectively, which indicates a similar active material utilization at different electrode depths at the investigated C-rate of 0.1 h^{-1}. Repeating the same approach at different C-rates, with prelithiated electrodes, or using capacity-limited cycling procedures would offer insights into the build-up of concentration gradients across the coatings, the uniformity of the prelithiation method and/or the aging of capacitively oversized electrodes. A more detailed description of this experiment as well as an in-depth analysis of the lithium density profile across the thickness of the SiG anode as a function of the state-of-charge is currently in preparation.[212]

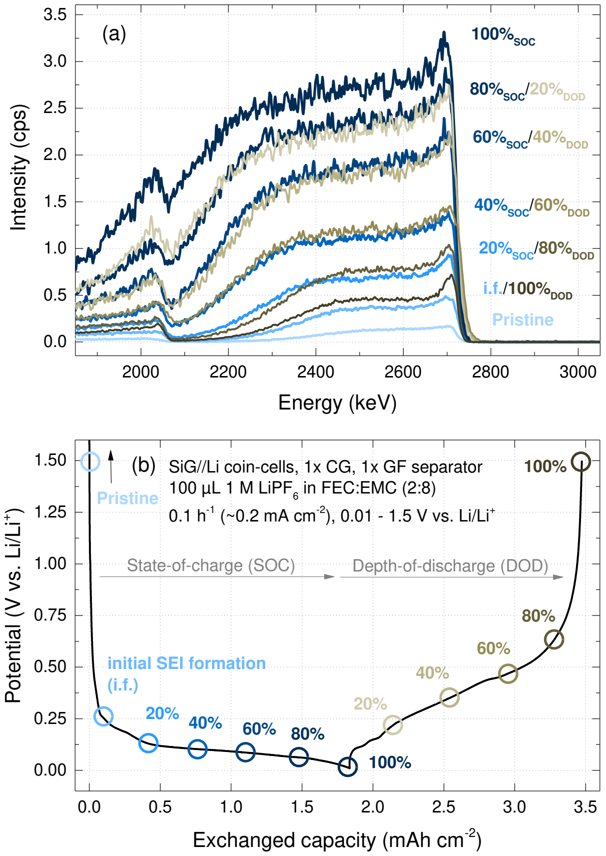

Figure 3.1 (a) NDP spectra obtained *ex situ* from SiG anodes (35 wt% silicon, ~1.8 mAh cm^{-2}) which were lithiated to different state-of-charge (SOC, blue lines) and delithiated to different depth-of-discharge (DOD, brown lines). The initial SEI formation (i.f.) refers to the reductive decomposition of electrolyte constituents between the open-circuit voltage (OCV) of the fresh electrode and 0.25 V vs. Li$^+$/Li, i.e., prior to the lithiation of silicon. The electrode preparation is described in detail elsewhere.[102,212] (b) Corresponding potential profile of the SiG anodes during the first cycle at 0.1 h^{-1} between cutoff potentials of 0.01 and 1.5 V vs. Li$^+$/Li.

(ii) The *depth-distribution* of *binder molecules* was shown to significantly influence the mechanical and electrochemical properties of porous electrodes for lithium-ion batteries.[213–215] For graphite-based anodes, the formation of binder gradients across the coating is especially critical. The coating process induced accumulation of binder molecules in the surface-near pores (e.g., by fast drying)[213] impairs the transport properties and promotes concentration gradients in the electrolyte solution at higher C-rates, thus increasing the risk of lithium plating at the electrode/separator interface.[216] Despite the relevance of this topic, there exist only few studies in the literature describing the formation of binder gradients across the thickness of graphite electrodes with application-relevant areal capacities of ~3 mAh cm^{-2} (i.e., ~90 µm thickness prior to calendering). The low percentage of polymeric binder in the coatings makes it difficult to separate and quantify the binder signal using conventional analytical techniques, including energy dispersive

X-ray spectroscopy (EDS),[213,214] thermogravimetric analysis (TGA),[217] and Raman spectroscopy.[218] These methods often display a trade-off because they either require extremely thick coatings of 400-1500 µm to evaluate the entire cross-section or they suffer from a limited depth-resolution of about ±20 µm. In addition, they usually provide just a semi-quantitative analysis of the binder content, which can vary depending on compositional differences between individual cross-sections. In contrast, using NDP as a highly lithium-sensitive technique allows to quantify the lithium density of an elliptical area of ~17.8 mm^2 and its depth-profile within the upper ~50 µm of a typical anode electrode coating at a very high depth resolution of less than 1 µm.

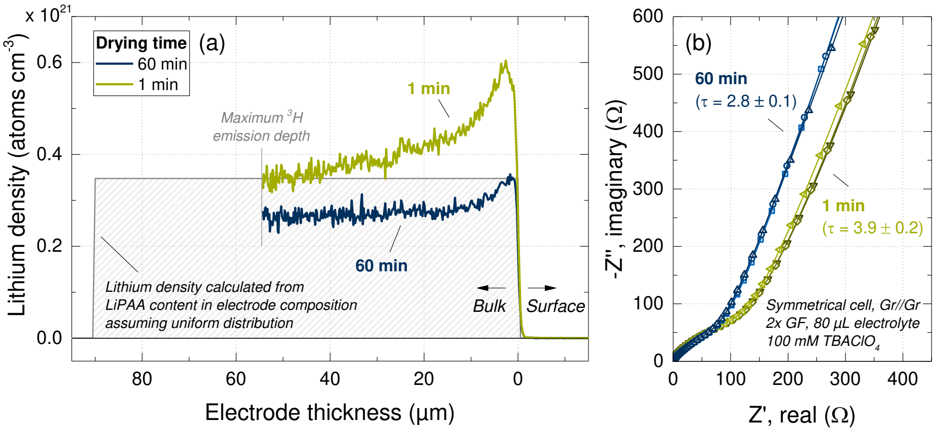

Figure 3.2 (a) Lithium density profiles of two pristine, uncompressed graphite anodes (areal capacity: ~3 mAh cm^{-2}, thickness: 90 µm, porosity: 55±2%) as a function of the coating thickness. The coatings were dried at different rates, including (i) a slow procedure at 25°C in humid atmosphere for 60 min (marine line), and (ii) a fast procedure at 70°C using an infrared (IR) irradiation for 1 min (green line). (b) Impedance response of symmetrical graphite//graphite cells in presence of a non-intercalating 100 mM $TBAClO_4$ electrolyte solution in EC:DEC (50 wt%:50 wt%). For each condition, three repeat measurements with new electrodes are plotted.

Figure 3.2a shows the lithium density profiles of two aqueous-based graphite anode coatings (95 wt% graphite, 5 wt% LiPAA binder), which were dried at different rates, including (i) a slow procedure at 25°C in humid atmosphere for 60 min, and (ii) a fast procedure at 70°C using infrared (IR) irradiation for 1 min. A considerably larger amount of the lithium-containing LiPAA binder can be observed in the surface-near layers (<20 µm) of the electrode which was dried at a faster rate. This finding agrees with the impedance measurements of symmetrical cells in blocking conditions (see Figure 3.2b),[219] indicating a notably higher pore resistance and thus a higher tortuosity for the same electrodes (the porosity is ~55% for both electrodes). Nevertheless, the 30-40% larger area below the lithium density profile for the electrode dried at 70°C also indicates a proportionally larger total lithium content across the investigated electrode thickness. As both electrodes contain nominally the same amount of LiPAA binder (which is the only source of lithium in these electrodes), there must exist another reason for this discrepancy, which is still subject to further investigation. Besides an irregularity during the electrode preparation process (i.e., different actual binder contents), a notable drop of the LiPAA content near the Cu current collector (i.e., between 60 and 90 µm electrode depth which was not monitored by NDP) for the fast-dried electrode (green line) are two possible explanations. In either case, this study demonstrates three important insights: (i) NDP indeed allows to monitor the depth-distribution of aqueous-based lithium-containing binders, e.g., LiPAA or Li-CMC,[220,221] across the thickness of electrode coatings with a very high resolution. This offers new insights into the investigation of transport-limiting phenomena in battery electrodes as well as the optimization of process parameters such as the drying rate. (ii) Similar to most neutron-based techniques, NDP experiments need to be complemented by other analytical techniques in order to elucidate the spectra. (iii) Ideally, the mass loading of the electrode coatings is adjusted such that the NDP signal can be monitored across the entire thickness, i.e., the full ~90 µm and not just the first ~55 µm as in the present investigation. Nevertheless, there exists a trade-off between the maximum electrode depth which is accessible by NDP and the transport limitations across the thickness of the electrode coating.

Possible approaches to increase the sample thickness and effectively double the accessible electrode depth include (a) consecutive measurements of the same electrode coating from the top and the backside (after carefully scratching off the coating from the current collector) and (b) the use of mesh coatings or coatings on ^{3}H-permeable Kapton® foil which are measured simultaneously by two opposite detectors. Due to the two-body kinematics of the nuclear reaction between thermal neutrons with ^{6}Li, the resulting ^{3}H and ^{4}He particles are emitted back-to-back. Thus, the particles emanating from the top-surface of the electrode can be measured by one detector and the particles emanating through the mesh/foil and the backside of the electrode can be measured by another detector.

3.3 Evaluation of New Strategies to Realize Practical Silicon-Based Anodes

While the previous sections focused on the investigation of degradation phenomena in SiG anodes, this section attempts to evaluate new strategies to mitigate them. Emphasis is put on the efficacy and applicability of the approaches with respect to the attainable cycle life and specific energy of practical lithium-ion batteries that feature a limited amount of electrolyte and cyclable lithium from the cathode. Two of the following three articles describe approaches to increase the lithium inventory in lithium-ion full-cells, comprising either an NMC811 or an LNMO cathode.[222,223] The first article evaluates the electrochemical prelithiation of a capacitively largely oversized SiG anode,[224–227] while the second introduces a composite cathode comprising a sacrificial salt which is oxidized during the first charge of the battery.[228] The last article addresses the problem at its root by introducing a new electrolyte additive to improve the stability of the solid-electrolyte-interphase (SEI), thus reducing the ongoing consumption of cyclable lithium and electrolyte compounds.

3.3.1 Prelithiation of Silicon-Graphite Anodes in SiG//NMC811 cells

This section presents the article "Mitigating the Impedance Growth in SiG//NMC811 Lithium-Ion Batteries by Prelithiation of the Silicon-Graphite Anode".[229] At the time of the submission of this PhD thesis, the article has not yet been submitted for publication. This study was presented as a poster at the 19th International Meeting on Lithium Batteries (IMLB) in Kyoto, Japan (June 17-22, 2018), Abstr. #P035TUE.

Lithium-ion batteries consisting of a SiG anode and a nickel-rich nickel manganese cobalt oxide cathode (e.g., NMC811) offer high theoretical specific energies of >300 Wh kg^{-1} on a cell-level.[24,75] However, realization of these theoretical values poses a significant challenge because of two major obstacles: (i) An ongoing consumption of cyclable lithium and electrolyte caused by side reactions at the silicon/electrolyte interface.[53,102,175] (ii) A limitation of the cell end-of-charge voltage due to side reactions at the NMC811 cathode at higher potentials, including the release of lattice oxygen, electrolyte oxidation, surface film formation, and transition metal dissolution, which lead to increased capacity fading.[39,230–232]

In the present article, we investigated SiG//NMC811 full-cells with respect to the influence of prelithiation on the upper cell cutoff voltage and the resulting cycling stability at 45°C. Hence, we first benchmarked the NMC811 cathodes (~2.0 mAh cm^{-2} at 4.1 V vs. Li^{+}/Li) in half-cells against lithium metal anodes by applying upper cutoff voltages between 4.0 and 4.6 V vs. Li^{+}/Li. In the next step, we extended our analysis to SiG//NMC811 full-cells, using a capacitively largely oversized SiG anode (~7.0 mAh cm^{-2}), and investigated them regarding their cycling stability and electrode polarization at different C-rates between 0.1 and 1.0 h^{-1}. For selected conditions, the SiG anodes were electrochemically prelithiated to obtain different lithium inventories (up to 4.6 mAh cm^{-2}). Using either a lithium metal reference electrode or a gold-wire micro-reference electrode, we then monitored the potentials and the impedance growth of the individual electrodes as a function of cycle number and upper cell cutoff voltage. Finally, we complemented the impedance measurements by an *operando* gas evolution analysis of the NMC811 cathode using on-line electrochemical mass spectrometry (OEMS).

This study generated three important insights into SiG//NMC811 lithium-ion batteries: (i) The comparatively high lithiation potential of the SiG anode leads to an upward shift of the upper cutoff potential of the NMC811 cathode. At potentials above 4.3 V vs. Li^{+}/Li, oxygen is released from the surface-near layers of the NMC811 lattice and results in a dramatic increase of the cell impedance which lowers the reversible capacity especially at higher C-rates. (ii) Prelithiation of the SiG anode offers an effective approach to lower its average lithiation potential and thus reduces the risk of oxygen release during voltage slippage of the NMC811 cathode. (iii) Without prelithiation, the SiG//NMC811 cell chemistry reveals a poor reversible capacity after 250 cycles at 45°C which lags far behind its high theoretical specific energy. However, increasing the lithium inventory greatly improves the cycling stability, resulting in a specific energy of ~340 Wh kg^{-1} (normalized to the mass of both electrodes) after 250 cycles at 45°C. This value matches state-of-the-art graphite//NMC622 cells with an upper cell cutoff voltage of 4.4 V$_{cell}$ after 250 cycles at 25°C.

To focus on industrially relevant electrodes, this PhD thesis initiated a collaboration with the Volkswagen Varta Microbattery Forschungsgesellschaft mbH (VW-VM) in Ellwangen, which provided the SiG anode and NMC811 cathode sheets as well as the electrolyte solution.

Author contributions

S.O. and S.C. prepared the electrode sheets and the electrolyte solution. M.W. performed the electrochemical testing. M.W. and D.P. conducted the impedance measurements. A.F. performed the OEMS gas analysis and did the data treatment. M.W. analyzed the electrochemical and impedance data. M.W. wrote the manuscript. All authors discussed the results and commented on the manuscript.

Mitigating the Impedance Growth in SiG//NMC811 Lithium-Ion Batteries by Prelithiation of the Silicon-Graphite Anode

Morten Wetjen,[a,#,*] **Anna T.S. Freiberg,**[a,*] **Daniel Pritzl,**[a,*] **Stefanie Ostermeyer,**[b]
Stefanie Cadus,[b] **and Hubert A. Gasteiger**[a,**]

[a] Chair of Technical Electrochemistry, Department of Chemistry and Catalysis
Research Center, Technische Universität München, D-85748 Garching, Germany

[b] VW-VM Forschungsgesellschaft mbH & Co KG, Daimlerstrasse 1, 73479 Ellwangen
Jagst, Germany

---

[*] Electrochemical Society Student Member
[**] Electrochemical Society Member
[#] E-mail: morten.wetjen@tum.de

Abstract

In the present work, we investigate the impact of the upper cell cutoff voltage on the cycling stability of silicon-graphite//NMC811 lithium-ion batteries at different C-rates over 250 cycles at 45 °C. Using a gold-wire micro-reference electrode and electrochemical impedance spectroscopy (EIS), we monitor the potential evolution and the impedance growth of the individual electrodes as a function of the cycle number and the upper cell cutoff voltage. Further, we complement our analysis by a characterization of the NMC811 cathode by means of half-cell cycling against lithium metal electrodes and a gas evolution analysis using on-line electrochemical mass spectrometry (OEMS).

Our results indicate that the relatively high lithiation potential of the capacitively oversized SiG anode causes a gradual upward shift of the end-of-charge potential of the NMC811 cathode, leading to the release of oxygen from the NMC811 lattice and a concomitant impedance growth at the positive electrode even at comparatively low cell cutoff voltages. To cope with this challenge, we demonstrate that prelithiation of SiG anodes represents an effective strategy to reduce the average anode potential and thus mitigate an upward shift of the end-of-charge potential of the NMC811 cathode, while additionally providing a sufficiently large lithium inventory to allow a reversible capacity of >180 mAh g^{-1}_{NMC} after 250 cycles at 45 °C.

Keywords: NMC811, silicon-graphite, oxygen release, cutoff potential, prelithiation

Introduction

Lithium-ion batteries consisting of a silicon-based anode and a layered lithium nickel manganese cobalt oxide $Li(Ni_xMn_yCo_z)O_2$-based cathode offer the potential of high cell-level energy densities >300 Wh kg^{-1}.[1,2] However, the realization of these theoretical values continues to pose a significant challenge. The two major obstacles include (i) the ongoing consumption of active lithium and electrolyte constituents caused by side reactions at the silicon/electrolyte interface,[3–5] and (ii) the limitation of the end-of-charge potential of the NMC811 cathode due to side reactions occurring at high voltages, such as the release of lattice oxygen, electrolyte oxidation, surface film formation, and transition metal dissolution, which lead to subsequent capacity fading.[6–9]

The interest in silicon-based anodes originates from their high theoretical capacity of 3579 mAh g^{-1}_{Si} and their relatively low mean delithiation potential of ~0.4 V vs. Li^+/Li.[10] Although the potential is higher compared to graphite (0.1-0.2 V vs. Li^+/Li) it is still considerably lower than alternative high capacity anode materials, e.g., tin or tin oxide, which have mean delithiation potentials of 1.1-1.3 V vs. Li^+/Li and thus offer much lower energy densities.[11,12] However, the high capacity of silicon correlates with large volumetric changes during (de-)lithiation of the particles, which result in perpetual side reactions at the silicon/electrolyte interface and cause an ongoing loss of active lithium and electrolyte constituents upon cycling.[13–15] In accordance with Obrovac et al.,[16] the molar volume occupied by lithium in these binary alloys follows Vegard's law, which leads to a continuous volume expansion of the alloy with an increasing capacity utilization, i.e., with an increasing x in Li_xSi. To balance these properties, a capacitively oversized silicon-based anode offers a trade-off between a higher specific capacity compared to graphite and a restricted volume expansion due to a limited lithiation and thus a smaller change in the average state-of-charge.[17–20] Yet, for commercial cells this approach requires a careful evaluation of the resulting energy density, because the additional silicon also increases the inactive coating volume, the electrolyte demand and the irreversible capacity.[10,21]

On the cathode side, layered lithium nickel manganese cobalt oxides $Li(Ni_xMn_yCo_z)O_2$ are among the most promising active materials because of their high specific capacity and good cycling stability.[22] Their sloped voltage profile results in a gradual increase of the specific capacity with an increasing end-of-charge potential.[8,9] Yet, it is not possible to use the full theoretical specific capacity of ~275 mAh g^{-1}_{NMC} because of structural instabilities and side reactions occurring once a certain amount of lithium is extracted from the layered oxide.[7,23–27] Therefore, two approaches are commonly pursued to maximize the utilization of the theoretical capacity of $Li(Ni_xMn_yCo_z)O_2$ cathodes, including (i) an increase of the Ni content in these compositions,[6,28] and (ii) an optimization of the end-of-charge potential.[29,30] Noh et al.[28] reported an increasing first cycle capacity of the layered oxides with increasing Ni content from 163 mAh g^{-1}_{NMC} for $LiNi_{0.33}Mn_{0.33}Co_{0.33}O_2$ (NMC111) to 203 mAh g^{-1}_{NMC} for $LiNi_{0.8}Mn_{0.1}Co_{0.1}O_2$ (NMC811) at 0.1 h^{-1} and an end-of-charge potential of 4.3 V vs. Li^+/Li. However, it was also shown that the layered oxides reveal a lower capacity retention[28,31,32] and inferior thermal stability[28,33] for compositions with higher Ni contents. Further, Jung et al.[6] demonstrated that graphite//NMC811 full-cells provide a stable cycling performance only at end-of-charge voltages as low as 4.0 V, because the NMC811 undergoes phase transitions at high voltages which are accompanied by the release of surface-near lattice oxygen within the first cycles. In accordance with these results, earlier studies already reported that the subsequent formation of a spinel-like layer at the particle surface increases the cell polarization and ultimately leads to accelerated capacity fading.[34–36] As silicon-based anodes usually have a higher mean potential compared to graphite, it is thus important to evaluate the NMC811 cathodes at a given cell voltage by taking into account the anode potential in order to assess the practically achievable energy density and durability of this promising lithium-ion cell chemistry.

In the present work, we investigate the impact of the upper cell cutoff voltage on the cycling stability and the electrode polarization of SiG//NMC811 full-cells over 250 cycles at 45 °C. Hence, we first benchmark the NMC811 cathodes in coin-cells against lithium metal anodes by applying upper cutoff potentials between 4.0 and 4.6 V vs. Li^+/Li. Further, we evaluate the gas evolution of the NMC811 cathode using on-line electrochemical mass spectrometry. Next, we investigate SiG//NMC811 full-cells, utilizing a capacitively oversized SiG anode, with respect to their cycling stability and electrode polarization at different C-rates. Using a gold-wire micro-reference electrode we monitor the potentials and the impedance growth of the individual electrodes as a function of the cycle number and the upper cell cutoff voltage. Finally, we prelithiate SiG anodes in half-cells against lithium metal and evaluate the resulting cycling stability and electrode potential evolution in SiG//NMC811 full-cells.

Experimental

Electrode preparation.— The calendared NMC811 cathodes used in this study consisted of a 94:2:3:1 wt% mixture of $LiNi_{0.8}Mn_{0.1}Co_{0.1}O_2$ (NMC811) active material, PVdF binder (Solvay, France), SFG 6L, and C65 conductive carbon (both Timcal / Imerys Graphite & Carbon, Switzerland), which was casted onto an aluminum foil current collector. The NMC811 mass loading was adjusted to ~12.5 mg_{NMC} cm^{-2}, corresponding to a nominal areal capacity of ~2.0 mAh cm^{-2} (160 mAh g^{-1}_{NMC}) at an upper cutoff potential of 4.1 V vs. Li^+/Li. The theoretical specific capacity of 275 mAh g^{-1}_{NMC} is only achieved at higher potentials of about 4.8 V vs. Li^+/Li.

The silicon-graphite (SiG) anodes consisted of a 70:23:5:2 wt% mixture of silicon nanoparticles (Wacker Chemie AG, Germany), KS6L (Imerys Graphite and Carbon, Switzerland), poly(acrylic acid) binder (M_W = 250’000 g mol^{-1}, Sigma-Aldrich, Germany), and C65 conductive carbon (Timcal / Imerys Graphite & Carbon, Switzerland), which was casted onto a copper foil current collector. The combined mass loading of silicon and graphite was ~3.7 mg_{SiG} cm^{-2}, which provided a practical first cycle delithiation capacity of ~7.0 mAh cm^{-2} at a current density of 0.5 mA cm^{-2} and a lower cutoff potential of 0.01 vs. Li^+/Li.

All electrode sheets were prepared by the Volkswagen Varta Microbattery (VW-VM) Forschungsgesellschaft mbH, following a proprietary ink procedure with either water (for SiG anodes) or N-methylpyrrolidone (NMP) (for NMC811 cathodes) as solvent. Prior to cycling, electrode discs of 11 mm in diameter (~0.94 cm^{-2}) were punched out of the sheets and were dried at 120 °C for at least 12 h under vacuum in a glass oven (Büchi, Switzerland), before being transferred into an Ar atmosphere MBraun glovebox (H_2O and O_2 concentration <0.1 ppm) without exposure to ambient atmosphere.

Half-cell measurements.— Electrochemical characterization of the NMC811 cathodes as well as the electrochemical prelithiation of the SiG anodes were performed in CR2032 coin-cells (Hohsen, Japan) with a lithium metal foil (450 µm thickness, 13 mm diameter, Rockwood Lithium, USA) acting as counter and reference electrode, respectively. The cells were assembled by sandwiching two porous glass fiber separators (250 µm thickness, 16 mm diameter, VWR, USA) soaked with 100 µL electrolyte between a lithium metal foil and either an NMC811 electrode (~2.0 mAh cm^{-2}, 11 mm diameter) or

SiG electrode (~7.0 mAh cm^{-2}, 11 mm diameter). As electrolyte, a mixture of 1 M $LiPF_6$ in fluoroethylene carbonate:ethyl methyl carbonate (FEC:EMC, 20:80 vol%) (BASF, Germany) was used.

Full-cell and impedance measurements.— Electrochemical and impedance characterization of the SiG//NMC811 full-cells was performed in Swagelok®-type T-cells (Swagelok, Germany), featuring a lithiated gold-wire micro-reference electrode as described in detail by Solchenbach et al.[37] The cells were assembled by sandwiching two porous glass fiber separators (250 µm thickness, 11 mm diameter, VWR, USA) soaked with 60 µL electrolyte between a SiG anode (~7.0 mAh cm^{-2}, 11 mm diameter) and an NMC811 cathode (~2.0 mAh cm^{-2}, 11 mm diameter). For the full-cells, the same electrolyte was used as for the half-cell measurements, viz., 1 M $LiPF_6$ in FEC:EMC (20:80 vol%).

Battery cycling.— The electrode polarization and cycling stability of the Li//NMC811 half-cells and SiG//NMC811 full-cells were evaluated by means of constant current constant voltage (CCCV) cycling. Hence, the lower cutoff voltage was kept constant at 2.8 V_{cell} across all measurements, whereas the upper (charge) cutoff voltage was varied between 4.0 and 4.6 V vs. Li^+/Li for the half-cells and 4.0 and 4.4 V_{cell} for the full-cells. The voltage was controlled between the cathode and the anode, therefore, furtheron the individual electrode potentials vs. Li^+/Li are abbreviated by V_{Li}, whereas the cell voltage is described by V_{cell}. Initially, two formation cycles were performed at low current density (~0.2 mA cm^{-2}, 0.1 h^{-1}). Consecutive cycling was performed in sequences of 48 cycles at 1.0 h^{-1} (~2.0 mA cm^{-2}) and 2 slow cycles at 0.1 h^{-1} (~0.2 mA cm^{-2}). The C-rate was adjusted in accordance with the upper cutoff voltage, resulting in 1.0 h^{-1} current densities between 2.0-2.5 mA cm^{-2}. All measurements were performed in a climate chamber (Binder, Germany) at 45 °C (±0.5 °C) using a battery cycler (Series 4000, Maccor, USA).

Electrochemical impedance spectroscopy (EIS).— Impedance measurements were performed every 50 cycles during the 2nd slow intermediate cycle at 0.1 h^{-1}, using the Swagelok®-type T-cell setup described above. Hence, the SiG//NMC811 full-cells were charged to a cell voltage of 3.7 V_{cell} and then relaxed at open potential for 2 hours. Afterwards, potentiostatic electrochemical impedance spectroscopy (PEIS) was measured in the frequency range of 100 kHz – 50 mHz, using a perturbation of 15 mV. All impedance measurements were performed in a climate chamber (Binder, Germany) at 45 °C (±0.5 °C) using multi-channel potentiostat VMP3 (BioLogic, France).

On-line electrochemical mass spectrometry (OEMS).— In order to monitor the gases that are evolved during the repeated lithiation of the NMC811 cathodes at 45 °C, operando gas analysis was performed by means of on-line electrochemical mass spectrometry (OEMS). The measurements were conducted in a custom cell hardware (~10.5 ml head space volume) that was described in detail by Tsiouvaras et al.[38] Hence, two glass fiber separators (22 mm diameter, VWR, USA, dried for 3 days at 300°C under vacuum in a glass oven) soaked with 250 µL of the above described electrolyte were sandwiched between a porous NMC811 working electrode and a partially delithiated $Li_{0.05}FePO_4$ counter and reference electrode (~3.2 mAh cm^{-2}, 17 mm, Custom Cells, Germany). Porous NMC811 cathodes were previously prepared by coating an ink, consisting of a 94:3:3 wt% mixture of NMC811:PVdF (Kynar, Arkema, France):C65 (Timcal, Switzerland) in NMP (Sigma-Aldrich, Germany), onto porous woven wire mesh (#500 Mesh SS316 Grade, The Mesh Company, UK). The areal capacity of the resulting electrodes with a diameter of 15 mm amounted to ~2.2 mAh cm^{-2} (based on the theoretical value of 275 mAh g^{-1}_{NMC}). All electrodes were dried at least for 24 h at 120 °C under vacuum in a glass oven (Büchi, Switzerland).

The OEMS measurements were carried out at 45 °C in a climatic chamber (Binder, Germany). Following a 4 h OCV step for background stabilization to ensure decent baseline extrapolation, a galvanostatic formation procedure with a Biologic potentiostat VMP3 (BioLogic, France) between 3.0 and 4.6 V vs. Li^+/Li (-0.45 – 1.15 V cell voltage) was conducted to delithiate (i.e., charge) the NMC811 cathodes with a current rate of 0.1 h^{-1} and subsequently re-lithiate them at 0.2 h^{-1}. The mass signals were quantified using a calibration gas containing H_2, CO, O_2 and CO_2 (2000 ppm in Ar, Westfalen AG, Germany).

Results and Discussion

***Cycling stability and on-line gas evolution analysis of NMC811 cathodes at 45 °C.*— Figure 1** shows the specific discharge capacities of Li//NMC811 half-cells for different upper (charge) cutoff potentials (4.0, 4.2, 4.4, and 4.6 V_{Li}) and a constant lower cutoff potential of 2.8 V_{Li} at (a) 0.1 h^{-1} and (b) at 1.0 h^{-1}, which were obtained from CCCV cycling at 45 °C. Selected cycles and the corresponding capacity retention at different current densities are summarized in **Table I**. As expected, the 2nd cycle discharge capacities at 0.1 h^{-1} increase with the upper cutoff potential from 144, 183, 216 to 226 mAh g^{-1}. Taking into account the respective mean discharge voltages, these capacities translate into specific discharge energies of 500, 652, 782, and 825 mWh g^{-1}_{NMC}. Although the discharge capacity of NMC811 is larger compared to other $LiNi_xMn_yCo_zO_2$ materials with lower Ni contents ($x < 0.8$), the energy density does not increase proportionally because of its flatter potential profile.[28] Thus, (i) to meet the target value of 700-800 mWh g^{-1}_{CAM} for the specific energy for future cathode active materials (CAM) in automotive applications[1,29] and (ii) to compete against state-of-the-art NMC622 cathodes, which provide an initial specific energy of ~685 mWh g^{-1}_{CAM} in NMC622//graphite cells (at 0.1 h^{-1}, 40 °C, and an upper cutoff potential of ~4.4 V_{Li}),[39] an end-of-charge potential of at least 4.3-4.4 V_{Li} is required for NMC811.

Nonetheless, there exists a trade-off between the initial capacity of NMC811 and its capacity retention upon cycling which results in a higher capacity fading with increasing upper cutoff potential. While at 4.0 and 4.2 V_{Li} high capacity retentions of ~99% and ~95% are realized after 250 cycles with a C-rate of 0.1 h^{-1}, at 4.4 and 4.6 V_{Li} the fading becomes more severe, resulting in notably lower capacity retentions of ~85% and ~76% during the same period (compare **Table I**). Further, at higher upper cutoff potentials a strong dependence of the capacity fading on the applied current density can be observed by comparing **Figure 1**(a) and (b), which results in accelerated fading rates at higher currents. For example, at 4.0 V_{Li} the capacity retention approaches ≥99% at either current density, whereas at 4.6 V_{Li} the fading is significantly higher after 250 cycles at 1.0 h^{-1}, resulting in a capacity retention of ~51% at 1.0 h^{-1} compared to ~76% after 250 cycles at 0.1 h^{-1}. As a result, the cycling performance of NMC811 cathodes is governed by at least two degradation phenomena, which differ in their extent and rate-dependence. The first phenomenon shows only minor dependence on the applied current density and results loss of reversible capacity even at low rates. This is usually attributed to the structural instability of Ni-rich NMC cathodes, leading either to cation mixing between Ni and Li cations in Li layers[29] or transition metal dissolution, e.g., of manganese, at potentials ≥4.6 V_{Li}, as reported by Wandt et al.[26] In contrast, the second phenomenon results in a strong polarization of the NMC811 active material upon discharge, which accelerates capacity fading at higher rates (here: 1.0 h^{-1}), but the capacity can be partially recovered at lower rates (here: 0.1 h^{-1}). This degradation can be associated with the structural transition from hexagonal to hexagonal (H2⟶H3),[40,41] which was shown to coincide with the release of lattice oxygen and subsequent formation of a surface-near spinel-like or rock-salt type layer.[6,42]

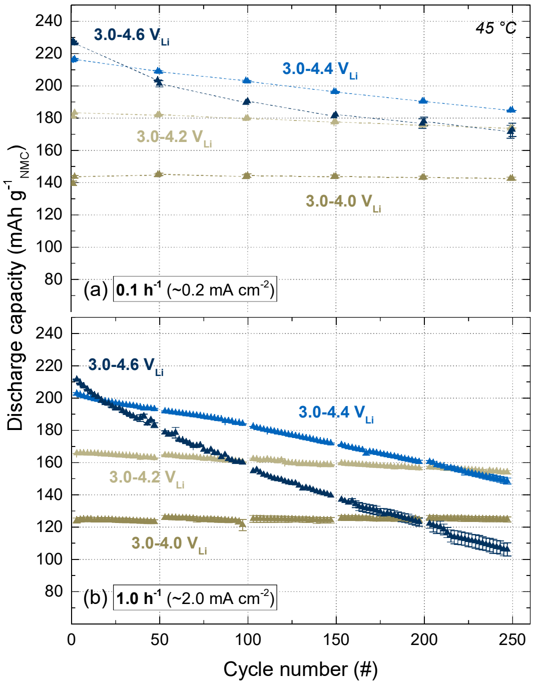

Figure 1. Specific discharge capacity of Li//NMC811 coin-cells (~12.5 mg_{NMC} cm^{-2}) (a) at 0.1 h^{-1} and (b) at 1.0 h^{-1} as a function of the cycle number in 1 M $LiPF_6$ FEC:EMC (20:80 vol%) electrolyte, operated at different upper cutoff potentials (4.0, 4.2, 4.4, and 4.6 V vs. Li^+/Li) and a constant lower cutoff potential of 2.8 V vs. Li^+/Li, using CCCV cycling at 45 °C. Two formation cycles were performed at 0.1 h^{-1}, then repeated sequences of 48 cycles at 1.0 h^{-1} and 2 cycles at 0.1 h^{-1}. The error bars represent the standard deviation of at least two independent repeat measurements.

Recently, Li et al.[30] demonstrated by in-situ XRD measurements of NMC811 that the H2⟶H3 transition coincides with a rapid shrinkage of the c-parameter. Building up on this, Jung et al.[6] proposed that this decrease likely stems from a decreasing repulsion of the oxygen layers, which is caused by the oxidation of the oxygen anions. Eventually, this reaction leads to the release of lattice oxygen, which they showed for different $LiNi_xMn_yCo_zO_2$ materials, including NMC811, by means of on-line electrochemical mass spectrometry (OEMS). Further, the authors concluded that due to the limited diffusion length of oxygen anions in the bulk NMC particles, which was formerly reported by Strehle et al.,[42] the oxygen release and subsequent formation of a spinel-like or rock-salt type layer is restricted to the surface-near region, while the bulk structure stays intact, which was reported analogously for various layered oxides.[36,43,44]

Table I. Specific discharge capacity and capacity retention of Li//NMC811 coin-cells at 0.1 h^{-1} and 1.0 h^{-1}, respectively, in dependence on the upper cutoff potential at 45 °C. The data were extracted from the cycling data shown in **Figure 1** and represent the average of at least two independent repeat measurements. The error ranges represent the standard deviations of at least two independent repeat measurements.

Cutoff potentials	**Capacity @ 0.1 h^{-1} / mAh g^{-1}** 2nd cycle	**Capacity @ 0.1 h^{-1} / mAh g^{-1}** 250th cycle	**Capacity retention / %**	**Capacity @ 1.0 h^{-1} / mAh g^{-1}** 5th cycle	**Capacity @ 1.0 h^{-1} / mAh g^{-1}** 245th cycle	**Capacity retention / %**
2.8-4.0 V_{Li}	144 ± 0.7	143 ± 0.9	99 ± 0.1	125 ± 1.4	125 ± 1.5	100 ± 0.0
2.8-4.2 V_{Li}	183 ± 0.0	174 ± 0.1	95 ± 0.1	166 ± 0.1	154 ± 0.7	93 ± 0.4
2.8-4.4 V_{Li}	216 ± 0.6	185 ± 0.0	85 ± 0.1	202 ± 0.6	149 ± 1.8	74 ± 1.2
2.8-4.6 V_{Li}	226 ± 0.3	173 ± 4.0	76 ± 1.7	209 ± 0.2	106 ± 3.9	51 ± 1.8

To determine the onset of the release of lattice oxygen from the here investigated active material **Figure 2** shows (a) the voltage profile of a mesh-coated NMC811 cathode during the first galvanostatic charge/discharge at 0.1 h^{-1}/0.2 h^{-1} against a partially delithiated $Li_{0.05}FePO_4$ electrode. The corresponding (b) integral gas evolution and (c) gas evolution rate of oxygen (O_2, m/z = 32, marine), carbon dioxide (CO_2, m/z = 44, blue), and carbon monoxide (CO, m/z = 28, brown) are also depicted. A small activation peak can be observed in the voltage profile of the NMC811 within the first few minutes which results from the initial removal of surface contaminants that likely originate from the storage of the active material.[45] Yet, almost no gas evolution can be observed within the first 8 hours except for a slow, almost linear increase of the CO_2 mass signal (blue line). Originally, this feature has been related to the electrochemical oxidation of carbonate impurities at the NMC particle surface,[46,47] whereas recently, Jung et al.[39] proposed based on measurements with a ^{13}C-labelled ethylene carbonate (EC) electrolyte that the initial CO_2 formation most likely stems from the oxidation of electrolyte impurities. The oxidation of the impurities leads to a nearly quantitative release of CO_2, even though no O_2 release is detected yet. In contrast, at about 4.25 V_{Li}, viz., once the NMC811 state-of-charge exceeds 80% (referring to a total specific capacity of 275 mAh g^{-1}_{NMC}), a distinct increase of the oxygen signal (marine line) can be observed in **Figure 2**(b). During the same period, a rapid increase in the CO_2 and CO can be detected, indicating the oxidative decomposition of electrolyte constituents. This rapid change in the gas evolution rates can be rationalized by the onset of a fundamentally different oxidation mechanism. While the first part was dominated by the oxidation of impurities, minor electrochemical electrolyte decomposition, and likely the thermal decomposition of fluoroethylene carbonate (FEC),[48,49] at potentials above 4.25 V_{Li} reactive oxygen is released from the NMC811 active material which leads to a chemical oxidation of the alkyl carbonate electrolyte. Again, we would like to highlight that this phenomenon is not due to electrochemical oxidation of the electrolyte, because similar experiments by Jung et al.,[48] with 1 M $LiPF_6$ in EC:EMC in presence of either C65 or LNMO revealed no electrolyte decomposition at potentials below 5.0 V_{Li} but instead related to chemical oxidation. By operando emission spectroscopy, Wandt et al.[50] recently proved that singlet oxygen is evolved upon delithation exceeding roughly 80% state-of-charge for layered transition metal oxides as NMCs. For NMC811 the evolution of this highly reactive oxygen species is especially critical for battery aging as this state-of-charge is reached at a lower charging potential due to the flatter potential profile with higher Ni content.

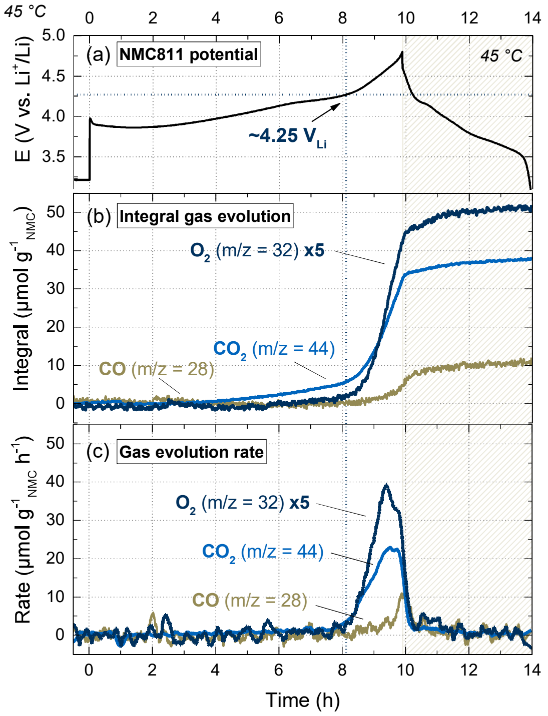

Figure 2. Gas evolution during the first galvanostatic charge/discharge of a NMC811 cathode (~2.2 mAh cm^{-2}) at 0.1 h^{-1}/0.2 h^{-1}. (a) NMC811 potential calculated from the $Li_{0.05}FePO_4$//NMC811 cell voltage as a function of time. (b) Integral gas evolution and (c) gas evolution rate of oxygen (O_2, m/z = 32, marine line), carbon dioxide (CO_2, m/z = 44, blue line), and carbon monoxide (CO, m/z = 28, brown line) as a function of time. Electrolyte: 1 M $LiPF_6$ in FEC:EMC (20:80 vol%), temperature: 45 °C. The OEMS data are smoothed, baseline corrected and converted into units of µmol g^{-1}_{NMC}. The results were confirmed by three independent repeat measurements.

Although the structural transformation of the NMC811 also results in a permanent loss of reversible capacity, the formation of the oxygen-depleted layer additionally impedes the diffusion of Li^+ ions and increases the charge-transfer resistance. This results in an increase of the electrode's overpotential and further lowers the reversible capacity at higher C-rates. Because the thickness growth of this layer strongly depends on the upper cutoff potential and thus impacts the cycling stability and rate capability of NMC811,[6,7,30] we focus our analysis on the implications for the realizable capacity and the aging behavior of the SiG//NMC811 full-cells.

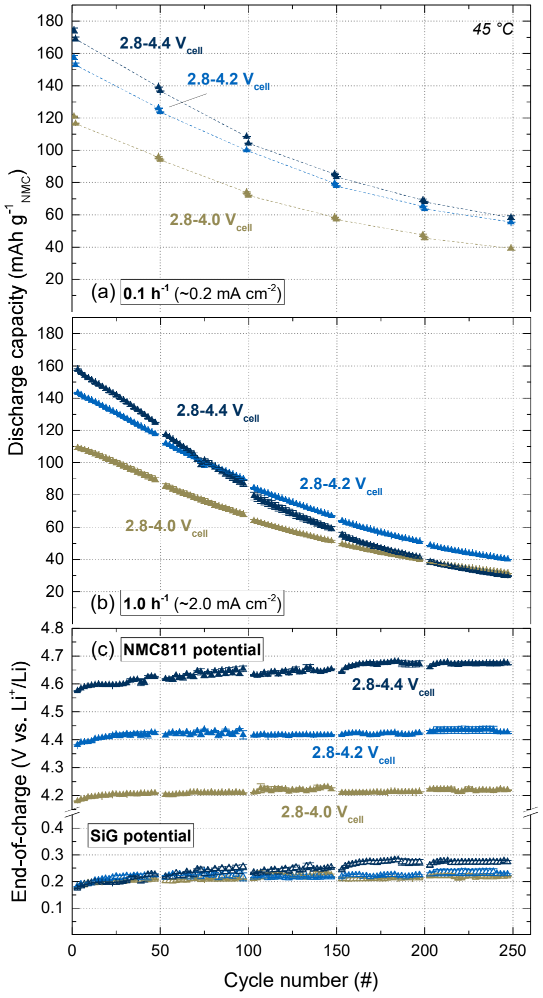

Figure 3. (a, b) Specific discharge capacity of SiG//NMC811 Swagelok®-type T-cells (a) at 0.1 h^{-1}, (b) at 1.0 h^{-1}, and (c) the corresponding end-of-charge electrode potentials of the NMC811 cathode (solid symbols) and the SiG anode (hollow symbols) monitored by a lithiated gold-wire micro-reference electrode as a function of the cycle number in 1 M $LiPF_6$ FEC:EMC (20:80 vol%) electrolyte, operated at different upper cell cutoff voltages (4.0, 4.2, and 4.4 V_{cell}) and a constant lower cell cutoff voltage of 2.8 V_{cell}, using CCCV cycling at 45 °C. Two formation cycles were performed at 0.1 h^{-1}, then repeated sequences of 48 cycles at 1.0 h^{-1} and 2 cycles at 0.1 h^{-1}. The error bars represent the standard deviation of at least two independent repeat measurements.

Cycling performance of SiG//NMC811 full-cells at different upper cutoff voltages.**—** **Figure 3** shows the cycling stability of SiG//NMC811 full-cells (a) at 0.1 h^{-1} and (b) at 1.0 h^{-1}, obtained from CCCV cycling between a constant lower cutoff voltage of 2.8 V_{cell} and different upper cutoff voltages of 4.0, 4.2, and 4.4 V_{cell} at 45 °C. Analogous to the half-cell measurements, the second cycle discharge capacities increase with increasing upper cutoff voltage from 116, 153 to 169 mAh g^{-1}_{NMC} (see **Table II**), which corresponds to areal capacities of 1.5, 1.9, and 2.1 mAh cm^{-2}, respectively. Considering a reversible SiG anode capacity of about 7.0 mAh cm^{-2} (see **Figure 6**), this translates into a balancing (n:p) ratio of 4.7-3.3, depending on the upper cutoff voltage. In other words, the reversible capacity of the NMC811 cathode accounts only for 21-30% of the reversible capacity of the SiG anode. Since silicon-based electrodes usually reveal a higher coulombic efficiency and less capacity fading when their capacity and thus the volumetric changes are restricted,[10,20] the lower anode capacity utilization is expected to improve the cycling stability of the SiG//NMC811 full-cells. Yet, according to **Figure 3**(a) all cells show a rapid capacity decay upon continued cycling at 45 °C that largely exceeds the fading observed in the half-cell measurements shown in **Figure 1**. After 250 cycles, the residual capacities of the full-cells amount to 39, 55, and 58 mAh g^{-1}_{NMC} at 0.1 h^{-1}, thus corresponding to similar capacity retentions of 34-36% (compare **Table II**). In contrast, at higher rates shown in **Figure 3**(b) the fading notably increases at higher upper cutoff voltages of 4.4 V_{cell}, leading to a lower capacity retention of 19% compared to 28-29% at 4.0 and 4.2 V_{cell}, respectively. As recently pointed out by Klett et al.,[51] these differences in the capacity retention at different C-rates suggest that at 4.0 and 4.2 V_{cell} the cycling stability is mostly governed by the loss of active lithium from the NMC811 cathode caused by perpetual side reactions at the SiG anode, whereas at 4.4 V_{cell} the cycling stability is increasingly influenced by an additional electrode polarization, which has only minor impact at low current density but increasingly impedes the cell performance at higher current densities.

Because the SiG//NMC811 full-cells were controlled by the cell voltage, the evolution of the individual electrode potentials (V vs. Li^+/Li) plays a major role in understanding the discrepancy of the cycling stability at different upper cutoff voltages. **Figure 4** shows the cell voltage of a SiG//NMC full-cell (marine line) and the corresponding electrode potentials of the SiG anode (dotted blue line) and the NMC811 cathode (dashed brown line), respectively, which were monitored by a lithiated gold-wire micro-reference electrode and confirmed by an independent measurement with a lithium metal reference electrode (data not shown). As a result of the capacitively oversized SiG anode and the high average lithiation potential of silicon,[3,19] the SiG anode potential remains at values above 0.16 V_{Li} even at the end of charge, which in turn leads to a shift of the NMC811 potential by the same extent towards more positive potentials. Considering an upper cutoff voltage of 4.4 V_{cell}, this translates into an end-of-charge potential of ~4.56 V_{Li} for the NMC811 cathode, i.e., the electrode operates well above the onset of the oxygen release and subsequent formation of the resistive spinel-like layer at the NMC811 particle surface, as demonstrated by **Figure 2**.

Table II. Specific charge/discharge capacity, coulombic efficiency and capacity retention of SiG//NMC811 Swagelok®-type T-cells of selected cycles at 0.1 and 1.0 h^{-1}, respectively, in dependence on the upper cell cutoff voltage at 45 °C. The data were extracted from the cycling data shown in **Figure 3** and represent the average of at least two independent repeat measurements.

		Cutoff voltages		
	Units	2.8-4.0 V_{cell}	2.8-4.2 V_{cell}	2.8-4.4 V_{cell}
1st charge-discharge cycle				
Charge capacity	mAh g^{-1}_{NMC}	180 ± 1.2	222 ± 0.7	241 ± 0.3
Discharge capacity	mAh g^{-1}_{NMC}	121 ± 0.3	157 ± 1.3	174 ± 1.6
Irreversible capacity loss	mAh g^{-1}_{NMC}	59 ± 1.5	64 ± 0.7	67 ± 1.9
Coulombic efficiency	%	67 ± 0.6	71 ± 0.4	72 ± 0.7
Capacity @ 0.1 h^{-1}				
2nd cycle discharge	mAh g^{-1}_{NMC}	116 ± 0.2	153 ± 1.1	169 ± 1.3
250th cycle discharge	mAh g^{-1}_{NMC}	39 ± 0.8	55 ± 0.1	58 ± 1.2
Capacity retention	%	34 ± 0.6	36 ± 0.0	34 ± 0.4
Capacity @ 1.0 h^{-1}				
5^{5h} cycle discharge	mAh g^{-1}_{NMC}	108 ± 0.9	142 ± 0.1	156 ± 0.2
245th cycle discharge	mAh g^{-1}_{NMC}	32 ± 0.1	40 ± 0.1	30 ± 0.4
Capacity retention	%	29 ± 0.2	28 ± 0.1	19 ± 0.2

To monitor the evolution of the individual electrode potentials, **Figure 3**(c) shows the end-of-charge potentials of the SiG anode (lower panel) and the NMC811 cathode (upper panel) as a function of the cycle number. An eventual potential drift of the lithiated gold-wire micro-reference electrode was mitigated by periodic re-lithiation after every 50 cycles (prior to impedance measurements). Accordingly, the end-of-charge potential of the SiG anode reveals a rapid increase up to ~0.2 V_{Li} within the first 10 cycles independent of the upper cell cutoff voltage. This can be ascribed to the higher average lithiation potential of amorphous silicon compared to the uncycled crystalline silicon particles.[52] In addition, the large capacity excess of the SiG anode relative to the capacity-limiting NMC811 cathode results on average in a low degree of lithiation and thus a higher average SiG anode potential. Upon cycling, the electrode potential increases further because of the loss of active lithium, which translates into a minor but continuous increase of the end-of-charge potential to 0.22 V_{Li}. At an upper cutoff voltage of 4.4 V_{cell} (marine symbols) the potential shift is even larger, which likely stems from increased side reactions at the SiG anode, which are caused at higher NMC811 potentials as will be discussed in the next section.

The comparatively high end-of-charge potential of ~0.2 V_{Li} of the SiG anode has three important implications for SiG//NMC811 lithium-ion batteries: (i) It results in an upward shift of the NMC811 cathode potential, which constantly operates at least ~200 mV above the controlled cell voltage and thus may cause a concern both in terms of durability and safety. (ii) It lowers the effective energy density compared to conventional graphite electrodes, which are operated on average at about 100-150 mV lower potentials.[6] (iii) It results in an operation of the SiG anodes at low degrees of lithiation (here between 0 and 31% SOC), which was previously shown to be less favorable compared to an operation at higher degrees of lithiation (e.g., 60-90% SOC) both in terms of cycling stability and coulombic efficiency.[14,18]

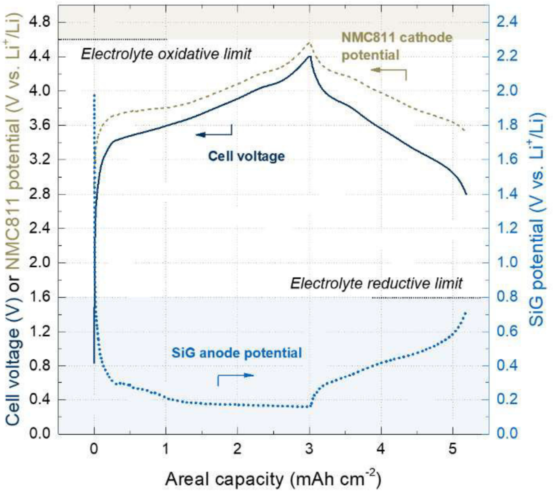

Figure 4. Cell voltage of a SiG//NMC811 Swagelok®-type T-cell (marine line, left panel) and electrode potentials of the NMC811 cathode (brown dashed line, left panel) and the SiG anode (blue dotted line, right panel) as a function of the areal capacity during the first charge/discharge cycle, obtained from CCCV cycling between 2.8 and 4.4 V_{cell} at 0.1 h^{-1} and 45 °C. The electrode potentials were monitored by a lithiated gold-wire micro-reference electrode. The brown and the blue shaded areas indicate the oxidative and the reductive stability limit of the carbonate-based electrolyte.

Impedance growth of SiG//NMC811 full-cells at different upper cutoff voltages.— To confirm the the higher electrode impedance at cutoff potentials above 4.25 V_{Li}, impedance spectroscopy of the SiG//NMC811 full-cells was measured every 50 cycles during the charge of the second intermediate 0.1 h^{-1} cycle at 3.7 V_{cell} after 120 min at open circuit potential. The gold-wire micro-reference electrode setup allows to separate the impedance contributions of anode and cathode, whereby the sum of both electrodes equals the overall full-cell impedance.[37] **Figure 5**(a) shows the Nyquist plot of representative impedance responses of the NMC811 cathodes after 150 cycles at different upper cell cutoff voltages. Accordingly, the impedance is characterized by a large distorted semicircle in the interfacial impedance frequency range (1 kHz – 1 Hz), which consists of the pore resistance R_{pore} and the charge-transfer resistance R_{ct} at the NMC811/electrolyte interface. The offset along the Z'-axis reflects the high frequency resistance R_{HFR} which remains almost constant upon cycling. In contrast, the smaller distorted feature at frequencies above 1 kHz occurring in the cells cycled to 4.2 and 4.4 V_{cell} likely originates from a contact resistance that is caused by HF-induced degradation of the aluminum current collector, as described by Gaberscek et al.[53] Further, a linear slope at low frequencies (< 1 Hz) can be observed for the cells at 4.0 and 4.2 V_{cell}, which corresponds to the Warburg diffusion Z_W. Because the impedance in the present study was only measured in non-blocking conditions,[54] it is not possible to adequately distinguish the individual impedance contribution, thus, we will furtheron only consider the low frequency resistance R_{LFR} which describes the sum of R_{HFR}, $R_{contact}$, R_{pore} and R_{ct}. Yet, we would like to emphasize that the dominating feature that is increasing upon cycling is the large semicircle comprising the pore resistance and the charge-transfer resistance at the NMC811/electrolyte interface.

Figure 5(b) and (c) summarize the low frequency resistances R_{LFR} of the SiG anode and the NMC811 cathode as a function of the cycle number and the applied upper cutoff voltage at 45 °C. The R_{LFR} were obtained by fitting of the Nyquist impedance spectra using a serial connection of a resistor, two RQ-elements (i.e., a resistor and constant phase element in parallel) and a Warburg element Z_W, whereby R_{LFR} equals the sum of the three resistors.[55] As can be seen, both the SiG anode and the NMC811 reveal a continuous impedance growth upon cycling. Yet, their growth rates differ notably in dependence on the upper cell cutoff voltage. The SiG anode impedance increases from 3-4 Ω cm^2 during the second cycle to 20, 45, and 80 Ω cm^2 after 250 cycles at an upper cutoff voltage of 4.0, 4.2, and 4.4 V_{cell}, respectively. The moderate increase of the growth rate between 4.0 and 4.2 V_{cell} can be explained by the higher charge throughput and thus a higher amount of electrolyte decomposition products in the SiG anode.[3] In contrast, the larger increase of the anode impedance at an upper cell cutoff voltage of 4.4 V_{cell} indicates the presence of an additional degradation mechanism which likely originates from cross-diffusion of oxidation products, resulting from parasitic reactions occurring at the NMC811 cathode at high potentials.[25,56,57]

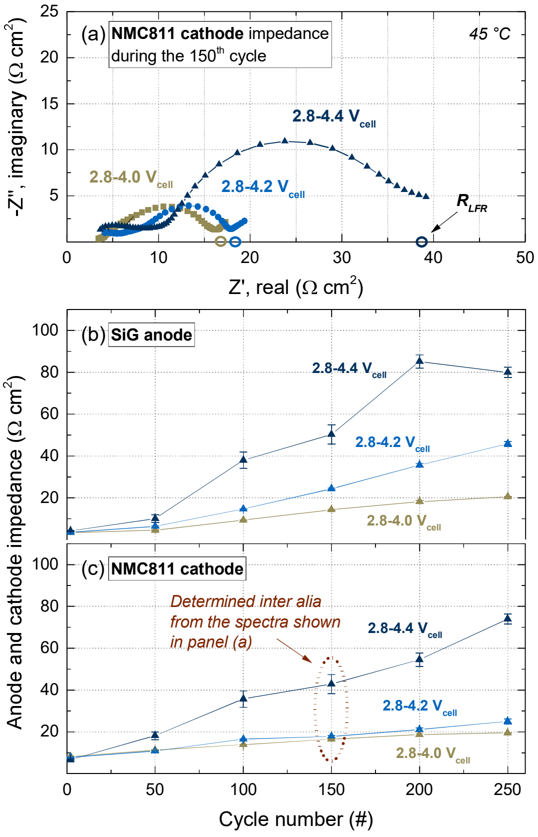

Figure 5. (a) Nyquist plot of the NMC811 cathode impedance exemplarily shown for the 150th charge/discharge cycle. Spectra were recorded at 45 °C from the SiG//NMC811 Swagelok®-type T-cells shown in **Figure 3** which were cycled at different upper cell cutoff voltages, including 2.8-4.0 V_{cell} (brown), 2.8-4.2 V_{cell} (blue), and 2.8-4.4 V_{cell} (marine). Potentiostatic impedance spectroscopy was measured with a perturbation of 15 mV and a frequency range of 100 kHz – 50 mHz after charging the cells to 3.7 V_{cell} and holding them at open circuit potential for 120 min. (b, c) Evolution of the lower frequency resistance (R_{LFR}) of (b) the SiG anode and (c) the NMC811 cathode in dependence on the upper cell cutoff voltage as a function of the cycle number.

On the cathode side, the cells which were cycled at 4.0 and 4.2 V_{cell} show a very similar increase of the NMC811 impedance from 6-8 to 20-25 Ω cm^2 after 250 cycles. In contrast, the cells with an upper cutoff voltage of 4.4 V_{cell} reveal a significant jump up to 74 Ω cm^2 during the same period. To explain this discrete voltage-dependent impedance growth, three mechanisms need to be distinguished that lead to an increase of the low frequency resistance R_{LFR} of the investigated NMC811 cathodes and also affect the SiG anode: (i) At lower cutoff voltages, i.e., at 4.0 and 4.2 V_{cell}, respectively, the small increase in the impedance can be partially attributed to low electrochemical oxidation rates that occur at potentials below 5.0 V_{Li}, especially at elevated temperatures. These may add up to a significant extent of oxidative charge and oxidation products during long-term cycling and thus may contribute to long-term impedance growth.[58–60] Nonetheless, we think that the electrochemical oxidation is not the dominating mechanism, because the Tafel-slope kinetics would suggest a linear increase, which contradicts the strong impedance growth at an upper cutoff voltage of 4.4 V_{cell}. Further, Jung et al.[48] recently demonstrated that the intrinsic oxidative stability of an LP57 electrolyte (1 M $LiPF_6$ in EC:EMC, 30:70 wt%) on either $LNi_{0.5}Mn_{1.5}O_4$ or pure C65 conductive carbon was rather high at room temperature. Instead, (ii) Kim et al.[49] recently reported that the thermal instability of FEC in $LiPF_6$-based electrolytes at elevated temperatures (here: 45 °C) may lead to a defluorination of FEC by PF_5 and subsequent formation of vinylene carbonate (VC) and HF. These products cause parasitic reactions, including the oxidation of VC and dissolution of transition metal from the NMC811 cathode, and thus contribute to a further increase of the charge-transfer resistance R_{ct}.[61] While the first two phenomena occur across all investigated upper cutoff voltages and evidently result in a comparatively 'small' impedance increase of factor ~2 after 250 cycles at 45 °C, an additional mechanism is required to account for the rapid growth of the impedance between 4.2 and 4.4 V_{cell}, leading to an almost 10-fold increase during the same period as shown in **Figure 5**(c). Jung et al.[48] proposed the chemical electrolyte oxidation caused by the release of lattice oxygen and formation of an oxygen-depleted layer at the surface of the NMC811 particles as an alternative pathway, which agrees well with the significant increase of the low frequency resistance R_{LFR} once the cell voltage exceeds a certain value between 4.2 and 4.4 V_{cell}. This process has two negative implications for the resistance at the NMC811/electrolyte interface, including (i) the formation of a resistive spinel-like layer at the NMC811 particle surface as well as (ii) a subsequent accumulation of reaction products from the electrolyte oxidation. In accordance with **Figure 5**(b), the oxidation products may also diffuse from the cathode to the SiG anode, as reported recently by Metzger et al.,[25] and result in additional parasitic reactions which further increase the anode impedance. As a corollary, the rate of the anode impedance growth also correlates with the amount of side reactions occurring at the NMC811 cathode. Moreover, silicon-based electrodes are particularly prone to cross-diffusional degradation, because of the usually much larger surface area compared to graphite and the volumetric changes upon (de-)lithiation which result in a poor passivation of the silicon/electrolyte interface caused by repeated cracking and renewal of the SEI, in particular at elevated temperatures.

Our results from impedance spectroscopy and gas analysis demonstrate unanimously that NMC811 cathodes reveal a high sensitivity toward the upper cutoff voltage. Once the cathode exceeds ~80% state-of-charge, corresponding here to an electrode potential of ~4.25 V_{Li}, reactive oxygen is released from the NMC lattice which results in the formation of an oxygen depleted layer and chemical electrolyte oxidation at the cathode surface, thus leading to a significant impedance growth. In full-cells consisting of SiG anodes and NMC811 cathodes, this problem becomes even more severe, because the comparatively positive anode potential results in an upward shift of the NMC811 cathode of up to ~200 mV to more positive potentials. Therefore, SiG//NMC811 full-cells that were cycled to upper cutoff voltages of 4.4 V_{cell} indicate a much lower capacity retention at higher current densities. To cope with this challenge, various strategies were deployed by researchers aiming on a stabilization of the NMC811 surface, including core-shell[62] and concentration gradient materials,[63,64] with nickel contents ≥75% and ≤56% in the particle center and the surface, respectively. In addition, surface coatings of alumina[65,66] and $LiMn_2O_4$[67] as well as aluminum doping[68,69] were shown to improve the cycling stability of Ni-rich NMC cathodes. However, we think that these strategies are only successful as long as the release of oxygen is prevented by limited diffusion of the oxygen anions through a thick shell. Once the NMC particles start to break due to the repeated volumetric stress upon (de-)lithiation, as recently reported by Janek and co-workers, oxygen release may occur at the sites of fractures, thus leading to an additional impedance growth.[70]

Influence of prelithiation of SiG anodes on the cycling stability of SiG//NMC811 full-cells.— In the present study, we investigate the prelithiation of the SiG anode as an alternative route to mitigate the release of oxygen from NMC811 cathodes in SiG//NMC811 full-cells. Prelithiation of anodes is thermodynamically more complex compared to cathode materials, because a more reactive lithium source is required and the lithiated active materials are usually more reactive and harder to control.[71] Yet this approach offers several advantages, including (i) a lower average anode potential, (ii) a mitigation of the irreversible capacity loss during formation, and (iii) a reservoir of active lithium to compensate ongoing side reactions at the silicon-electrolyte interface upon cycling.[21,72–74] Since the goal of our present study is to evaluate the influence of prelithiation of SiG anodes on the end-of-charge potential of the NMC811 cathode, we applied electrochemical prelithiation of the SiG anodes against lithium metal counter electrodes. On a lab-scale, this offers a convenient method to quantify accurately the amount of reversibly prelithiated lithium in the anode active materials. **Figure 6**(a) shows potential profiles of SiG anodes during the first lithiation/delithiation using different end-of-lithiation potentials (200, 110, 100 and 10 mV_{Li}). The flat potential profile during the first cycle is characteristic for the lithiation of the initially crystalline silicon particles and leads to large changes of the areal capacity even if the potential differs only by few mV.[20] For that reason, the prelithiation of silicon-based electrodes is usually defined by a constant capacity rather than a potential-limit. To understand how much lithium was inserted into the SiG anodes and which fraction of it is available furtheron as active lithium, **Figure 6**(b) summarizes the prelithiation capacity as well as the reversible delithiation capacity of the SiG anodes as a function of the end-of-lithiation potential. Accordingly, a lithiation to 200 mV_{Li} corresponds to an insertion of ~0.4 mAh cm^{-2} into the SiG anodes, whereby ~0.2 mAh cm^{-2} are consumed by irreversible processes, e.g., SEI formation, and ~0.2 mAh cm^{-2} (~53%) can be extracted reversibly. Further lithiation to 110 and 100 mV_{Li} results in an increase of the coulombic efficiency up to 80-82%, as the SEI losses are compensated by an increasing lithiation capacity of ~2.9 and ~5.8 mAh cm^{-2}, respectively. Full lithiation of the SiG anode to 10.3 mAh cm^{-2} is realized by applying an end-of-lithiation potential of about 10 mV_{Li}. However, the coulombic efficiency decreases again to 68% due to the immobilization of lithium in the silicon active material across the thick SiG coating and increased side reactions caused by the reactivity of the highly lithiated Li_xSi phases.[75] Nonetheless, because the active lithium of the NMC811 cathode also needs to be accommodated by the SiG anode during the first charge of the SiG//NMC811 full-cells, which amounts up to 3.0 mAh cm^{-2} (see **Figure 4**) depending on the prelithiation and the upper cutoff voltage, we selected 100 mV$_{Li}$, i.e., ~5.8 mAh cm^{-2}, as the maximum prelithitiation capacity to maintain a safety margin of at least ~15% (= 3.0 + 5.8 mAh cm^{-2} divided by 10.3 mAh cm^{-2}; compare **Figure 6**) and thus avoid lithium plating at the SiG anode. In the following, the cells are always labelled by their prelithiation capacity, viz., 0.4 (blue), 2.9 (marine), and 5.8 mAh cm^{-2} (green).

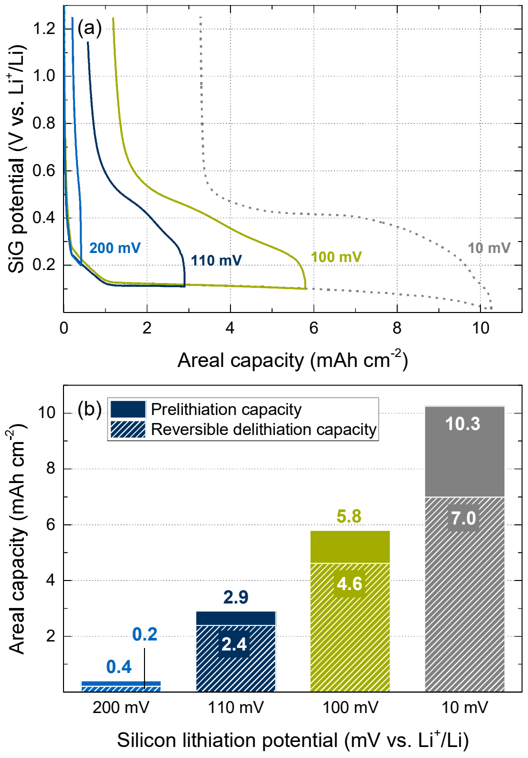

Figure 6. (a) SiG electrode potential as a function of the areal capacity during the first lithiation/delithiation in Li//SiG coin-cells (~3.7 mg$_{SiG}$ cm^{-2}), obtained from galvanostatic cycling at 0.5 mA cm^{-2} and 45 °C in 1 M LiPF$_6$ FEC:EMC (20:80 vol%) electrolyte using different lower cutoff potentials (200, 110, 100, and 10 mV vs. Li$^+$/Li) and a constant upper cutoff potential of 1.25 V vs. Li$^+$/Li. (b) Areal prelithiation capacity (solid) and reversible delithiation capacity (patterned) as a function of the lower cutoff potential during electrochemical prelithiation against lithium metal counter electrodes.

Figure 7 shows the areal discharge capacity of SiG//NMC811 full-cells (a) at 0.1 h^{-1} and (b) at 1.0 h^{-1}, as well as (c) the corresponding end-of-charge potentials of the SiG anode and the NMC811 cathode, respectively, which were operated at cell cutoff voltages between 2.8 and 4.1 V_{cell}. As expected, the SiG//NMC811 full-cells with a pristine SiG anode (brown) reveal a similar cycling stability as the full-cells shown in **Figure 3**, which were operated at upper cutoff voltages of 4.0 and 4.2 V_{cell}, respectively. During the second cycle at 0.1 h^{-1}, they realized a discharge capacity of 1.83 mAh cm^{-2} but showed a continuous decay to 0.68 mAh cm^{-2} after 250 cycles at 45 °C, which corresponds to a capacity retention of 37% (146 → 54 mAh g^{-1}_{NMC}). A prelithiation capacity of ~0.4 mAh cm^{-2} in the SiG anode (blue) lifts the initial discharge capacity by almost the same amount, resulting in a second cycle discharge capacity of 2.18 mAh cm^{-2} (174 mAh g^{-1}_{NMC}), because less lithium is consumed from the NMC811 cathode for the SEI formation and thus still contributes the reversible capacity. However, the higher utilization of the SiG anode also resulted in an increased loss of active lithium, which is reflected by a stronger capacity fade within the first 100 cycles, when compared to the pristine SiG anode. Further prelithiation with ~2.9 mAh cm^{-2} (marine) resulted in an even higher initial discharge capacity of 2.38 mAh cm^{-2} (191 mAh g^{-1}_{NMC}) in the SiG//NMC811 full-cells. Although this capacity remained fairly stable during the first 50 cycles, an abrupt decay can be observed thereafter, which can be rationalized by considering that any lithium loss is only compensated until the reservoir in the SiG anode is depleted. Nonetheless, **Figure 7**(c) shows that the higher lithium content in the anode also resulted in a shift of the end-of-charge potential towards more negative potentials of 0.14-0.16 V_{Li} compared to the 0.16-0.22 V_{Li}, obtained from the pristine SiG anode. As a corollary, the NMC811 is also operated at a ~60 mV lower end-of-charge potential. Moreover, the relatively stable end-of-charge potential of the SiG anode upon prolonged cycling indicates that a large fraction of the prelithiated lithium remains trapped in the anode and does not contribute to the compensation of the active lithium loss. As the impedance of the SiG anode increases upon cycling, the amount of the immobilized lithium likely also increases. In other words, the amount of reversibly accessible lithium is effectively lower as indicated by the first cycle delithiation capacity of the Li//SiG half-cells shown in **Figure 6**.

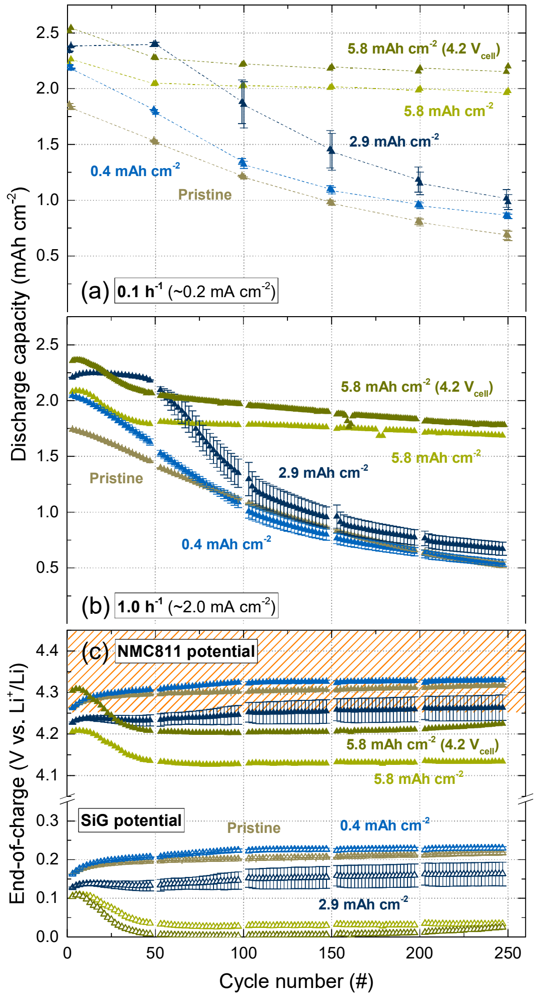

Figure 7. (a, b) Areal discharge capacity of SiG//NMC811 Swagelok®-type T-cells (a) at 0.1 h^{-1}, (b) at 1.0 h^{-1}, and (c) the corresponding end-of-charge electrode potentials of the NMC811 cathode (solid symbols) and the SiG anode (hollow symbols) monitored by a lithium metal reference electrode as a function of the cycle number in 1 M $LiPF_6$ FEC:EMC (20:80 vol%) electrolyte, operated with differently prelithiated SiG anodes (pristine, 0.4, 2.9, and 5.8 mAh cm^{-2}; compare **Figure 6**) between cell cutoff voltages of 2.8-4.1 V_{cell} (or 4.2 V_{cell}, see dark green symbols) using CCCV cycling at 45 °C. The procedure was the same as for the cells in **Figure 3**, including two formation cycles were performed at 0.1 h^{-1}, then repeated sequences of 48 cycles at 1.0 h^{-1} and 2 cycles at 0.1 h^{-1}. The error bars represent the standard deviation of at least two independent repeat measurements. The orange dashed area indicates the NMC811 cathode potential of 4.25 V_{Li} above which oxygen was released during the OEMS measurements shown in **Figure 2**.

A further prelithiation with ~5.8 mAh cm^{-2} (green) resulted in a slightly lower second cycle discharge capacity of 2.26 mAh cm^{-2}, which is caused by the reduced end-of-charge potential of the NMC811. Afterwards, a fairly stable cycling is observed over 250 cycles at 45 °C due to the larger lithium reservoir, yielding a residual capacity of 1.98 mAh cm^{-2} at 0.1 h^{-1} and 1.69 mAh cm^{-2} at 1.0 h^{-1}, respectively. Remarkably, the high capacity retention is not only accomplished at 0.1 h^{-1} (182 → 158 mAh g^{-1}_{NMC}, ~87%) but also at higher C-rate of 1.0 h^{-1} (168 → 133 mAh g^{-1}_{NMC}, ~80%).

This can be explained by the end-of-charge potentials shown in **Figure 7**(c). While in presence of the pristine or moderately prelithiated SiG anode (i.e., 0.4 and 2.9 mAh cm^{-2}), the NMC811 is still repeatedly operated above the critical potential of 4.25 V_{Li}, a higher prelithiation of the SiG anode with 5.8 mAh cm^{-2} resulted in a shift of the anode potential profile towards lower values. As a corollary, the NMC811 is operated a lower end-of-charge potentials which mitigates the release of lattice oxygen from the active material and subsequent growth of the resistive spinel-like layer at the NMC811 particle surface. Thus, prelithiation of the SiG anode does not only allow to compensate the loss of active lithium for a limited number of cycles but also maintains the rate capability of the NMC811 cathode by reducing its end-of-charge potential and thus making it less susceptible to the release of oxygen upon voltage slippage over prolonged cycling. Furthermore, the lower end-of-charge potential of the NMC811 cathode even allows to increase the upper cell cutoff voltage from 4.1 to 4.2 V_{cell}, while still avoiding the critical potential region above ~4.25 V_{Li}. SiG//NMC811 full-cells which were operated between 2.8 and 4.2 V_{cell} with a SiG anode prelithiated to a reversible capacity of ~5.8 mAh cm^{-2} (dark green) provided a second cycle discharge capacity of 2.54 mAh cm^{-2} and residual capacity as high as 2.2 mAh cm^{-2} at 0.1 h^{-1} after 250 cycles at 45 °C (217 → 187 mAh g$^{-1}_{NMC}$, ~86%). As expected, a similar retention of 75% (201 → 152 mAh g$^{-1}_{NMC}$) was also obtained at a higher C-rate of 1.0 h^{-1}. However, the low potential of the SiG anode shown in **Figure 7**(c) also demonstrates a limitation of this approach. Once the state-of-charge of the anode becomes too high, its potential approaches 0 V vs. Li$^+$/Li and thus enables lithium plating which in turn increases the amount of side reactions and raises safety concerns.

As a corollary, our results demonstrate that the prelithiation of a capacitively oversized SiG anode offers an attractive approach to obtain high areal capacities and a fairly stable cycling in SiG//NMC811 full-cells, while mitigating the release of lattice oxygen by reducing the end-of-charge potential of the NMC811 cathode. However, for commercially-sensible electrodes it is also important to evaluate the impact of the oversized anode on the effective energy density of the cell as well as the risk of lithium plating at high degrees of prelithiation. In addition, we would like to emphasize that the focus of the present study was mostly on the evolution of the electrode potentials and the resulting cycling stability at different C-rates. To evaluate whether the use of SiG//NMC811 lithium-ion batteries indeed allows to realize the required specific energy target of 300-350 Wh kg^{-1} on a cell-level we encourage researchers to provide more information concerning the electrolyte consumption and the mass contributions from both the anode and the electrode coating. In fact, the practical gain compared to graphite-based electrodes will likely be in the order of less than 30%[10,11] because of the still higher irreversible capacity and the higher electrolyte demand of silicon-based full-cells. Thus, closing the gap to the specific energy target will require combined strategies which include an optimization of the NMC811 cathode to allow an operation at higher potentials, and thus higher state-of-charge, as well as an optimization of the SiG anode by stabilization of the silicon/electrolyte interface and possibly by prelithiation.

Conclusions

In the present study, we investigated silicon-graphite//NMC811 full-cells, utilizing a capacitively oversized SiG anode, with respect to their cycling stability at different C-rates over 250 cycles at 45 °C. Based on half-cell measurements against lithium metal electrodes and gas evolution analysis by means of on-line electrochemical mass spectrometry we demonstrated that NMC811 cathodes are very sensitive to the end-of-charge potential. Our results showed that at potentials above ~4.25 V vs. Li^+/Li, viz., at about 80% state-of-charge, oxygen is released from the NMC811 lattice, which resulted in (i) a chemical oxidation of the electrolyte and (ii) the formation of a resistive surface layer at the NMC811 particles, causing in a strong electrode polarization and reduced capacity retention at higher current densities. SiG//NMC811 full-cells are particularly prone to this aging mechanism even at relatively low cell cutoff voltages, because the comparatively high lithiation potential of the SiG anode results in an upward shift of the end-of-charge potential of the NMC811 cathode. Using a lithiated gold-wire micro-reference electrode we demonstrated that the resulting oxygen release did not only cause a distinct increase of the impedance growth at the NMC811 cathode but also at the SiG anode, which we explained by the cross-diffusion of electrolyte decomposition products resulting from the chemical oxidation of electrolyte compounds at the NMC811 cathode. Therefore, the capacity retention of both half and full-cells was notably decreased once the oxygen release occurred at the NMC811 cathode at potentials above ~4.25 V vs. Li^+/Li. To cope with the challenge, we demonstrated that prelithiation of the capacitively oversized SiG anodes is an effective approach to mitigate the rapid impedance growth of the SiG//NMC811 full-cells by lowering the average anode potential and thus reducing the effective end-of-charge potential of the NMC811 cathode at a given cell cutoff voltage. Further, the excess of active lithium, which was introduced by the prelithiation, additionally improved the capacity retention by compensating the ongoing side reactions at the silicon/electrolyte interface and even allowed to increase the upper cell voltage which resulted in residual capacities of >180 mAh g^{-1}_{NMC} after 250 cycles at 45 °C. Thus, our results demonstrated that the prelithiation of capacitively oversized silicon-based anodes offers an additional lever for combined strategies to improve the practical specific energy of future lithium-ion batteries.

Acknowledgements

The German Federal Ministry for Economic Affairs and Energy is acknowledged for funding under the auspices of the "LiMo" project (funding number 03ET6045D). Roland Jung, Sophie Solchenbach, and Benjamin Strehle (all TUM) are gratefully acknowledged for fruitful discussions. D.P. acknowledges funding by BASF SE through its electrochemistry and battery research network. The authors greatly acknowledge Wacker Chemie AG for providing the silicon nanoparticles.

References

(1) Andre, D.; Kim, S.-J.; Lamp, P.; Lux, S. F.; Maglia, F.; Paschos, O.; Stiaszny, B. *J. Mater. Chem. A* **2015**, *3*, 6709–6732.

(2) Gröger, O.; Gasteiger, H. A.; Suchsland, J.-P. *J. Electrochem. Soc.* **2015**, *162* (14), A2605–A2622.

(3) Wetjen, M.; Pritzl, D.; Jung, R.; Solchenbach, S.; Ghadimi, R.; Gasteiger, H. A. *J. Electrochem. Soc.* **2017**, *164* (12), A2840–A2852.

(4) Jung, R.; Metzger, M.; Haering, D.; Solchenbach, S.; Marino, C.; Tsiouvaras, N.; Stinner, C.; Gasteiger, H. A. *J. Electrochem. Soc.* **2016**, *163* (8), A1705–A1716.

(5) Petibon, R.; Chevrier, V.; Aiken, C. P.; Hall, D. S.; Hyatt, S.; Shunmugasundaram, R.; Dahn, J. R. *J. Electrochem. Soc.* **2016**, *163* (7), A1146–A1156.

(6) Jung, R.; Metzger, M.; Maglia, F.; Stinner, C.; Gasteiger, H. A. *J. Electrochem. Soc.* **2017**, *164* (7), A1361–A1377.

(7) Jung, S.-K.; Gwon, H.; Hong, J.; Park, K.-Y.; Seo, D.-H.; Kim, H.; Hyun, J.; Yang, W.; Kang, K. *Adv. Energy Mater.* **2014**, *4*, 1300787.

(8) Yabuuchi, N.; Makimura, Y.; Ohzuku, T. *J. Electrochem. Soc.* **2007**, *154* (4), A314–A321.

(9) Kim, M. G.; Shin, H. J.; Kim, J.-H.; Park, S.-H.; Sun, Y.-K. *J. Electrochem. Soc.* **2005**, *152* (7), A1320–A1328.

(10) Obrovac, M. N.; Chevrier, V. L. *Chem. Rev.* **2014**, *114*, 11444–11502.

(11) Andre, D.; Hain, H.; Lamp, P.; Maglia, F.; Stiaszny, B. *J. Mater. Chem. A* **2017**, *5*, 17174–17198.

(12) Nitta, N.; Wu, F.; Lee, J. T.; Yushin, G. *Mater. Today* **2015**, *18* (5), 252–264.

(13) Beaulieu, L. Y.; Hatchard, T. D.; Bonakdarpour, A.; Fleischauer, M. D.; Dahn, J. R. *J. Electrochem. Soc.* **2003**, *150* (11), A1457–A1464.

(14) Wetjen, M.; Solchenbach, S.; Pritzl, D.; Hou, J.; Tileli, V.; Gasteiger, H. A. *J. Electrochem. Soc.* **2018**, *165* (7), A1503–A1514.

(15) McDowell, M. T.; Ryu, I.; Lee, S. W.; Wang, C.; Nix, W. D.; Cui, Y. *Adv. Mater.* **2012**, *24*, 6034–6041.

(16) Obrovac, M. N.; Christensen, L.; Le, D. B.; Dahn, J. R. *J. Electrochem. Soc.* **2007**, *154* (9), A849–A855.

(17) Delpuech, N.; Dupre, N.; Moreau, P.; Bridel, J. S.; Gaubicher, J.; Lestriez, B.; Guyomard, D. *ChemSusChem* **2016**, *9*, 841–848.

(18) Kimura, K.; Matsumoto, T.; Nishihara, H.; Kasukabe, T.; Kyotani, T.; Kobayashi, H. *J. Electrochem. Soc.* **2017**, *164* (6), A995–A1001.

(19) Klett, M.; Gilbert, J. A.; Trask, S. E.; Polzin, B. J.; Jansen, A. N.; Dees, D. W.; Abraham, D. P. *J. Electrochem. Soc.* **2016**, *163* (6), A875–A887.

(20) Obrovac, M. N.; Krause, L. J. *J. Electrochem. Soc.* **2007**, *154* (2), A103–A108.

(21) Chevrier, V. L.; Liu, L.; Wohl, R.; Chandrasoma, A.; Vega, J. A.; Eberman, K. W.; Stegmaier, P.; Figgemeier, E. *J. Electrochem. Soc.* **2018**, *165* (5), A1129–A1136.

(22) Gallagher, K. G.; Goebel, S.; Greszler, T.; Mathias, M.; Oelerich, W.; Eroglu, D.; Srinivasan, V. *Energy Environ. Sci.* **2014**, *7*, 1555–1563.

(23) Gabrisch, H.; Yi, T.; Yazami, R. *Electrochem. Solid-State Lett.* **2008**, *11* (7), A119–A124.

(24) Whittingham, M. S. *Chem. Rev.* **2004**, *104*, 4271–4301.

(25) Metzger, M.; Strehle, B.; Solchenbach, S.; Gasteiger, H. A. *J. Electrochem. Soc.* **2016**, *163* (5), 798–809.

(26) Wandt, J.; Freiberg, A.; Thomas, R.; Gorlin, Y.; Siebel, A.; Jung, R.; Gasteiger, H. A.; Tromp, M. *J. Mater. Chem. A* **2016**, *4*, 18300–18305.

(27) Buchberger, I.; Seidlmayer, S.; Pokharel, A.; Piana, M.; Hattendorff, J.; Kudejova, P.; Gilles, R.; Gasteiger, H. A. *J. Electrochem. Soc.* **2015**, *162* (14), A2737–A2746.

(28) Noh, H. J.; Youn, S.; Yoon, C. S.; Sun, Y. K. *J. Power Sources* **2013**, *233*, 121–130.

(29) Myung, S.-T.; Maglia, F.; Park, K.-J.; Yoon, C. S.; Lamp, P.; Kim, S.-J.; Sun, Y.-K. *ACS Energy Lett.* **2017**, *2*, 196–223.

(30) Li, J.; Downie, L. E.; Ma, L.; Qiu, W.; Dahn, J. R. *J. Electrochem. Soc.* **2015**, *162* (7), A1401–A1408.

(31) Zheng, J.; Kan, W. H.; Manthiram, A. *ACS Appl. Mater. Interfaces* **2015**, *7* (12), 6926–6934.

(32) Liu, W.; Oh, P.; Liu, X.; Lee, M. J.; Cho, W.; Chae, S.; Kim, Y.; Cho, J. *Angew. Chemie - Int. Ed.* **2015**, *54*, 4440–4457.

(33) Bak, S.-M.; Hu, E.; Zhou, Y.; Yu, X.; Senanayake, S. D.; Cho, S.-J.; Kim, K.-B.; Chung, K. Y.; Yang, X.-Q.; Nam, K.-W. *ACS Appl. Mater. Interfaces* **2014**, *6* (24), 22594–22601.

(34) Yim, T.; Choi, S. J.; Park, J.-H.; Cho, W.; Jo, Y. N.; Kim, T.-H.; Kim, Y.-J. *Phys. Chem. Chem. Phys.* **2014**, *17*, 2388–2393.

(35) Abraham, D. P.; Twesten, R. D.; Balasubramanian, M.; Petrov, I.; McBreen, J.; Amin, K. *Electrochem. commun.* **2002**, *4*, 620–625.

(36) Abraham, D. P.; Twesten, R. D.; Balasubramanian, M.; Kropf, J.; Fischer, D.; McBreen, J.; Petrov, I.; Amine, K. *J. Electrochem. Soc.* **2003**, *150* (11), A1450.

(37) Solchenbach, S.; Pritzl, D.; Kong, E. J. Y.; Landesfeind, J.; Gasteiger, H. A. *J. Electrochem. Soc.* **2016**, *163* (10), A2265–A2272.

(38) Tsiouvaras, N.; Meini, S.; Buchberger, I.; Gasteiger, H. A. *J. Electrochem. Soc.* **2013**, *160* (3), A471–A477.

(39) Jung, R.; Strobl, P.; Maglia, F.; Stinner, C.; Gasteiger, H. A. **2018**, submitted.

(40) Li, W.; Reimers, J.; Dahn, J. *Solid State Ionics* **1993**, *67*, 123–130.

(41) Woo, S.-U.; Yoon, C. S.; Amine, K.; Belharouak, I.; Sun, Y.-K. *J. Electrochem. Soc.* **2007**, *154* (11), A1005–A1009.

(42) Strehle, B.; Kleiner, K.; Jung, R.; Chesneau, F.; Mendez, M.; Hubert, A. *J. Electrochem. Soc.*

2017, *164* (2), 400–406.

(43) Andersson, A. M.; Abraham, D. P.; Haasch, R.; MacLaren, S.; Liu, J.; Amine, K. *J. Electrochem. Soc.* **2002**, *149* (10), A1358.

(44) Muto, S.; Sasano, Y.; Tatsumi, K.; Sasaki, T.; Horibuchi, K.; Takeuchi, Y.; Ukyo, Y. *J. Electrochem. Soc.* **2009**, *156* (5), A371.

(45) Jung, R.; Morasch, R.; Karayaylali, P.; Phillips, K.; Maglia, F.; Stinner, C.; Shao-Horn, Y.; Gasteiger, H. A. *J. Electrochem. Soc.* **2018**, *165* (2), A132–A141.

(46) McCloskey, B. D.; Bethune, D. S.; Shelby, R. M.; Girishkumar, G.; Luntz, A. C. *J. Phys. Chem. Lett.* **2011**, *2* (10), 1161–1166.

(47) Strehle, B.; Kleiner, K.; Jung, R.; Chesneau, F.; Mendez, M.; Hubert, A.; Gasteiger, H. A.; Piana, M. *J. Electrochem. Soc.* **2017**, *164* (2), A400–A406.

(48) Jung, R.; Metzger, M.; Maglia, F.; Stinner, C.; Gasteiger, H. *J. Phys. Chem. Lett.* **2017**, *8*, 4820–4825.

(49) Kim, K.; Park, I.; Ha, S. Y.; Kim, Y.; Woo, M. H.; Jeong, M. H.; Shin, W. C.; Ue, M.; Hong, S. Y.; Choi, N. S. *Electrochim. Acta* **2017**, *225*, 358–368.

(50) Wandt, J.; Freiberg, A. T. S.; Ogrodnik, A.; Gasteiger, H. A. *Mater. Today* **2018**, accepted.

(51) Klett, M.; Gilbert, J. A.; Pupek, K. Z.; Trask, S. E.; Abraham, D. P. *J. Electrochem. Soc.* **2017**, *164* (1), A6095–A6102.

(52) Obrovac, M. N.; Christensen, L. *Electrochem. Solid-State Lett.* **2004**, *7* (5), A93–A96.

(53) Gaberscek, M.; Moskon, J.; Erjavec, B.; Dominko, R.; Jamnik, J. *Electrochem. Solid-State Lett.* **2008**, *11* (10), A170.

(54) Landesfeind, J.; Pritzl, D.; Gasteiger, H. A. *J. Electrochem. Soc.* **2017**, *164* (7), A1773–A1783.

(55) Pritzl, D.; Solchenbach, S.; Wetjen, M.; Gasteiger, H. A. *J. Electrochem. Soc.* **2017**, *164* (12), A2625–A2635.

(56) Dedryvère, R.; Foix, D.; Franger, S.; Patoux, S.; Daniel, L.; Gonbeau, D. *J. Phys. Chem. C* **2010**, *114*, 10999–11008.

(57) Burns, J. C.; Kassam, A.; Sinha, N. N.; Downie, L. E.; Solnickova, L.; Way, B. M.; Dahn, J. R. *J. Electrochem. Soc.* **2013**, *160* (9), A1451–A1456.

(58) Nelson, K. J.; d'Eon, G. L.; Wright, A. T. B.; Ma, L.; Xia, J.; Dahn, J. R. *J. Electrochem. Soc.* **2015**, *162* (6), A1046–A1054.

(59) Nelson, K. J.; Abarbanel, D. W.; Xia, J.; Lu, Z.; Dahn, J. R. *J. Electrochem. Soc.* **2016**, *163* (2), A272–A280.

(60) Abarbanel, D. W.; Nelson, K. J.; Dahn, J. R. *J. Electrochem. Soc.* **2016**, *163* (3), A522–A529.

(61) Ellis, L. D.; Allen, J. P.; Thompson, L. M.; Harlow, J. E.; Stone, W. J.; Hill, I. G.; Dahn, J. R. *J. Electrochem. Soc.* **2017**, *164* (14), A3518–A3528.

(62) Sun, Y. K.; Kim, D. H.; Yoon, C. S.; Myung, S. T.; Prakash, J.; Amine, K. *Adv. Funct. Mater.* **2010**, *20*, 485–491.

(63) Sun, Y.-K.; Chen, Z.; Noh, H.-J.; Lee, D.-J.; Jung, H.-G.; Ren, Y.; Wang, S.; Yoon, C. S.; Myung, S.-T.; Amine, K. *Nat. Mater.* **2012**, *11*, 942–947.

(64) Lee, E. J.; Noh, H. J.; Yoon, C. S.; Sun, Y. K. *J. Power Sources* **2015**, *273*, 663–669.

(65) Han, B.; Paulauskas, T.; Key, B.; Peebles, C.; Park, J. S.; Klie, R. F.; Vaughey, J. T.; Dogan, F. *ACS Appl. Mater. Interfaces* **2017**, *9* (17), 14769–14778.

(66) Han, B.; Key, B.; Lapidus, S. H.; Garcia, J. C.; Iddir, H.; Vaughey, J. T.; Dogan, F. *ACS Appl. Mater. Interfaces* **2017**, *9* (47), 41291–41302.

(67) Cho, Y.; Lee, S.; Lee, Y.; Hong, T.; Cho, J. *Adv. Energy Mater.* **2011**, *1*, 821–828.

(68) Dogan, F.; Vaughey, J. T.; Iddir, H.; Key, B. *ACS Appl. Mater. Interfaces* **2016**, *8* (26), 16708–16717.

(69) Croguennec, L.; Bains, J.; Bréger, J.; Tessier, C.; Biensan, P.; Levasseur, S.; Delmas, C. *J.*

Electrochem. Soc. **2011**, *158* (6), A664–A670.

(70) Kondrakov, A. O.; Schmidt, A.; Xu, J.; Geßwein, H.; Mönig, R.; Hartmann, P.; Sommer, H.; Brezesinski, T.; Janek, J. *J. Phys. Chem. C* **2017**, *121*, 3286–3294.

(71) Luo, F.; Liu, B.; Zheng, J.; Chu, G.; Zhong, K.; Li, H.; Huang, X.; Chen, L. *J. Electrochem. Soc.* **2015**, *162* (14), A2509–A2528.

(72) Vanchiappan, A.; Yun-Sung, L.; Srinivasan, M. *Adv. Energy Mater.* **2017**, *7*, 1602607.

(73) Solchenbach, S.; Wetjen, M.; Pritzl, D.; Schwenke, K. U.; Gasteiger, H. A. *J. Electrochem. Soc.* **2018**, *165* (3), 512–524.

(74) Marinaro, M.; Weinberger, M.; Wohlfahrt-Mehrens, M. *Electrochim. Acta* **2016**, *206*, 99–107.

(75) Key, B.; Bhattacharyya, R.; Morcrette, M.; Sezne, V.; Tarascon, J.; Grey, C. P. *J. Am. Chem. Soc.* **2009**, *131*, 9239–9249.

3.3.2 Lithium Oxalate as Capacity and Cycle-Life Enhancer for Silicon-based Full-Cells

This section presents the article “Lithium Oxalate as Capacity and Cycle-Life Enhancer in LNMO/Graphite and LNMO/SiG Full Cells”,[222] which was published in February 2018 in the *Journal of The Electrochemical Society*. It is an open access article distributed under the terms of the Creative Commons Attribution 4.0 License. The main research work was done by Sophie Solchenbach, who is also the first author of the paper. The permanent web-link to the article is http://dx.doi.org/10.1149/2.0611803jes.

In accordance with the previous sections, the irreversible capacity loss of silicon-based anodes remains a huge challenge. Different approaches were pursued to increase the lithium inventory in lithium-ion full-cells, however, most of them are *ex situ* and require the addition of further steps to the manufacturing process, which slows down the production and increases costs.[227,233,234] Moreover, the handling of lithiated anodes is much more difficult compared to lithiated cathodes, because of their higher reactivity.[185] For that reason, the following article deals with a method to increase the lithium inventory *in situ* by using lithium oxalate as a sacrificial salt in combination with a lithium nickel manganese oxide (LNMO) cathode.[222,228] In contrast to alternative approaches reported in the literature, which involve the synthesis of an overlithiated LNMO active material,[223] lithium oxalate can be added directly during the ink procedure of the cathode coating which greatly improves the handling and flexibility of the manufacturing process. Furthermore, among the sacrificial salts lithium oxalate is especially attractive for lithium-ion batteries because its oxidative decomposition causes no unwanted side products but releases only lithium and CO_2, which was even shown to have a beneficial effect on the solid-electrolyte-interphase of silicon-based electrodes.[235]

First, we investigated the electrochemical oxidation of lithium oxalate to CO_2, which occurs around 4.7 V vs. Li^+/Li and lies well within the plateaus of the Ni^{2+}/Ni^{3+} and Ni^{3+}/Ni^{4+} redox couples. The resulting gas evolution was quantified by means of on-line electrochemical mass spectrometry (OEMS). Using half-cells, we then tested the influence of the addition of 2.5 or 5 wt% lithium oxalate to the LNMO cathodes, which increased the theoretical specific capacity of the first charge by about 10%

or 20%. To investigate the effect of the increased lithium inventory on the cycling stability of lithium-ion full-cells, the LNMO cathodes were combined either with graphite anodes or with the same SiG anodes which were also used in our previous work[102] (see Section 3.1.1). Usually, silicon-based anodes are operated with a fluoroethylene carbonate (FEC)-containing electrolyte solution, which is known to significantly improve the cycling stability.[103,175] For that reason, we also investigated the consumption rates of FEC and CO_2 as well as the resulting cycle life of the SiG//LNMO full-cells in dependence on the concentrations of the two additives.

This study generated three important insights about the use of lithium oxalate in combination with LNMO cathodes for SiG anodes: (i) The addition of 2.5 or 5 wt% lithium oxalate to LNMO improves the initial capacity (up to ~11%) of full-cells featuring a graphite anode and reduces their capacity fade over 300 cycles (from 19% to 12% or 8%, respectively). For SiG anodes, this effect is even larger, resulting in a notably increased capacity retention after 250 cycles (45% instead of 20%), even in the presence of an FEC-containing electrolyte. (ii) CO_2 is an effective SEI-forming additive that indicates a synergistic effect with FEC on the lifetime of silicon-based full-cells. The removal of one of the two additives leads to a reduction of the cycle life. (iii) Similar to a sacrificial salt,[228] the addition of lithium oxalate offers a convenient method to introduce a defined amount of lithium and CO_2 into a lithium-ion battery without the addition of further manufacturing steps. However, depending on the cell housing and the amount of CO_2, the pressure build-up during the first charge needs to be evaluated carefully.

Author contributions

S.S. prepared the lithium oxalate-containing LNMO cathodes and did the electrochemical testing. M.W. prepared the SiG anodes and the FEC-containing electrolytes. D.P. prepared the graphite anodes. S.S. performed the OEMS gas analysis and the data treatment. S.S. and M.W. did the ^{19}F-NMR experiments and discussed the consumption rates of FEC and CO_2. S.S. analyzed the data. S.S. and H.G. wrote the manuscript. All authors discussed the results and commented on the manuscript.

A512 Journal of The Electrochemical Society, **165** (3) A512-A524 (2018)

Lithium Oxalate as Capacity and Cycle-Life Enhancer in LNMO/Graphite and LNMO/SiG Full Cells

Sophie Solchenbach,*,z **Morten Wetjen,*** **Daniel Pritzl,*** **K. Uta Schwenke,**
and Hubert A. Gasteiger**

Chair of Technical Electrochemistry, Department of Chemistry and Catalysis Research Center, Technical University of Munich, Garching, Germany

In the present study, we explore the use of lithium oxalate as a "sacrificial salt" in combination with lithium nickel manganese spinel (LNMO) cathodes. By online electrochemical mass spectrometry (OEMS), we demonstrate that the oxidation of lithium oxalate to CO_2 (corresponding to 525 mAh/g) occurs quantitatively around 4.7 V vs. Li/Li^+. LNMO/graphite cells containing 2.5 or 5 wt% lithium oxalate show an up to ~11% higher initial discharge capacity and less capacity fade over 300 cycles (12% and 8% vs. 19%) compared to cells without lithium oxalate. In LNMO/SiG full-cells with an FEC-containing electrolyte solution, lithium oxalate leads to a better capacity retention (45% vs 20% after 250 cycles) and a higher coulombic efficiency throughout cycling (~1%) compared to cells without lithium oxalate. When CO_2 from lithium oxalate oxidation is removed after formation, a similar capacity fading as in LNMO/SiG cells without lithium oxalate is observed. Hence, we attribute the improved cycling performance to the presence of CO_2 in the cells. Further analysis (e.g., FEC consumption by ^{19}F-NMR) indicate that CO_2 is an effective SEI-forming additive for SiG anodes, and that a combination of FEC and CO_2 has a synergistic effect on the lifetime of full-cells with SiG anodes.

[DOI: 10.1149/2.0611803jes]

Manuscript submitted January 12, 2018; revised manuscript received February 14, 2018. Published February 22, 2018. This was Paper 393 presented at the National Harbor, Maryland Meeting of the Society, October 1–5, 2017.

Lithium nickel manganese spinel ($LiNi_{0.5}Mn_{1.5}O_4$, LNMO) is a promising cathode material for high energy lithium ion batteries due to its high operating potential around 4.7 V vs. Li/Li^+, its high rate capability, structural stability and the absence of cobalt. However, its lower specific capacity (146 mAh/g_{LNMO}) compared to layered oxide materials (e.g. lithium nickel manganese cobalt oxide (NMC), specific capacity 150–250 mAh/g_{NMC})[1] is regarded as a major drawback. In full-cells, the practically achievable capacity of LNMO is even lower, as the formation of the solid-electrolyte interphase (SEI) on the graphite anode consumes active lithium. For many layered oxide cathodes, however, the first cycle irreversible capacity of the cathode is similar to the capacity needed for SEI formation (~20 mAh/g_{NMC}), and hence the practical discharge capacity of the cathode and the remaining active lithium are more or less balanced again.[2,3] In contrast, the first cycle irreversible capacity of LNMO (~6 mAh/g_{LNMO}) is much lower than the capacity needed for SEI formation. This leads to a mismatch between active lithium and practical cathode capacity, i.e., there is not enough active lithium available to fully discharge the LNMO cathode during subsequent cycling.

In cells with silicon-based anodes, active lithium losses on the anode are even higher compared to graphite, as the expansion of the silicon particles during the first lithiation leads to a continuous exposure of fresh, unpassivated silicon surface.[4] On this new surface, electrolyte reduction occurs instantaneously, which reduces the total lithium reservoir in the cell. Therefore, different ideas to increase the amount of active lithium in lithium ion full-cells have been suggested, for example via prelithiation of silicon anodes with metallic lithium.[5–8] Recently, Gabrielli et al.[9] successfully used LNMO that had been chemically overlithiated to compensate for the initial lithium loss in LNMO/silicon-carbon full cells. Alternatively, Shanmukaraj et al.[10] proposed "sacrificial salts" as an additional source of lithium ions: A lithium salt is incorporated in the active material/carbon black matrix of the cathode. During the initial charge, the anion of the sacrificial salt is oxidized yielding mostly gaseous products, while the corresponding lithium cation is intercalated into the graphite anode; the gas can then be removed after formation. Lithium oxalate has a high specific charge capacity of 525 mAh/g (based on $Li_2C_2O_4 \rightarrow 2\,Li^+ + 2\,e^- + 2\,CO_2$), but was disregarded as a sacrificial salt for typical 4 V cell chemistries due to its high oxidation potential around 4.6–4.7 V vs. Li/Li^+.[10] However, this potential matches well with the charging plateau of LNMO. Additionally, lithium oxalate releases only CO_2 during oxidation, which is considered to improve the interfacial stability of graphite as well as of lithium metal anodes.[11–15] Strehle et al.[16] showed that the presence of CO_2 can suppress the formation of soluble lithium alkoxides and the follow-up electrolyte transesterification reactions. CO_2 can act further as a scavenger for detrimental trace water and protons.[17] Recently, Krause et al.[18] demonstrated that CO_2 is also an effective additive for silicon-based cells, increasing their capacity retention and coulombic efficiency.

In the present study, we use lithium oxalate as a capacity enhancer in LNMO/graphite and LNMO/silicon-graphite (SiG) full cells. First, we investigate the electrochemical oxidation of lithium oxalate and the resulting gas evolution by online electrochemical mass spectrometry (OEMS) in order to quantify its decomposition reaction and potential. As a next step, we test the addition of 2.5 or 5 wt% of lithium oxalate to LNMO composite electrodes in half cells, which increases the theoretical capacity of the initial charge by about 10% or 20%, respectively. To investigate the effect of the increased lithium inventory in full-cells, we cycle LNMO composite electrodes containing 0, 2.5, or 5 wt% lithium oxalate in full-cells against graphite anodes. We further test LNMO composite electrodes with 0 or 5 wt% lithium oxalate with silicon-graphite electrodes (SiG, 35 wt% silicon, 45 wt% graphite) in an electrolyte solution containing fluoroethylene carbonate (FEC). This additive is known to improve the cycling stability of silicon-based electrodes[19–25] and is commonly employed for cell chemistries containing silicon. As the LNMO/SiG cells with lithium oxalate showed less capacity fade and a higher coulombic efficiency throughout cycling than their counterparts without lithium oxalate, we investigate the effect of CO_2 on cycling performance and FEC consumption in LNMO/SiG cells. Lastly, we discuss the opportunities and challenges associated with the use of lithium oxalate as a sacrificial salt in LNMO/graphite and LNMO/SiG cells.

Experimental

Lithium oxalate/carbon black electrode preparation.—2 g Commercial lithium oxalate (99% purity, average particle size ~40 μm, Alfa Aesar, United States) was ballmilled with zirconia balls (Ø 3 mm, 30 g) at 400 rpm for 1 h without solvent (dry), then for 1.5 h in 2 mL N-methyl pyrrolidone (NMP, anhydrous, Sigma-Aldrich, United States) until an average particle size of 0.2 μm was reached. The particle sizes before and after ballmilling were quantified by

---

*Electrochemical Society Student Member.
**Electrochemical Society Fellow.
zE-mail: sophie.solchenbach@tum.de

Table I. Electrode composition and properties of cathodes and anodes used for LNMO/Li half-cells and LNMO/graphite and LNMO/SiG full-cells. Theoretical capacities for LNMO, lithium oxalate (LO), graphite, and silicon were taken as 146 mAh/g_{LNMO}, 525 mAh/g_{LO}, 372 mAh/$g_{graphite}$, and 3579 mAh/g_{Si}. Practical 1st charge/discharge capacities for LNMO and graphite electrodes were determined at a C-rate of 0.1 h^{-1} in lithium half-cells, while the practical capacities for SiG electrodes were taken from Ref. 25. For simplicity, all cathode capacities are given per gram of LNMO, neglecting the weight of lithium oxalate. Mass loadings refer to LNMO for the cathode and graphite or graphite+silicon for the anode. Areal capacities are based on practical 1st charge/discharge capacities.

Electrode/cell properties	Units	LNMO	+ 2.5 wt% LO	+ 5 wt% LO	graphite	SiG
LNMO	wt%	90.0	87.80	85.72	–	–
Lithium oxalate	wt%	–	2.44	4.76	–	–
Graphite	wt%	–	–	–	95.0	45.0
Silicon	wt%	–	–	–	–	35.0
Carbon black (C65)	wt%	5.0	4.88	4.76	–	–
PVDF	wt%	5.0	4.88	4.76	5.0	–
Carbon fibers	wt%	–	–	–	–	9.0
LiPAA	wt%	–	–	–	–	11.0
Theoretical 1st charge capacity	mAh/g	146	161 (146 + 15)	175 (146 + 29)	372	1420
Practical 1st charge capacity	mAh/g	145	160	173	353	1466
Practical 1st discharge capacity	mAh/g	140	140	140	332	1265
LNMO / lithium half cells						
LNMO mass loading	mg/cm^2	10.8 ± 0.1	11.2 ± 0.1	13.1 ± 0.1	–	–
1st charge areal capacity	mAh/cm^2	1.6 ± 0.0	1.8 ± 0.0	2.3 ± 0.0	–	–
1st discharge areal capacity	mAh/cm^2	1.5 ± 0.0	1.6 ± 0.0	1.8 ± 0.0	–	–
LNMO / graphite full-cells						
LNMO / graphite mass loading	mg/cm^2	11.4 ± 0.4	11.1 ± 0.1	13.1 ± 0.1	6.8 ± 0.9	–
1st charge areal capacity	mAh/cm^2	1.7 ± 0.1	1.8 ± 0.0	2.3 ± 0.0	2.4 ± 0.3	–
1st discharge areal capacity	mAh/cm^2	1.6 ± 0.1	1.5 ± 0.0	1.8 ± 0.0	2.3 ± 0.3	–
LNMO / SiG full-cells						
LNMO / SiG mass loading	mg/cm^2	15.7 ± 1.8	11.3 ± 0.1	15.5 ± 1.7	–	1.9 ± 0.3
1st charge areal capacity	mAh/cm^2	2.3 ± 0.3	1.8 ± 0.0	2.7 ± 0.3	–	2.8 ± 0.4
1st discharge areal capacity	mAh/cm^2	2.2 ± 0.3	1.6 ± 0.0	2.2 ± 0.2	–	2.4 ± 0.4

dynamic light scattering (LA-950, Horiba, Japan) with NMP as dispersion media. To investigate the oxidation of lithium oxalate and the associated gas evolution, lithium oxalate/carbon black electrodes were prepared by mixing 200 mg ballmilled lithium oxalate with 200 mg Super C65 (Timcal, Imerys, Switzerland) and 3.2 g NMP, and dispersing the mixture with an ultrasonication horn. Polyvinylene difluoride (PVDF, Kynar HSV 900, Arkema, France) was dissolved in NMP at a weight ratio of 1:9, and then 490 mg of this PVDF solution was added to the lithium oxalate / carbon dispersion, followed by mixing in a planetary mixer (Thinky mixer, 2000 rpm, 5 min) to create a homogeneous ink. The resulting ink was coated onto Celgard trilayer separator foil (polypropylene (PP)-polyethylene (PE)-polypropylene (PP), C480, Celgard, United States) using a Mayer rod technique (100 μm wire thickness), and dried at 50°C for 6 hours. Afterwards, electrodes with a diameter of 15 mm were punched out, dried under dynamic vacuum at 95°C for at least 12 h, and then transferred into an argon-filled glove box (MBraun, Germany) without exposure to air. The final electrodes had a weight composition of 45:45:10 (lithium oxalate:carbon:PVDF) and a lithium oxalate loading of 0.4 mg/cm^2.

Lithium oxalate/LNMO electrode preparation.—Lithium manganese nickel spinel electrodes ($LiMn_{1.5}Ni_{0.5}O_4$, LNMO, 0.9 m^2_{BET}/g, BASF SE, Germany) with 2.5 or 5 wt% lithium oxalate were prepared by first dispersing C65 carbon and lithium oxalate (1:1 by weight) in NMP with an ultrasonication horn as described above. LNMO, PVDF and C65 were added to the dispersion according to the compositional ratios given in Table I. The compositions were chosen in order to keep a fixed weight ratio of LNMO:C65:PVDF of 90:5:5 in all electrodes once all lithium oxalate would be oxidized. NMP was added to yield a solid content of 40%, and the slurry was mixed in a planetary mixer (2000 rpm, 15 min). LNMO electrodes without lithium oxalate were prepared by combining LNMO, C65, and PVDF in ratios according to Table I (using the same mixing procedure). The slurries were then coated onto aluminum foil (15 μm, MTI, United states) using a gap bar (300 μm wet film thickness, ∼11–13 mg_{LNMO}/cm^2). To match the higher areal capacities of the SiG electrodes, additional LNMO coatings with 0 and 5 wt% lithium oxalate were prepared with a wet film thickness of 450 μm (∼14–16 mg_{LNMO}/cm^2). For OEMS measurements with LNMO or LNMO + 5 wt% lithium oxalate electrodes, the corresponding slurries were coated onto perforated aluminum foil (Micrograd Al 25, Dexmet, United States; ∼25 μm thickness). All LNMO coatings were dried at 50°C for 6 h in a convection oven. Electrodes with a diameter of 14 mm were punched out and compressed with 150 MPa, which resulted in electrode thicknesses ∼55 μm and ∼75 μm, respectively, and a porosity of 35%.

Graphite and silion-graphite (SiG) electrode preparation.—Graphite electrodes were prepared by mixing graphite (T311, BET surface area 5 m^2/g, SGL Carbon, Germany) and PVDF according to the ratio given in Table I with NMP in a planetary mixer (2000 rpm, 10 min). The ink (50% solid content) was coated onto copper foil (MTI, United States) using a 150 μm gap bar and dried at 50°C for 6 h in a convection oven. Silicon-graphite electrodes were prepared from silicon nanoparticles (∼200 nm, Wacker Chemie AG, Germany), graphite, vapor grown carbon fibers (VCGF-H, Showa Denko, Japan) and lithium poly(acrylate) (LiPAA, Sigma-Aldrich, Germany) by a ballmilling routine as described in Wetjen et al.[25] Graphite and SiG coatings were punched into 15 mm electrodes. The final loadings and compositions for all electrodes are given in Table I. Prior to cell assembly, all electrodes were dried under dynamic vacuum at 120°C for at least 12 h and then transferred into an argon-filled glove box (MBraun, Germany) without exposure to air.

Cell assembly and cycling.—2032 coin cells were assembled in an Ar-filled glove box (MBraun, H_2O, O_2 < 0.1 ppm) with LNMO (with or without lithium oxalate) as cathodes (Ø 14 mm) and either graphite or SiG electrodes as anodes (Ø 15 mm). Individual anodes and cathodes were paired in a such a way that the anode/cathode areal capacity balancing for all cells was ∼1.2–1.3 (based on their practical 1st discharge capacity, see Table I), in order to accommodate any excess lithium from the lithium oxalate oxidation. The electrodes were separated by 2 glass fiber separators (Whatman, Ø 16 mm) and wetted with 80 μL LP57 electrolyte solution (30 wt% ethylene carbonate (EC), 70 wt% ethyl methyl carbonate (EMC), 1 M lithium hexafluorophosphate ($LiPF_6$), Selectilyte, BASF SE) or 80 μL LP57 + 5 wt% fluoroethylene carbonate (FEC, BASF SE). LNMO/graphite cells were cycled galvanostatically between 3.5–4.8 V at 1C (≈1.7 mA/cm^2) after 2 formation cycles at a rate of C/10. LNMO/SiG cells were cycled galvanostatically between 4.0–4.8 V at C/2 (≈1.1 mA/cm^2) after 3 formation cycles at a rate of C/10. The lower cutoff voltage of 4.0 V was chosen, as Si-based cells have shown better cycling stability when high anode potentials were omitted.[21] Note that due to the lower potential of silicon during its first lithiation, the upper cutoff voltage was set to 4.9 V in the first cycle of the LNMO/SiG cells. For both cell chemistries, a constant voltage (CV) step was performed with a current limit of C/20 after each galvanostatic charging step. All cells were cycled with a battery cycler (Series 4000, Maccor, USA, coulombic efficiency accuracy ~300 ppm[26]) in a climate chamber (Binder, Germany) at 25°C. Specific capacities and coulombic efficiencies are given as the average of two duplicate cells, whereas error bars represent the deviation of these cells from the average. Note that the Maccor coulombic efficiency accuracy is not included in the error bars, because the focus of this study lies on comparing different cell configurations and not on an exact estimate of the cells' lifetime.

On-line electrochemical mass spectrometry (OEMS).—The cell design of the on-line electrochemical mass spectrometry (OEMS) system has been described in previous publications.[27] To study the oxidation of lithium oxalate, a lithium oxalate / carbon black electrode was charged galvanostatically vs. a lithium metal counter electrode (Ø 17 mm, 450 μm thickness, Rockwood Lithium, United States) with a nominal rate of C/10 (≈0.02 mA/cm^2, based on the theoretical capacity of 525 mAh/g for lithium oxalate). To avoid reactions of CO_2 with the lithium anode, a sealed 2-compartment setup[28] where the cathode and anode compartment are separated by an aluminum-sealed lithium-ion conductive glass ceramics (LICGC, Ohara Corp., Japan) was used, with a glass fiber separator soaked with 250 μL LP57 in the lithium anode compartment, and a Celgard trilayer separator (H2013) soaked with 80 μL LP57 in the lithium oxalate/carbon black cathode compartment, respectively.

OEMS measurements on LNMO/SiG full-cells were performed in 1-compartment OEMS cells (i.e., without barrier between anode and cathode compartment) using LNMO electrodes (~11.4 mg_{LNMO}/cm^2) without or with 5 wt% lithium oxalate coated onto perforated aluminum foil as cathodes in combination with SiG anodes, and using 150 μL of electrolyte solution (LP57 pure or with 5 wt% FEC) and two Celgard separators (H2013, Ø 28 mm). To eliminate the effect of the SiG electrode, we also performed an OEMS measurement using the same cathode, separator and electrolyte solution, but a Ø 15 mm delithiated $LiFePO_4$ electrode (LFP, 3.5 mAh/cm^2, Custom Cells, Itzehoe) as anode. Prior to the OEMS measurement, the LFP electrode was cycled once at a rate of C/10 vs. a lithium metal electrode between 2 V and 4 V, and then electrochemically delithiated to a lithium content of 0.15 by a galvanostatic charge at C/10 with a capacity cutoff at 3 mAh/cm^2. The cell was then disassembled inside an Ar-filled glove box and the LFP electrode directly transferred to the OEMS cell. All OEMS experiments were performed in a climate chamber (Binder, Germany) at 25°C.

FEC quantification by NMR.—The consumption of fluoroethylene carbonate (FEC) during cycling of LNMO/SiG cells with and without lithium oxalate was investigated by ^{19}F-NMR of the recovered electrolyte solutions from full-cells. To this purpose, LNMO/SiG full-cells with or without lithium oxalate and LP57 + 5 wt% FEC were cycled as described above, and carefully disassembled after 50 cycles or 250 cycles. One of the glass fiber separators was removed and immersed into 700 μL deuterated dimethyl sulfoxide (DMSO-d6, anhydrous, Sigma-Aldrich, USA). The solutions were then filled into air-tight NMR tubes and ^{19}F-NMR spectra were measured on a Bruker Ascend 400 (400 MHz). As the obtained ^{19}F-NMR spectra show only peaks that can either be ascribed to PF_6^- or FEC, and assuming that changes in the PF_6^- concentration in the electrolyte solution during cycling are negligible, the PF_6^- anion can be used as an internal standard.[22] The amount of FEC remaining in the electrolyte solution can thus be determined by the ratio of PF_6^- and FEC peak integrals. A more detailed description of this method can be found in a recent publication by Jung et al.[22]

Results

Electrochemical characterization of lithium oxalate/carbon and lithium oxalate/LNMO electrodes.—To investigate the electrochemical oxidation of lithium oxalate within the potential window of an LNMO cathode, we first tried to understand the electrochemical oxidation of lithium oxalate by itself, i.e., in the absence of any active material. Therefore, we fabricated model electrodes that contain only lithium oxalate in a conductive carbon matrix, similar to the ones used by Meini et al.,[29,30] who studied the anodic decomposition of lithium salts (Li_2O_2, Li_2CO_3, LiOH, and Li_2O). Figure 1a shows the potential during the galvanostatic charge of an electrode consisting of 45 wt% sub-micron lithium oxalate, 45 wt% carbon black and 10 wt% binder, with a nominal rate of C/10 (based on its theoretical decomposition capacity of 525 mAh/g_{LO}; see reaction 1 below). The potential profile shows a flat plateau around 4.7 V vs. Li/Li^+ until ~90% of the

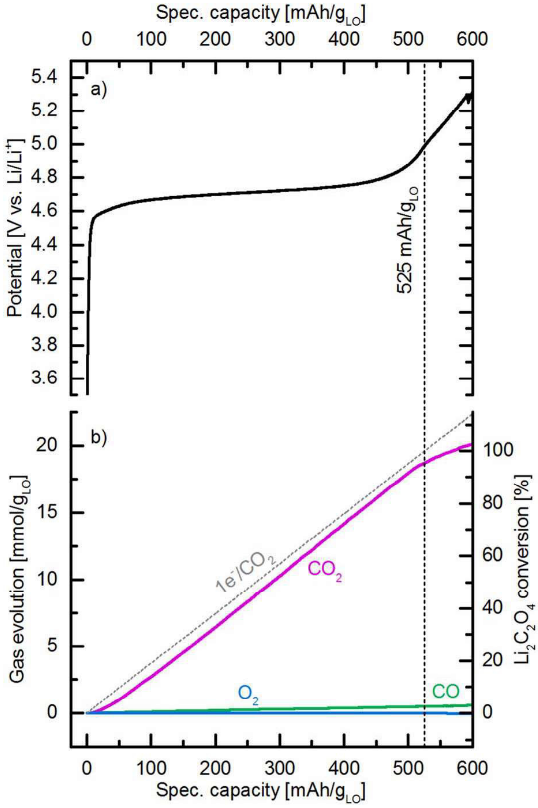

Figure 1. a) Potential vs. specific capacity during the oxidation of a lithium oxalate/carbon electrode with a nominal rate of C/10 in LP57 (EC:EMC 3:7 by weight, 1 M $LiPF_6$) at 25°C. The black dashed vertical line corresponds to the theoretical specific oxidation capacity of lithium oxalate (525 mAh/g_{LO}; see reaction 1). b) Gas evolution during the electrochemical oxidation of lithium oxalate either normalized to the mass of lithium oxalate (left y-axis) or referenced to the theoretical amount predicted by reaction 1 (right y-axis). The gray dashed line marks the theoretically expected $1e^-/CO_2$ slope.

theoretical capacity (~470 mAh/g_{LO}) is reached, from which point on the potential rises continuously. The concomitant gas evolution, as measured by on-line electrochemical mass spectrometry (OEMS) during this first charge, is shown Figure 1b. Here it is important to note that this experiment was conducted in a sealed 2-compartment cell,[28] so that there are no contributions to the measured gas evolution from the lithium metal counter electrode nor any consumption of the gas evolved at the working electrode by the lithium metal electrode. During charge, a linear increase of the CO_2 (m/z = 44) concentration in the cell headspace is observed (pink line in Figure 1b), indicating a constant gas evolution of CO_2. Carbon monoxide (m/z = 28, green line) and particularly oxygen (m/z = 32, blue line) are only detected in negligible trace amounts throughout the entire measurement. The slope of the CO_2 evolution vs. charge during the bulk oxidation of lithium oxalate is close to the 1 e^-/CO_2 line (gray dashed line in Figure 1b), suggesting a 1-electron process. As the CO_2 evolution from electrolyte oxidation is negligible at potentials ≤ 5 V vs. Li/Li^+ on a carbon black electrode at room temperature,[31] we can attribute the CO_2 evolution entirely to the oxidation of lithium oxalate. Once the theoretical charging capacity of $Li_2C_2O_4$ has been reached (black dashed line in Figure 1), the CO_2 evolution slows down. This indicates that lithium oxalate is quantitatively oxidized around 4.7 V vs. Li/Li^+ according to reaction 1:[32]

$$Li_2C_2O_4 \rightarrow 2Li^+ + 2e^- + 2CO_2 \qquad [1]$$

The slight deviation downwards from the 1 e^-/CO_2 line can be explained by two effects: i) the lithium oxalate used here contains about 1% Li_2CO_3 as impurity, whose oxidation also gives CO_2, but in a ≥ 2 e^-/CO_2 process;[29] and ii) about 2.5% of the total CO_2 remain dissolved in the electrolyte solution and are thus not detectable by OEMS (for details see Discussion section of this paper).

The oxidation potential of 4.7 V vs. Li/Li^+ for lithium oxalate lies well within the plateaus of the Ni^{2+}/Ni^{3+} and Ni^{3+}/Ni^{4+} redox couple of high-voltage lithium nickel manganese spinel ($LiNi_{0.5}Mn_{1.5}O_4$, LNMO) at 4.7 V and 4.75 V vs. Li/Li^+, respectively.[33] In the following, we explore the use of lithium oxalate as a sacrificial salt in combination with LNMO cathodes. Figure 2a shows the first charge/discharge profile of a LNMO cathode vs. Li at C/10 with 0 wt% (black line), 2.5 wt% (purple line) or 5 wt% lithium oxalate (pink line) added to the cathode slurry during electrode fabrication. The ratios of LNMO to binder and conductive carbon were kept constant in all electrode compositions (see Table I). During charge, the LNMO cathode without lithium oxalate (black lines in Figure 2a) can be delithiated to a capacity of 145 mAh/g_{LNMO}, which is essentially identical with the theoretical capacity of 146 mAh/g_{LNMO} (black dashed line in Figure 2). LNMO cathodes with 2.5 wt% lithium oxalate (purple lines in Figure 2a) deliver ~160 mAh/g_{LNMO} charge capacity, which also comes close to the theoretically expected 161 mAh/g_{LNMO} for these electrodes based on the combined capacity of LNMO and lithium oxalate (see Table I and purple dashed line in Figure 2). Accordingly, the charge capacity of the cathode with 5% lithium oxalate (pink lines in Figure 2) is about 173 mAh/g_{LNMO} (theoretical capacity: 175 mAh/g_{LNMO}, see pink dashed line). Note that all capacities are given per gram of LNMO, neglecting the weight of the lithium oxalate, as the latter is virtually completely oxidized to CO_2 and Li^+-ions during the first charge. Considering the potential profiles, one can see that the transition between the Ni^{2+}/Ni^{3+} and the Ni^{3+}/Ni^{4+} plateaus is gradually shifted toward higher specific capacities with increasing lithium oxalate content. This indicates that a large fraction (but not all) of the lithium oxalate is already oxidized during the Ni^{2+}/Ni^{3+} plateau. The subsequent discharge is equally long for all three electrode compositions, i.e., amounting to the same first discharge capacity of 140 mAh/g_{LNMO} (see Table I). Furthermore, the charge/discharge capacities as well as the potential profiles of the second cycle at C/10 are identical for the three different compositions (see Figure 2b). Theoretically, the oxidation of all lithium oxalate will increase the LNMO electrode porosity from ~35% to ~38% or ~40% for electrodes containing 2.5 wt% or 5 wt% lithium oxalate, respectively. However, based on the capacities and potential profiles obtained during the second cycle (see Figure 2b), we can conclude that the effect of this porosity change is only minor, and the oxidation of lithium oxalate within the cathode has not altered the subsequent electrochemical behavior.

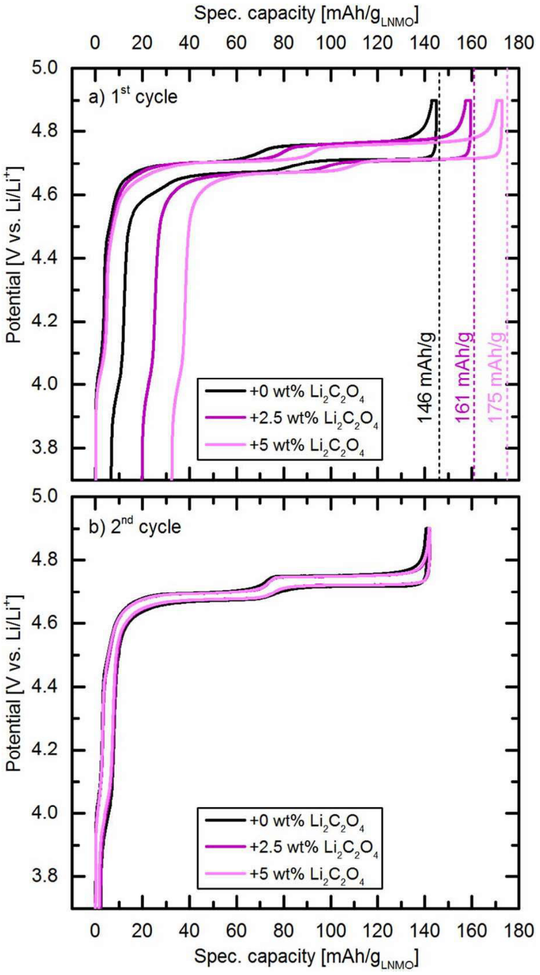

Figure 2. a) First charge/discharge and b) second charge/discharge of LNMO electrodes with 0 wt% (black line), 2.5 wt% (purple line) and 5 wt% (pink line) lithium oxalate in the composite cathode vs. Li metal in LP57 at a rate of C/10 between 3.5-4.9 V at 25°C. The dashed lines mark the respective theoretical first charge capacities listed in Table I. For LNMO loadings, see Table I.

The effect of lithium oxalate in LNMO/graphite full cells.—In the above shown LNMO/Li half-cells, the anode consisted of a massive lithium reservoir, meaning that at least with regards to the availability of active lithium, the LNMO cathode could be fully relithiated in all cases. However, in full-cells with a graphite anode, the amount of active lithium in the cell is limited, and the relithiation capacity of the cathode depends on the amount of lithium still available, i.e., lithium that has not been consumed for SEI formation. Therefore, we expect higher discharge capacities for cathode compositions that have shown higher capacities in their first charge in LNMO/graphite cells, i.e., for those cells which have a higher lithium oxalate content in the cathode. Figure 3a shows the discharge capacities (closed symbols) and 1st cycle charge capacities (open symbols) for LNMO/graphite full-cells with different lithium oxalate contents (0, 2.5, and 5 wt%) in the LNMO cathode for two formation cycles at C/10 and further cycling at 1C (all at 25°C). The areal capacity of the graphite anodes was kept

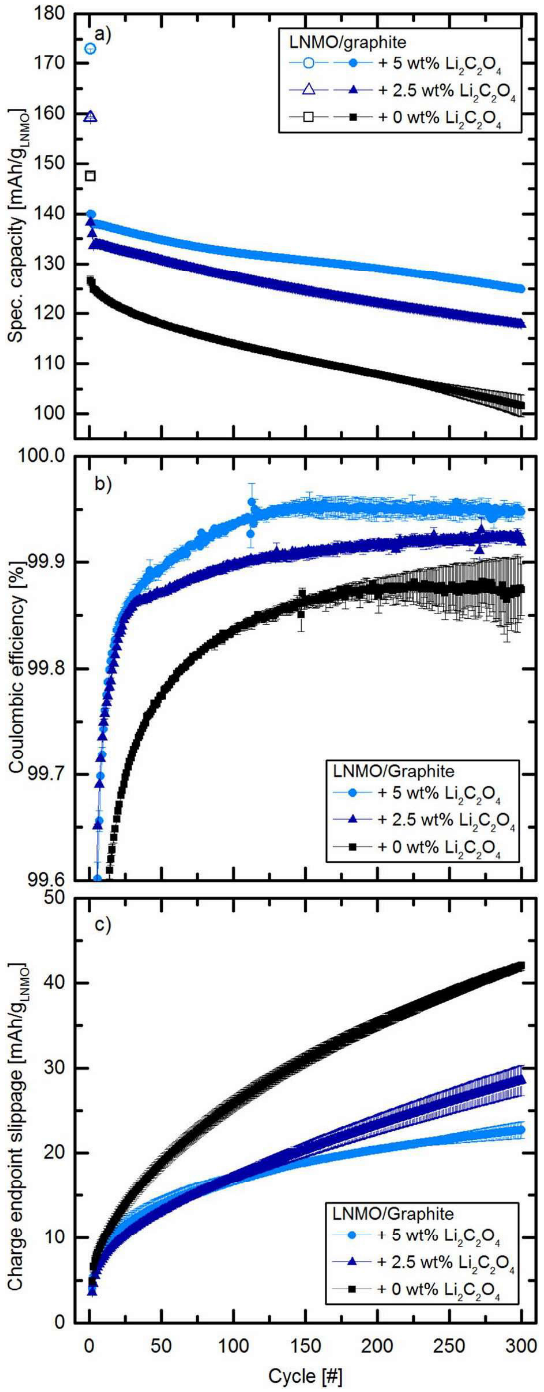

Figure 3. a) Specific discharge (closed symbols) and 1st cycle specific charge (open symbols) capacities, b) coulombic efficiencies and c) charge end point slippage of LNMO/graphite cells with 0 wt% (black squares), 2.5 wt% (dark blue triangles) and 5 wt% (light blue circles) lithium oxalate in the cathode composite during cycling in LP57 at 1C between 3.5-4.8 V and 25°C. The first two cycles were performed at C/10. All symbols represent the average of two replicate cells. whereas error bars represent the deviation between the replicates. The LNMO and graphite loadings are given in Table I.

constant in order to have a comparable first cycle irreversible capacity for all cells. Similar to the LNMO/Li half cells, the first charge capacity is 146 mAh/g_{LNMO}, 159 mAh/g_{LNMO}, and 173 mAh/g_{LNMO} for cells with 0, 2.5, and 5 wt% lithium oxalate in the cathode (closed symbols in Figure 3a). The discharge capacity is now however different for the three compositions: while the cells without lithium oxalate reach a first cycle discharge capacity of 125 mAh/g_{LNMO}, the cells with 2.5 wt% lithium oxalate have a first cycle discharge capacity of 138 mAh/g_{LNMO}, which means that the first irreversible capacity of these different cells is in both cases ~21 mAh/g_{LNMO}. The cells with 5 wt% lithium oxalate have a first cycle discharge capacity of around 139 mAh/g_{LNMO}. Assuming a similar irreversible capacity as for the cells with 0 wt% and 2.5 wt% lithium oxalate, one would expect a discharge capacity of around 152 mAh/ g_{LNMO}; however, this is above the practical reversible capacity of LNMO of 140 mAh/g (as shown in Figure 2). The additional lithium (corresponding to ~12 mAh/g_{LNMO}) thus remains as a reservoir in the graphite anode.

During the subsequent cycles at 1C, the difference in discharge capacity between the three different cathode compositions is retained up to 300 cycles. Interestingly, the cells with lithium oxalate also show better capacity retention: While cells without lithium oxalate drop about 19% in capacity between cycle 3 (i.e., the first cycle at 1C) and cycle 300, the cells with 2.5 and 5 wt% lithium oxalate lose only about 12% and 8% capacity, respectively. These cells also show an improved average coulombic efficiency between cycles 3–300 of 99.88% (2.5 wt% lithium oxalate) and 99.92% (5 wt% lithium oxalate), compared to 99.81% for cells without lithium oxalate (see Figure 3b). This phenomenon could be explained by i) the additional lithium reservoir and its effect on the graphite potential at the end of discharge, and/or, ii) by the effect of CO_2 as an SEI-forming additive. In the cells with 5 wt% lithium oxalate, some lithium remains in the graphite after formation. Hu et al.[34] have shown that LNMO/graphite cells show an improved cycling behavior as long as the cells contain an excess of active lithium (added in their case as metallic lithium or by ex-situ pre-lithiation of the graphite anode). However, the amount of additional lithium in our case is much lower compared to Hu et al.[34] (~10% vs. ~100% of the initial LNMO capacity) and should therefore only affect the very first cycles (i.e., until the additional capacity of ~12 mAh/g has been consumed). Still, if lithium is remaining in the graphite anode at the end of a discharge, the maximum graphite potential is lower compared to cells with less or without lithium oxalate. It has been shown that enhanced gas evolution related to SEI damage can occur when graphite is polarized to high potentials (>1.2 V vs. Li/Li^+).[35] Although a precise determination of the anode potential without a reference electrode is hardly possible, we can use following approximation: If we assume a maximum potential of 4.7 V vs. Li/Li^+ for LNMO at the end of discharge and consider that the difference between cathode and anode potential has to be at least 3.5 V (which is our lower cutoff penalty), the graphite potential is limited to a maximum of 1.2 V vs. Li/Li^+; hence, SEI damage should be avoided. Furthermore, the observed improvements in cycling stability of cells with 2.5 wt% lithium oxalate cannot be explained by different maximum potentials for graphite, as in this case, no lithium is remaining in the graphite and the upper cutoff potential during graphite delithiation should be very similar to cells without lithium oxalate.

Consequently, this brings us back to the effect of CO_2 as an SEI additive. In general, SEI instability and the consequent active lithium loss is regarded as a major fading mechanism in LNMO/graphite cells.[34–36] Pritzl et al.[37] recently showed that the cycling stability of LNMO/graphite cells can be improved by very small amounts of VC, an effective SEI former; however, if the amount of VC gets too large, the competitive oxidation of VC on LNMO counteracts its beneficial effect on the anode.[37,38] CO_2 has long been known to improve SEI properties on both lithium metal[14,15] and graphite.[12,13,39] Xiong et al. found that almost all CO_2 generated on the cathode can be consumed on the graphite anode in commercial-scale NMC422/graphite full-cells, given that no other strong SEI-forming additives are present.[40] Krause et al. showed that CO_2 can have a similar effect on the cycling stability of graphite electrodes in EC-free electrolyte solutions as

VC.[18] Recently, our group demonstrated that CO_2 can stop the transesterification reactions occurring from alkoxides generated through the reduction of linear carbonates.[16] Furthermore, the CO_2^- radical from the reduction of CO_2 on graphite can act as an H_2O/H^+ scavenger, yielding lithium formate and lithium carbonate as SEI products.[17] As protons are a possible product of electrolyte oxidation,[28] this effect would be especially relevant for high-voltage lithium ion cell chemistries like the LNMO/graphite system.

Sloop et al.[41] suggested that the reduction of CO_2 could lead to lithium oxalate formation at the anode, which could dissolve and be re-oxidized at the cathode, generating a shuttling current followed by self-discharge. To assess whether the presence of CO_2 indeed leads to enhanced side reactions, we calculated the charge end point slippage (the cumulative irreversible charge capacity, i.e., the charge capacity of each cycle subtracted by the previous discharge, summed up over all cycles), which is an indicator for oxidative or shuttling side reactions.[42] The charge end point slippage for LNMO/graphite cells with 0, 2.5, or 5 wt% lithium oxalate is shown in Figure 3c. As a CO_2/oxalate shuttle mechanism would contribute to the charge capacity but not the discharge capacity, cells with lithium oxalate should show a higher charge end point slippage compared to cells which do not contain lithium oxalate or CO_2. However, it becomes clear from Figure 3c that the charge end point slippage for cells with lithium oxalate is lower compared to cells without lithium oxalate. Hence, under the present conditions, the CO_2/oxalate shuttle effect is either negligible or nonexistent and does not contribute to the side reactions in the cell. This is in agreement with Xiong et al.,[40,43] who showed that there is no re-generation of CO_2 from a lithium oxalate/CO_2 shuttle detectable in NMC422/graphite cells.

The effect of lithium oxalate in LNMO/SiG full cells.—The use of a sacrificial salt to compensate for SEI losses is even more relevant if LNMO cathodes are combined with silicon or silicon/graphite anodes, which typically have much higher SEI losses due to i) the high specific surface area of the nanometer-sized silicon particles, and, ii) the expansion of the silicon particles during their lithiation, creating fresh surface area in every cycle that triggers further SEI growth. Hence, we investigate the use of lithium oxalate as capacity enhancer in combination with silicon/graphite (SiG) electrodes containing 35 wt% nano-Si and 45 wt% graphite. These electrodes, which have been investigated in more detail in a previous study by our group,[25] show a typical first cycle coulombic efficiency of ~85%. Therefore, we combine them with LNMO cathodes containing 5 wt% lithium oxalate, as the amount of lithium oxalate in these electrodes should largely compensate the irreversible loss during the first cycle. As electrolyte solution, we use LP57 + 5 wt% fluoroethylene carbonate (FEC), as this additive is known to improve the capacity retention of silicon-based electrodes.[19–25] The capacity retention and the coulombic efficiency of the LNMO/SiG cells with 5 wt% (green symbols) and without lithium oxalate (black symbols) in the cathode are shown in Figures 4a and 4b, respectively. The first charge capacities are 145 mAh/g_{LNMO} for cells without lithium oxalate and 173 mAh/g_{LNMO} for cells with 5 wt% lithium oxalate (open symbols), similar to the corresponding cells with graphite anodes. The first discharge capacities of 128 mAh/g_{LNMO} for cells with 5 wt% lithium oxalate and 109 mAh/g_{LNMO} without lithium oxalate are however lower compared to the corresponding LNMO/graphite cells. This was expected due to the higher irreversible capacity of the SiG anodes. It is to note that the first cycle irreversible capacity of cells with 5% lithium oxalate is slightly higher compared to the cells without lithium oxalate (45 mAh/g_{LNMO} vs. 36 mAh/g_{LNMO}); this effect can be explained as the 20% larger charge capacity results in a ~17% higher degree of lithiation (considering the balancing factor of ~1.3) The stronger expansion of the silicon particles creates more fresh surface and requires a higher irreversible capacity to passivate the selfsame.

During cycling, all SiG-based cells show a much stronger capacity fade compared to the LNMO/graphite cells (Figure 3). Yet, also for the LNMO/SiG system, the cells with lithium oxalate show a more stable cycling behavior and a higher coulombic efficiency compared to their counterparts without lithium oxalate. While this difference was rather small in the LNMO/graphite cells, in the case of the LNMO/SiG cells, the average coulombic efficiency is almost 1% point higher during the first 50 cycles for cells containing 5 wt% lithium oxalate (black vs. green symbols in Figure 4b). At the same time, the capacity retention after 250 cycles is ~45% for cells with 5 wt% lithium oxalate and only ~20% for cells without lithium oxalate (referenced to the discharge capacity of cycle 4, i.e., the first cycle at C/2). Again, this effect could be attributed to either the additional lithium, or the CO_2 present in the cell. Markevich et al.[21] reported that the cycling stability of silicon is improved if complete delithiation is omitted; and similar to LNMO/graphite cells, LNMO/Si cells show a stable cycling performance if a sufficiently large lithium reservoir is available.[44] However, in both cell types used here (i.e., LNMO/SiG with and without lithium oxalate), the discharge capacity is always at least 20 mAh/g_{LNMO} lower than the maximum relithiation capacity of the LNMO cathode, which means that the potential of the LNMO cathode

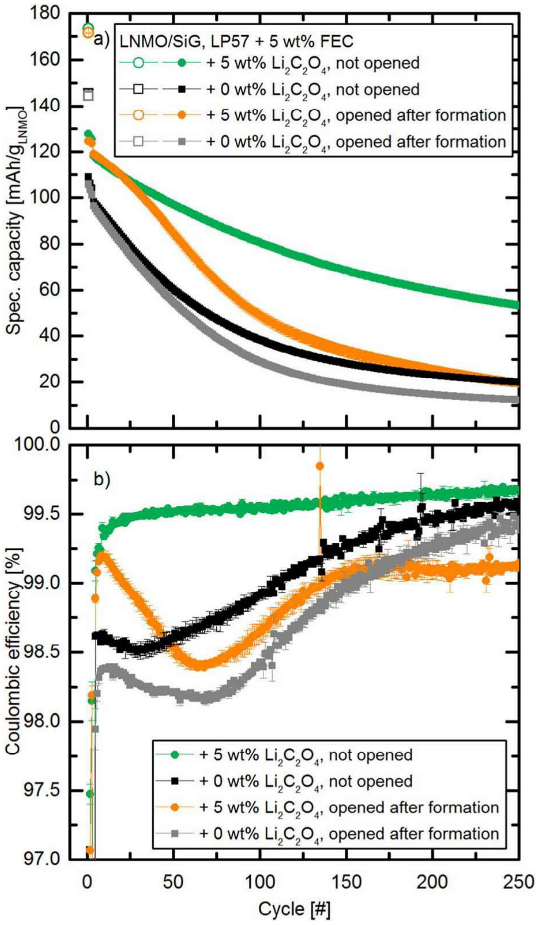

Figure 4. a) Specific discharge (closed symbols) and 1st cycle charge (open symbols) capacities and b) coulombic efficiencies of LNMO/SiG cells with 0 wt% (black and gray squares) or 5 wt% (green and orange circles) lithium oxalate in the cathode matrix during cycling in LP57 + 5 wt% FEC at C/2 and 25°C between 4.0–4.8 V. The first three cycles were performed at C/10. Cells represented by black and green symbols ("not opened") were then cycled at C/2. Cells represented by gray and orange symbols ("opened after formation") were reopened after the third cycle inside an Ar-filled glove box and both electrodes of each cell were transferred to a new cell with fresh separators and electrolyte solution. Cycling was then continued at C/2. All symbols represent the average of two replicate cells, whereas error bars represent the deviation between the replicates. The LNMO and SiG loadings are given in Table I.

is still around ~4.7 V when the cells reaches the lower cutoff voltage (compare the half-cell potentials from Figure 2). As the lower cell cutoff is limited to 4.0 V, this corresponds to a maximum voltage of ~0.7 V at the anode for both cells, where structural damage due to complete delithiation is unlikely.

In the LNMO/graphite cells, we have attributed the clearly improved cycling performance of cells with lithium oxalate to the effect of CO_2 as an SEI-forming additive. In contrast, in the LNMO/SiG cells there is already an SEI-forming additive (namely FEC), yet the differences between cells with and without lithium oxalate are much more pronounced for SiG anodes. In order to understand whether the additional lithium or CO_2 leads to the improved capacity retention, we repeated the cycling experiments with SiG anodes and LNMO cathodes containing either 0 or 5 wt% of lithium oxalate. This time, however, we stopped the cells after formation (i.e., after the initial 3 cycles at C/10) in the discharged state and disassembled them inside an Ar-filled glove box. The electrodes were then reassembled in new coin cells with fresh electrolyte solution and separators. In this way, all CO_2 was removed from the void space in the cell body and from the electrolyte solution, while the amount of active lithium was not altered. The gray and orange symbols in Figure 4 show the capacity retention and coulombic efficiency of these reassembled cells. The capacities of the first three cycles of both cell types look identical to Figure 4, as expected. After reassembly, the performance of the cells without lithium oxalate (gray symbols in Figure 4a) is slightly worse than the same cells which had not been opened (black symbols in Figure 4a), which can be attributed to a partial re-dissolution of the SEI in the fresh electrolyte solution. The minor differences however indicate that the reassembly procedure did not alter the cell performance substantially. The cells with lithium oxalate (orange symbols in Figure 4a) show the same discharge capacity directly after reassembly as before the reopening procedure, which also indicates that they were not damaged during the reassembly. However, from cycle 20 onwards, these cells show a much stronger capacity decrease compared to the cells with lithium oxalate that had not been opened (green symbols in Figure 4a). From cycle 10 on (i.e., almost directly after the reassembly), the coulombic efficiency of the reassembled cells with lithium oxalate (orange symbols in Figure 4b) starts to decline, while it is continuously rising in the cells with lithium oxalate that have not been opened (green symbols in Figure 4b). Around cycle 50, the coulombic efficiency of the reassembled cells with lithium oxalate (orange symbols) has reached the level of the cells without lithium oxalate (black and gray symbols). Apparently, the removal of CO_2 leads to an increase in irreversible reactions, which lowers the coulombic efficiency and depletes the active lithium, ultimately causing a drop in capacity.

FEC consumption in LNMO/SiG full cells with and without lithium oxalate.—To understand to which extent CO_2 participates in SEI formation when FEC is present, we conducted a post-mortem analysis of the electrolyte solution of aged LNMO/SiG cells without lithium oxalate and with 5 wt% lithium oxalate after 50 and 250 cycles, quantifying the amount of residual FEC by ^{19}F-NMR (for more details see Jung et al.[22]). The upper x-axis of Figure 5 shows the amount of residual FEC found in the electrolyte solution. As more remaining FEC is found in the cells with lithium oxalate (green symbols) compared to their counterparts without lithium oxalate that underwent the same number of cycles (black symbols), it is apparent that the FEC consumption per cycle for cells containing both FEC and lithium oxalate is lower. Previous studies have shown that the amount of consumed FEC correlates linearly with the cumulative irreversible discharge capacity (i.e., the sum of the differences between discharge and charge capacity over a certain amount of cycles),[22] which has recently also been demonstrated for SiG anodes with identical composition.[25] Therefore, the cumulative irreversible discharge capacity for each of the analyzed cells is shown on the y-axis of Figure 5, while the amount of consumed FEC in μmol is shown on the lower x-axis. The dashed lines show different e^-/FEC ratios, among them the empirically found 4 e^-/FEC (= 0.107 mAh$_{irr}$/μmol) relationship observed by Jung et al.[22] The offset of the e^-/FEC ratios on the y-axis in Figure 5 can be explained by considering the following: As the lower cell cutoff potential is restricted to 4.0 V, the potential of the SiG anode is limited to a maximum of ~0.7 V vs. Li/Li$^+$ (assuming a maximum cathode potential of 4.7 V vs Li/Li$^+$). At this potential, only about 85% of all lithium is extracted from the SiG electrode during discharge,[25] leading to an apparently higher irreversible capacity for the first cycle, which is however not related to FEC consumption.

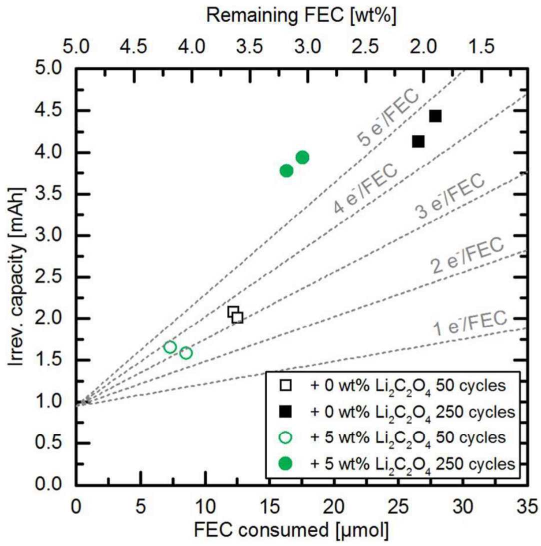

Figure 5. Cumulative irreversible discharge capacity vs. remaining FEC (upper x-axis) and consumed FEC (lower x-axis) in LNMO/SiG cells with 5 wt% (green circles) or 0 wt% lithium oxalate (black squares) in the cathode composite during cycling in LP57 + 5 wt% FEC at C/2 and 25°C between 4.0–4.7 V after 50 cycles (open symbols) or 250 cycles (closed symbols). The two identical symbols represent results from two replicate cells.

It is to note that in contrast to References 22 and 25, in the present study the silicon-based anode is not the capacity-limiting electrode, and side reactions occurring at the LNMO cathode may not be negligible, which makes an analysis of the cumulative irreversible capacity less obvious. Still, the cells without lithium oxalate (black symbols) lie reasonably close to the previously found 4 e^-/FEC linear correlation, which holds also true for the cells with 5 wt% lithium oxalate after 50 cycles (open green circles). After 250 cycles, however, the irreversible capacity is about 1 mAh higher (or the FEC consumption is 10 μmol lower) than the 4 e^-/FEC correlation for cells with 5 wt% lithium oxalate (closed green circles in Figure 5). This indicates that there is an additional process related to the irreversible discharge capacity, which does not consume FEC. It is likely that this additional process is the electrochemical reduction of CO_2 on the SiG anode, as this reaction would contribute to the cumulative irreversible capacity, but not the FEC consumption.

Consumption of carbon dioxide in LNMO/SiG full cells.—To investigate the consumption of CO_2 on the SiG anode, we performed 1-compartment OEMS measurements on the first cycle of LNMO/SiG full-cells. If a significant amount of the CO_2 from lithium oxalate oxidation were to be consumed on the SiG anode during this first formation cycle, the overall CO_2 evolution should be lower than expected for the essentially complete lithium oxalate oxidation in the first cycle. As a benchmark for the maximum CO_2 evolution that can be practically achieved from our LNMO/lithium oxalate cathodes, we also measured a LNMO electrode containing 5 wt% lithium oxalate vs. an oversized delithiated LFP electrode. Due to the high potential of the LFP (~3.4 V vs. Li/Li$^+$), we do not expect any reductive consumption of CO_2 in this system. The yellow line in Figure 6a shows

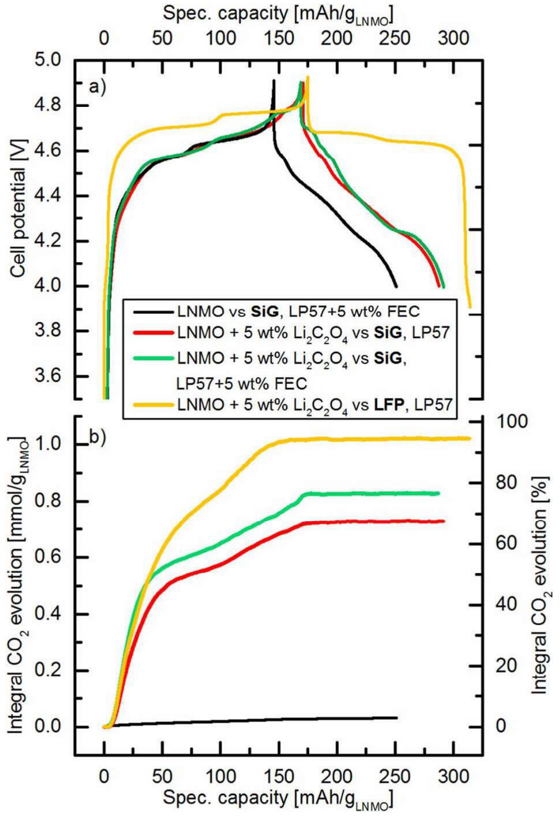

Figure 6. a) Potential profile and b) CO_2 evolution during the first charge/discharge cycle of an LNMO/SiG cell with 0 wt% lithium oxalate in LP57 + 5 wt% FEC (black lines), an LNMO/SiG cell with 5 wt% lithium oxalate in LP57 (red lines), an LNMO/SiG cell with 5 wt% lithium oxalate in LP57 + 5 wt% FEC (green lines), and an LNMO/LFP cell with 5 wt% lithium oxalate in LP57 (yellow lines). Cycling was done at C/5 and 25°C in a 1-compartment OEMS cell.

the potential profile of an LNMO/LFP cell with 5 wt% lithium oxalate (the cell potential was converted to the Li/Li$^+$ scale by adding 3.42 V, the equilibrium potential of LFP[45]), whereas the yellow line in Figure 6b shows the corresponding CO_2 evolution. The first charge capacity (174 mAh/g$_{LNMO}$) in the LNMO/LFP + 5 wt% lithium oxalate OEMS cell is similar to the capacity achieved in LNMO half cells containing 5 wt% lithium oxalate vs. lithium (compare Figure 2). The CO_2 evolution in the LNMO/LFP + 5 wt% lithium oxalate OEMS cell rises to 1.02 mmol/g$_{LNMO}$, which corresponds to ~95% of the theoretical amount of CO_2 based on conversion of all lithium oxalate (see right y-axis in Figure 6b). The deviation from 100% is likely due to Li_2CO_3 impurities as well as partial dissolution of CO_2 in the electrolyte solution, as discussed previously.

As a next step, we repeated this experiment but replaced the LFP counter electrode with a SiG anode, while the cathode (LNMO + 5 wt% lithium oxalate) and the electrolyte solution (LP57 + 5 wt% FEC) remained identical (green lines in Figures 6a and 6b). With the SiG anode, the total CO_2 evolution was significantly lowered to 0.83 mmol/g$_{LNMO}$ (~77% of the theoretical CO_2). In the absence of FEC (i.e., in pure LP57), the total CO_2 evolution of the LNMO/SiG cells with 5 wt% lithium oxalate (red lines in Figures 6a and 6b) is further decreased to 0.73 mmol/g$_{LNMO}$, i.e., to ~68% of the theoretical CO_2. These results indicate that a significant amount of the practically available CO_2 (~19% for cell with LP57 + 5 wt% FEC or ~28% for cells with LP57) is already reduced in the first cycle of LNMO/SiG cells. To evaluate whether the apparently lower CO_2 consumption in FEC-containing vs. FEC-free electrolyte solutions may not simply be due to the additional release of CO_2 by the reduction of FEC,[22,46] we also investigated an LNMO/SiG cell without lithium oxalate in LP57 + 5 wt% FEC by OEMS (black lines in Figures 6a and 6b). While a minor extent of CO_2 is formed in this case, it amounts to only 0.03 mmol/g$_{LNMO}$, which is small compared to the ~0.10 mmol/g$_{LNMO}$ difference between the lithium oxalate containing LNMO/SiG cells with and without FEC. These observations are consistent with the findings by Krause et al.,[18] who showed that CO_2 dosed to cells with silicon anodes gets consumed at the silicon anode, and that its consumption rate is reduced in the presence of FEC.

In contrast to FEC, where the consumed amount can be easily determined by ^{19}F-NMR, a quantification of the remaining CO_2 after extended cycling is not easily possible from the coin cells used in this study. However, Krause et al.[18] showed that once all added CO_2 is consumed, Si alloy-based cells suffer from a severe drop in coulombic efficiency and capacity retention, analogously to what both Jung et al.[22] and Petibon et al.[24] demonstrated for the complete consumption of FEC from Si-based cells. Additionally, also the significantly different coulombic efficiencies from LNMO/SiG cells where CO_2 was either left in the cells (green symbols in Figure 4) or purposely removed (orange symbols in Figure 4) indicate that a drop in coulombic efficiency can be expected at the point where all CO_2 is depleted. Therefore, we repeated the cycling experiment from Figure 4 with LNMO/SiG cells containing different amounts of lithium oxalate (namely 0, 2.5, and 5 wt%) in pure LP57, i.e., without FEC in the electrolyte solution. Furthermore, with this experiment we investigate the effectiveness of CO_2 by itself as an SEI-forming additive for silicon-based anodes. Figure 7 shows the capacity retention for LNMO/SiG cells with LP57 and 0, 2.5, and 5 wt% lithium oxalate in the LNMO cathode. The initial charge/discharge capacities for cells with 0 wt% and 5 wt% lithium oxalate are similar to the cells with the same electrodes in FEC-containing electrolyte solution (see Figure 4), namely 145/110 mAh/g$_{LNMO}$ and 173/123 mAh/g$_{LNMO}$, respectively, whereas the first cycle charge/discharge capacity of cells with 2.5 wt% lithium oxalate lies in between these two (160/112 mAh/g$_{LNMO}$). During cycling, the cells with 0 wt% lithium oxalate decline dramatically in capacity, while their coulombic efficiency drops to <90% (black symbols). After 100 cycles, there is essentially zero capacity left in these cells. Comparing the cells without lithium oxalate (i.e., without CO_2) from Figure 4 and Figure 7 (both black symbols), once again illustrates how important SEI-forming additives like FEC are for silicon-based anodes to achieve a minimum of stable cycling.

The LNMO/SiG cells with pure LP57 and 5 wt% lithium oxalate (red spheres in Figure 7), however, show initially a much improved cycling stability and a coulombic efficiency of around 99.5%, which is much higher than the ~98.5% of the cells with FEC but without lithium oxalate (i.e., without CO_2; black symbols in Figure 4) and essentially identical with that of the cells with FEC and 5 wt% lithium oxalate (i.e., with CO_2; green symbols in Figure 4). This comparison clearly demonstrates that CO_2 forms an even more effective SEI than FEC. The cells with 2.5 wt% lithium oxalate (brown triangles in Figure 7) show a ~9 mAh/g lower capacity compared to their counterparts with 5 wt% lithium oxalate, which we ascribe to the lower amount of additionally available active lithium in the former. However, their coulombic efficiencies in the first tens of cycles are essentially identical due to the presence of CO_2. Around cycle 36 and 89, respectively, the cells with 2.5 wt% and 5 wt% lithium oxalate show a distinct decline in coulombic efficiency from ~99.5% to ~94% (for cells with 2.5 wt% lithium oxalate) or 97% (for cells with 5 wt% lithium oxalate), which in both cases is followed by a rapid decay in capacity.

In analogy to the rapid capacity fade and coulombic efficiency loss which was observed for silicon electrodes in FEC containing electrolye (without CO_2) once all FEC was being consumed,[22,24] and the observations made by Krause et al.,[18] it is very likely that it is the complete consumption of CO_2 which leads to the onset of the decline in coulombic efficiency around cycle 36 and 89 in cells with lithium oxalate (i.e., with CO_2) in the FEC-free electrolyte solution

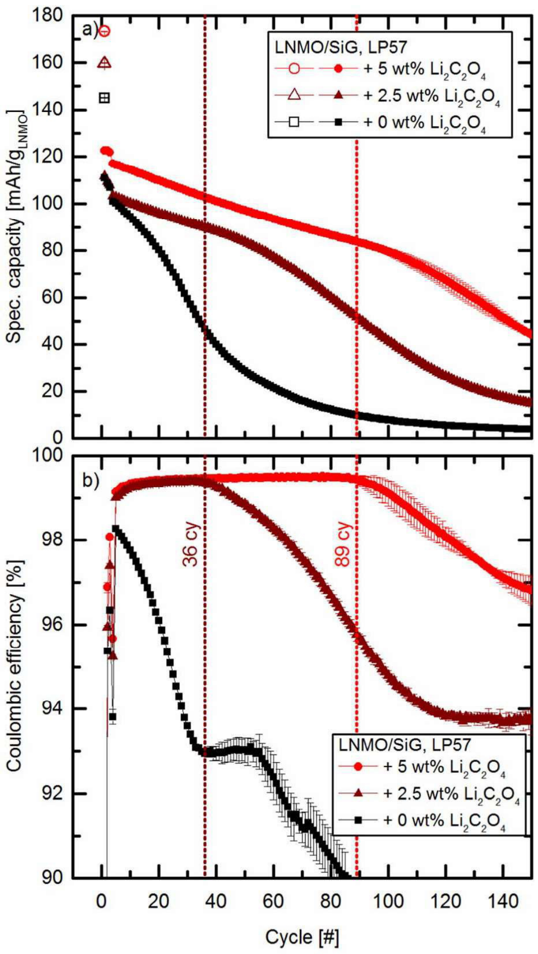

Figure 7. Specific charge (closed symbols) and discharge (open symbols) capacities (upper panel) and coulombic efficiencies (lower panel) of LNMO/SiC cells with 0 wt% (black squares), 2.5 wt% (brown triangles), and 5 wt% (red circles) lithium oxalate in the cathode composite during cycling in pure LP57 at C/2 and 25°C between 4.0–4.8 V. The first three cycles were performed at C/10. All symbols represent the average of two replicate cells, whereas error bars represent the deviation between the replicates. The LNMO and SiG loadings are given in Table I.

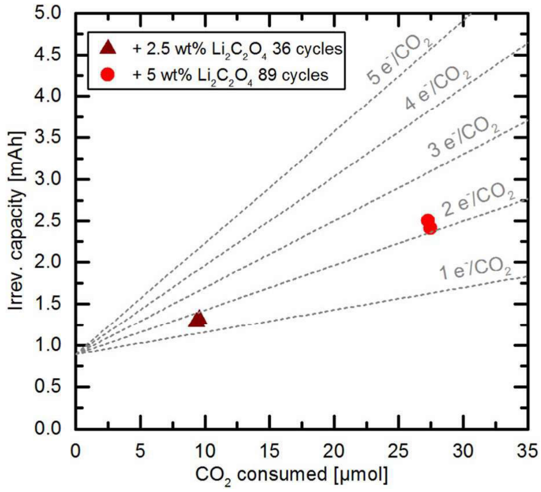

Figure 8. Cumulative irreversible discharge capacity vs. consumed CO_2 in LNMO/SiG cells with 5 wt% (red circles) or 2.5 wt% lithium oxalate (brown triangles) in the cathode composite during cycling in LP57 at C/2 and 25°C between 4.0–4.7 V after 36 cycles (2.5 wt% lithium oxalate) or 89 cycles (5 wt% lithium oxalate). These data are derived from Figure 7.

(see Figure 7). Under this assumption, we can examine whether there is a similar correlation between consumed CO_2 and cumulative irreversible capacity as we had done for FEC-containing electrolyte solution (see Figure 5), by taking the cumulative irreversible discharge capacity after cycle 36 (for cells with 2.5 wt% lithium oxalate) and cycle 89 (for cells with 5 wt% lithium oxalate) and the total theoretical amount of CO_2 that was available from lithium oxalate oxidation (see reaction 1) in these cells. Note that due to the ~30% lower loading of the LNMO electrodes with 2.5 wt% lithium oxalate (see Table I), the total theoretical amount of CO_2 in these cells is not 50% of the amount in the cells with 5 wt% lithium oxalate, but somewhat lower. The resulting correlation is shown in Figure 8; interestingly, the points lie close to a $2\ e^-/CO_2$ linear slope, whereas the often assumed reduction of CO_2 to carbonate and CO (acc. to: $2\ CO_2 + 2\ e^- \rightarrow CO_3^{2-} + CO$)[47–49] as well as the reduction of CO_2 to oxalate (acc. to: $2\ CO_2 + 2\ e^- \rightarrow C_2O_4^{-2}$)[49–51] both would correspond to $1\ e^-/CO_2$. Apparently, a more complex reduction mechanism is taking place. One possible pathway is the formation of formate anions from CO_2 and protic species (i.e., protons from trace HF or electrolyte oxidation products), which would correspond to a total of $2\ e^-/CO_2$ (acc. to: $CO_2 + 2\ e^- + H^+ \rightarrow HCOO^-$).[47,51] Furthermore, it may be possible that a fraction of the cumulative irreversible capacity is related to decomposition reactions of the electrolyte solvent. A more detailed analysis of the possible reduction reactions of CO_2 on lithium ion battery anodes is currently under investigation.[17]

In the LNMO/SiG cells with pure LP57 and 5 wt% lithium oxalate (red spheres in Figure 7) as well as in the reassembled LNMO/SiG cells with 5 wt% lithium oxalate, i.e., after the removal of CO_2 (orange spheres in Figure 4), we have observed a rapid drop in coulombic efficiency (to a less pronounced degree also in capacity) at the point where no CO_2 was left. However, such a coulombic efficiency drop is not observable for the cells with 5 wt% lithium oxalate with LP57 + 5 wt% FEC (green spheres in Figure 4). To our current understanding, this would indicate that CO_2 has not been completely consumed in these cells even after 250 cycles. To estimate the amount of remaining CO_2 in these cells, we again consider the irreversible capacity vs. FEC consumption relationship shown in Figure 5. As previously discussed, the irreversible capacity for the cells with 5 wt% lithium oxalate is higher compared to the experimentally found $4\ e^-/FEC$ ($= 0.107\ mAh/\mu mol_{FEC}$) line (green circles in Figure 5). If we assume that this additional irreversible capacity (~1 mAh) is associated with the reduction of CO_2, we can use the empirically found correlation of $2\ e^-/CO_2$ ($= 0.0536\ mAh/\mu mol_{CO2}$) from Figure 8 to estimate that ~18.6 μmol of CO_2 have been consumed after 250 cycles. The fact that this amount is still lower than the available amount of CO_2 (28.2 μmol) suggests that CO_2 is still remaining in these cells after 250 cycles, which would explain why no rapid coulombic efficiency drop has occurred until this point for the cells with 5 wt% lithium oxalate in FEC-containing electrolyte solution (green circles in Figure 4). For the same cells after 50 cycles, the irreversible capacity lies close to the $4\ e^-/FEC$ line, which means that an assessment of the CO_2 consumption through the irreversible capacity cannot be undertaken. We believe that due to both the low consumption of FEC after 50 cycles as well as the low irreversible capacity, a definitive correlation cannot be made. Nevertheless, it is possible that a fraction of the irreversible capacity is used for the reduction of CO_2; the large differences in coulombic efficiency between cells with and without lithium oxalate (see Figure 4) as well as the results from OEMS measurements (see Figure 6) suggest that CO_2 is modifying the SEI already during early cycles.

Discussion

Implications for the deliverable capacity of LNMO / SiG cells.— Besides the continuous loss of active lithium, the lifetime of cells with Si-based anodes is largely dependent on the amount of SEI-forming additives available.[18,22,24,25] The experiments in the present study have shown that LNMO/SiG cells with lithium oxalate show a better capacity retention and coulombic efficiency compared to their counterparts without lithium oxalate even in the presence of FEC, and that the co-reduction of CO_2 and FEC occurs simultaneously. However, the question remains how "efficient" the combination of FEC and CO_2 is in terms of additive consumption and active lithium loss. To elucidate this, Figure 9a shows the cumulative delivered discharge capacity, i.e., the sum of discharge capacities over all cycles up to a certain point, per cumulative irreversible discharge capacity for cells with only FEC (gray bars), only CO_2 (red bars) or both additives (green bars). While for cells containing FEC, the data after 50 and 250 cycles (gray solid and dashed bars) are shown, we plotted the data from cycle 36 and 89 for cells without FEC and only CO_2, as these are the cycles for which there is strong evidence that all CO_2 has been consumed. Comparing only FEC- or only CO_2-containing cells (gray and red bars in Figure 9a), it becomes clear that CO_2 improves the delivered capacity per irreversible capacity. The largest impact, however, has the combination of FEC and CO_2 (green bars in Figure 9a), which leads to a doubling of the delivered capacity per irreversible capacity after 50 and 250 cycles compared to FEC by itself.

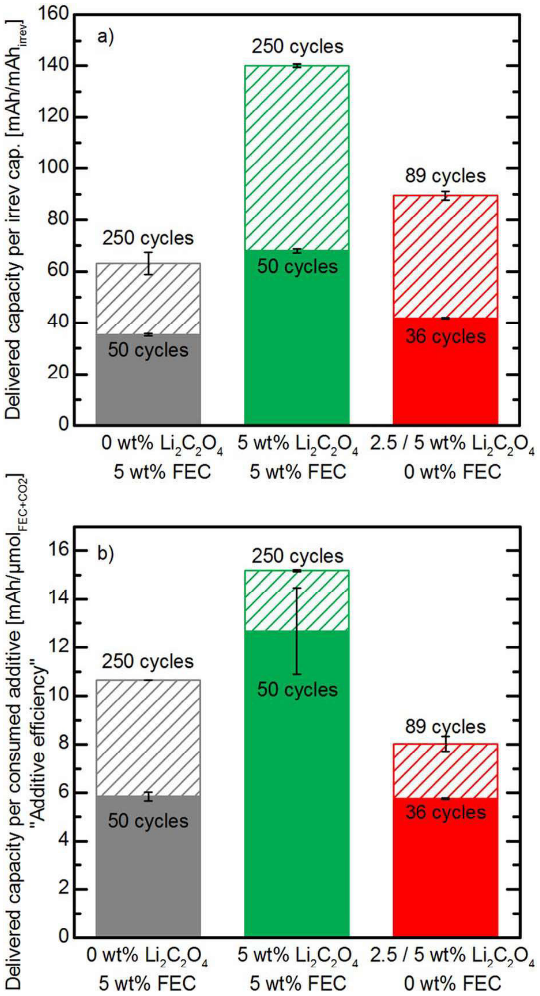

Figure 9. Cumulative delivered discharge capacity a) per cumulative irreversible discharge capacity, and, b) per µmol of additives (FEC+CO_2) for LNMO/SiG cells without lithium oxalate and LP57 + 5 wt% FEC (gray bars), cells with 5 wt% lithium oxalate and LP57 + 5 wt% FEC (green bars), and cells with 2.5 or 5 wt% lithium oxalate and LP57 (red bars). The solid bars represent the delivered capacity after 50 (36 for cells without FEC) cycles, while the dashed bars represent the delivered capacity after 250 (89 for cells without FEC) cycles. Bars represent the average result from two replicate cells, whereas error bars represent the deviation between the replicates.

Figure 9b shows the cumulative delivered discharge capacity per µmol of consumed additive (i.e., the sum of CO_2 and FEC), for the same points as in Figure 9a. To estimate the amount of CO_2 consumed in the LNMO/SiG cells with both lithium oxalate and FEC, we used the above described approximation based on the additional irreversible capacity. From Figure 9b, it is apparent that the combination of CO_2 and FEC (green bars) in LNMO/SiG cells leads to an improved additive efficiency (i.e., delivered capacity per mol of additive) compared to the use of single additives (gray and red bars). This effect is especially pronounced during the early stage of cycling ($\leq$50 cycles), where the additive efficiency for cells with lithium oxalate and FEC is more than two times higher compared to the cells with only FEC (13.1 mAh/µmol vs 5.9 mAh/µmol, respectively). Interestingly, the additive efficiency of only FEC cells (gray bars) is similar to only CO_2 cells (red bars), whereas the delivered capacity per irreversible capacity is clearly lower for cells containing only FEC than for only CO_2 cells (gray and red bars in Figure 9a). However, this agrees with the lower number of electrons required for the reduction of CO_2 in contrast to FEC (compare Figure 5 and Figure 8). For all cells, the additive efficiency grows for a higher number of cycles, which fits well to the observation that coulombic efficiencies also tend to increase during cycling as long as FEC and/or CO_2 have not been consumed (see Figure 4 and Figure 7 as well as Reference 25). In the case of graphite anodes (see Figure 3), this is related to the formation of a gradually more passivating and thicker SEI; in the case of silicon anodes, the additional effect leading to an improvement of the coulombic efficiency is the fact that as the capacity fades, the state-of-charge change per cycle becomes lower, which causes less volume expansion/contraction and thus less and less SEI rupture.

Implications for the energy density of LNMO/graphite cells.— To consider the effect of lithium oxalate on commercial-scale cells, we take a step back to the LNMO/graphite cells that were shown in Figure 3. Figure 10 shows the specific energy density (using the charge-averaged discharge voltage) during cycle 5 and cycle 300 of the LNMO/graphite cells with different amounts of lithium oxalate from Figure 3 at 1C discharge. The addition of 2.5 wt% lithium oxalate increases the initial (5th cycle) cathode specific energy density from 555 Wh/kg$_{LNMO}$ to 600 Wh/kg$_{LNMO}$; the addition of 5 wt% lithium oxalate does not improve the energy density much further in the 5th cycle (to 615 Wh/kg$_{LNMO}$). These values are ~5-10% lower than the energy density of NMC622/graphite cells cycled at the same conditions to 4.4 V, the highest possible cutoff potential which still shows stable performance.[52] After 300 cycles, the cathode specific energy density of the LNMO/graphite cells without lithium oxalate drops to 453 Wh/kg$_{LNMO}$ ($\equiv$82% energy density retention), while ~16% higher specific energies of 527 Wh/kg$_{LNMO}$ ($\equiv$88% energy density retention) are observed for cells with 2.5 wt% lithium oxalate; at the higher level of 5 wt% lithium oxalate, the specific energies of 555 Wh/kg$_{LNMO}$ are ~23% higher than without oxalate and the energy density retention is 90%. These energy retentions are very comparable to that of the above mentioned NMC622/graphite cells.[52] While the lithium oxalate containing LNMO/graphite cells do have a ~5-10% lower energy density, they are an interesting option for cobalt-free lithium ion battery cells, which may become critical in the future due to the rising cost and geographic concentration of cobalt.[53,54]

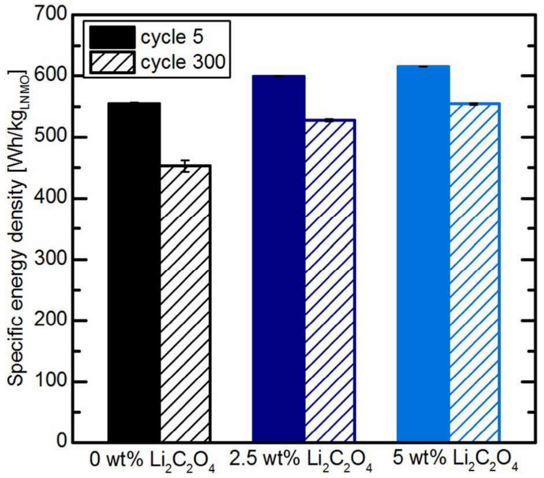

Figure 10. Cathode specific energy density during 1 C discharge of LNMO/graphite cells with 0 wt% (black bars), 2.5 wt% (dark blue bars), and 5 wt% lithium oxalate (light blue bars) at cycle 5 (solid bars) and cycle 300 (dashed bars) at 25°C. Bars represent the average result from two replicate cells, whereas error bars represent the deviation between the replicates. The data are based on Figure 3.

Assuming all electrodes used here have the same initial porosity of 35%, the specific volume of electrode (including voids) per gram LNMO increases from 0.44 cm^3/g_{LNMO} to 0.46 cm^3/g_{LNMO} or 0.48 cm^3/g_{LNMO} by adding 2.5 wt% or 5 wt% lithium oxalate, respectively (calculated from electrode compositions given in Table I and bulk densities of 4.4 g/cm^3 for LNMO, 1.8 g/cm^3 for PVDF, 2.2 g/cm^3 for C65 and 2.1 g/cm^3 for lithium oxalate).[55] Accordingly, the oxidation of lithium oxalate leads to a porosity increase from 35% to 38% in the electrodes with 2.5 wt% and to 40% in the electrodes with 5 wt% lithium oxalate. The resulting volumetric energy density, here defined as energy per entire electrode volume including voids, is around 1272 $Wh/L_{electrode}$ at cycle 5 for cells without lithium oxalate and rises about 3% to 1315 $Wh/L_{electrode}$ for cells containing 2.5 wt% lithium oxalate. Cells with 5 wt% lithium oxalate deliver only 1291 $Wh/L_{electrode}$ at cycle 5, as the higher porosity now counteracts the slight increase in gravimetric energy density. This effect can be avoided if electrodes with lithium oxalate are calendered to initial porosities of 32% (2.5 wt% lithium oxalate) or 30% (5 wt% lithium oxalate). In this way, the porosity reaches 35% after lithium oxalate oxidation for all electrodes, and the resulting volumetric energy densities at cycle 5 for electrodes containing 0, 2.5 or 5 wt% lithium oxalate are 1272 $Wh/L_{electrode}$, 1376 $Wh/L_{electrode}$ or 1412 $Wh/L_{electrode}$.

Gas evolution in large-format cells.—As for LNMO/graphite cells, the use of more than 2.5 wt% lithium oxalate shows the biggest improvement factor and perhaps is the best compromise between the amount of electrode additive and specific energy retention. Therefore, the following considerations are all based on electrodes containing 2.5 wt% lithium oxalate. The CO_2 evolution from the oxidation of lithium oxalate during formation could be an issue in commercial-scale cells due to swelling (in pouch cells) or pressure buildup (in hard-case cells). This is largely related to the fact that in commercial-scale cells, the ratio of active materials to electrolyte solution and void volume is typically ~10 times higher compared to the lab-scale cells used here.[37,56] Strehle et al.[16] recently showed that under these conditions, the majority of CO_2 released from VC reduction would remain dissolved in the electrolyte solution instead of being released into the gas headspace of the cell. This is illustrated by first estimating the amount of dissolved CO_2 by Henry's law 2:

$$\frac{p_{CO_2(gas)}}{K_H} = \frac{n_{CO_2(el)}}{V_{el}\ c_{el} + n_{CO_2(el)}} \qquad [2]$$

Table II. Expected pressure buildup for coin or 18650 cells or volume expansion for pouch cells as well as the fraction of CO_2 dissolved in the electrolyte solution for a cathode electrode with 2.5 wt% lithium oxalate at room temperature (25°C) and a surrounding pressure of 1 bar. Note that CO_2 consumption at the anode is not taken into account here.

Cell type	2023 coin cell (2.6 mAh)	pouch cell (180 mAh)	18650 cell (3 Ah)
Cell headspace V_{gas} [mL]	0.5	–	1
Electrolyte solution V_{el} [mL]	0.08	0.75	7.6
Cathode material [g]	0.017	0.9	20.4
Total CO_2 $n_{CO2(total)}$ [μmol]	9.3	460	10 400
Fraction of CO_2 in the electrolyte solution [%]	30.3	17.9	95.4
Pressure buildup Δp [MPa]	0.032	–	1.19
Volume expansion ΔV [mL]	–	9.3	–

where $n_{CO2(el)}$ is the amount of CO_2 dissolved in the liquid electrolyte solution, V_{el} is the volume of the electrolyte solution, c_{el} is the total molar concentration of the electrolyte solution (i.e., solvent and salt) and K_H is the Henry constant of CO_2 in the electrolyte solution in units of pressure. Combining this with the ideal gas law and the assumption that $V_{el}\ c_{el} + n_{CO2(el)} \approx V_{el}\ c_{el}$, the fraction of CO_2 dissolved in the electrolyte solution can now be given as 3:

$$\frac{n_{CO_2(el)}}{n_{CO_2(total)}} = \frac{V_{el}\ RTc_{el}}{V_{el}RTc_{el} + V_{gas}K_H} \qquad [3]$$

where $n_{CO2(total)}$ is the total amount of CO_2 present in the system and V_{gas} is the volume of the cell's gas headspace. Assuming a constant gas volume, as would be the case for a hard-case cell, the pressure buildup can be expressed as 4:

$$\Delta p = n_{CO_2(total)} \frac{K_H RT}{V_{el}RTc_{el} + V_{gas}K_H} \qquad [4]$$

On the other hand, in soft pouch cells, gas evolution would typically lead to expansion (or bulging) of the cell. This volume expansion at a given pressure can be calculated by 5:

$$\Delta V = RT\left(\frac{n_{CO_2(total)}}{p} - \frac{V_{el}c_{el}}{K_H}\right) \qquad [5]$$

To assess how much pressure buildup or volume expansion would actually occur in a commercial-scale cell containing 2.5 wt% lithium oxalate in the cathode electrode, we use a similar approximation for a commercial-scale 3 Ah cell as shown in ref. 16, where the weight for cathode active material and electrolyte solution were taken from Wagner et al.[57] Furthermore, we also calculate the expected volume expansion for a 180 mAh pouch cell containing ~ 0.75 mL electrolyte solution as used by Xia et al.,[58] assuming a constant pressure of 1 bar in the cell. In both cases, the composite cathode is approximated to consist of 96% active material and 2.5 wt% lithium oxalate. For comparison, the 2032-type coin cells used in this study are also included in this assessment.

Table II summarizes the expected pressure buildup and volume expansion for the respective cells. The pressure increase in coin cells is low (~0.03 MPa), due to the relatively large void space compared to electrolyte solution and cathode active material volume. In a 180 mAh pouch cell, the estimated gas evolution would be ~9.3 mL at 1 bar, which is about 5 times larger than the gas evolution normally expected for these cells during formation.[58] The pressure buildup in the hard case 18650 cell is ~1.2 MPa; this causes that 95% of the CO_2 remains dissolved in the electrolyte solution. However, the oxidation of lithium oxalate is completed after the first charge, which means that the gas evolution will stop thereafter. As many commercial-scale cells are vented during or after formation, the high pressure/volume increase is only a matter of the very first cycles. We have further not considered the consumption of CO_2 on the graphite or silicon/graphite anode: Strehle et al.[16] showed that up to 40 μmol ($\approx$1 mL) CO_2 can be consumed per square meter graphite surface area during the first formation cycle, which agrees well with previous reports by Xiong et al.[40] The graphite electrodes used in the present study have a specific surface area of 0.034 m_{BET}^2/cm_{geom}^2, hence 40 $\mu mol/m_{BET}^2$ would correspond to a CO_2 consumption of 1.4 $\mu mol/cm_{geom}^2$, which is about ~20% of the evolved CO_2 (6 $\mu mol/cm_{geom}^2$). As long as the ratio of lithium oxalate to graphite or the specific surface area of the graphite do not change drastically, the same fraction of CO_2 would also be consumed during formation in other cell formats. For silicon-based anodes, the previous OEMS measurements have shown that the CO_2 consumption of SiG anodes during the first charge can be about 19–28% of the theoretically available CO_2 (see Figure 6). Assuming a consumption of 25% CO_2 in the first cycle, the volume expansion in pouch cells would be decreased to ~6.5 mL, while the pressure rise in 18650 cells would be limited to ~0.89 MPa. Although a venting of some of the excess gas is probably still required in this case, a complete removal of CO_2 after formation is not desirable, as the amount of CO_2 within the cell should remain high during cycling to benefit from its properties as an SEI-forming additive, as was shown here and in Reference 18.

Conclusions

In this paper, we assessed the use of lithium oxalate as a "sacrificial salt", i.e., a lithium ion donor, in combination with LNMO cathodes. We have shown that the incorporation of 2.5 wt% or 5 wt% lithium oxalate into the cathode electrode increases the first cycle charge capacity by about 10% and 20%, respectively, without affecting the electrochemical performance of the cathode during subsequent cycles. The effect of lithium oxalate and CO_2 released from its oxidation was investigated in LNMO/graphite and LNMO/silicon-graphite (SiG) cells. The former showed increased initial capacity according to the increased pool of active lithium, as well as a higher coulombic efficieny and capacity retention, when lithium oxalate was added to the cathode matrix. For LNMO/SiG cells, a significantly improved cycling stability and coulombic efficiency was found for cells containing lithium oxalate and FEC compared to cells with only FEC but no lithium oxalate, which we ascribe to the beneficial effect of CO_2 on the cycling stability of silicon-based anodes.

By OEMS measurements and analysis of the cumulative irreversible discharge capacity, we can conclude that CO_2 and FEC are simultaneously reduced, following and overall ~4 e^-/FEC and ~2 e^-/CO_2 process. Furthermore, the combination of these two additives is more efficient in terms of deliverable capacity per irreversible capacity and per mol of consumed additive than either of them alone. In this context, the use of lithium oxalate in the cathode matrix is not limited to its use as a "sacrificial salt" in the original sense, but also displays an easy and controllable way to introduce defined amounts of CO_2 into lithium ion cells with graphite or silicon-based anodes.

Acknowledgments

Sophie Solchenbach and Daniel Pritzl gratefully acknowledge the BASF Battery Research Network for financial support. Funding for Morten Wetjen was provided by the German Federal Ministry for Economic Affairs and Energy (BMWi; funding number 03ET6045D). Wacker Chemie AG is kindly acknowledged for providing the silicon nanoparticles. Furthermore, the authors want to thank Dr. Stefano Meini for fruitful discussions.

ORCID

Sophie Solchenbach https://orcid.org/0000-0001-7142-452X

References

1. D. Andre, S.-J. Kim, P. Lamp, S. F. Lux, F. Maglia, O. Paschos, and B. Stiaszny, *J. Mater. Chem. A*, **3**, 6709 (2015).
2. I. Buchberger, S. Seidlmayer, A. Pokharel, M. Piana, J. Hattendorff, P. Kudejova, R. Gilles, and H. A. Gasteiger, *J. Electrochem. Soc.*, **162**, A2737 (2015).
3. M. Klett, J. A. Gilbert, K. Z. Pupek, S. E. Trask, and D. P. Abraham, *J. Electrochem. Soc.*, **164**, A6095 (2017).
4. J. C. Arrebola, A. Caballero, H. Göhr, L. Hernán, J. Morales, and L. Sánchez, *Electrochem. commun.*, **11**, 1061 (2009).
5. C. R. Jarvis, M. J. Lain, M. V. Yakovleva, and Y. Gao, *J. Power Sources*, **162**, 800 (2006).
6. I. W. Seong, K. T. Kim, and W. Y. Yoon, *J. Power Sources*, **189**, 511 (2009).
7. N. Liu, L. Hu, M. T. McDowell, A. Jackson, and Y. Cui, *ACS Nano*, **5**, 6487 (2011).
8. M. Marinaro, M. Weinberger, and M. Wohlfahrt-Mehrens, *Electrochim. Acta*, **206**, 99 (2016).
9. G. Gabrielli, M. Marinaro, M. Mancini, P. Axmann, and M. Wohlfahrt-Mehrens, *J. Power Sources*, **351**, 35 (2017).
10. D. Shanmukaraj, S. Grugeon, S. Laruelle, G. Douglade, J.-M. Tarascon, and M. Armand, *Electrochem. commun.*, **12**, 1344 (2010).
11. J. O. Besenhard, M. W. Wagner, M. Winter, A. D. Jannakoudakis, P. D. Jannakoudakis, and E. Theodoridou, *J. Power Sources*, **44**, 413 (1993).
12. Y. Ein-Eli, B. Markovsky, D. Aurbach, Y. Carmeli, H. Yamin, and S. Luski, *Electrochim. Acta*, **39**, 2559 (1994).
13. D. Aurbach, Y. Ein-Eli, O. Chusid, Y. Carmeli, M. Babai, and H. Yamin, *J. Electrochem. Soc.*, **141**, 603 (1994).
14. T. Osaka, T. Momma, T. Tajima, and Y. Matsumoto, *J. Electrochem. Soc.*, **142**, 1057 (1995).
15. D. Aurbach and Y. S. Cohen, *J. Electrochem. Soc.*, **144**, 3355 (1997).
16. B. Strehle, S. Solchenbach, M. Metzger, K. U. Schwenke, and H. A. Gasteiger, *J. Electrochem. Soc.*, **164**, A2513 (2017).
17. K. U. Schwenke, S. Solchenbach, J. Demeaux, B. L. Lucht, and H. A. Gasteiger, Manuscript in preparation.
18. L. J. Krause, V. L. Chevrier, L. D. Jensen, and T. Brandt, *J. Electrochem. Soc.*, **164**, A2527 (2017).
19. H. Nakai, T. Kubota, A. Kita, and A. Kawashima, *J. Electrochem. Soc.*, **158**, A798 (2011).
20. V. Etacheri, O. Haik, Y. Goffer, G. A. Roberts, I. C. Stefan, R. Fasching, and D. Aurbach, *Langmuir*, **28**, 965 (2012).
21. E. Markevich, K. Fridman, R. Sharabi, R. Elazari, G. Salitra, H. E. Gottlieb, G. Gershinsky, A. Garsuch, G. Semrau, M. A. Schmidt et al., *J. Electrochem. Soc.*, **160**, A1824 (2013).
22. R. Jung, M. Metzger, D. Haering, S. Solchenbach, C. Marino, N. Tsiouvaras, C. Stinner, and H. A. Gasteiger, *J. Electrochem. Soc.*, **163**, A1705 (2016).
23. E. Markevich, G. Salitra, and D. Aurbach, *ACS Energy Lett.*, **2**, 1337 (2017).
24. R. Petibon, V. Chevrier, C. P. Aiken, D. S. Hall, S. Hyatt, R. Shunmugasundaram, and J. R. Dahn, *J. Electrochem. Soc.*, **163**, 1146 (2016).
25. M. Wetjen, D. Pritzl, R. Jung, S. Solchenbach, R. Ghadimi, and H. A. Gasteiger, *J. Electrochem. Soc.*, **164**, A2840 (2017).
26. T. M. Bond, J. C. Burns, D. A. Stevens, H. M. Dahn, and J. R. Dahn, *J. Electrochem. Soc.*, **160**, A521 (2013).
27. N. Tsiouvaras, S. Meini, I. Buchberger, and H. A. Gasteiger, *J. Electrochem. Soc.*, **160**, A471 (2013).
28. M. Metzger, B. Strehle, S. Solchenbach, and H. A. Gasteiger, *J. Electrochem. Soc.*, **163**, A798 (2016).
29. S. Meini, N. Tsiouvaras, K. U. Schwenke, M. Piana, H. Beyer, L. Lange, and H. A. Gasteiger, *Phys. Chem. Chem. Phys.*, **15**, 11478 (2013).
30. S. Meini, S. Solchenbach, M. Piana, and H. A. Gasteiger, *J. Electrochem. Soc.*, **161**, A1306 (2014).
31. R. Jung, M. Metzger, F. Maglia, C. Stinner, and H. A. Gasteiger, *J. Phys. Chem. Lett.*, **8**, 4820 (2017).
32. A. A. Isse, A. Gennaro, and F. Maran, *Acta Chem. Scand.*, **53**, 1013 (1999).
33. B. Li, L. Xing, M. Xu, H. Lin, and W. Li, *Electrochem. commun.*, **34**, 48 (2013).
34. L. Hu, K. Amine, and Z. Zhang, *Electrochem. commun.*, **44**, 34 (2014).
35. B. Michalak, B. B. Berkes, H. Sommer, T. Brezesinski, and J. Janek, *J. Phys. Chem. C*, **121**, 211 (2017).
36. B. Michalak, B. B. Berkes, H. Sommer, T. Bergfeldt, T. Brezesinski, and J. Janek, *Anal. Chem.*, **88**, 2877 (2016).
37. D. Pritzl, S. Solchenbach, M. Wetjen, and H. A. Gasteiger, *J. Electrochem. Soc.*, **164**, A2625 (2017).
38. Y. Dong, J. Demeaux, and B. L. Lucht, *J. Electrochem. Soc.*, **163**, 2413 (2016).
39. Y. Zhang, L. Wang, H. Feng, A. Zhang, C. Zhang, and P. Zhang, *Ionics (Kiel).*, **17**, 677 (2011).
40. D. J. Xiong, L. D. Ellis, R. Petibon, T. Hynes, Q. Liu, and J. R. Dahn, *J. Electrochem. Soc.*, **164**, 340 (2017).
41. S. E. Sloop, J. B. Kerr, and K. Kinoshita, *J. Power Sources*, **119–121**, 330 (2003).
42. A. J. Smith, J. C. Burns, D. Xiong, and J. R. Dahn, *J. Electrochem. Soc.*, **158**, A1136 (2011).
43. D. J. Xiong, R. Petibon, M. Nie, L. Ma, J. Xia, and J. R. Dahn, *J. Electrochem. Soc.*, **163**, 546 (2016).
44. K. Fridman, R. Sharabi, R. Elazari, G. Gershinsky, E. Markevich, G. Salitra, D. Aurbach, A. Garsuch, and J. K. Lampert, *Electrochem. commun.*, **33**, 31 (2013).
45. A. Yamada, H. Koizumi, S.-I. Nishimura, N. Sonoyama, R. Kanno, M. Yonemura, T. Nakamura, and Y. Kobayashi, *Nat. Mater.*, **5**, 357 (2006).
46. M. E. Spahr, T. Palladino, H. Wilhelm, A. Würsig, D. Goers, H. Buqa, M. Holzapfel, and P. Novák, *J. Electrochem. Soc.*, **151**, A1383 (2004).
47. L. V Haynes and D. T. Sawyer, *Anal. Chem.*, **39**, 332 (1958).

48. D. Aurbach and O. Chusid, *Electrochem. Soc. Lett.*, **140**, L155 (1993).
49. A. Gennaro, A. A. Isse, M.-G. Severin, E. Vianello, I. Bhugunb, and J.-M. Saveant, *J. Chem. Soc. Faraday Trans.*, **92**, 3963 (1996).
50. U. Kaiser and E. Heitz, *Berichte der Bunsen-Gesellschaft*, **77**, 818 (1973).
51. C. Amatore and J.-M. Saveant, *J. Am. Chem. Soc.*, **103**, 5021 (1981).
52. R. Jung, M. Metzger, F. Maglia, C. Stinner, and H. A. Gasteiger, *J. Electrochem. Soc.*, **164**, A1361 (2017).
53. R. L. Moss, E. Tzimas, P. Willis, J. Arendorf, L. Tercero Espinoza, F. Marscheider-Weidemann, M. Soulier, A. Lüllmann, C. Sartorius, and K. Ostertag, *JRC Sci. Tech. Reports* (2013).
54. P. A. Nelson, K. G. Gallagher, I. Bloom, and D. W. Dees, *Argonne National Laboratory Report ANL-11/32* (2011).
55. E. J. Berg, C. Villevieille, D. Streich, S. Trabesinger, and P. Novák, *J. Electrochem. Soc.*, **162**, A2468 (2015).
56. S. Solchenbach, D. Pritzl, E. J. Y. Kong, J. Landesfeind, and H. A. Gasteiger, *J. Electrochem. Soc.*, **163**, 2265 (2016).
57. F. T. Wagner, B. Lakshmanan, and M. F. Mathias, *J. Phys. Chem. Lett.*, **1**, 2204 (2010).
58. J. Xia, R. Petibon, A. Xiao, W. M. Lamanna, and J. R. Dahn, *J. Electrochem. Soc.*, **163**, A1637 (2016).

3.3.3 DiFEC as Electrolyte Additive for Silicon Electrodes

This section presents the article "Evaluating EC, FEC, and DiFEC as Electrolyte Constituents for Silicon-Graphite Electrodes: Reduction Mechanism and Consumption".[236] At the time of the submission of this PhD thesis, the article has not yet been submitted for publication. This study was presented on international conferences, for example at the 231st Meeting of The Electrochemical Society in New Orleans, Louisiana (May 28 – Jun 1, 2017), Abstr. #213.

This article deals with the evaluation of a fluorinated EC-derivate as electrolyte additive for the stabilization of the silicon/electrolyte interface. The SEI on silicon faces several challenges that exceed the requirements of conventional graphite electrodes. Besides (i) a high electrical resistivity to avoid further reduction of electrolyte compounds and (ii) a selective permeability for lithium ions to allow fast (de-)lithiation kinetics,[6,44] the SEI on silicon also needs to be able (iii) to sustain the large mechanical stresses arising from the continuous volumetric changes during (de-)lithiation.[208] If the latter condition is not given, side reactions at the silicon/electrolyte interface result in an ongoing electrolyte decomposition and a gradual loss of cyclable lithium from the positive electrode.[237] As a result, silicon-based electrodes typically reveal a lower coulombic efficiency and a notably reduced cycle life in lithium-ion full-cells compared to graphite.[112,173] While the reduction of ethylene carbonate (EC) was shown to yield a stable SEI on graphite, allowing a high coulombic efficiency above 99.9%,[238] a poor cycling performance has been reported for silicon-based electrodes with EC.[239] In contrast, fluoroethylene carbonate (FEC) has been demonstrated to substantially improve the coulombic efficiency and capacity retention of silicon electrodes.[240–242] The origin of this beneficial effect has been related to the different reduction mechanism of the FEC molecule which yields in the formation of a more flexible and kinetically stable SEI.[103,243]

In this article, we evaluated di-fluoroethylene carbonate (DiFEC) as an alternative electrolyte additive for silicon-based electrodes. Considering the beneficial effect of FEC on the cycling performance of silicon electrodes, we aimed to enhance the properties of the electrolyte additive and reduce the electrolyte consumption rate by addition of a second fluorine atom. First, we investigated the reductive decomposition of the differently fluorinated EC-derivatives by differential capacity analysis of reductive scans in half-cells and the concomitant gas evolution by on-line electrochemical mass spectrometry (OEMS). Further, we evaluated the cycling performance and polarization of the SiG anodes against capacitively oversized $LiFePO_4$ positive electrodes and quantified the consumption of the different additives upon cycling by *post mortem* ^{19}F-NMR analysis.[102,103]

This study generated three important insights about the use of di-fluoroethylene carbonate (DiFEC) as electrolyte additive for SiG anodes: (i) DiFEC has a very similar reductive behavior on SiG anodes like the widely used fluoroethylene carbonate (FEC), which involves a more positive reduction potential than ethylene carbonate (EC), the release of CO_2, and the consumption of a total of four electrons per (Di)FEC molecule. (ii) SiG anodes cycled in the presence of DiFEC and an excess of cyclable lithium showed a 7%-points higher capacity retention after 100 charge/discharge cycles compared to FEC. However, an in-depth analysis revealed that the total charge+discharge capacity exchanged by silicon per consumed mole of (Di)FEC is the same. As a corollary, the higher reversible capacity was obtained at the expense of a higher irreversible capacity, which suggests that DiFEC does not offer an advantage in terms of the SEI stability in silicon-based lithium-ion batteries. Nonetheless, (iii) SiG anodes cycled in the presence of DiFEC indicated a reduced loss of interparticle contact pressure within the first 60 cycles when compared to FEC. Although this phenomenon is still subject to further investigations, it indicates that there is room to further improve the mechanical properties of the SEI on silicon active materials.

Author contributions

M.W. and G.H. prepared the SiG electrodes, performed the electrochemical testing and did the ^{19}F-NMR analysis. M.W. and D.P. conducted the impedance measurements. G.H. and S.S. performed the OEMS gas analysis and did the data treatment. M.W. analyzed the data. M.W. wrote the manuscript. All authors discussed the results and commented on the manuscript.

Evaluating EC, FEC, and DiFEC as Electrolyte Constituents for Silicon-Graphite Electrodes: Reduction Mechanism and Consumption

Morten Wetjen,[#,*] Gloria Hong,[*] Sophie Solchenbach,[*] Daniel Pritzl,[*]
and Hubert A. Gasteiger [**]

Chair of Technical Electrochemistry, Department of Chemistry and Catalysis Research
Center, Technische Universität München, D-85748 Garching, Germany

---

[*] Electrochemical Society Student Member

[**] Electrochemical Society Member

[#] E-mail: morten.wetjen@tum.de

Abstract

In silicon-based lithium-ion batteries, electrolyte additives play a crucial role in the kinetic stabilization of the silicon/electrolyte interface. In the present study, we investigate di-fluoroethylene carbonate (DiFEC) as an alternative additive to the widely used fluoroethylene carbonate (FEC). Using 1 M $LiPF_6$ in EC:EMC (30:70 wt%) as base electrolyte, we add either 5 wt% FEC or DiFEC to evaluate their effect on the electrochemistry of silicon-graphite (SiG) electrodes with 35 wt% silicon nanoparticles. First, we investigate the reductive behavior of the fluorinated EC-derivates at the silicon/electrolyte interface by means of differential capacity analysis and electrochemical impedance spectroscopy. Using on-line electrochemical mass spectrometry (OEMS), we then examine the gas evolution during repeated (de-)lithiation of the SiG electrodes and derive the reduction mechanisms for EC, FEC, and DiFEC. Further, we evaluate the impact of the fluorinated EC-derivatives on the cycling stability and the polarization of the SiG electrodes by means of galvanostatic cycling in pseudo full-cells with capacitively oversized $LiFePO_4$ cathodes. Using post-mortem ^{19}F-NMR spectroscopy, we finally quantify the consumption of FEC and DiFEC upon cycling and compare their efficacy with respect to commercial lithium-ion batteries.

Keywords: Silicon-graphite electrode, electrolyte additive, DiFEC, FEC, EC

Introduction

Silicon-based lithium-ion batteries offer the potential of high cell-level energy densities above 300 Wh kg^{-1}.[1,2] However, the realization of these theoretical values continues to pose a significant challenge. The repeated alloying/dealloying of ~3.75 Li atoms per Si atom causes large volumetric changes by up to +280%, leading to mechanical degradation of the solid-electrolyte-interphase (SEI) as well as to severe morphological changes of the silicon particles.[3,4] As a result, the SEI on silicon faces several challenges that exceed the requirements of state-of-the-art graphite-based electrodes. Besides (i) a low electrical conductivity to avoid further reduction of electrolyte constituents and (ii) a sufficiently high but selective permeability for Li ions to allow fast (de-)lithiation kinetics,[5,6] the SEI on silicon additionally needs to be able (iii) to sustain the large mechanical stress arising from the repeated volume changes during (de-)lithiation.[7] If the latter condition is not given, side reactions at the silicon/electrolyte interface result in an ongoing consumption of active lithium[8,9] and decomposition of electrolyte constituents.[10–12] Therefore, silicon electrodes typically reveal a lower coulombic efficiency and a notably reduced cycle life in lithium-ion full-cells when compared to graphite.[13]

The electrolyte plays a crucial role in the formation of the SEI at the negative electrode.[14] While the reduction of ethylene carbonate (EC) was shown to form a stable SEI on graphite electrodes allowing high coulombic efficiency above 99.9%,[15] a poor passivation has been reported for silicon electrodes due to an insufficient mechanical stability.[16] In contrast, fluoroethylene carbonate (FEC) has been demonstrated to substantially improve the coulombic efficiency and capacity retention of silicon electrodes.[17–19] The origin of this beneficial effect has been related to the different reduction mechanism of the FEC molecule yielding in the formation of a more flexible and kinetically stable SEI. As reported by Shkrob et al.,[20] the reduction of EC follows a ring-opening and subsequent formation of a radical anion, whereas the FEC reduction causes the cleavage of two C-O bonds leading to a concerted defluorination and decarboxylation which results in a highly cross-linked network with elastomeric properties. In addition, several groups demonstrated by XPS analysis an increased LiF and Li_2O content as well as a fluoride modification of the silicon oxide layer at the silicon surface, which is believed to further improve the kinetic stability of the SEI.[21–23]

Recently, Jung et al.[10] and Petibon et al.[24] showed independently by post-mortem ^{19}F-NMR analysis and gas chromatography, respectively, that the partial replacement of organic carbonates by FEC suppresses the reduction of EC and thus improves the cycling stability of silicon electrodes. However, once the molar quantity of FEC was depleted from the electrolyte, the cells suffered a strong polarization and rapid capacity decay. Thus, the lifetime of silicon-based lithium-ion batteries is directly related to the FEC consumption rate at the silicon surface as well as the molar quantity of FEC in the electrolyte.[12] Since the electrolyte volume in commercial lithium-ion batteries is very low (~5 µL cm^{-2}), the main lever to improve the cycle life of silicon electrodes is therefore to decrease the FEC consumption rate, i.e., by mitigating the side reactions at the silicon/electrolyte interface.

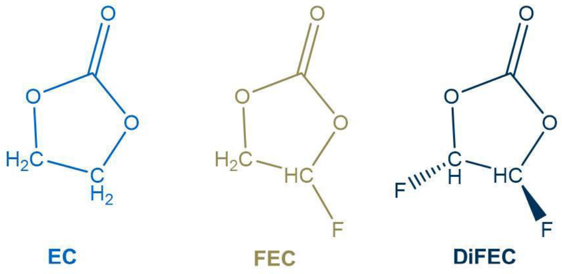

Scheme 1. Chemical structures of the electrolyte constituents that were investigated in this study: Ethylene carbonate (EC) fluoroethylene carbonate (FEC), and di-fluoroethylene carbonate (DiFEC).

In the present study, we evaluate di-fluoroethylene carbonate (DiFEC) as an electrolyte additive for silicon electrodes. Considering the beneficial effect of FEC on the cycling stability, we seek to enhance the additive's properties and reduce its consumption rate by introduction of a second fluorine atom (see **Scheme 1**). In 2013, Markevich et al.[21] investigated silicon thin-film electrodes in mixtures of FEC or DiFEC with DMC, demonstrating a superior cycling stability compared to EC or PC-based electrolytes. Later, Yariv et al.[25] evaluated the effect of the temperature and the electrolyte constituents, including DiFEC, on carbon negative electrodes. More recently, several groups analyzed DiFEC with respect to its oxidative decomposition in graphite//NMC cells.[26–28] In contrast, here we focus on the reduction mechanism and the consumption of fluorinated EC-derivates on silicon-graphite (SiG) electrodes with 35 wt% silicon nanoparticles and a delithiation capacity of 1.7-1.8 mAh cm^{-2}. Hence, we prepared three electrolytes, consisting of (i) 1 M $LiPF_6$ in EC:EMC (30:70 wt%) – also referred to as LP57;

(ii) 5 wt% FEC in LP57, and (iii) 5 wt% DiFEC in LP57. First, we investigate the reductive decomposition of the fluorinated EC-derivatives using differential capacity analysis of Li//SiG half-cells, and the concomitant gas evolution by means of on-line electrochemical mass spectrometry (OEMS). Based on these results, we summarize the reduction mechanisms of EC, FEC, and DiFEC to discuss the role of the fluorine substituents. Next, we investigate the cycling stability and polarization of SiG electrodes in pseudo full-cells featuring a capacitively oversized $LiFePO_4$ cathode.[12] Finally, we evaluate the consumption of FEC and DiFEC using post-mortem ^{19}F-NMR spectroscopy[10] and derive implications for their efficacy in commercial lithium-ion batteries.

Experimental

Silicon-graphite (SiG) electrode preparation.— SiG electrodes, consisting of 35 wt% silicon nanoparticles (~200 nm dimensions, Wacker Chemie AG, Germany), 45 wt% graphite (~20 µm, T311, SGL Carbon, Germany), 10 wt% vapor grown carbon fibers (VGCF-H, Showa Denko, Japan), and 10 wt% lithium poly(acrylate) binder (LiPAA) were prepared through an aqueous ink procedure.[12] The LiPAA was prepared by diluting a 35 wt% poly(acrylic acid) solution (PAA, MW = 250,000 g mol^{-1}, Sigma-Aldrich, Germany) with deionized water and neutralizing it with lithium hydroxide (Sigma-Aldrich, Germany) to a pH-value of ~8.[13] All electrodes were dried for 12 h at 120 °C under vacuum in a glass oven (Büchi, Switzerland) before being transferred into an Ar atmosphere glovebox (H_2O and O_2 concentration <0.1 ppm, MBraun, Germany). The electrode mass loading was adjusted to ~1.4 $mg_{electrode}$ cm^{-2}, which corresponds to a theoretical capacity of 1.9-2.0 mAh cm^{-2}. This value was also used to define the C-rate, i.e., 1 h^{-1} equals ~2 mA cm^{-2}. Practically, first cycle delithation capacities of 1.7-1.8 mAh cm^{-2} (~1280 mAh g^{-1}_{el}) were obtained at 0.1 h^{-1}.[3]

Electrolytes.— Three different electrolytes were prepared: (i) 1 M $LiPF_6$ in ethylene carbonate: ethyl methyl carbonate (EC:EMC, 30:70 wt%) (BASF, Germany) – also referred to as LP57; (ii) 5 wt% FEC (BASF, Germany) in LP57; and (iii) 5 wt% DiFEC (HSC Corporation, China) in LP57. The water content of these electrolytes was determined by Karl-Fischer titration, revealing sufficiently low values of < 5 ppm for LP57 and 5 wt% FEC in LP57, as well as < 20 ppm for 5 wt% DiFEC in LP57.

Test cell assembly.— Electrochemical characterization was performed in coin-cells (CR2032, Hohsen, Japan) and Swagelok®-type T-cells (Swagelok, Germany). The cells were assembled by sandwiching two electrolyte-soaked glass fiber separators (thickness 250 µm, VWR, USA) between a SiG anode and a capacitively oversized $LiFePO_4$ (LFP) cathode (3.5 mAh cm^{-2}, Custom cells, Germany).[12] For the investigation of the electrolyte decomposition, the LFP was exchanged by a lithium metal electrode (~450 µm thickness, Rockwood Lithium, USA) to reliably determine the SiG electrode potential during the entire first reductive scan. Because of the different electrode areas in coin-cells (1.54 cm^2) and T-cells (0.94 cm^2), the electrolyte amounts differed slightly between ~84 µL cm^{-2} and ~64 µL cm^{-2}, respectively, but always largely exceeded commercial cells (~5 µL cm^{-2}).

Reductive decomposition of electrolyte constituents.— The reductive decomposition and SEI formation behavior of the different electrolytes was investigated by galvanostatic polarization of Li//SiG coin-cells between the open-circuit potential (~2.6 V vs. Li^+/Li) and a lithiation cutoff potential of 0.01 V vs. Li^+/Li, using a C-rate of 0.02 h^{-1}. All measurements were performed in a climate chamber (Binder, Germany) at 25 °C using a battery cycler (Series 4000, Maccor, USA).

Electrochemical impedance spectroscopy.— The impedance of SiG electrodes in the different electrolytes was investigated using a lithiated gold-wire micro-reference electrode in a T-cell.[29] First, a galvanostatic reductive scan was performed at 0.1 h^{-1} from open-circuit potential to 0.01 V vs. Li^+/Li, which was followed by a 5 h rest period at close to ~100% state-of-charge (SOC). At the end of the rest period, impedance spectroscopy was conducted using a frequency range of 100 kHz – 100 mHz and a current perturbation of 0.8 mA. All measurements were performed in a climate chamber (Binder, Germany) at 25 °C using a multi-channel potentiostat VMP3 (BioLogic, France).

On-line electrochemical mass spectrometry (OEMS).— In order to quantify the gases that are evolved during the (de-)lithiation of SiG electrodes in the different electrolytes, a gas evolution analysis was performed by means of on-line electrochemical mass spectrometry (OEMS). The measurements were conducted in a custom cell hardware (~9.5 ml head space volume), using two Celgard separators (Ø 26 mm, Celgard® 2325, Celgard, USA) and 130 µL of the above described electrolytes.[30] SiG electrodes were prepared by coating the above described ink onto porous woven wire mesh (#500

Mesh SS316 Grade, The Mesh Company, UK). A standard graphite electrode with 95 wt% graphite (T311, SGL Carbon GmbH, Germany) and 5 wt% PVdF (Kynar, Arkema, France) was prepared analogously as a reference. The capacity of the resulting electrodes with a diameter of 14 mm amounted to ~2.45 mAh cm^{-2}. Partially delithiated $Li_{0.9}FePO_4$ (Custom Cells, Germany) was used as counter electrode (Ø 15 mm, ~3.2 mAh cm^{-2}). All electrodes were dried for 3 days at 120 °C under vacuum in a glass oven (Büchi, Switzerland).

The OEMS measurements were carried out at 25 °C in a climate chamber (Binder, Germany). Following a 4 h OCV step for background stabilization to ensure decent baseline extrapolation, a galvanostatic formation procedure with a Series G300 potentiostat (Gamry, USA) between 0.01 and 1.25 V vs. Li^+/Li (3.44 – 2.2 V cell voltage) was conducted with a C-rate of 0.1 h^{-1} in the first lithiation, and 0.2 h^{-1} during the subsequent two charge/discharge cycles. A constant voltage step was entered at the end of each lithiation at 0.01 V vs. Li^+/Li with a time limit of 1 h. The mass signals were quantified using a calibration gas containing H_2, CO, O_2 and CO_2 (2000 ppm in Ar, Westfalen AG, Germany).

Battery cycling.— Cycling stability and polarization of SiG electrodes in the different electrolytes was investigated by galvanostatic cycling of SiG//LFP coin-cells. The SiG cutoff potentials of 0.01 V vs. Li^+/Li during lithiation and 1.25 V vs. Li^+/Li during delithiation were controlled by the cell voltage (3.44-2.2 V), using the stable potential of the oversized LFP cathode (~3.45 V vs. Li^+/Li) as a reference.[12] In addition, 10 min rest periods were entered at the end of each lithiation and delithiation. Initially, two formation cycles were performed at 0.1 h^{-1}, while in consecutive cycles the C-rate was increased to 0.33 h^{-1}. All measurements were performed in a climate chamber (Binder, Germany) at 25 °C using a battery cycler (Series 4000, Maccor, USA).

Electrolyte consumption.— Consumption of FEC and DiFEC during galvanostatic cycling was investigated by post-mortem ^{19}F-NMR spectroscopy of fresh and cycled electrolytes. Hence, SiG//LFP coin-cells were disassembled after 100 cycles and the electrolyte-soaked glass fiber separators were dipped into deuterated dimethyl sulfoxide (DMSO-d6 *anhydrous*, Sigma-Aldrich, USA). The solutions were then filled into air-tight NMR tubes and ^{19}F-NMR spectroscopy was measured at room temperature using a Bruker Ascend 400. The resulting ^{19}F-NMR spectra show only peaks that can either be ascribed to PF_6^- or (Di)FEC.[10] Considering that the large concentration of PF_6^- in the electrolyte remains fairly constant at the given conditions, changes in the ratio of the PF_6^- and (Di)FEC peak integrals can be used to monitor the consumption of (Di)FEC after 100 cycles.

Results and Discussion

***Reductive decomposition and initial SEI formation of EC, FEC, and DiFEC.*— Figure 1a** shows the differential capacity curves of the first reductive scan in Li//SiG coin-cells with different electrolytes: LP57 (blue), 5 wt% FEC in LP57 (brown), and 5 wt% DiFEC in LP57 (marine). The onset for the DiFEC reduction occurs at more positive potentials (~1.7 V vs. Li^+/Li) compared to FEC (~1.3 V vs. Li^+/Li). In addition, the capacity resulting from the reduction of DiFEC (~2.15 μAh), which is represented by the peak area, is ~2.3 times larger compared to FEC (~0.93 μAh). This indicates a higher consumption of lithium and likely also DiFEC molecules during the initial SEI formation. As expected, no EC reduction (~0.8 V vs. Li^+/Li) can be observed for the FEC- and DiFEC-containing electrolytes.[10,31]

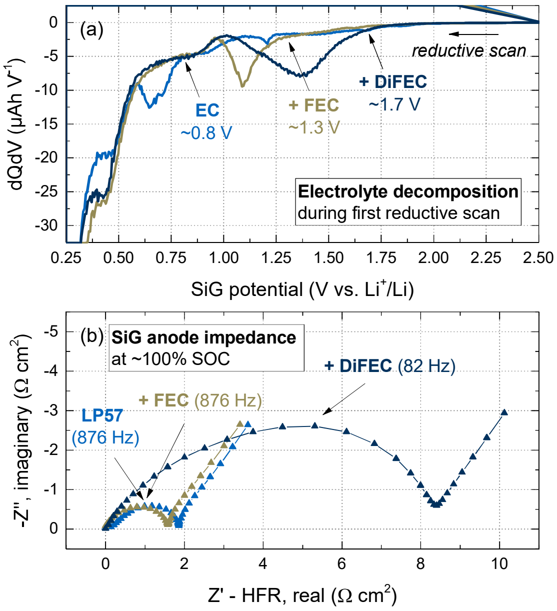

Figure 1. (a) Differential capacity curves of the first galvanostatic reductive scan at 0.02 h^{-1} (lithiation of silicon and graphite) in Li//SiG coin-cells with different electrolytes: LP57 (blue), 5 wt% FEC in LP57 (brown), and 5 wt% DiFEC in LP57 (marine). (b) Impedance response of SiG electrodes at close to 100% SOC after the first galvanostatic lithiation to 0.01 V vs. Li^+/Li and a 5 h rest period, obtained by a lithiated gold-wire micro-reference electrode in a SiG//LFP T-cell. The high-frequency resistance (HFR) was subtracted from Z'; perturbation: 0.8 mA; frequency range: 100 kHz – 100 mHz.

To characterize the initial SEI layer of the different electrolytes on the SiG electrode, impedance spectroscopy was performed at the end of the first lithiation at close to 100% SOC. The gold-wire micro-reference electrode setup allows to separate the impedance contributions of anode and cathode, whereby **Figure 1b** only depicts the impedance responses of the SiG electrodes.[29] The high-frequency resistance was subtracted because it remains very similar across the measurements (~4 Ω cm^2) and small differences mainly result from the cell setup. For all investigated electrolytes, the SiG electrodes show a distorted semi-circle with a maximum frequency between 82 and 876 Hz, followed by a linear Warburg diffusion slope in the low frequency region. The semi-circle mainly represents the interfacial resistance at the electrode/electrolyte interface, comprising both the surface film (SEI) resistance and the charge-transfer resistance. Although it is not possible to separate the individual contributions at this SOC, all electrolytes show a reasonable interfacial resistance of less than 10 Ω cm^2, which is similar to graphite electrodes after one formation cycle with vinylene carbonate.[32] Yet, a direct comparison of the here investigated electrolytes reveals that the interfacial resistance of 5 wt% DiFEC in LP57 (~8 Ω cm^2) is notably larger compared to LP57 or 5 wt% FEC in LP57 (~2 Ω cm^2 each). This agrees well with the ~2.3 times larger capacity resulting from the reductive decomposition of DiFEC. As a result, more DiFEC is required to obtain a similar initial passivation of the active materials as with EC or FEC.

Gas evolution of EC, FEC, and DiFEC on SiG electrodes.— The gas evolution of the different electrolytes on SiG electrodes during galvanostatic (de-)lithiation was investigated by on-line electrochemical mass spectrometry (OEMS). **Figure 2a** shows the SiG electrode potential, while (b) and (c) depict the BET surface area-normalized integral gas evolution of CO_2 (m/z = 44) and C_2H_4 (m/z = 25) for all investigated electrolytes, including LP57 (blue), 5 wt% FEC in LP57 (brown), and 5 wt% DiFEC in LP57 (marine). In addition, a reference measurement with a graphite electrode was conducted in LP57 (grey dotted line). For all measurements, the integral gas evolution was calculated by considering the molar gas volume of 24.5 L mol^{-1} at 25 °C/1 bar, the head space volume of 9.5 mL of the OEMS cell as well as the proportional BET surface area of all electronically conducting electrode constituents (silicon 40 m$^2_{BET}$ g^{-1}, graphite 5 m$^2_{BET}$ g^{-1}, VGCF-H 13 m$^2_{BET}$ g^{-1}). During the first lithiation of the SiG electrodes, both the FEC- and DiFEC-containing electrolyte evolve large quantities of CO_2 (see **Figure 2b**). In contrast, the delithiation reveals only minor additional CO_2 evolution and the following re-lithiations even indicate a temporary decrease of the CO_2 concentration in the cell headspace. The latter likely originates from CO_2 reduction on freshly exposed silicon surface during particle expansion.[33,34] Consequently, the integral gas evolution of CO_2 is mainly determined by the first lithiation (see vertical dashed black line). As expected, the DiFEC-containing electrolyte generates more CO_2 (~34 $\mu mol_{CO2}\ m^{-2}{}_{BET}$) compared to FEC (~14 $\mu mol_{CO2}\ m^{-2}{}_{BET}$), indicating a ~2.4 times higher additive consumption which agrees well with the ~2.3 times higher reduction capacity calculated from **Figure 1a**. Without any additive, LP57 shows only a small temporary increase of the CO_2 mass trace (~1 $\mu mol_{CO2}\ m^{-2}{}_{BET}$) on the SiG electrode within the first two hours which rapidly decreases to zero thereafter. This phenomenon can be ascribed to the hydrolysis of EC which is catalyzed by OH^- traces originating from the reduction of trace water.[35] However, the small amount of CO_2 is consumed swiftly at the surface of the SiG electrode, once the potential decreases further. As expected, the reference measurement of the graphite electrode in LP57 also shows hardly any CO_2 evolution.[36,37]

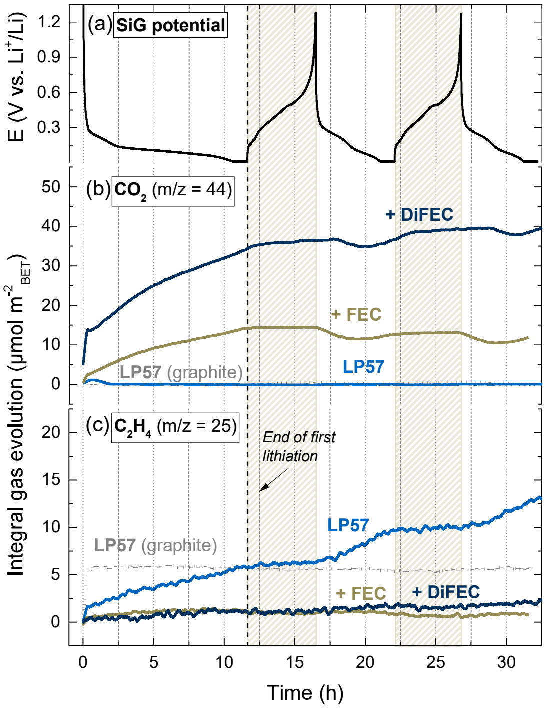

Figure 2. Gas evolution during 2.5 charge/discharge cycles at 0.1 h^{-1} and 0.2 h^{1}, respectively, of SiG electrodes and a graphite electrode in different electrolytes: (a) SiG electrode potential (black line). (b, c) Integral gas evolution of carbon dioxide (CO_2, m/z = 44) and ethylene (C_2H_4, m/z = 25) as a function of time, obtained from SiG electrodes in LP57 (blue), 5 wt% FEC in LP57 (brown) or 5 wt% DiFEC in LP57 (marine), and from a graphite electrode in LP57 (grey dotted line). The OEMS data are smoothed, baseline corrected and converted into units of ppm.

Figure 2c shows the integral gas evolution of C_2H_4. Interestingly, it exhibits an almost inverse behavior compared to the CO_2 mass trace. While the FEC- and DiFEC-containing electrolyte reveal no C_2H_4 evolution, LP57 shows a distinct increase both for the graphite and the SiG electrode. The C_2H_4 evolution profile, however, differs considerably for the active materials. The graphite electrode shows a discrete increase of the C_2H_4 signal up to 5.8 $\mu mol_{C2H4}\ m^{-2}{}_{BET}$ within the first minutes of lithiation followed by a fairly stable concentration during subsequent cycles.[36,38] In contrast, the SiG electrode shows an ongoing C_2H_4 evolution up to 5.8 $\mu mol_{C2H4}\ m^{-2}{}_{BET}$ during the first lithiation, which continues throughout the following reductive half-cycles. We summarize the characteristics for the two types of active materials as follows: (i) A similar quantity of C_2H_4 per BET surface area is evolved during the first lithiation.[12] (ii) The gas evolution at silicon and graphite occurs at a considerably different rate, whereby the disparity of the different gas evolution rates over time can be ascribed to the different volume changes of silicon and graphite active materials during (de-)lithiation. While the Li_xSi alloy expands by up to +280% during lithiation, graphite experiences a comparatively small volume change of +10% during the intercalation of lithium.[4] As EC is known to insufficiently passivate silicon due to its poor stability toward the mechanical deformation upon cycling,[22] it is repeatedly decomposed on freshly exposed silicon surface, thus resulting in an ongoing evolution of C_2H_4 up to ~13 $\mu mol_{C2H4}\ m^{-2}{}_{BET}$ after the third lithiation.

Reduction mechanisms of fluorinated EC-derivatives on SiG electrodes.— **Scheme 2** summarizes our results from the gas analysis which extent previously reported reduction mechanisms of EC and FEC to SiG electrodes,[10,37] and additionally allow us to propose a mechanism for the reductive decomposition of DiFEC. Accordingly, the prevalent pathway for the reduction of EC is the ring-opening by fission of a single C-O bond, followed by the formation of the $^{\bullet}CH_2CH_2OCO_2Li$ radical.[20] Subsequent radical recombination leads to the formation of lithium ethylene dicarbonate (LEDC), which coincides with the elimination of C_2H_4.[37,39] In contrast, for the reduction of FEC on SiG electrodes the first electron transfer likely occurs at the carbonyl atom, thus leading to a ring-opening and formation of the $^{\bullet}CO_2CH_2CHFOLi$ radical.[10,24] Subsequent elimination of CO_2 and LiF results in the formation of the mesomeric-stabilized vinoxyl radical ($^{\bullet}CH_2CHO$), which was first predicted by Balbuena and co-workers[39,40] through ab-initio modelling. Later, Shkrob et al.[20] experimentally confirmed the presence of the vinoxyl radical by in-situ EPR spectroscopy. In the same study, it was also shown that the vinoxyl radical can initiate a chain reaction that causes further FEC decomposition and radical polymerization by abstracting another hydrogen atom from FEC. Further defluorination within the resulting polymer leads to additional radicals that migrate and recombine to produce a highly cross-linked network with elastomeric properties. Therefore, we can conclude that despite the structural similarity of EC and FEC, the possibility to eliminate fluoride and to subsequently form the vinoxyl radical leads to a considerably different reduction mechanism for FEC that evolves CO_2 instead of C_2H_4. In addition, the cross-linked polymer network with elastomeric properties whose formation is facilitated by the defluorination likely results in the superior mechanical stability of the SEI layer toward repeated volume changes during cycling of the SiG electrodes. In agreement with the former work by Jung et al.[10] and Martinez et al.,[41] our results from ^{19}F-NMR analysis – which will be discussed in detail later – further indicate that in total four electrons are consumed per reduced FEC molecule. Therefore, further reduction of the vinoxyl radical described in **Scheme 2** and formation of the final reduction products requires a sequential transfer of three more electrons. Although the identification of the resulting SEI compounds exceeds the methods deployed in the present work, it is known from other studies based on XPS and TOF-SIMS analysis, that the reduction of FEC on Li_xSi results not only in the formation of a polymeric network,[20] but also in a fluoride modification of the silicon oxide overlayer covering the silicon particles[23] as well as the deposition of inorganic lithium species, including LiF, Li_2CO_3, and Li_2O.[22,31]

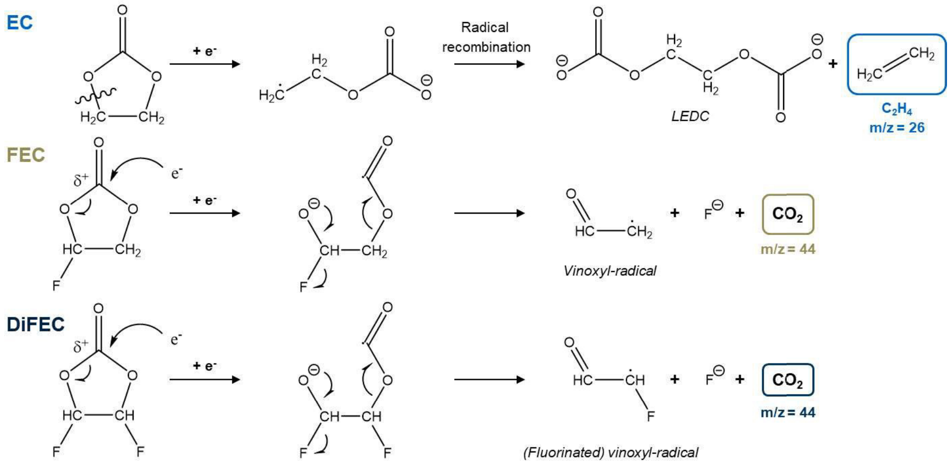

Scheme 2. Mechanisms of the first electron transfer for the reductive decomposition of EC, FEC, and DiFEC on SiG electrodes in agreement with the literature (EC[37] and FEC[10]) and proposed for DiFEC based on the present work.

Transferring this knowledge to DiFEC and complementing it with our results from the gas evolution and ^{19}F-NMR analysis indicates that the reduction of DiFEC on SiG electrodes is similar to that of FEC, thus differing considerably from EC. Accordingly, the reduction of DiFEC occurs at more positive potentials compared to EC and even FEC, which is most likely caused by the additional electronegative effect of the second fluorine substituent and the increased positive partial charge at the carbonyl atom. Purushotham et al.[42] calculated the frontier molecular orbital energies (in eV) for propylene carbonate (PC), FEC, and DiFEC. They reported notably lower-lying LUMOs for FEC (-0.641 eV) and DiFEC (-0.659 eV) compared to the non-fluorinated cyclic carbonate (here: PC, -0.599 eV), which supports the earlier reduction onset. As proposed in **Scheme 2**, we expect the first electron transfer to DiFEC to occur at the carbonyl atom, thus leading to the fission of two C-O bonds. Subsequently, this results in a defluorination (-LiF), the release of carbon dioxide (-CO_2), and the concomitant formation of a mesomeric-stabilized vinoxyl radical $^{\bullet}$(CFHCHO). In contrast to FEC, this radical is still fluorinated, which has two important implications for the resulting SEI: (i) As the cross-linking of the polymeric network was associated with the defluorination and subsequent recombination of radical species,[20] we expect the SEI originating from DiFEC to have a higher degree of cross-linking, and thus a higher mechanical stability. (ii) Although our ^{19}F-NMR analysis indicates that the reductive decomposition of DiFEC requires – similar to FEC – in total four electrons,[10] further defluorination of the vinoxyl radical results in an SEI with a higher relative LiF content compared to FEC,[33] thus altering the electrochemical properties of the SiG electrodes, as will be discussed in a later section.

Trans-esterification of asymmetric linear carbonates on SiG electrodes.— In addition to ongoing side reactions at the silicon/electrolyte interface, the insufficient passivation of the EC decomposition products on silicon likely also leads to changes in the LP57 bulk electrolyte. Strehle et al.[43] demonstrated for an LP57 electrolyte that during the reduction of EMC on SLP30 graphite electrodes, lithium alkoxide-type species (LiOR) are evolved which are accompanied by the release of carbon monoxide (CO). In accordance with the reaction mechanism shown in **Scheme 3**, these highly reactive LiOR species act as nucleophiles and attack the carbonyl atom of the linear carbonate (EMC), resulting in a conversion of the co-solvent into two symmetric linear carbonates, here dimethyl carbonate (DMC) and diethyl carbonate (DEC), in a stoichiometric 50:25:25 equilibrium.[43,44] This ester exchange reaction, also described as trans-esterification, leads to a decrease of the EMC-related mass traces (m/z = 29, 45, 59, and 77),[43] but at the same time an increase due to the formation of DMC and DEC, which can be monitored at the unique mass traces m/z = 62 (DMC) and m/z = 63 (DEC).

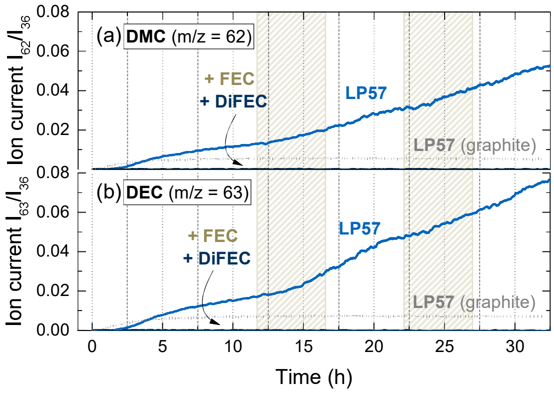

Figure 3. Development of the I_{36}-normalized mass traces of (a) DMC (m/z = 62), and (b) DEC (m/z = 63) during 2.5 charge/discharge cycles at 0.1 h^{-1} and 0.2 h^{1}, respectively, evaluated from the same OEMS measurement as shown in **Figure 2**, using a SiG electrode in LP57 (blue), 5 wt% FEC in LP57 (brown) or 5 wt% DiFEC in LP57 (marine), and a graphite electrode in LP57 (grey dotted line).

Figure 3 shows the Argon current (I_{36})-normalized mass traces of DMC and DEC, which allow to evaluate the extent of the trans-esterification during the 2.5 charge/discharge cycles from the same OEMS measurement depicted in **Figure 2**. As expected from the reaction shown in **Scheme 3**, the pure LP57 electrolyte reveals an initial increase of the mass traces m/z = 62 and m/z = 63 in a ratio of about 1:1.3 both at the SiG and the graphite electrode. The deviation from a perfect ratio of 1:1 mainly results from the intrinsic intensity of these two mass traces.[43] Analogously to the ethylene traces shown in **Figure 2c**, the graphite electrode shows a steep increase of m/z = 62 and 63 during the first two hours which is followed by a plateau. In contrast, the SiG electrode reveals a stepwise increase of the DMC and DEC mass traces during each lithiation, i.e., whenever new LiOR species are formed the rate of conversion accelerates. As a corollary, the extent of the trans-esterification in LP57 on graphite is limited by the passivation of the active material's surface resulting from EC reduction, whereas on silicon the insufficient passivation in LP57 leads to an ongoing release of highly reactive lithium alkoxide species (LiOR), and thus, an increasing extent of the trans-esterified products. Although this poses a serious issue concerning the properties of the optimized electrolyte composition,[45] **Figure 3** also indicates that for silicon this phenomenon is most likely less relevant during early stages of cycling. Accordingly, in presence of either FEC or DiFEC no mass traces of the symmetric carbonates (i.e., DMC, DEC) could be observed, which indicates that the trans-esterification is entirely suppressed. A similar phenomenon was also reported by Strehle et al.[43] who demonstrated that CO_2 acts as scavenger by reacting with the highly reactive alkoxide-species to form non-reactive $LiOCO_2R$. Since both FEC and DiFEC evolve large quantities of CO_2 during the first reductive scan on silicon, any LiOR species that may be released would be immediately deactivated. As a result, trans-esterification poses only a minor threat to asymmetric linear carbonate-containing electrolytes on silicon electrodes, at least as long as an SEI-forming and CO_2-evolving electrolyte additive is present.

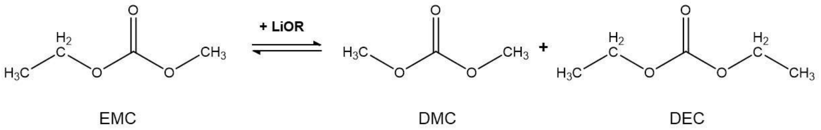

Scheme 3. Schematic reaction of the lithium alkoxide (LiOR)-initiated trans-esterification of ethyl methyl carbonate (EMC) to dimethyl carbonate (DMC) and diethyl carbonate (DEC) as reported by Strehle et al.[43]

Cycling stability of SiG electrodes in presence of EC, FEC, and DiFEC.— The cycling stability of SiG electrodes in presence of the fluorinated EC-derivatives was investigated by galvanostatic charge/discharge cycling of SiG//LFP coin-cells with a capacitively oversized LFP cathode. **Figure 4** shows (a) the coulombic efficiency and (b) the delithiation capacity for LP57 (blue), 5 wt% FEC in LP57 (brown), and 5 wt% DiFEC in LP57 (marine). **Table I** summarizes the 1st, 5th, and 100th cycle delithiation capacity, coulombic efficiency, and capacity retention. Accordingly, all SiG electrodes provide a similar first cycle delithiation capacity of 1.7-1.8 mAh cm^{-2} without notable differences between the individual electrolytes. In contrast, the first cycle coulombic efficiency clearly indicates a dependency on the type of additive, whereby the DiFEC-containing electrolyte shows a considerably lower value of 79.3 ± 0.2% compared to FEC (84.7 ± 0.3%) and LP57 (85.9 ± 0.1%). This observation agrees well with our gas evolution analysis, according to which more DiFEC is required to passivate the silicon/electrolyte interface. During the following cycles, the DiFEC-containing electrolyte continues to show a lower coulombic efficiency of ~97.7% compared to FEC (~98.2%), but increases steadily up to >99.2%. This trend is only interrupted by a small depression starting after ~40 cycles. In contrast, the coulombic efficiency of the FEC-containing electrolyte initially remains almost constant but starts to decrease after ~25 cycles to form a minimum. Remarkably, after 100 cycles both additives (viz., FEC and DiFEC) demonstrate the same coulombic efficiency of 99.2-99.3%. Based on a recent publication from our group,[3] the lower coulombic efficiency within the first 60 cycles can be ascribed to morphological changes of the silicon nanoparticles which are caused by dealloying reactions upon repeated (de-)lithiation. As these reactions approach a steady-state upon prolonged cycling, the coulombic efficiency also increases and any differences between FEC and DiFEC become very small.

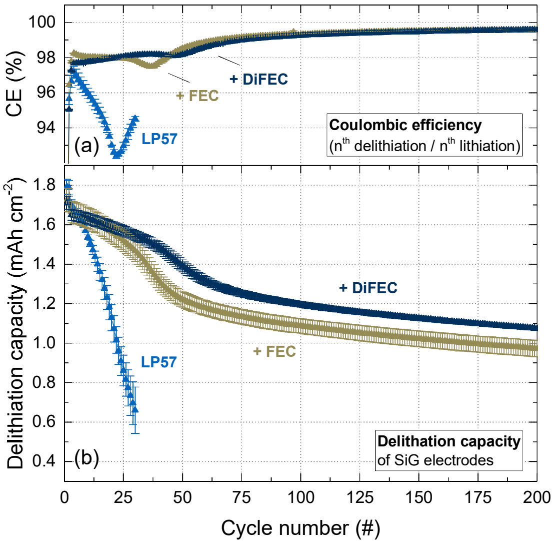

Figure 4. (a) Coulombic efficiency and (b) delithiation capacity obtained from galvanostatic cycling of SiG//LFP coin-cells with different electrolytes: LP57 (blue), 5 wt% FEC in LP57 (brown), and 5 wt% DiFEC in LP57 (marine). C-rate: 0.1 h^{-1} during two formation cycles and 0.33 h^{-1} during consecutive cycles; cut-off potentials: 0.01 and 1.25 V vs. Li^+/Li. The error bars represent the standard deviation of at least two independent repeat measurements.

The delithiation capacity shown in **Figure 4b** shows that both FEC and DiFEC significantly improve the cycling stability of the SiG electrodes compared to the LP57 base electrolyte. While the FEC- and DiFEC-containing electrolytes reveal reasonable capacity retentions of 63 ± 0.1% and 70 ± 0.5% after 100 cycles, SiG electrodes cycled in LP57 suffer a rapid capacity fade with less than 30% retention after 30 cycles. Interestingly, the cycling behavior of the FEC and DiFEC-containing electrolytes differs only in a very narrow range within the first 100 cycles. The delithiation capacity reveals two plateaus that are separated by a distinct decay starting after 25-40 cycles, which occurs 10-15 cycles earlier and to a slightly larger extent (~0.1 mAh cm^{-2}) in presence of FEC. Between the

100th and 200th cycle, however, both additives show again a very similar cycling behavior with only minor ongoing capacity fading of 0.11% per cycle. Therefore, DiFEC demonstrates an improved capacity retention of ~7%-points after 200 cycles, which mainly results from a reduced capacity decay within the first 100 cycles. It is to note that this difference is not related to a depletion of active lithium or electrolyte additive, because all cells were operated with a capacitively oversized LFP cathode and an excess of electrolyte. Instead, the capacity drop can be ascribed to a loss of interparticle contact pressure and subsequent electrical isolation of active material, leading to incomplete delithiation of the silicon nanoparticles.[12,46] Remarkably, the addition of DiFEC instead of FEC seems to reduce the extent of the particle isolation.

Table I. Delithiation capacity, coulombic efficiency and capacity retention for SiG//LFP cells with different electrolytes after selected cycles. The C-rate was 0.1 h^{-1} in the 1st cycle and 0.33 h^{-1} in the 5th and 100th cycles, respectively. The ± values represent the standard deviation of at least two independent repeat measurements.

	Delithiation capacity / mAh cm^{-2}			**Coulombic efficiency** / %			**Capacity retention** / %	
Electrolyte	1st	5th	100th	1st	5th	100th	5th-100th	5th-200th
LP57	1.79 ± 0.04	1.66 ± 0.02	-	85.9 ± 0.1	92.9 ± 0.1	-	-	-
+ 5 wt% FEC	1.72 ± 0.06	1.66 ± 0.05	1.09 ± 0.04	84.7 ± 0.3	98.2 ± 0.1	99.3 ± 0.1	63 ± 0.1	58 ± 0.5
+ 5 wt% DiFEC	1.71 ± 0.03	1.65 ± 0.03	1.20 ± 0.01	79.3 ± 0.2	97.7 ± 0.1	99.2 ± 0.1	70 ± 0.5	65 ± 0.3

To further evaluate this observation, **Figure 5** shows the potential (a) rise or (b) drop ΔV_{OCP} of the SiG electrodes during the 10 min rest period after reaching either the lithiation (0.01 V vs. Li^+/Li) or delithiation (1.25 V vs. Li^+/Li) cutoff potential. Switching from a constant current during (de-)lithiation to open-circuit conditions allows the concentration gradients in the electrode to relax, which results in a change of the electrode potential. The extent of the electrode's potential rise or drop during these rest periods can thus be used as a sensitive indicator for the resistance of the electrodes.[13] In addition, the open-circuit potential after delithiation is also indicative for the amount of immobilized lithium in the electrode. At the end of lithiation shown in **Figure 5a**, only a minor increase in the potential rise can be observed from ~70 to 80 mV during the investigated 200 cycles for either FEC or DiFEC, although the latter indicates an offset of about 5 mV to higher values. This observation agrees with the ~6 Ω cm^2 higher interfacial resistance of the DiFEC-containing electrolyte shown in **Figure 1b**, which translates into an additional ohmic drop of ~4 mV at a current of ~0.6 mA cm^{-2}. In contrast, at the end of the delithiation shown in **Figure 5b**, a significant increase of the potential drop occurs after 25-40 cycles from ~300 mV to ~700 mV in the DiFEC-containing electrolyte and even exceeding

750 mV in the FEC-containing electrolyte. Comparing the onset of this feature with the capacity decay shown in **Figure 4b** reveals that the potential drop ΔV_{OCP} occurs almost simultaneously with the loss in reversible capacity. Therefore, this analysis indicates that the amount of immobilized lithium in the SiG electrode strongly increases after 25-40 cycles as a result of an increasing electrode resistance at low degrees of lithiation, i.e. when the silicon particles are contracted. Vice versa, it remains widely stable at high degrees of lithiation, i.e. when silicon particles are fully expanded, thus supporting our explanation of an increased interparticle contact resistance due to a decreased contact pressure.[12] As a corollary, the superior capacity retention of DiFEC (in presence of an excess of active lithium) can be related to an improved mechanical integrity between the silicon particles that partially compensates the detrimental effect of the loss of interparticle contact pressure upon cycling. Taking into account our gas analysis, we explain this difference by the fluorinated vinoxyl-radical which is formed upon the reductive decomposition of DiFEC: (i) Defluorination of the radical was shown to increase the degree of cross-linking of the resulting polymeric SEI which improves its elastomeric properties and thus increases the mechanical integrity between the silicon nanoparticles.[20] (ii) The presence of LiF in the final decomposition products was reported to act as a glue by forming strong bindings between the fluorine atom and the lithium atoms of multiple organic SEI compounds.[47] Although this effect occurs both with FEC and DiFEC, the higher fluorine content of DiFEC likely promotes its impact on reducing the loss of interparticle contact pressure. Nonetheless, further spectroscopic investigation is required to understand the compositional differences of the SEI formed by FEC and DiFEC in more detail.

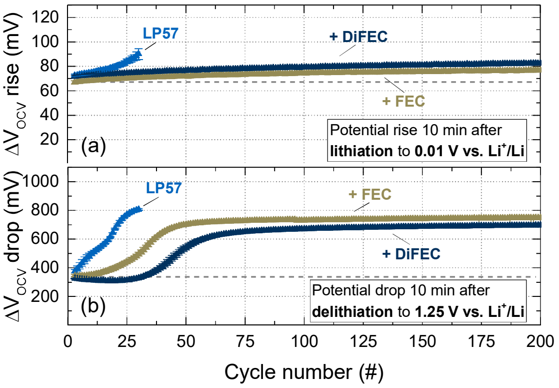

Figure 5. Potential changes of the SiG electrodes in different electrolytes during a 10 min rest period after lithiation at 0.33 h^{-1} to 0.01 V vs. Li$^+$/Li or delithiation at 0.33 h^{-1} to 1.25 V vs. Li$^+$/Li, evaluated from the same cycling measurements as shown in **Figure 4.** The two formation cycles at a lower C-rate of 0.1 h^{-1} are omitted.

Quantification of FEC and DiFEC consumption on SiG electrodes.— To quantify the loss of FEC and DiFEC upon cycling, ^{19}F-NMR spectroscopy was performed of the electrolytes after 100 cycles. Analogous to the ^{19}F-NMR analysis of FEC in LP57, which was first reported by Jung et al.,[10] the characteristic doublet of doublets in the ^{19}F-spectra of DiFEC allows to determine the residual amount of DiFEC through a peak integral analysis with the PF_6^- signal as an internal standard. **Figure 6** shows the ^{1}H-decoupled ^{19}F-NMR spectra of these fresh electrolytes, consisting of LP57 (blue), 5 wt% FEC in LP57 (brown), and 5 wt% DiFEC in LP57 (marine). The signal of the PF_6^- anion can be observed at -74.5 ppm, while the -CHF- signal from the FEC occurs at -126.6 ppm. In the DiFEC-containing electrolyte, the signal is notably shifted towards higher chemical shifts to -136.1 ppm, which results from the electronegative effect of the second fluorine substituent. The chemical shift of the doublet of doublets around -136.1 ppm also identifies the present DiFEC as the *trans*-isomer.[48]

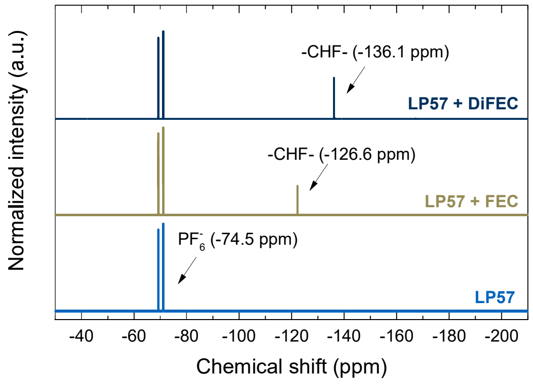

Figure 6. ^{1}H-decoupled ^{19}F-NMR spectra of different electrolyte solutions: LP57 (blue), 5 wt% FEC in LP57 (brown), and 5 wt% DiFEC in LP57 (marine). The intensity ratios of the (Di)FEC and PF_6^- peaks were calculated from the non-decoupled spectra.

To evaluate the consumption of the electrolyte additives upon cycling, **Figure 7a** shows the total charge+discharge capacity (in mAh) per µmol of either FEC (brown) or DiFEC (marine) after 100 cycles. In other words, this ratio compares how much capacity the SiG electrodes can exchange until one µmol of the additive is consumed. Within the range of one standard deviation, the capacity per additive is very similar for FEC (11.3 ± 0.1 mAh $\mu mol^{-1}{}_{FEC}$) and DiFEC (10.8 ± 0.2 mAh $\mu mol^{-1}{}_{DiFEC}$). Therefore, a commercial lithium-ion battery with a SiG anode and an electrolyte with the same molar quantity of either FEC or DiFEC would deliver almost the same capacity until depletion of the additive.

Interestingly, a comparison with the capacity per FEC of a similar 35 wt% silicon electrode from our previous publication on SiG electrodes with different active material ratios and the same 5 wt% FEC in LP57 electrolyte reveals a higher capacity of 14.5 ± 0.8 mAh $\mu mol^{-1}{}_{FEC}$.[12] We ascribe this difference to the absence of a constant voltage step in the present study. As a result, we expect the total capacity per additive shown in **Figure 7a** to be increased further by the introduction of a constant voltage step which allows to partially compensate the increased electrode impedance upon cycling and thus increase the amount of reversible lithium in a certain potential range.

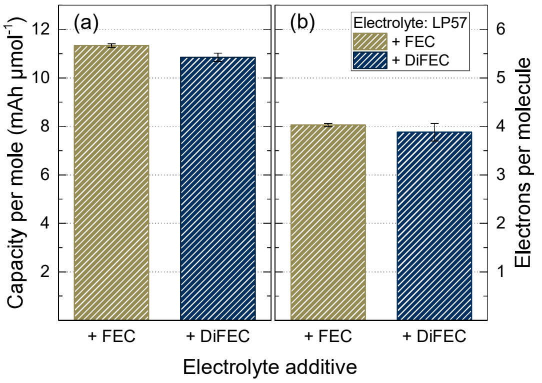

Figure 7. (a) Total charge+discharge capacity per $\mu mol_{(Di)FEC}$ of either FEC (brown) or DiFEC (marine). (b) Number of electrons per reduced additive molecule, obtained from ^{19}F-NMR analysis. The error bars represent the standard deviation of at least two independent repeat measurements.

Finally, we were interested, whether DiFEC shows a similar linear relation between the total irreversible capacity and the amount of consumed additive, as recently reported for FEC by our group.[10,12] Considering the absence of C_2H_4 mass traces in the gas analysis shown in **Figure 2c**, and thus the suppression of the EC reduction in presence of either FEC or DiFEC, we expect that despite a small fraction of immobilized lithium that remains in the SiG electrodes, the irreversible capacity loss in the FEC- and DiFEC-containing electrolytes originates almost fully from the decomposition of the respective additive. Based on this premise, the total irreversible capacity can be converted into the number of transferred electrons by using Faraday’s law, which amounts to 3.9-4.0 for both additives (**Figure 7b**). Thus, four electrons are required to completely reduce either one FEC or one DiFEC molecule. Using Faraday’s law again, the same number of electrons can also be expressed by a constant ratio of the amount of reduced additive and the irreversible capacity, viz., 9.4 ± 0.4 $\mu mol_{(Di)FEC}$ $mAh^{-1}{}_{irr}$.

In absence of other side reactions, this ratio allows to estimate the consumption of either FEC or DiFEC based on the irreversible capacity loss and thus predict the cycle life of a silicon-based lithium-ion battery with a given molar quantity of (Di)FEC in the electrolyte.

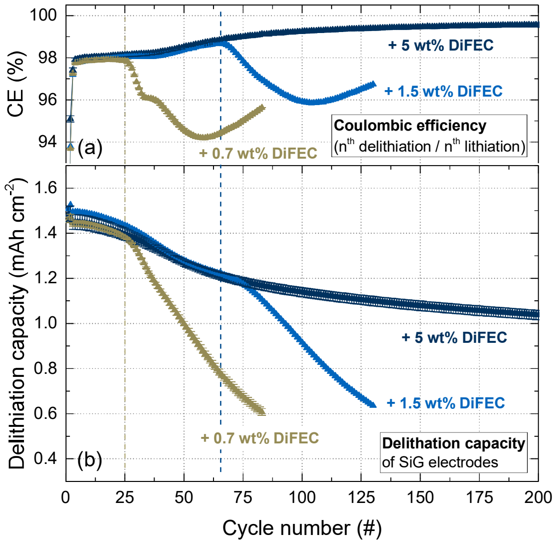

Figure 8. (a) Coulombic efficiency and (b) delithiation capacity obtained from galvanostatic cycling of SiG//LFP coin-cells with LP57 and different DiFEC concentrations, including 0.5 wt% DiFEC (brown), 1 wt% DiFEC (blue), and 5 wt% DiFEC (marine). C-rate: 0.1 h^{-1} during two formation cycles and 0.33 h^{-1} during consecutive cycles; cut-off potentials: 0.01 and 1.25 V vs. Li^+/Li. The dashed vertical lines indicate the forecasted depletion of DiFEC based on the ratio derived from ^{19}F-NMR measurements (see **Table II**). The error bars represent the standard deviation of at least two independent repeat measurements.

Influence of the DiFEC concentration on the cycling stability of SiG electrodes.— To verify that the suppression of the EC reduction is just a function of the absolute molar quantity of DiFEC in the electrolyte, **Figure 8** shows the cycling stability of the SiG electrodes in electrolytes with different DiFEC concentrations. The SiG//LFP cells (with an excess of active lithium) reveal a rapid capacity loss that occurs earlier with a decreasing DiFEC concentration in the electrolyte and is caused by the depletion of DiFEC.[12] In accordance with the constant ratio of the amount of consumed DiFEC and the irreversible capacity of 9.4 ± 0.4 $\mu mol_{(Di)FEC}\ mAh^{-1}{}_{irr}$, the failure of the cells would be expected after an irreversible capacity of 1.05 $mAh_{irr}\ cm^{-2}$ (0.7 wt% DiFEC) and 2.09 $mAh_{irr}\ cm^{-2}$ (1.5 wt% DiFEC), respectively. This agrees well with experimentally obtained capacity losses (see **Table II**). In contrast, the amount of DiFEC in the 5 wt% electrolyte is large enough to sustain a total irreversible capacity loss of more than 6 $mAh_{irr}\ cm^{-2}$ (= 62.35 μmol_{DiFEC} / 9.4 $\mu mol_{DiFEC}\ mAh_{irr}$), therefore no rapid capacity loss could be detected within the first 200 cycles. A similar behavior was recently reported for FEC by Jung et al.[10] and Petibon et al.[24], who demonstrated that the suppression of the EC reduction only lasts as long as there is FEC present in the electrolyte. Therefore, we can conclude that DiFEC is similarly consumed upon cycling and its depletion leads to a strong polarization due to reductive decomposition of EC, which is followed by a sudden cell failure. In addition, the constant ratio of the molar quantity of (Di)FEC per irreversible capacity of 9.4 ± 0.4 $\mu mol_{(Di)FEC}$ mAh_{irr} can thus be used to forecast the loss of both FEC and DiFEC from the cycling data.

Table II. Forecasted and measured irreversible capacity drop Q_{drop}^{irr} as a function of the DiFEC concentration in the electrolyte.

DiFEC concentration in LP57		**Forecasted Q_{drop}^{irr}**	**Measured Q_{drop}^{irr}**	
wt%	μmol_{DiFEC} cm^{-2}	mAh_{irr} cm^{-2}	mAh_{irr} cm^{-2}	# of cycles
0.7	9.32	1.05	1.10	25
1.5	18.44	2.09	2.15	65
5.0	62.35	6.63	-	-

Conclusions

In the present study, we investigated EC, FEC, and DiFEC as electrolyte constituents for SiG electrodes. By on-line gas analysis and differential capacity analysis we demonstrated that DiFEC has a very similar reductive behavior on SiG electrodes like the widely used FEC, which involves (i) a preferential reduction at a more positive potential than EC, (ii) the release of CO_2, and (iii) the consumption of in total four electrons per (Di)FEC molecule. Our results from galvanostatic cycling of SiG electrodes vs. capacitively oversized $LiFePO_4$ electrodes revealed a significantly improved capacity retention both for FEC- and DiFEC-containing electrolyte compared to EC, which we ascribe to the release of CO_2 and the formation of a cross-linked polymeric SEI from FEC and DiFEC.

Notwithstanding these similarities, we also showed that DiFEC indicates notable differences compared to FEC, including (i) an inferior passivation of the initial SEI, leading to a higher irreversible capacity within the first cycles, (ii) a ~2.3 times higher initial CO_2 evolution, and (iii) a ~3 times larger interfacial resistance after the first lithiation. SiG electrodes cycled in a DiFEC-containing electrolyte and an excess of active lithium even showed a 7%-points higher capacity retention than FEC after 100 cycles. We related this improvement to a reduced loss of interparticle contact pressure due to the higher fluorine content in the DiEFC decomposition products. Yet, an in-depth analysis revealed that the total charge+discharge capacity exchanged by the SiG electrodes per consumed mole of (Di)FEC is the same. As a corollary, the higher reversible capacity was obtained at the expense of a higher irreversible capacity, which suggests that for silicon-based lithium-ion batteries with a limited lithium inventory DiFEC does not offer an advantage with respect to the cycling stability. Finally, we could demonstrate by means of ^{19}F-NMR analysis that in the absence of other side reactions the ratio of 9.4 ± 0.4 $\mu mol_{(Di)FEC}$ $mAh^{-1}{}_{irr}$ can be used to estimate the consumption of either FEC or DiFEC based on the irreversible capacity loss and thus predict the cycle life of a silicon-based lithium-ion battery with a given molar quantity of (Di)FEC in the electrolyte.

Acknowledgements

The German Federal Ministry for Economic Affairs and Energy is acknowledged for funding (funding number 03ET6045D). The authors kindly acknowledge Brett Lucht (Rhode Island University), Michael Metzger, Benjamin Strehle, and Roland Jung (all TUM) for very fruitful discussions. Wacker Chemie AG is kindly acknowledged for providing the silicon nanoparticles.

References

(1) Andre, D.; Kim, S.-J.; Lamp, P.; Lux, S. F.; Maglia, F.; Paschos, O.; Stiaszny, B. *J. Mater. Chem. A* **2015**, *3*, 6709–6732.

(2) Gröger, O.; Gasteiger, H. A.; Suchsland, J.-P. *J. Electrochem. Soc.* **2015**, *162* (14), A2605–A2622.

(3) Wetjen, M.; Solchenbach, S.; Pritzl, D.; Hou, J.; Tileli, V.; Gasteiger, H. A. *J. Electrochem. Soc.* **2018**, *165* (7), A1503–A1514.

(4) Obrovac, M. N.; Chevrier, V. L. *Chem. Rev.* **2014**, *114*, 11444–11502.

(5) Aurbach, D. *J. Power Sources* **2000**, *89*, 206–218.

(6) Verma, P.; Maire, P.; Novák, P. *Electrochim. Acta* **2010**, *55*, 6332–6341.

(7) Nie, M.; Abraham, D. P.; Chen, Y.; Bose, A.; Lucht, B. L. *J. Phys. Chem. C* **2013**, *117*, 13403–13412.

(8) Klett, M.; Gilbert, J. A.; Pupek, K. Z.; Trask, S. E.; Abraham, D. P. *J. Electrochem. Soc.* **2017**, *164* (1), A6095–A6102.

(9) Delpuech, N.; Dupre, N.; Moreau, P.; Bridel, J. S.; Gaubicher, J.; Lestriez, B.; Guyomard, D. *ChemSusChem* **2016**, *9*, 841–848.

(10) Jung, R.; Metzger, M.; Haering, D.; Solchenbach, S.; Marino, C.; Tsiouvaras, N.; Stinner, C.; Gasteiger, H. A. *J. Electrochem. Soc.* **2016**, *163* (8), A1705–A1716.

(11) Petibon, R.; Chevrier, V. L.; Aiken, C. P.; Hall, D. S.; Hyatt, S. R.; Shunmugasundaram, R.; Dahn, J. R. *J. Electrochem. Soc.* **2016**, *163* (7), A1146–A1156.

(12) Wetjen, M.; Pritzl, D.; Jung, R.; Solchenbach, S.; Ghadimi, R.; Gasteiger, H. A. *J. Electrochem. Soc.* **2017**, *164* (12), A2840–A2852.

(13) Chevrier, V. L.; Liu, L.; Le, D. B.; Lund, J.; Molla, B.; Reimer, K.; Krause, L. J.; Jensen, L. D.; Figgemeier, E.; Eberman, K. W. *J. Electrochem. Soc.* **2014**, *161* (5), A783–A791.

(14) Xu, K. *Chem. Rev.* **2014**, *114*, 11503–11618.

(15) Xiong, D.; Burns, J. C.; Smith, A. J.; Sinha, N.; Dahn, J. R. *J. Electrochem. Soc.* **2011**, *158* (12), A1431–A1435.

(16) Xu, C.; Lindgren, F.; Philippe, B.; Gorgoi, M.; Björefors, F.; Edström, K.; Gustafsson, T. *Chem. Mater.* **2015**, *27*, 2591–2599.

(17) Choi, N.-S. S.; Yew, K. H.; Lee, K. Y.; Sung, M.; Kim, H.; Kim, S.-S. S. *J. Power Sources* **2006**, *161*, 1254–1259.

(18) Nakai, H.; Kubota, T.; Kita, A.; Kawashima, A. *J. Electrochem. Soc.* **2011**, *158* (7), A798–A801.

(19) Etacheri, V.; Haik, O.; Goffer, Y.; Roberts, G. A.; Stefan, I. C.; Fasching, R.; Aurbach, D. *Langmuir* **2012**, *28*, 965–976.

(20) Shkrob, I. A.; Wishart, J. F.; Abraham, D. P. *J. Phys. Chem. C* **2015**, *119*, 14954–14964.

(21) Markevich, E.; Fridman, K.; Sharabi, R.; Elazari, R.; Salitra, G.; Gottlieb, H. E.; Gershinsky, G.; Garsuch, A.; Semrau, G.; Schmidt, M. A.; Aurbach, D. *J. Electrochem. Soc.* **2013**, *160* (10), A1824–A1833.

(22) Schroder, K.; Alvarado, J.; Yersak, T. A.; Li, J.; Dudney, N.; Webb, L. J.; Meng, Y. S.; Stevenson, K. J. *Chem. Mater.* **2015**, *27*, 5531–5542.

(23) Philippe, B.; Dedryvère, R.; Gorgoi, M.; Rensmo, H.; Gonbeau, D.; Edström, K. *Chem. Mater.* **2013**, *25* (3), 394–404.

(24) Petibon, R.; Chevrier, V.; Aiken, C. P.; Hall, D. S.; Hyatt, S.; Shunmugasundaram, R.; Dahn, J. R. *J. Electrochem. Soc.* **2016**, *163* (7), A1146–A1156.

(25) Yariv, O.; Hirshberg, D.; Zinigrad, E.; Meitav, A.; Aurbach, D.; Jiang, M.; Powell, B. R. *J. Electrochem. Soc.* **2014**, *161* (9), A1422–A1431.

(26) Xia, J.; Petibon, R.; Xiao, A.; Lamanna, W. M.; Dahn, J. R. *J. Electrochem. Soc.* **2016**, *163* (8), A1637–A1645.

(27) Su, C.-C.; He, M.; Redfern, P. C.; Curtiss, L. A.; Shkrob, I.; Zhang, Z. *Energy Environ. Sci.*

2017, *10*, 900–904.

(28) Xia, J.; Liu, Q.; Hebert, A.; Hynes, T.; Petibon, R.; Dahn, J. R. *J. Electrochem. Soc.* **2017**, *164* (6), A1268–A1273.

(29) Solchenbach, S.; Pritzl, D.; Kong, E. J. Y.; Landesfeind, J.; Gasteiger, H. A. *J. Electrochem. Soc.* **2016**, *163* (10), A2265–A2272.

(30) Tsiouvaras, N.; Meini, S.; Buchberger, I.; Gasteiger, H. A. *J. Electrochem. Soc.* **2013**, *160* (3), A471–A477.

(31) Nie, M.; Demeaux, J.; Young, B. T.; Heskett, D. R.; Chen, Y.; Bose, A.; Woicik, J. C.; Lucht, B. L. *J. Electrochem. Soc.* **2015**, *162* (13), 7008–7014.

(32) Pritzl, D.; Solchenbach, S.; Wetjen, M.; Gasteiger, H. A. *J. Electrochem. Soc.* **2017**, *164* (12), A2625–A2635.

(33) Krause, L. J.; Chevrier, V. L.; Jensen, L. D.; Brandt, T. *J. Electrochem. Soc.* **2017**, *164* (12), A2527–A2533.

(34) Solchenbach, S.; Wetjen, M.; Pritzl, D.; Schwenke, K. U.; Gasteiger, H. A. *J. Electrochem. Soc.* **2018**, *165* (3), 512–524.

(35) Metzger, M.; Strehle, B.; Solchenbach, S.; Gasteiger, H. A. *J. Electrochem. Soc.* **2016**, *163* (7), A1219–A1225.

(36) Bernhard, R.; Metzger, M.; Gasteiger, H. A. *J. Electrochem. Soc.* **2015**, *162* (10), A1984–A1989.

(37) Zhang, B.; Metzger, M.; Solchenbach, S.; Payne, M.; Meini, S.; Gasteiger, H. A.; Garsuch, A.; Lucht, B. L. *J. Phys. Chem. C* **2015**, *119*, 11337–11348.

(38) Metzger, M.; Strehle, B.; Solchenbach, S.; Gasteiger, H. A. *J. Electrochem. Soc.* **2016**, *163* (5), 798–809.

(39) Martinez del la Hoz, J. M.; Leung, K.; Balbuena, P. B. *Appl. Mater. Interfaces* **2013**, *5*, 13457–13465.

(40) Leung, K.; Rempe, S. B.; Foster, M. E.; Ma, Y.; Martinez del la Hoz, J. M.; Sai, N.; Balbuena, P. B. *J. Electrochem. Soc.* **2014**, *161* (3), A213–A221.

(41) Martinez del la Hoz, J. M.; Balbuena, P. B. *Phys. Chem. Chem. Phys.* **2014**, *16* (32), 17091–17098.

(42) Purushotham, U.; Takenaka, N.; Nagaoka, M. *RSC Adv.* **2016**, *6* (69), 65232–65242.

(43) Strehle, B.; Solchenbach, S.; Metzger, M.; Schwenke, K. U.; Gasteiger, H. A. *J. Electrochem. Soc.* **2017**, *164* (12), A2513–A2526.

(44) Takeuchi, E. S.; Gan, H.; Palazzo, M.; Leising, R. A.; Davis, S. M. *J. Electrochem. Soc.* **1997**, *144* (6), 1944–1948.

(45) Sasaki, T.; Jeong, S.-K.; Abe, T.; Iriyama, Y.; Inaba, M.; Ogumi, Z. *J. Electrochem. Soc.* **2005**, *152* (10), 1963–1968.

(46) Yoon, T.; Nguyen, C. C.; Seo, D. M.; Lucht, B. L. *J. Electrochem. Soc.* **2015**, *162* (12), A2325–A2330.

(47) Okuno, Y.; Ushirogata, K.; Sodeyama, K.; Takeyama, Y. *Phys. Chem. Chem. Phys.* **2016**, *18*, 8643–8653.

(48) Kobayashi, M.; Inoguchi, T.; Iida, T.; Tanioka, T.; Kumase, H.; Fukai, Y. *J. Fluor. Chem.* **2003**, *120* (2), 105–110.

4 Conclusions

The overarching goal of this PhD thesis was to develop a more comprehensive and quantitative understanding of the degradation phenomena of SiG anodes for lithium-ion batteries. Figure 4.1 summarizes the investigated degradation phenomena, the developed analytical techniques, and the evaluated strategies for SiG anodes that were subject to this thesis.

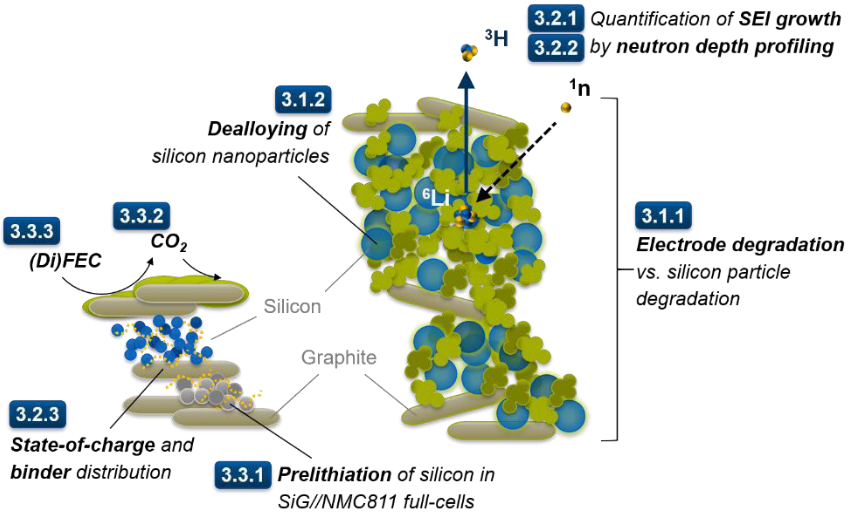

Figure 4.1 Graphical summary of the investigated degradation phenomena, the developed analytical techniques, and the evaluated strategies for pristine (left) and aged (right) SiG anodes that were subject to this thesis. The numbers in the blue boxes refer to respective sections in this thesis.

In the first part of this thesis, we aimed to separate and quantify the contributions from different degradation phenomena of SiG anodes and thus derive implications for practical lithium-ion batteries. Hence, we developed a pseudo full-cell configuration consisting of a capacitively oversized $LiFePO_4$ cathode and an FEC-containing electrolyte (Section 3.1.1).[102] Using different active material ratios and *post mortem* ^{19}F-NMR spectroscopy of the electrolyte solution, we identified two major degradation phenomena in blended SiG anodes, which we described as *silicon particle degradation* and *electrode degradation*. In a collaboration with the group of Vasiliki Tileli at the EPFL (Lausanne, Switzerland) we discovered that the first phenomenon is independent of the active material ratio and can be ascribed to dealloying reactions of the silicon nanoparticles upon repeated (de-)lithiation (Section 3.1.2).[132] Although nanoparticles were reported to be less prone to strain-induced fracturing,[121] we could demonstrate that they are still susceptible to dealloying reactions, leading to a significant morphological degradation and to increased irreversible capacity losses upon cycling. This reinforced concerns about the applicability of silicon nanoparticles in commercial lithium-ion batteries, emphasizing the need for alternative approaches. In contrast, the second degradation phenomenon, which we ascribed to the electrode coating, was found to be mostly driven by a loss of interparticle contact pressure, resulting in a decay of the reversible capacity. Interestingly, we could demonstrate that this mechanism depends both on the amount of electrically conducting graphite and the upper cutoff potential. For the latter, we proposed an explanation based on theoretical considerations that the relative surface area changes between end-of-charge and end-of-discharge are more important than the often-cited volumetric changes. As a corollary, operating silicon particles at higher state-of-charge leads to reduced relative surface area changes (despite the same volumetric changes), which coincides with a significantly improved coulombic efficiency.[132] Our findings thus explained a common observation made by other research groups, namely that silicon electrodes show an improved cycling stability when the upper (delithiation) cutoff potential is limited.[173,178,187] This has an important implication for battery management systems controlling the operating voltage range of practical lithium-ion batteries with silicon-based anodes.

In the second part of this thesis, in a collaboration with the Physics Department and the Heinz Maier-Leibnitz Zentrum (MLZ), we applied for the first time neutron depth profiling as a powerful technique to monitor lithium concentration gradients across silicon and graphite-based anodes. After successfully conducting the first experiments at the newly installed N4DP experiment at the PGAA facility at MLZ, we applied this technique for the first time to quantify the SEI growth across SiG anodes over prolonged cycling up to 140 charge/discharge cycles (Section 3.2.1).[151] We validated the NDP results by a thorough *post mortem* analysis of the same electrodes, *inter alia* by means of high-resolution SEM images. Thus, we could demonstrate that the SEI growth in SiG anodes occurs uniformly across the thickness of the electrode coatings, which indicated the absence of a dominating transport-limiting process and at the same time a uniform capacity utilization of the silicon particles (Section 3.2.2).[167] This supported our previous findings concerning the degradation phenomena in SiG anodes and highlighted the need (i) to improve the passivation of the silicon/electrolyte interface, and (ii) to develop a hierarchical electrode structure that maintains good electron and lithium ion transport not only across the thickness of the electrode but also between the silicon particles.

In the final part of this thesis, we evaluated three strategies to overcome the challenges associated with silicon-based anodes. In a collaboration with the Volkswagen Varta Microbattery Forschungsgesellschaft mbH on SiG//NMC811 full-cells featuring a capacitively largely oversized SiG anode, we showed that the comparatively high lithiation potential of ~0.2 V vs. Li^+/Li of silicon results in an upward shift of the upper cutoff potential of the NMC811 cathode (Section 3.3.1).[229] At potentials above 4.3 V vs. Li^+/Li, this shift led to the release of oxygen from the NMC811 lattice followed by a rapid increase in the cell impedance. Nevertheless, our results also indicated that the average lithiation potential can be lowered by prelithiation of the SiG anode which mitigates the risk of oxygen release during voltage slippage of the NMC811 cathode. Further, we showed that the excess of cyclable lithium results in an improved capacity retention of the SiG//NMC811 cells, demonstrating a residual specific energy of ~340 Wh kg^{-1} (normalized to the mass of both electrodes) after 250 cycles at 45°C. This value matches state-of-the-art graphite//NMC622 cells with an upper cell cutoff voltage of 4.4 V_{cell} after 250 cycles at 25°C.

In the second strategy, we evaluated lithium oxalate in combination with high-voltage spinel cathodes as capacity enhancer in SiG//LNMO and graphite//LNMO full-cells (Section 3.3.2).[222] By *on-line* gas analysis, galvanostatic cycling, and *post mortem* ^{19}F-NMR spectroscopy we could demonstrate that lithium oxalate is oxidized around 4.7 V vs. Li^+/Li to form quantitative amounts of CO_2. Full-cells featuring LNMO cathodes with either 2.5 or 5 wt% lithium oxalate showed an improved capacity retention, whereby the effect was even more pronounced with SiG anodes. Further, we could demonstrate that CO_2 acts as an effective additive for the passivation of SiG anodes, which has a synergistic effect with the commonly used FEC. Yet, our measurements also revealed that in spite of the improved coulombic efficiency, both additives are continuously consumed during charge-discharge cycling, leading to a rapid cell failure upon their depletion.[222]

In our final study, we evaluated di-fluroethylene carbonate (DiFEC) as alternative electrolyte additive for silicon-based electrodes to the commonly used FEC (Section 3.3.3).[236] In a comparison of EC, FEC, and DiFEC by means of an *on-line* gas analysis and ^{19}F-NMR spectroscopy, we could show that both fluorinated EC-derivatives follow a similar reduction mechanism which differs considerably from the one of EC. While the reduction of EC results in the formation of ethylene, the reduction of FEC and DiFEC consumes four electrons, yielding gaseous CO_2 and a vinoxyl radical. Yet, when cycled in presence of a capacitively oversized $LiFePO_4$ cathode, our SiG anodes revealed a higher capacity retention with DiFEC compared to FEC. We explained this phenomenon by a reduced loss of interparticle contact pressure due to the higher fluorine content in the electrolyte decomposition products. Nevertheless, considering the capacity exchanged by silicon per mole of consumed additive, which is a measure for the passivation at the silicon/electrolyte interface, we could finally demonstrate that there is no gain compared to FEC. As a corollary, DiFEC shows favorable cycling stability in half-cells with an excess of lithium but offers no advantage to improve the cycle life of practical lithium-ion full-cells.

This PhD thesis has demonstrated that silicon is indeed a promising anode active material for future high-energy lithium-ion batteries. However, the realization of its theoretical advantage over graphite requires to rethink the use of lithium-alloys and to develop a more comprehensive understanding of their (de-)lithiation chemistry as well as the underlying aging mechanisms. Our investigations have shown that despite of more than 30 years of research on alloy materials, there is still room for insights and alternative solution concepts. Both are urgently needed to address the two major challenges of silicon-based electrodes which still remain: (i) the stabilization of the silicon/electrolyte interface and (ii) the design of alloy-based electrodes that can cope with the morphological changes and maintain good electron and lithium ion transport properties even upon prolonged cycling. Because of the complex nature of alloy materials, this PhD thesis encourages future studies to focus on experimental approaches that allow to derive implications for application-relevant lithium-ion batteries. This will ensure to realistically evaluate the gap between the theoretical and the practical performance of alloy-based electrodes and thus support the development of a sustainable advantage compared to state-of-the-art insertion materials like graphite.

References

(1) Yoshino, A. *Angew. Chemie - Int. Ed.* **2012**, *51*, 5798–5800.

(2) Thackeray, M. M.; Wolverton, C.; Isaacs, E. D. *Energy Environ. Sci.* **2012**, *5*, 7854–7863.

(3) Yoshio, M.; Brodd, R. J.; Kozawa, A. *Lithium-Ion Batteries*; Springer: New York, 2009.

(4) Brandt, K. *Solid State Ionics* **1994**, *69*, 173–183.

(5) Aurbach, D.; Zinigrad, E.; Cohen, Y.; Teller, H. *Solid State Ionics* **2002**, *148*, 405–416.

(6) Aurbach, D. *J. Power Sources* **2000**, *89*, 206–218.

(7) Blomgren, G. E. *J. Electrochem. Soc.* **2017**, *164* (1), A5019–A5025.

(8) Nishi, Y. *Interface* **2016**, *25*, 71–74.

(9) Scrosati, B. *J. Electrochem. Soc.* **1992**, *139* (10), 2776–2781.

(10) Whittingham, M. S. *Chem. Rev.* **2004**, *104*, 4271–4301.

(11) Nishi, Y. *Macromol. Symp.* **2000**, *156*, 187–193.

(12) Scrosati, B.; Garche, J. *J. Power Sources* **2010**, *195*, 2419–2430.

(13) Whittingham, M. S. *Science* **1976**, *192*, 1126–1127.

(14) Whittingham, M. S. *J. Electrochem. Soc.* **1976**, *123* (3), 315–320.

(15) Whittingham, M. S. *Prog. Solid State Chem.* **1978**, *12* (1), 41–99.

(16) Thackeray, M. M.; David, W. I. F.; Bruce, P. G.; Goodenough, J. B. *Mater. Res. Bull.* **1983**, *18* (4), 461–472.

(17) Mizushima, K.; Jones, P. C.; Wiseman, P. J.; Goodenough, J. B. *Solid State Ionics* **1981**, *3/4*, 171–174.

(18) Fong, R.; von Sacken, U.; Dahn, J. R. *J. Electrochem. Soc.* **1990**, *137* (7), 2009–2013.

(19) Dahn, J. R.; von Sacken, U.; Juzkow, M. W.; Aljanaby, H. *J. Electrochem. Soc.* **1991**, *138* (8), 2207–2211.

(20) Peled, E. *J. Electrochem. Soc.* **1979**, *126* (12), 2047–2051.

(21) Peled, E.; Menkin, S. *J. Electrochem. Soc.* **2017**, *164* (7), A1703–A1719.

(22) Armand, M.; Tarascon, J. M. *Nature* **2008**, *451*, 652–657.

(23) Gallagher, K. G.; Goebel, S.; Greszler, T.; Mathias, M.; Oelerich, W.; Eroglu, D.; Srinivasan, V. *Energy Environ. Sci.* **2014**, *7*, 1555–1563.

(24) Andre, D.; Kim, S.-J.; Lamp, P.; Lux, S. F.; Maglia, F.; Paschos, O.; Stiaszny, B. *J. Mater. Chem. A* **2015**, *3*, 6709–6732.

(25) McKinsey&Company. *Electrifying insights: How automakers can drive electrified vehicle sales and profitability*; McKinsey&Company: Munich, Germany, 2017.

(26) Deutsche Bank AG. *Deutsche Bank Markets Research Industry Lithium 101*; Deutsche Bank AG: Sydney, Australia, 2016.

(27) Gröger, O.; Gasteiger, H. A.; Suchsland, J.-P. *J. Electrochem. Soc.* **2015**, *162* (14), A2605–A2622.

(28) Ahmed, S.; Bloom, I.; Jansen, A. N.; Tanim, T.; Dufek, E. J.; Pesaran, A.; Burnham, A.; Carlson, R. B.; Dias, F.; Hardy, K.; Keyser, M.; Kreuzer, C.; Markel, A.; Meintz, A.; Michelbacher, C.; Mohanpurkar, M.; Nelson, P. A.; Robertson, D. C.; Scoffield, D.; Shirk, M.; Stephens, T.; Vijayagopal, R.; Zhang, J. *J. Power Sources* **2017**, *367*, 250–262.

(29) Michelbacher, C.; Ahmed, S.; Bloom, I.; Burnham, A.; Carlson, B.; Dias, F.; Dufek, E. J.; Jansen, A. N.; Keyser, M.; Markel, A.; Meintz, A.; Mohanpurkar, M.; Pesaran, A.; Scoffield, D.; Shirk, M.; Stephens, T.; Tanim, T.; Vijayagopal, R.; Zhang, J. *J. Power Sources* **2017**, *367*, 214–215.

(30) NOAA National Centers for Environmental Information. Global Climate Report for March 2018 https://www.ncdc.noaa.gov/sotc/global/201803 (accessed Apr 28, 2018).

(31) Joos, F.; Plattner, G.; Stocker, T. F.; Marchal, O.; Schmittner, A. *Science* **1999**, *284*, 464–467.

(32) Lashof, D. A.; Ahuja, D. R. *Nature* **1990**, *344*, 529–531.

(33) European Environment Agency. *Monitoring CO2 emissions from new passenger cars and vans in 2016*; European Environment Agency: Copenhagen, Denmark, 2017.

(34) Dunn, B.; Kamath, H.; Tarascon, J. *Sci. Mag.* **2011**, *334*, 928–936.

(35) Gallagher, K. G.; Trask, S. E.; Bauer, C.; Woehrle, T.; Lux, S. F.; Tschech, M.; Lamp, P.; Polzin, B. J.; Ha, S.; Long, B.; Wu, Q.; Lu, W.; Dees, D. W.; Jansen, A. N. *J. Electrochem. Soc.* **2016**, *163* (2), A138–A149.

(36) Wagner, F. T.; Lakshmanan, B.; Mathias, M. F. *J. Phys. Chem. Lett.* **2010**, *1*, 2204–2219.

(37) Jung, R.; Metzger, M.; Maglia, F.; Stinner, C.; Gasteiger, H. *J. Phys. Chem. Lett.* **2017**, *8*, 4820–4825.

(38) Strehle, B.; Kleiner, K.; Jung, R.; Chesneau, F.; Mendez, M.; Hubert, A. *J. Electrochem. Soc.* **2017**, *164* (2), 400–406.

(39) Jung, R.; Metzger, M.; Maglia, F.; Stinner, C.; Gasteiger, H. A. *J. Electrochem. Soc.* **2017**, *164* (7), A1361–A1377.

(40) Pritzl, D.; Solchenbach, S.; Wetjen, M.; Gasteiger, H. A. *J. Electrochem. Soc.* **2017**, *164* (12), A2625–A2635.

(41) Nie, M.; Demeaux, J.; Young, B. T.; Heskett, D. R.; Chen, Y.; Bose, A.; Woicik, J. C.; Lucht, B. L. *J. Electrochem. Soc.* **2015**, *162* (13), 7008–7014.

(42) Nie, M.; Lucht, B. L. *J. Electrochem. Soc.* **2014**, *161* (6), A1001–A1006.

(43) Schroder, K.; Alvarado, J.; Yersak, T. A.; Li, J.; Dudney, N.; Webb, L. J.; Meng, Y. S.; Stevenson, K. J. *Chem. Mater.* **2015**, *27*, 5531–5542.

(44) Verma, P.; Maire, P.; Novák, P. *Electrochim. Acta* **2010**, *55*, 6332–6341.

(45) Xu, K. *Chem. Rev.* **2004**, *104*, 4303–4417.

(46) Besenhard, J. O.; Winter, M.; Yang, J.; Biberacher, W. *J. Power Sources* **1995**, *54*, 228–231.

(47) Yoon, T.; Milien, M. S.; Parimalam, B. S.; Lucht, B. L. *Chem. Mater.* **2017**, *29*, 3237–3245.

(48) Zhan, C.; Lu, J.; Jeremy Kropf, A.; Wu, T.; Jansen, A. N.; Sun, Y. K.; Qiu, X.; Amine, K. *Nat. Commun.* **2013**, *4*, 2437–2444.

(49) Ochida, M.; Domi, Y.; Doi, T.; Tsubouchi, S.; Nakagawa, H.; Yamanaka, T.; Abe, T.; Ogumi, Z. *J. Electrochem. Soc.* **2012**, *159* (7), A961–A966.

(50) Xu, K. *Chem. Rev.* **2014**, *114*, 11503–11618.

(51) Aurbach, D.; Ein-Eli, Y.; Markovsky, B.; Zaban, A.; Luski, S.; Carmeli, Y.; Yamin, H. *J. Electrochem. Soc.* **1995**, *142* (9), 2882–2890.

(52) Logan, E. R.; Tonita, E. M.; Gering, K. L.; Ma, L.; Bauer, M. K. G.; Li, J.; Beaulieu, L. Y.; Dahn, J. R. *J. Electrochem. Soc.* **2018**, *165* (3), A705–A716.

(53) Xia, J.; Petibon, R.; Xiong, D.; Ma, L.; Dahn, J. R. *J. Power Sources* **2016**, *328*, 124–135.

(54) Valøen, L. O.; Reimers, J. N. *J. Electrochem. Soc.* **2005**, *152* (5), A882–A891.

(55) Logan, E. R.; Tonita, E. M.; Gering, K. L.; Li, J.; Ma, X.; Beaulieu, L. Y.; Dahn, J. R. *J. Electrochem. Soc.* **2018**, *165* (2), A21–A30.

(56) Petibon, R.; Sinha, N. N.; Burns, J. C.; Aiken, C. P.; Ye, H.; Vanelzen, C. M.; Jain, G.; Trussler, S.; Dahn, J. R. *J. Power Sources* **2014**, *251*, 187–194.

(57) Burns, J. C.; Kassam, a.; Sinha, N. N.; Downie, L. E.; Solnickova, L.; Way, B. M.; Dahn, J. R. *J. Electrochem. Soc.* **2013**, *160* (9), A1451–A1456.

(58) Xia, J.; Petibon, R.; Xiao, A.; Lamanna, W. M.; Dahn, J. R. *J. Electrochem. Soc.* **2016**, *163* (8), A1637–A1645.

(59) Zhang, B.; Metzger, M.; Solchenbach, S.; Payne, M.; Meini, S.; Gasteiger, H. A.; Garsuch, A.; Lucht, B. L. *J. Phys. Chem. C* **2015**, *119*, 11337–11348.

(60) Xia, J.; Liu, Q.; Hebert, A.; Hynes, T.; Petibon, R.; Dahn, J. R. *J. Electrochem. Soc.* **2017**, *164* (6), A1268–A1273.

(61) Metzger, M.; Marino, C.; Sicklinger, J.; Haering, D.; Gasteiger, H. A. *J. Electrochem. Soc.* **2015**, *162* (7), A1123–A1134.

(62) Ma, L.; Glazier, S. L.; Petibon, R.; Xia, J.; Peters, J. M.; Liu, Q.; Allen, J.; Doig, R. N. C.; Dahn, J. R. *J. Electrochem. Soc.* **2017**, *164* (1), A5008–A5018.

(63) Nitta, N.; Wu, F.; Lee, J. T.; Yushin, G. *Mater. Today* **2015**, *18* (5), 252–264.

(64) Andre, D.; Hain, H.; Lamp, P.; Maglia, F.; Stiaszny, B. *J. Mater. Chem. A* **2017**, *5*, 17174–17198.

(65) Obrovac, M. N.; Christensen, L.; Le, D. B.; Dahn, J. R. *J. Electrochem. Soc.* **2007**, *154* (9), A849–A855.

(66) Qi, Y.; Guo, H.; Hector, L. G.; Timmons, A. *J. Electrochem. Soc.* **2010**, *157* (5), A558–A566.

(67) Dahn, J. R. *Phys. Rev. B* **1991**, *44* (17), 9170–9177.

(68) Dresselhaus, M. S.; Dresselhaus, G. *Adv. Phys.* **2002**, *51* (1), 1–186.

(69) Vinodkumar Etacheri, Rotem Marom, Ran Elazari, G. S. and D. A. *Energy Environ. Sci.* **2011**, *4*, 3243–3262.

(70) Hesse, H.; Schimpe, M.; Kucevic, D.; Jossen, A. *Energies* **2017**, *10*, 1–42.

(71) He, Y. B.; Li, B.; Liu, M.; Zhang, C.; Lv, W.; Yang, C.; Li, J.; Du, H.; Zhang, B.; Yang, Q. H.; Kim, J. K.; Kang, F. *Sci. Rep.* **2012**, *2*, 33–35.

(72) Besenhard, J. O.; Yang, J.; Winter, M. *J. Power Sources* **1997**, *68*, 87–90.

(73) Dey, A. N. *J. Electrochem. Soc.* **1971**, *118* (10), 1547–1549.

(74) Park, O. K.; Cho, Y.; Lee, S.; Yoo, H.-C.; Song, H.-K.; Cho, J. *Energy Environ. Sci.* **2011**, *4*, 1621–1633.

(75) Myung, S.-T.; Maglia, F.; Park, K.-J.; Yoon, C. S.; Lamp, P.; Kim, S.-J.; Sun, Y.-K. *ACS Energy Lett.* **2017**, *2*, 196–223.

(76) Noh, H. J.; Youn, S.; Yoon, C. S.; Sun, Y. K. *J. Power Sources* **2013**, *233*, 121–130.

(77) Julien, C.; Mauger, A.; Zaghib, K.; Groult, H. *Materials.* **2016**, *9*, 1–26.

(78) Bak, S.-M.; Hu, E.; Zhou, Y.; Yu, X.; Senanayake, S. D.; Cho, S.-J.; Kim, K.-B.; Chung, K. Y.; Yang, X.-Q.; Nam, K.-W. *ACS Appl. Mater. Interfaces* **2014**, *6* (24), 22594–22601.

(79) Nam, K.-W.; Bak, S.-M.; Hu, E.; Yu, X.; Zhou, Y.; Wang, X.; Wu, L.; Zhu, Y.; Chung, K.-Y.; Yang, X.-Q. *Adv. Funct. Mater.* **2013**, *23*, 1047–1063.

(80) Hwang, S.; Kim, S. M.; Bak, S. M.; Cho, B. W.; Chung, K. Y.; Lee, J. Y.; Chang, W.; Stach, E. A. *ACS Appl. Mater. Interfaces* **2014**, *6*, 15140–15147.

(81) Croguennec, L.; Bains, J.; Bréger, J.; Tessier, C.; Biensan, P.; Levasseur, S.; Delmas, C. *J. Electrochem. Soc.* **2011**, *158* (6), A664–A670.

(82) Thackeray, M. M.; Kang, S.-H.; Johnson, C. S.; Vaughey, J. T.; Benedek, R.; Hackney, S. A. *J. Mater. Chem.* **2007**, *17*, 3112–3125.

(83) Hong, J.; Gwon, H.; Jung, S.-K.; Ku, K.; Kang, K. *J. Electrochem. Soc.* **2015**, *162* (14), A2447–A2467.

(84) Ohzuku, T.; Takeda, S.; Iwanaga, M. *J. Power Sources* **1999**, *81–82*, 90–94.

(85) Liu, D.; Zhu, W.; Trottier, J.; Gagnon, C.; Barray, F.; Guerfi, A.; Mauger, A.; Groult, H.; Julien, C. M.; Goodenough, J. B.; Zaghib, K. *RSC Adv.* **2014**, *4*, 154–167.

(86) Goodenough, J. B.; Kim, Y. *Chem. Mater.* **2010**, *22*, 587–603.

(87) Padhi, A. K.; Nanjundaswamy, K. S.; Goodenough, J. B. *J. Electrochem. Soc.* **1997**, *144* (4), 1188–1194.

(88) Padhi, A. K.; Nanjundaswamy, K. S.; Masquelier, C.; Okada, S.; Goodenough, J. B. *J. Electrochem. Soc.* **1997**, *144* (5), 1609–1613.

(89) Yuan, L.-X.; Wang, Z.-H.; Zhang, W.-X.; Hu, X.-L.; Chen, J.-T.; Huang, Y.-H.; Goodenough, J. B. *Energy Environ. Sci.* **2011**, *4*, 269–284.

(90) Chen, G.; Richardson, T. J. *J. Power Sources* **2010**, *195*, 1221–1224.

(91) Jianlong, L.; Yan, W.; Jinhua, W.; Hang, Z.; Hao, W.; Yun, Z.; Heng, L. *ChemElectroChem* **2017**, *4*, 175–182.

(92) Obrovac, M. N.; Chevrier, V. L. *Chem. Rev.* **2014**, *114*, 11444–11502.

(93) Park, C.-M.; Kim, J.-H.; Kim, H.; Sohn, H.-J. *Chem. Soc. Rev.* **2010**, *39*, 3115–3141.

(94) Nitta, N.; Yushin, G. *Part. Part. Syst. Charact.* **2014**, *31*, 317–336.

(95) Kaskhedikar, N. A.; Maier, J. *Adv. Mater.* **2009**, *21*, 2664–2680.

(96) Chen, Z.; Belharouak, I.; Sun, Y. K.; Amine, K. *Adv. Funct. Mater.* **2013**, *23*, 959–969.

(97) Xu, W.; Wang, J.; Ding, F.; Chen, X.; Nasybulin, E.; Zhang, Y.; Zhang, J.-G. *Energy Environ. Sci.* **2014**, *7*, 513–537.

(98) Beaulieu, L. Y.; Eberman, K. W.; Turner, R. L.; Krause, L. J.; Dahn, J. R. *Electrochem. Solid-State Lett.* **2001**, *4* (9), A137–A140.

(99) Beaulieu, L. Y.; Hewitt, K. C.; Turner, R. L.; Bonakdarpour, A.; Abdo, A. A.; Christensen, L.; Eberman, K. W.; Krause, L. J.; Dahn, J. R. *J. Electrochem. Soc.* **2003**, *150* (2), A149–A156.

(100) Yoon, T.; Nguyen, C. C.; Seo, D. M.; Lucht, B. L. *J. Electrochem. Soc.* **2015**, *162* (12), A2325–A2330.

(101) Besenhard, J. O.; Hess, M.; Komenda, P. *Solid State Ionics* **1990**, *40/41*, 525–529.

(102) Wetjen, M.; Pritzl, D.; Jung, R.; Solchenbach, S.; Ghadimi, R.; Gasteiger, H. A. *J. Electrochem. Soc.* **2017**, *164* (12), A2840–A2852.

(103) Jung, R.; Metzger, M.; Haering, D.; Solchenbach, S.; Marino, C.; Tsiouvaras, N.; Stinner, C.; Gasteiger, H. A. *J. Electrochem. Soc.* **2016**, *163* (8), A1705–A1716.

(104) Petibon, R.; Chevrier, V. L.; Aiken, C. P.; Hall, D. S.; Hyatt, S. R.; Shunmugasundaram, R.; Dahn, J. R. *J. Electrochem. Soc.* **2016**, *163* (7), A1146–A1156.

(105) Beaulieu, L. Y.; Hatchard, T. D.; Bonakdarpour, A.; Fleischauer, M. D.; Dahn, J. R. *J. Electrochem. Soc.* **2003**, *150* (11), A1457–A1464.

(106) Rhodes, K.; Dudney, N.; Lara-Curzio, E.; Daniel, C. *J. Electrochem. Soc.* **2010**, *157* (12), A1354–A1360.

(107) Chao, S. C.; Song, Y. F.; Wang, C. C.; Sheu, H. S.; Wu, H. C.; Wu, N. L. *J. Phys. Chem. C* **2011**, *115*, 22040–22047.

(108) Chen, Q.; Sieradzki, K. *Nat. Mater.* **2013**, *12*, 1102–1106.

(109) Woo, S.; Mcdowell, M. T.; Berla, L. A.; Nix, W. D.; Cui, Y. *PANS* **2012**, *109* (11), 4080–4085.

(110) McDowell, M. T.; Ryu, I.; Lee, S. W.; Wang, C.; Nix, W. D.; Cui, Y. *Adv. Mater.* **2012**, *24*, 6034–6041.

(111) Winter, M.; Besenhard, J. O. *Electrochim. Acta* **1999**, *45*, 31–50.

(112) Delpuech, N.; Dupre, N.; Moreau, P.; Bridel, J. S.; Gaubicher, J.; Lestriez, B.; Guyomard, D. *ChemSusChem* **2016**, *9*, 841–848.

(113) Mazouzi, D.; Lestriez, B.; Roué, L.; Guyomard, D. *Electrochem. Solid-State Lett.* **2009**, *12* (11), A215–A218.

(114) Du, Z.; Dunlap, R. A.; Obrovac, M. N. *J. Electrochem. Soc.* **2014**, *161* (10), A1698–A1705.

(115) Chevrier, V. L.; Liu, L.; Le, D. B.; Lund, J.; Molla, B.; Reimer, K.; Krause, L. J.; Jensen, L. D.; Figgemeier, E.; Eberman, K. W. *J. Electrochem. Soc.* **2014**, *161* (5), A783–A791.

(116) Chevrier, V. L.; Liu, L.; Wohl, R.; Chandrasoma, A.; Vega, J. A.; Eberman, K. W.; Stegmaier, P.; Figgemeier, E. *J. Electrochem. Soc.* **2018**, *165* (5), A1129–A1136.

(117) Seefurth, R. N.; Sharma, R. A. *J. Electrochem. Soc.* **1974**, *124* (8), 1207–1214.

(118) Sharma, R. A.; Seefurth, R. N. *J. Electrochem. Soc.* **1976**, *123* (12), 1763–1768.

(119) Wen, C. J.; Huggins, R. A. *J. Solid State Chem.* **1981**, *37*, 271–278.

(120) Wilson, A. M.; Dahn, J. R. *J. Electrochem. Soc.* **1995**, *142* (2), 326–332.

(121) McDowell, M. T.; Lee, S. W.; Nix, W. D.; Cui, Y. *Adv. Mater.* **2013**, *25*, 4966–4985.

(122) Obrovac, M. N.; Krause, L. J. *J. Electrochem. Soc.* **2007**, *154* (2), A103–A108.

(123) Limthongkul, P.; Jang, Y. Il; Dudney, N. J.; Chiang, Y. M. *Acta Mater.* **2003**, *51*, 1103–1113.

(124) Chevrier, V. L.; Zwanziger, J. W.; Dahn, J. R. *J. Alloys Compd.* **2010**, *496*, 25–36.

(125) Key, B.; Bhattacharyya, R.; Morcrette, M.; Sezne, V.; Tarascon, J.; Grey, C. P. *J. Am. Chem. Soc.* **2009**, *131*, 9239–9249.

(126) Chan, M. K. Y.; Wolverton, C.; Greeley, J. P. *J. Am. Chem. Soc.* **2012**, *134*, 14362–14374.

(127) Li, J.; Dahn, J. R. *J. Electrochem. Soc.* **2007**, *154* (3), A156–A161.

(128) Obrovac, M. N.; Christensen, L. *Electrochem. Solid-State Lett.* **2004**, *7* (5), A93–A96.

(129) Liu, X. H.; Zhong, L.; Huang, S.; Mao, S. X.; Zhu, T.; Huang, J. Y. *ACS Nano* **2012**, *6* (2), 1522–1531.

(130) Liu, X. H.; Huang, J. Y. *Energy Environ. Sci.* **2011**, *4*, 3844–3860.

(131) McDowell, M. T.; Lee, S. W.; Harris, J. T.; Korgel, B. A.; Wang, C.; Nix, W. D.; Cui, Y. *Nano Lett.* **2013**, *13*, 758–764.

(132) Wetjen, M.; Solchenbach, S.; Pritzl, D.; Hou, J.; Tileli, V.; Gasteiger, H. A. *J. Electrochem. Soc.* **2018**, *165* (7), A1503–A1514.

(133) Christensen, J.; Newman, J. *J. Solid State Chem.* **2006**, *10*, 293–319.

(134) Kasavajjula, U.; Wang, C.; Appleby, A. J. *J. Power Sources* **2007**, *163*, 1003–1039.

(135) Li, H.; Huang, X. J.; Chen, L. Q.; Wu, Z. G.; Liang, Y. *Electrochem. Solid State Lett.* **1999**, *2* (11), 547–549.

(136) Holzapfel, M.; Buqa, H.; Scheifele, W.; Novák, P.; Petrat, F.-M. *Chem. Commun.* **2005**, 1566–1568.

(137) Ruffo, R.; Hong, S. S.; Chan, C. K.; Huggins, R. A.; Cui, Y. *J. Phys. Chem. C* **2009**, *113*, 11390–11398.

(138) Zamfir, M. R.; Nguyen, H. T.; Moyen, E.; Lee, Y. H.; Pribat, D. *J. Mater. Chem. A* **2013**, *1*, 9566–9586.

(139) Szczech, J. R.; Jin, S. *Energy Environ. Sci.* **2011**, *4*, 56–72.

(140) Ashuri, M.; He, Q.; Shaw, L. L. *Nanoscale* **2016**, *8*, 74–103.

(141) Shao, D.; Tang, D.; Mai, Y.; Zhang, L. *J. Mater. Chem. A* **2013**, *1*, 15068–15075.

(142) Yang, X. Q.; McBreen, J.; Yoon, W. S.; Yoshio, M.; Wang, H.; Fukuda, K.; Umeno, T. *Electrochem. commun.* **2002**, *4*, 893–897.

(143) Liu, N.; Wu, H.; Mcdowell, M. T.; Yao, Y.; Wang, C.; Cui, Y. *Nano Lett.* **2012**, *12*, 3315–3321.

(144) Liu, N.; Lu, Z.; Zhao, J.; Mcdowell, M. T.; Lee, H. W.; Zhao, W.; Cui, Y. *Nat. Nanotechnol.* **2014**, *9*, 187–192.

(145) Ma, D.; Cao, Z.; Hu, A. *Nano-Micro Lett.* **2014**, *6* (4), 347–358.

(146) Ziegler, J. F.; Cole, G. W.; Baglin, J. E. E. *J. Appl. Phys.* **1972**, *43*, 3809–3815.

(147) Biersack, J. P.; Fink, D.; Henkelmann, R.; Müller, K. *Nucl. Instruments Methods* **1978**, *149*, 93–97.

(148) Downing, R. G.; Fleming, R. F.; Langland, J. K.; Vincent, D. H. *Nucl. Instruments Methods Phys. Res.* **1983**, *218*, 47–51.

(149) Downing, R. G.; Lamaze, G. P.; Langland, J. K.; Hwang, S. T. *J. Res. Natl. Inst. Stand. Technol.* **1993**, *98* (1), 109–126.

(150) Oudenhoven, J. F. M.; Labohm, F.; Mulder, M.; Niessen, R. A. H.; Mulder, F. M.; Notten, P. H. L. *Adv. Mater.* **2011**, *23*, 4103–4106.

(151) Trunk, M.; Wetjen, M.; Werner, L.; Gernhäuser, R.; Märkisch, B.; Révay, Z.; Gasteiger, H. A.; Gilles, R. **2018**, submitted.

(152) Bethe, H. *Ann. Phys.* **1930**, *397* (3), 325–400.

(153) Whitney, S.; Biegalski, S. R.; Huang, Y. H.; Goodenough, J. B. *J. Electrochem. Soc.* **2009**, *156* (11), A886–A890.

(154) Whitney, S. M.; Biegalski, S. R. F.; Downing, G. *J. Radioanal. Nucl. Chem.* **2009**, *282*, 173–176.

(155) Nagpure, S. C.; Mulligan, P.; Canova, M.; Cao, L. R. *J. Power Sources* **2014**, *248*, 489–497.

(156) Nagpure, S. C.; Downing, R. G.; Bhushan, B.; Babu, S. S.; Cao, L. *Electrochim. Acta* **2011**, *56*, 4735–4743.

(157) Nagpure, S. C.; Gregory Downing, R.; Bhushan, B.; Babu, S. S. *Scr. Mater.* **2012**, *67*, 669–672.

(158) Lamaze, G. P.; Chen-Mayer, H. H.; Becker, D. A.; Vereda, F.; Goldner, R. B.; Haas, T.; Zerigian, P. *J. Power Sources* **2003**, *119–121*, 680–685.

(159) Wang, J.; Liu, D. X.; Canova, M.; Downing, R. G.; Cao, L. R.; Co, A. C. *J. Radioanal. Nucl. Chem.* **2014**, *301*, 277–284.

(160) Liu, D. X.; Wang, J.; Pan, K.; Qiu, J.; Canova, M.; Cao, L. R.; Co, A. C. *Angew. Chemie - Int. Ed.* **2014**, *53*, 9498–9502.

(161) Zhang, X.; Verhallen, T. W.; Labohm, F.; Wagemaker, M. *Adv. Energy Mater.* **2015**, 1500498.

(162) Ziegler, J. F.; Ziegler, M. D.; Biersack, J. P. *Nucl. Instruments Methods Phys. Res. Sect. B* **2010**, *268*, 1818–1823.

(163) He, Y.; Downing, R. G.; Wang, H. *J. Power Sources* **2015**, *287*, 226–230.

(164) Lamaze, G. P.; Chen-Mayer, H.; Langland, J. K.; Downing, R. G. *Surf. Interface Anal.* **1997**, *25*, 217–220.

(165) Maki, J. T.; Fleming, R. F.; Vincent, D. H. *Nucl. Inst. Methods Phys. Res. B* **1986**, *17*, 147–155.

(166) Skyrme, D. J. *Nucl. Instruments Methods* **1967**, *57*, 61–73.

(167) Wetjen, M.; Trunk, M.; Werner, L.; Gernhäuser, R.; Märkisch, B.; Révay, Z.; Gilles, R.; Gasteiger, H. A. *J. Electrochem. Soc.* **2018**, *165* (10), A2340-A2348.

(168) NIST. *Certificate of Analysis Standard Reference Material 2137,* **2010**.

(169) Erk, C.; Brezesinski, T.; Sommer, H.; Schneider, R.; Janek, J. *ACS Appl. Mater. Interfaces* **2013**, *5*, 7299–7307.

(170) Ryu, J. H.; Kim, J. W.; Sung, Y.; Oh, S. M. *Electrochem. Solid State Lett.* **2004**, *7* (10), 306–309.

(171) Yoon, T.; Chapman, N.; Seo, D. M.; Lucht, B. L. *J. Electrochem. Soc.* **2017**, *164* (9), A2082–A2088.

(172) Trask, S. E.; Pupek, K. Z.; Gilbert, J. A.; Klett, M.; Polzin, B. J.; Jansen, A. N.; Abraham, D. P. *J. Electrochem. Soc.* **2016**, *163* (3), A345–A350.

(173) Klett, M.; Gilbert, J. A.; Pupek, K. Z.; Trask, S. E.; Abraham, D. P. *J. Electrochem. Soc.* **2017**, *164* (1), A6095–A6102.

(174) Dupré, N.; Moreau, P.; De Vito, E.; Quazuguel, L.; Boniface, M.; Bordes, A.; Rudisch, C.; Bayle-Guillemaud, P.; Guyomard, D. *Chem. Mater.* **2016**, *28*, 2557–2572.

(175) Petibon, R.; Chevrier, V.; Aiken, C. P.; Hall, D. S.; Hyatt, S.; Shunmugasundaram, R.; Dahn, J. R. *J. Electrochem. Soc.* **2016**, *163* (7), A1146–A1156.

(176) Dose, W. M.; Piernas-Muñoz, M. J.; Maroni, V. A.; Trask, S. E.; Bloom, I.; Johnson, C. S. *Chem. Commun.* **2018**, *54*, 3586–3589.

(177) Kim, K.; Park, I.; Ha, S. Y.; Kim, Y.; Woo, M. H.; Jeong, M. H.; Shin, W. C.; Ue, M.; Hong, S. Y.; Choi, N. S. *Electrochim. Acta* **2017**, *225*, 358–368.

(178) Markevich, E.; Fridman, K.; Sharabi, R.; Elazari, R.; Salitra, G.; Gottlieb, H. E.; Gershinsky, G.; Garsuch, A.; Semrau, G.; Schmidt, M. A.; Aurbach, D. *J. Electrochem. Soc.* **2013**, *160* (10), A1824–A1833.

(179) Dupré, N.; Cuisinier, M.; Guyomard, D. *Interface* **2011**, *Fall*, 61–67.

(180) Michan, A. L.; Leskes, M.; Grey, C. P. *Chem. Mater.* **2015**, *28*, 385–398.

(181) Parimalam, B. S.; Lucht, B. L. *J. Electrochem. Soc.* **2018**, *165* (2), A251–A255.

(182) Tsiouvaras, N.; Meini, S.; Buchberger, I.; Gasteiger, H. A. *J. Electrochem. Soc.* **2013**, *160* (3), A471–A477.

(183) Solchenbach, S.; Pritzl, D.; Kong, E. J. Y.; Landesfeind, J.; Gasteiger, H. A. *J. Electrochem. Soc.* **2016**, *163* (10), A2265–A2272.

(184) Mittermeier, T.; Weiß, A.; Hasché, F.; Hübner, G.; Gasteiger, H. A. *J. Electrochem. Soc.* **2017**, *164* (2), F127–F137.

(185) Luo, F.; Liu, B.; Zheng, J.; Chu, G.; Zhong, K.; Li, H.; Huang, X.; Chen, L. *J. Electrochem. Soc.* **2015**, *162* (14), A2509–A2528.

(186) Zuo, X.; Zhu, J.; Müller-Buschbaum, P.; Cheng, Y. J. *Nano Energy* **2017**, *31*, 113–143.

(187) Kimura, K.; Matsumoto, T.; Nishihara, H.; Kasukabe, T.; Kyotani, T.; Kobayashi, H. *J. Electrochem. Soc.* **2017**, *164* (6), A995–A1001.

(188) Fuchsbichler, B.; Stangl, C.; Kren, H.; Uhlig, F.; Koller, S. *J. Power Sources* **2011**, *196*, 2889–2892.

(189) Gómez-Cámer, J. L.; Bünzli, C.; Hantel, M. M.; Poux, T.; Novák, P. *Carbon N. Y.* **2016**, *105*, 42–51.

(190) Klett, M.; Gilbert, J. A.; Trask, S. E.; Polzin, B. J.; Jansen, A. N.; Dees, D. W.; Abraham, D. P. *J. Electrochem. Soc.* **2016**, *163* (6), A875–A887.

(191) La Mantia, F.; Wessells, C. D.; Deshazer, H. D.; Cui, Y. *Electrochem. commun.* **2013**, *31*, 141–144.

(192) Mochizuki, T.; Aoki, S.; Horiba, T.; Schulz-Dobrick, M.; Han, Z.-J.; Fukuyama, S.; Oji, H.; Yasuno, S.; Komaba, S. *ACS Sustain. Chem. Eng.* **2017**, *5*, 6343–6355.

(193) Erlebacher, J.; Aziz, M. J.; Karma, A.; Dimitrov, N.; Sieradzki, K. *Nature* **2001**, *410*, 450–453.

(194) Sieradzki, K.; Dimitrov, N.; Movrin, D.; Mccall, C.; Vasiljevic, N. *J. Electrochem. Soc.* **2002**, *149* (8), B370–B377.

(195) Wandt, J.; Jakes, P.; Granwehr, J.; Eichel, R.-A.; Gasteiger, H. A. *Mater. Today* **2018**, *21* (3), 231–240.

(196) Burns, J. C.; Stevens, D. A.; Dahn, J. R. *J. Electrochem. Soc.* **2015**, *162* (6), A959–A964.

(197) Zinth, V.; Von Lüders, C.; Hofmann, M.; Hattendorff, J.; Buchberger, I.; Erhard, S.; Rebelo-Kornmeier, J.; Jossen, A.; Gilles, R. *J. Power Sources* **2014**, *271*, 152–159.

(198) Wandt, J.; Freiberg, A.; Thomas, R.; Gorlin, Y.; Siebel, A.; Jung, R.; Gasteiger, H. A.; Tromp, M. *J. Mater. Chem. A* **2016**, *4*, 18300–18305.

(199) Zheng, H.; Sun, Q.; Liu, G.; Song, X.; Battaglia, V. S. *J. Power Sources* **2012**, *207*, 134–140.

(200) Amine, K.; Chen, Z.; Zhang, Z.; Liu, J.; Lu, W.; Qin, Y.; Lu, J.; Curtis, L.; Sun, Y.-K. *J. Mater. Chem.* **2011**, *21*, 17754–17759.

(201) Burns, J. C.; Kassam, A.; Sinha, N. N.; Downie, L. E.; Solnickova, L.; Way, B. M.; Dahn, J. R. *J. Electrochem. Soc.* **2013**, *160* (9), A1451–A1456.

(202) Buchberger, I.; Seidlmayer, S.; Pokharel, A.; Piana, M.; Hattendorff, J.; Kudejova, P.; Gilles, R.; Gasteiger, H. A. *J. Electrochem. Soc.* **2015**, *162* (14), A2737–A2746.

(203) Michan, A. L.; Divitini, G.; Pell, A. J.; Leskes, M.; Ducati, C.; Grey, C. P. *J. Am. Chem. Soc.* **2016**, *138*, 7918–7931.

(204) Radvanyi, E.; Porcher, W.; De Vito, E.; Montani, A.; Franger, S.; Jouanneau Si Larbi, S. *Phys. Chem. Chem. Phys.* **2014**, *16*, 17142–17153.

(205) Key, B.; Morcrette, M.; Tarascon, J.-M.; Grey, C. P. *J. Am. Chem. Soc.* **2011**, *133*, 503–512.

(206) Oumellal, Y.; Delpuech, N.; Mazouzi, D.; Dupré, N.; Gaubicher, J.; Moreau, P.; Soudan, P.; Lestriez, B.; Guyomard, D. *J. Mater. Chem.* **2011**, *21*, 6201–6208.

(207) Delpuech, N.; Mazouzi, D.; Dupre, N.; Moreau, P.; Cerbelaud, M.; Bridel, J. S.; Vito, E. De; Guyomard, D.; Lestriez, B.; Humbert, B. *J. Phys. Chem. C* **2014**, *118*, 17318–17331.

(208) Nie, M.; Abraham, D. P.; Chen, Y.; Bose, A.; Lucht, B. L. *J. Phys. Chem. C* **2013**, *117*, 13403–13412.

(209) Komaba, S.; Yabuuchi, N.; Ozeki, T.; Han, Z. J.; Shimomura, K.; Yui, H.; Katayama, Y.; Miura, T. *J. Phys. Chem. C* **2012**, *116*, 1380–1389.

(210) Révay, Z.; Kudějová, P.; Kleszcz, K.; Söllradl, S.; Genreith, C. *Nucl. Instruments Methods Phys. Res. Sect. A* **2015**, *799*, 114–123.

(211) Wang, C.; Gong, Y.; Dai, J.; Zhang, L.; Xie, H.; Pastel, G.; Liu, B.; Wachsman, E.; Wang, H.; Hu, L. *J. Am. Chem. Soc.* **2017**, *139*, 14257–14264.

(212) Wetjen, M.; Trunk, M.; Werner, L.; Märkisch, B.; Revay, Z.; Gilles, R.; Gasteiger, H. A. **2018**, manuscript in preparation.

(213) Jaiser, S.; Müller, M.; Baunach, M.; Bauer, W.; Scharfer, P.; Schabel, W. *J. Power Sources* **2016**, *318*, 210–219.

(214) Müller, M.; Pfaffmann, L.; Jaiser, S.; Baunach, M.; Trouillet, V.; Scheiba, F.; Scharfer, P.; Schabel, W.; Bauer, W. *J. Power Sources* **2017**, *340*, 1–5.

(215) Westphal, B. G.; Bockholt, H.; Günther, T.; Haselrieder, W.; Kwade, A. *ECS Trans.* **2015**, *64* (22), 57–68.

(216) Landesfeind, J.; Eldiven, A.; Gasteiger, H. A. *J. Electrochem. Soc.* **2018**, *165* (5), A1122–A1128.

(217) Li, C.; Wang, Y. *J. Electrochem. Soc.* **2011**, *158* (12), A1361–A1370.

(218) Hagiwara, H.; Suszynski, W. J.; Francis, L. F. *J. Coatings Technol. Res.* **2014**, *11* (1), 11–17.

(219) Landesfeind, J.; Hattendorff, J.; Ehrl, A.; Wall, W. A.; Gasteiger, H. A. *J. Electrochem. Soc.* **2016**, *163* (7), A1373–A1387.

(220) Xie, L.; Zhao, L.; Wan, J.; Shao, Z.; Wang, F.; Lv, S. *J. Electrochem. Soc.* **2012**, *159* (4), A499–A505.

(221) Li, J.; Le, D.-B.; Ferguson, P. P.; Dahn, J. R. *Electrochim. Acta* **2010**, *55*, 2991–2995.

(222) Solchenbach, S.; Wetjen, M.; Pritzl, D.; Schwenke, K. U.; Gasteiger, H. A. *J. Electrochem. Soc.* **2018**, *165* (3), 512–524.

(223) Gabrielli, G.; Marinaro, M.; Mancini, M.; Axmann, P.; Wohlfahrt-Mehrens, M. *J. Power Sources* **2017**, *351*, 35–44.

(224) Sivakkumar, S. R.; Pandolfo, A. G. *Electrochim. Acta* **2012**, *65*, 280–287.

(225) Kim, H. J.; Choi, S.; Lee, S. J.; Seo, M. W.; Lee, J. G.; Deniz, E.; Lee, Y. J.; Kim, E. K.; Choi, J. W. *Nano Lett.* **2016**, *16*, 282–288.

(226) Elazari, R.; Salitra, G.; Gershinsky, G.; Garsuch, A.; Panchenko, A.; Aurbach, D. *Electrochem. commun.* **2012**, *14*, 21–24.

(227) Marinaro, M.; Weinberger, M.; Wohlfahrt-Mehrens, M. *Electrochim. Acta* **2016**, *206*, 99–107.

(228) Shanmukaraj, D.; Grugeon, S.; Laruelle, S.; Douglade, G.; Tarascon, J. M.; Armand, M. *Electrochem. commun.* **2010**, *12*, 1344–1347.

(229) Wetjen, M.; Freiberg, A. T. S.; Pritzl, D.; Ostermeyer, S.; Cadus, S.; Gasteiger, H. A. **2018**, manuscript in preparation.

(230) Jung, S.-K.; Gwon, H.; Hong, J.; Park, K.-Y.; Seo, D.-H.; Kim, H.; Hyun, J.; Yang, W.; Kang, K. *Adv. Energy Mater.* **2014**, *4*, 1300787.

(231) Yabuuchi, N.; Makimura, Y.; Ohzuku, T. *J. Electrochem. Soc.* **2007**, *154* (4), A314–A321.

(232) Kim, M. G.; Shin, H. J.; Kim, J.-H.; Park, S.-H.; Sun, Y.-K. *J. Electrochem. Soc.* **2005**, *152* (7), A1320–A1328.

(233) Varzi, A.; Bresser, D.; Von Zamory, J.; Müller, F.; Passerini, S. *Adv. Energy Mater.* **2014**, *4*, 1400054.

(234) Wang, Z.; Fu, Y.; Zhang, Z.; Yuan, S.; Amine, K.; Battaglia, V.; Liu, G. *J. Power Sources* **2014**, *260*, 57–61.

(235) Krause, L. J.; Chevrier, V. L.; Jensen, L. D.; Brandt, T. *J. Electrochem. Soc.* **2017**, *164* (12), A2527–A2533.

(236) Wetjen, M.; Hong, G.; Solchenbach, S.; Pritzl, D.; Gasteiger, H. A. **2018**, manuscript in preparation.

(237) Xiong, D. J.; Ellis, L. D.; Nelson, K. J.; Hynes, T.; Petibon, R.; Dahn, J. R. *J. Electrochem. Soc.* **2016**, *163* (14), A3069–A3077.

(238) Xiong, D.; Burns, J. C.; Smith, A. J.; Sinha, N.; Dahn, J. R. *J. Electrochem. Soc.* **2011**, *158* (12), A1431–A1435.

(239) Xu, C.; Lindgren, F.; Philippe, B.; Gorgoi, M.; Björefors, F.; Edström, K.; Gustafsson, T. *Chem. Mater.* **2015**, *27*, 2591–2599.

(240) Etacheri, V.; Haik, O.; Goffer, Y.; Roberts, G. A.; Stefan, I. C.; Fasching, R.; Aurbach, D. *Langmuir* **2012**, *28*, 965–976.

(241) Choi, N.-S.; Yew, K. H.; Lee, K.; Sung, M.; Kim, H.; Kim, S.-S. *J. Power Sources* **2006**, *161* (2), 1254–1259.

(242) Nakai, H.; Kubota, T.; Kita, A.; Kawashima, A. *J. Electrochem. Soc.* **2011**, *158* (7), A798–A801.

(243) Shkrob, I. A.; Wishart, J. F.; Abraham, D. P. *J. Phys. Chem. C* **2015**, *119*, 14954–14964.

Acknowledgements

First of all, I would like to thank my PhD supervisor Prof. Hubert Gasteiger for his invaluable guidance and genuine support during the previous years. The trust you put in your co-workers, your commitment to science, as well as your inspirational and encouraging attitude create a unique environment at the Chair of Technical Electrochemistry at TUM which allows students to grow personally and great science to evolve. Thank you for this.

I want to thank Veronika Pichler and Michele Piana for their support and unremitting engagement at our Chair. Without you, the TEC could not have grown to the place it is today. My thanks also go to all members of our group, for the exciting discussions, mutual support, and outstanding atmosphere. Never forget that you are the ones who write the next chapter of lithium-ion, fuel-cell, and electrolysis research.

Big thanks go to my LiMo team of Yelena Gorlin, Anne Berger, Manu Patel, and Qi He. In addition, I want to thank Sophie Solchenbach, Anna Freiberg, and Markus Trunk for proof reading of this thesis. Many thanks also go to my former students Anna Freiberg, Gloria Hong, Stefan Oswald, Stefan Niesen, Lukas Graser, and Wan Da Hao for their contributions and commitment to our joint research projects. I wish you all the best for your future.

I also want to thank my co-workers Markus Trunk, Lukas Werner, Roman Gernhäuser, and Bastian Märkisch from the Physics Department at TUM, as well as Zsolt Révay and Ralph Gilles from Heinz Maier-Leibnitz Zentrum (MLZ). I am glad to have been received so well on your team and to have been involved in the development of an exciting new experiment at the PGAA facility at MLZ.

Furthermore, I thank Vasiliki Tileli and Jing Hou from the École Polytechnique Fédérale de Lausanne (EPFL, Switzerland) for hosting me in February 2017 and for introducing me to transmission electron microscopy. I won't forget your great hospitality and your support to overcome one of the most challenging research questions during my PhD.

My special thanks go to Prof. Shinichi Komaba for inviting me to join his group at the Tokyo University of Science (Japan) and for offering me the chance to immerse into the Japanese culture and science.

I further want to thank my external project partners for fruitful discussions, the trustful collaboration as well as their great patience with my repeated inquiries. This includes Jürgen Pfeiffer, Robert Maurer, Stefan Haufe, Jürgen Stohrer, and Irmgard Buchberger from Wacker Chemie AG, Susanne Cornfine, Sonja Gürster, Tristan Harzer, and Reza Ghadimi from JEOL (Germany) GmbH, Markus Pompetzki, Stefanie Ostermeyer, Stefanie Cadus, and Konrad Holl from Volkswagen Varta Microbattery Forschungsgesellschaft mbH, as well as Oliver Gröger, Susanne Giesbers, and Wolfgang Zipprich from Volkswagen AG.

Before I started my PhD, I already had the chance to work alongside outstanding scientists from whom I have learned a lot not only about electrochemical energy storage but also about what it means to be a good scientist. This knowledge greatly helped me to return to science after almost three years in business and to join a highly reputable group such as Hubert’s. Therefore, I also want to thank Prof. Stefano Passerini and Guk-Tae Kim from the Helmholtz Institute in Ulm, Prof. Martin Winter and Mario Joost from the University of Münster, Prof. Bruno Scrosati, Jusef Hassoun, and Maria Assunta Navarra from the Universita Sapienza in Rome (Italy), Prof. Markus Bäumer from the University in Bremen, as well as Daniel Fenske from the Fraunhofer IFAM in Bremen. In addition, I want to thank Jake Christensen, Christina Johnson, Sarah Stewart, Reinhardt Klein, and Timm Lohmann from the Robert Bosch Research and Technology Center (RTC) in Sunnyvale (CA, USA) for giving me the opportunity to immerse into the innovative spirit of the Silicon Valley and to work in an inspiring and outstanding team on product-related research questions.

I gratefully acknowledge the financial support from the Federal Ministry of Economic Affairs and Energy under the auspices of the LiMo project (funding number 03ET6045D), and the German Academic Exchange Service (DAAD) for the travel scholarship to attend the 232nd ECS Meeting in National Harbor, MD, USA.

Finally, I would like to thank my partner Christine Teske as well as my parents Harry and Petra Wetjen for their continuous and tireless support throughout the last decades. Thank you for being the way you are and for being part of my life.

Scientific Contributions

Articles

M. Trunk,[=] **M. Wetjen**,[=] L. Werner, R. Gernhäuser, B. Märkisch, Zs. Révay, H.A. Gasteiger, and R. Gilles, "Materials Science Applications of Neutron Depth Profiling at the PGAA facility of Heinz Maier-Leibnitz Zentrum", *submitted.*

M. Wetjen,[=] M. Trunk,[=] L. Werner, R. Gernhäuser, B. Märkisch, Zs. Révay, R. Gilles, and H.A. Gasteiger, "Quantifying the Distribution of Electrolyte Decomposition Products in Silicon-Graphite Electrodes by Neutron Depth Profiling", *Journal of The Electrochemical Society*, **165** (10), A2340-A2348 (2018).

M. Wetjen, S. Solchenbach, D. Pritzl, J. Hou, V. Tileli, and H.A. Gasteiger, "Morphological Changes of Silicon Nanoparticles and the Influence of Cutoff Potentials in Silicon-Graphite Electrodes", *Journal of The Electrochemical Society*, **165** (7), A1503-A1514 (2018).

S. Solchenbach, **M. Wetjen**, D. Pritzl, K.U. Schwenke, and H.A. Gasteiger, "Lithium Oxalate as Capacity and Cycle-Life Enhancer in LNMO/Graphite and LNMO/SiG Full Cells", *Journal of The Electrochemical Society*, **165** (3), A512-524 (2018).

M. Wetjen, D. Pritzl, R. Jung, S. Solchenbach, R. Ghadimi, and H.A. Gasteiger, "Differentiating the Degradation Phenomena in Silicon-Graphite Electrodes for Lithium-Ion Batteries", *Journal of The Electrochemical Society*, **164** (12), A2840-A2852 (2017).

D. Pritzl, S. Solchenbach, **M. Wetjen**, and H.A. Gasteiger, "Analysis of Vinylene Carbonate (VC) as Additive in Graphite/$LiNi_{0.5}Mn_{1.5}O_4$ Cells", *Journal of The Electrochemical Society*, **164** (12), A2625-A2635 (2017).

[=] Authors contributed equally to this work

M. Wetjen, G.-T. Kim, M. Joost, G.B. Appetecchi, M. Winter, and S. Passerini, “Thermal and electrochemical properties of PEO-LiTFSI-Pyr$_{14}$TFSI-based composite cathodes, incorporating 4 V-class cathode active materials”, *Journal of Power Sources*, **243**, 846-857 (2014).

M. Wetjen, G.-T. Kim, M. Joost, M. Winter, and S. Passerini, “Temperature dependence of electrochemical properties of cross-linked poly(ethylene oxide)-lithium bis(trifluoromethanesulfonyl) imide-N-butyl-N-methylpyrrolidinium bis(trifluoro-methane sulfonyl)imide solid polymer electrolytes for lithium batteries”, *Electrochimica Acta*, **87**, 779-787 (2013).

M. Wetjen, M.A. Navarra, S. Panero, S. Passerini, B. Scrosati, and J. Hassoun, “Composite Poly(ethylene oxide) Electrolytes Plasticized by N-Alkyl-N-butylpyrrolidinium Bis(trifluoromethane-sulfonyl)imide for Lithium Batteries”, *ChemSusChem*, **6**, 1037-1043 (2013).

Articles in preparation

M. Wetjen, A.T.S. Freiberg, D. Pritzl, S. Ostermeyer, S. Cadus, and H.A. Gasteiger, “Mitigating the Impedance Growth in SiG//NMC811 Lithium-Ion Batteries by Prelithiation of the Silicon-Graphite Anode”, *manuscript in preparation.*

M. Wetjen, G. Hong, S. Solchenbach, D. Pritzl, and H.A. Gasteiger, “Evaluating EC, FEC, and DiFEC as Electrolyte Constituents for Silicon-Graphite Electrodes: Reduction Mechanism and Consumption”, *manuscript in preparation.*

M. Wetjen,$^{=}$ M. Trunk,$^{=}$ L. Werner, R. Gernhäuser, B. Märkisch, Zs. Révay, R. Gilles, and H.A. Gasteiger, “Monitoring the Lithium Concentration across the Thickness of Silicon-Graphite Electrodes during the first (De-)Lithiation”, *manuscript in preparation*.

D. Pritzl, A. Bumberger, **M. Wetjen**, J. Landesfeind, S. Solchenbach, and H.A. Gasteiger, “Identifying Contact Resistances in High-Voltage Cathodes by Impedance Spectroscopy”, *manuscript in preparation*.

Oral presentations

"Investigating the Distribution of Electrolyte Decomposition Products (SEI) in Silicon Electrodes By Neutron Depth Profiling", ECS AiMES Meeting, **Cancun**, Mexico, Abstr. #427 (**2018**) *accepted contribution*.

"Less is More! - Decreasing Silicon Particle Degradation By Limiting the Delithiation Cut-off Potential", 232nd ECS Meeting, **National Harbor**, Maryland, USA, Abstr. #424 (**2017**).

"DiFEC the Rescue? Evaluating Di-Fluoroethylene Carbonate as Additive for Silicon Electrodes", 231st ECS Meeting, **New Orleans**, Louisiana, USA, Abstr. #213 (**2017**).

"Silicon-Graphite Composite Electrodes for High Energy Density Li-Ion Battery Applications", ECS PRiME Meeting, **Honolulu**, Hawaii, USA, Abstr. #280 (**2016**).

"Composite Poly(ethylene oxide) Electrolytes Plasticized by N-Alkyl-N-butylpyrrolidinium Bis(trifluoromethane- sulfonyl)imide for Lithium Batteries", The 4th ITP International Symposium, **Rome**, Italy (**2011**).

Poster presentations

"Mitigating the Impedance Growth in SiG//NMC811 Lithium-Ion Batteries by Prelithiation of the Silicon-Graphite Anode", 19th International Meeting on Lithium Batteries (IMLB), **Kyoto**, Japan, Abstr. #P035TUE (**2018**).

"Investigation of the Porosity and Tortuosity of Silicon-Graphite Electrodes in Lithium-Ion Batteries", 232nd ECS Meeting, **National Harbor**, Maryland, USA, Abstr. #2176 (**2017**).

"Quantifying the Degradation Phenomena of Silicon-based Electrodes in Lithium-Ion Batteries", MSE Colloquium, **Munich**, Germany (**2017**).

"Reducing Electrolyte Consumption of Silicon-Electrodes through Capacity-Limited Cycling", 231st ECS Meeting, **New Orleans**, Louisiana, USA, Abstr. #1992 (**2017**).

"FEC, what else? Understanding the Degradation Mechanisms in Silicon-Graphite Composite Electrodes", 5th Workshop Lithium-Sulfur-Batteries, **Dresden**, Germany (**2016**).